EVALUATION OF THE STABILITY AND SUITABILITY OF ARTIFICIAL CONCRETE PILLARS IN LONGHOLE OPEN STOPING: A CASE STUDY OF AL MASANE AL KOBRA MINE, SAUDI ARABIA.

BY

DANIEL MABETI

THESIS SUBMITTED TO THE UNIVERSITY OF ZAMBIA IN FULFILMENT OF THE REQUIREMENTS FOR THE AWARD OF DEGREE OF DOCTOR OF PHILOSOPHY IN MINING ENGINEERING

UNIVERSITY OF ZAMBIA

LUSAKA

SEPTEMBER 2024

DECLARATION

I, **Daniel Mabeti,** declare that this work was done by myself, with valuable assistance from various people at the Al Masane Al Kobra mine in the Kingdom of Saudi Arabia and the University of Zambia, School of Mines, Mining Engineering Department. To the best of my knowledge, I declare that this dissertation has been audibly supervised by Professor Emmanuel K. Chanda, assisted by Professor Radhe Krishna, and has never been submitted before for the award of any Doctor of Philosophy (PhD) degree. All works of other researchers have been duly acknowledged.

Signature: ……

Date: ……

CERTIFICATE OF APPROVAL

This thesis of Daniel Mabeti is approved as a partial fulfilment of the requirement for the award of the degree of Doctor of Philosophy in Mining Engineering by the University of Zambia.

Principal Supervisor: Professor Emmanuel K. Chanda

Signature: …….

Date: …….

Co-Supervisor: Professor Radhe Krishna

Signature: …….

Date: …….

Internal Examiner: Dr. Bunda Besa

Signature: …….

Date: …….

Internal Examiner: Dr. Victor Mutambo

Signature: …….

Date: …….

External Examiner: Professor Fancis Decosta

Signature: ……..

Date: ……..

Examination Board of Chair:

Signature: ……..

Date: ……..

Dedication

To my family: my late Mom, my wife Bertha, my children Bukata, Daniel, and Mphatso, my Dad, and brothers and sisters.

Abstract

This study has demonstrated that artificial concrete pillars can stabilize the active stopes, especially in broader sections of the orebodies intercepted with geotechnical challenges such as high-stress change, spalling, slabbing, sloughing, etc. FLAC3D numerical code was successfully used to simulate the stopes before and after installing artificial concrete pillars. The challenges encountered in long-hole open stoping were briefly highlighted in the statement problem of this study. The structure of the study is also briefly stated in the initial chapter of the thesis. Literature on stope stability and pillar design theories was also reviewed. The Pillar Strength and Stress theories were also examined as the basis for artificial concrete pillars. The available constitutive models in the FLAC3D suitable for evaluating the stability of stopes and artificial concrete pillars are also discussed, and their shortcomings are noted. It was pointed out that the Hoek-Brown failure criterion was the best for analyzing rock mass properties compared to other available criteria. FLAC3D numerical code has also been described in detail, stating the steps involved in the numerical simulation, input parameters required, boundary condition, commands for excavation, convergence involved, and interpretation of the results.

Two case studies were presented, one of which involved mining a sill pillar and the other mining a crown pillar. Both case studies presented similar geotechnical challenges, such as poor rock mass, increased hydraulic radius, and collided ground support. Scaling and re-supporting were conducted before installing artificial pillars in the two stopes. Artificial concrete pillars were installed in these two stopes. The study has presented the construction of artificial concrete pillars for installation. Materials required for constructing artificial concrete pillars are aggregate (54.5%), and (27.3%) Cement (18.2%) and reinforcement wires. The water and cement ratio must also be maintained at 0.5 of cement slurry. Cement slurry and aggregate mixing were done by using a front-end loader. The artificial concrete pillars at 28 days of age should bear above 24Mpa as a requirement to be transported underground. This challenges quality control and assurance if the design mixing ratio is not achieved, as the concrete blocks will crumble during transportation or at the packing stage. Loading and unloading of the packs was done using telehandler.

After the concrete packs are installed in the stope, welded wire mesh is also installed around, and afterwards, 75-100 mm thick shotcrete is sprayed.

Geotechnical data was collected through underground mapping, laboratory testing, and field measurements. Underground mapping aided in defining the materials to be used in the FLAC3D numerical code. At the construction stage, samples were extracted from the mixed concrete and taken for laboratory testing. Uniaxial compressive strength, density, Young's modulus, internal friction angle, and cohesion were tested on these samples.

The material properties were used as input parameters in FLAC3D numerical code to simulate the stability of the stope before and after artificial concrete pillars were installed. The results for zones of displacement magnitude, local force ratio, state by average failure and convergence were considered in the analysis comparing before and after installing artificial concrete pillars. The results for zones of displacement with artificial concrete pillars installed presented a reduction in both cases by 97% and 99 % in cases 1 and 2, respectively. Zones' local force ratio presented an

85% and 71% reduction in cases 1 and 2, respectively, when installing artificial concrete pillars. Also, the zone convergence results showed a further reduction of 80% in case 1 and 63% in case 2 when artificial concrete pillars were installed. Zone state failures by average also showed a significant improvement in tensile and shearing in the roof and sidewalls of the two stopes.

Field measurements were conducted on the installed convergence pins using a tape extensometer. Both scenarios indicate a substantial 70% reduction in displacements before and after for the crown pillar's roof and a 60% reduction for the sill pillar. Notably, the sidewalls in both cases experienced a significant 10% reduction for the crown pillar and a 5% reduction for the sill pillar. These results underscore the effectiveness of the author's approach, reinforcing the success of the research and enhancing structural stability.

The above analysis has revealed that the designed artificial concrete pillars can be effectively used as a support system to prevent roof collapse in active stopes. FLAC3D numerical simulation and field measurements showed the stope's stable condition after installing artificial concrete pillars. Therefore, the designed artificial concrete pillars can be used to meet the needs of safety of mining operations; however, real-time stability monitoring of the concrete pillars must be emphasized at some key positions. The investigation has also revealed that artificial concrete pillars can replace original ore pillars in many mines worldwide; the problem encountered with such is the self-failure mechanism of artificial concrete pillars, which has been puzzling the safety of operations in many mines.

Acknowledgements

My most extreme gratitude to my Principal Supervisor, Professor Emmanuel K. Chanda, for his excellent supervision, guidance and constant interest in this dissertation. I have been amazingly fortunate and lucky to have a supervisor who allowed me to explore independently and encouraged me to ensure I finish my studies within the stipulated period. At times, I gave up, but he encouraged me to ensure I finished my research. I have also enormously benefited from his knowledge and learned much wisdom. I have also valued his outwardly continued supply of ideas, many of which have been incorporated into my thesis, and I also appreciate his willingness to read my research.

I am also grateful to Professor Radhe Krishna, my Co-Supervisor, for his suggestions, valuable contribution, and recommendations. As a renowned expert in the field of rock mechanics, his guidance was invaluable during my research. I would like to appreciate the valuable guidance he shared during my research. His words of encouragement and wisdom, especially when he was working with the University of Zambia. I enormously benefited from his knowledge and wisdom especially in the field of rock mechanics.

I want to acknowledge the Underground Mine Manager at Al Masane Al Kobra mine (AMAK), Mr. Sinan B AVCI, for his support throughout my Ph.D. studies. As the person responsible for overseeing the underground mining operations, his contribution and mentorship were crucial to ensure I included valuable steps in my studies, from data collection to result analysis.

Special thanks to the Itasca Consulting Group for their help throughout my studies. Being part of the Itasca Education Program (IEP) and having the opportunity to use geotechnical software helped me successfully conduct my research without any challenges.

I would also like to thank Mr Alex Cabrera, the Geomechanical Engineer for Itsaca, Chile, for his mentorship, guidance, and encouragement in using the Itasca code and interface.

I am also grateful to the Al Masane Al Kobra mine Technical team for the help they gave me in collecting valuable data for my research. Their expertise in mining operations and data collection was instrumental in my research. I want to thank Mr. Anderson Makunka for his valuable contributions to the artificial concrete pillars theories he shared with me. Thanks also to Mr. Lastone Mbiri, geological superintendent at Munali Nickel Mine for his encouragement and support for my studies at the University of Zambia.

I am very grateful to my Wife, Bertha, for encouraging me to finish my studies; it motivates her. I appreciate your valuable contribution, support, and help.

Above all, I thank the Almighty Jehovah God for the power and strength provided to me; it hasn't been easy without God's intervention.

Table of Contents

DECLARATION II
CERTIFICATE OF APPROVAL III
Dedication IV
Abstract V
Acknowledgements VII
List of Figures XII
List of Tables XV
Chapter 1 : INTRODUCTION 1
1.1. Research Background 1
1.2. Problem Statement 2
1.3. Main Objective 3
1.3.1. Secondary Objectives 3
1.4. Benefit of the Study 3
1.5. Research Approach 4
1.6. Research Framework 4
1.7. Thesis Structure 5
Chapter 2 : LITERATURE REVIEW 6
2.1. Introduction 6
2.2. Analytical Methods 6
2.2.1. Stress-Driven Failure 6
2.2.2. Gravity Driven Failure 11
2.2.3. Combination of Gravity and Stress Driven 14
2.3. Empirical Stability Design Methods 15
2.3.1. Geomechanics Classification System 15
2.3.2. Modified Rock Mass Rating (MRMR) 17
2.3.3. Modified Stability Number 19
2.4. Pillar Design Methods 23
2.4.1. Pillar Design Theories 23
2.5. Numerical Modeling Methods 37
2.5.1. Model Types 38

2.5.2. Constitutive Models in Numerical Modeling 39
2.6. Conclusions 51
Chapter 3 : METHODOLOGY 54
3.1. Introduction 54
3.2. FLAC3D Background 54
3.3. Material Properties 56
3.3.1. Intrinsic Deformability Properties 57
3.3.2. Intrinsic Material Strength Properties 60
3.3.3. Extrapolation to Field-Scale Properties 62
3.4. Boundary Conditions 65
3.4.1. Stress Boundary Condition 65
3.4.2. Excavation Command in FLAC3D 67
3.4.3. Displacement Boundary 68
3.5. Initial Conditions 68
3.5.1. Uniform Stresses without Gravity 69
3.5.2. Stresses with Gradients/Uniform Material 69
3.5.3. Initial Stress State with gravitational gradient 70
3.6. Reaching Equilibrium 70
3.6.1. Criteria for Determining Convergence 70
3.7. Result Interpretation 72
3.7.1. Unbalanced Force and Convergence Results 72
3.7.2. Gridpoint Velocity Results 73
3.7.3. Plastic Indicator Results 73
3.8. Case Study 74
3.8.1. Case Study 1: Mining a Sill Pillar 74
3.8.2. Case Study 2: Mining a Crown Pillar 76
3.8.3. Rock Mass Condition for Case Studies 77
3.8.4. Empirical Stope Stability Assessment 78
3.8.5. Installation of Artificial Concrete Pillars 80
3.9. Conclusion 85

Chapter 4 : APPLICATION TO A CASE STUDY – AL MASANE MINE 87
4.1. General Information about the Study Site 87
4.1.1. Location 87
4.1.2. General Geology 88
4.1.3. Al Masane Geotechnical Units 90
4.1.4. Al Masane Rock Mass Characterization 91
4.1.5. Mining Methods 110
4.2. Geotechnical Data Collected 113
4.2.1. Introduction 113
4.2.2. Data Collection Methodology 113
4.2.3. Geotechnical Input Parameters 116
4.3. Numerical Modeling 118
4.3.1. Introduction 118
4.3.2. Model Setup for SA-1498 Stope in FLAC3D 119
4.3.3. Model Setup for SA-1575 Stope in FLAC3D 119
4.3.4. Numerical modelling Results 120
4.3.5. Conclusion 131
Chapter 5 : DISCUSSION OF THE RESULTS 133
5.1. Introduction 133
5.1.1. Displacement Results 133
5.1.2. Convergence Results 134
5.1.3. State Failure By Average 134
5.1.4. Local Force Ratio Results 135
5.2. Conclusion 135
Chapter 6 : CONCLUSIONS AND RECOMMENDATIONS 137
6.1. Conclusions 137
6.2. Recommendations 139
REFERENCES 141
APPENDICES 153
Appendix 1: Geotechnical Mapping Sheet for data collection 153
Appendix 2: Displacement measurements data form 153

Appendix 3: FLAC3D Script 154
Appendix 4: Estimate of the Geological Strength Index (GSI) 156

List of Figures

Figure 2.1: Stress estimate by Kirsch's equations defined by the polar coordinates (Kirsch, 1898) 8
Figure 2.2: Basic concept of M-C failure criterion envelope (Sofiano and Nomikos, 2006) 9
Figure 2.3: Basic concept of H-B Failure Criterion (after Hoek et al., 2004) 10
Figure 2.4: Concept of the beam deflection (after Obert and Duval, 1967) 12
Figure 2.5: Parameters in the beam deflection concept (after Duval and Obert, 1967) 13
Figure 2.6: Stand-up time estimate using excavation span and RMR (Bieniawski,1993) 17
Figure 2.7: MRMR Stability graph (Laubscher, 2001) 19
Figure 2.8: Mathew's stability factors (after Potvin, 1988) 21
Figure 2.9: Modified Stability Graph with Support (after Nickson, 1992) 23
Figure 2.10: Plan view simplification of the area tributary method (Brady and Brown, 2004) 25
Figure 2.11: Vertical Cross Section for extraction ratio estimation (after Rydee and Jager, 2002) 26
Figure 2.12: Concept of the area tributary for pillar design (Hoek et al., 2002) 26
Figure 2.13: Pillar stability graph relating pillar strength to pillar stress (after Hadley and Grant, 1972) . 31
Figure 2.14: Pillar stability graph relating pillar width/height ratio to pillar stress (after Hedley and Grant, 1972) 32
Figure 2.15: Pillar Stability graph for Potvin et al (1989) 33
Figure 2.16: Pillar stability graph for Krauland and Soder (1987) 34
Figure 2.17: Pillar Stability Graph relating average pillar confinement and average pillar stress to UCS (after Lunder and Pakalnis, 1997) 35
Figure 2.18: Pillar Stability Graph relating Pillar width to height ratio and the average pillar stress to UCS (after Lunder and Pakalnis, 1997). 36
Figure 2.19: Intact rock mass response when load is applied at different geometric scale (Brady and Brown, 1985). 38
Figure 2.20: Mohr-Coulomb failure criterion (Itasca, 2022) 42
Figure 2.21: Mohr-Coulomb model-domains used in the definition of the flow (Itasca, 2021) 43
Figure 2.22: Relationship of H-B and M-C constitutive models (Itasca, 2022) 49
Figure 3.1: Local face axes defined by (d) dip direction, (s) strike direction, and (n) normal direction (Itasca, 2021) 66
Figure 3.2: Section of the mine where the study was conducted 74
Figure 3.3: Longitudinal section (a) and plan long hole drilling pattern (b) of the SA 1498 stope, respectively (Designed using i-ring Aegis software) 75
Figure 3.4: Saadah 1498 C23 Stope before ground support reinforcements were installed 75
Figure 3.5: Longitudinal Section of the SA 1575 Cross Cut 4 North Crown Pillar Stope 76
Figure 3.6: Status of the SA 1575 Cross Cut 4 Crown Pillar stope before artificial pillars were installed 77
Figure 3.7: Status of the SA 1575 Stope before artificial pillars were installed 77
Figure 3.8: Stope stability assessment using the Potvin (1998) Stability Graph for two stopes used as case studies 79
Figure 3.9: Artificial Concrete mold with reinforced wire (a) and concrete design for easy lifting by telehandler machine (b) 80
Figure 3.10: Pouring of the mixed concrete into the mold (a) and operator distributing the concrete (b) .. 81

Figure 3.11: Concrete pack constructed before being removed (a) and constructed concrete pack ready to underground. 82
Figure 3.12: Artificial pillar installation after packing (a) and after shotcreting the pillars (b) 83
Figure 3.13: Condition of the artificial concrete pillars during longhole drilling 83
Figure 3.14: Condition of the artificial pillars during production loading from draw-points (a) and the condition of the artificial pillar after the last blast (b) 84
Figure 3.15: Crushing of the poorly constructed concrete packs 85
Figure 4.1: Location of the Al Masane project (source: WGM, 2007) 87
Figure 4.2: Main geology for Al Masane Al Kobra mine (after Sabir and Pouit, 1982) 90
Figure 4.3: Joint character and condition data for the three main sets (Griffs et al, 2000) 91
Figure 4.4: Rock Mass rating distribution by Geotechnical Unit (WGM, 2007) 95
Figure 4.5: Regional Stress Map (Vita-Finzi and Saadi, 2001) 97
Figure 4.6: Stability Graph chart used to determine Stable spans (after Hutchinson and Diederichs, 1996) 101
Figure 4.7: Al Masane Al Kobra stope longitudinal section (Griffis et al., 2000) 104
Figure 4.8: Crown pillar thickness design for Saadah section (Griffs et al., 2000) 107
Figure 4.9: Crown Pillar Analysis C_s vs.Q (Carter and Milner, 1995) 108
Figure 4.10: Longitudinal bench and fill (WGM, 2007) 112
Figure 4.11: Sample preparation (a) and concrete strength testing (b) 114
Figure 4.12: Strength comparison with the curing time (days) 115
Figure 4.13: Model setup for SA-1498 Stope in FLAC3D. 119
Figure 4.14: Model Setup for SA1575 Stope 120
Figure 4.15: Zone Displacement Magnitude results before artificial concrete pillars were installed for SA1498 stope 121
Figure 4.16: Zone Displacement Magnitude results after artificial concrete pillars were installed for SA1498 stope 121
Figure 4.17: Zone Local Force Ratio results before artificial pillars were installed for the SA1498 stope. 122
Figure 4.18: Zone Local Force Ratio results after artificial pillars were installed for the SA1498 stope. 122
Figure 4.19: Zone State By Average results before artificial pillars were installed for the SA1498 stope 123
Figure 4.20: Zone State By Average results after artificial concrete pillars were installed in SA1498 stope. 124
Figure 4.21: Zone Convergence results before artificial concrete pillars were installed in the SA1498 stope 125
Figure 4.22: Zone Convergence results after artificial concrete pillars were installed in the SA1498 stope 125
Figure 4.23: Zone Displacement Magnitude results before artificial concrete pillars were installed in SA1575 Stope 126
Figure 4.24: Zone Displacement Magnitude results after artificial concrete pillars were installed in SA1575 Stope 127

Figure 4.25: Zone Local Force Ratio results before artificial concrete pillars were installed in the SA1575 stope 128
Figure 4.26: Zone Local Force Ratio results after artificial concrete pillars were installed in SA1575 stope 128
Figure 4.27: Zone State By Average results before artificial concrete pillars were installed in SA1575 stope 129
Figure 4.28: Zone State By Average results after artificial concrete pillars were installed in SA1575 stope 129
Figure 4.29: Zone Convergence results before artificial cocnrete pillars were installed in SA1575 Stope 130
Figure 4.30: Zone Convergence results after artificial concrete pillars were installed in SA1575 stope. 130

List of Tables

Table 2.1: Description of the rating systems for RMR (Bieniawski, 1989) and in situ RMR (Laubscher, 1992). 18
Table 3.1: Geotechnical numerical modeling steps recommended in FLAC3D 54
Table 3.2: Selected elastic constants (laboratory-scale) for Rocks (Goodman, 1980) 58
Table 3.3: Elastic constant values for transversely isotropic rocks (Batugin and Nirenburg, 1972) 58
Table 3.4: Selected strength Properties (laboratory-scale) for Rocks (adapted from Goodman, 1980) 61
Table 3.5: Rock Mass Condition for two sections used as case studies 78
Table 3.6: Values of β amd μ (adopted from Ardiaca, 2009). 85
Table 4.1: Summary of lithological and geotechnical units observed at Al Masane (WGM, 2007) 92
Table 4.2: Summary of mean structural discontinuity orientations (Griffs et al, 2000). 93
Table 4.3: Summary of RMR '76 Data (Griffs et al, 2000) 93
Table 4.4: Summary of NGI-Q Data (Griffs et al, 2000) 94
Table 4.5: Summary of Al Masane rock strength data (WGM, 2007) 96
Table 4.6: Al Masane Drift Support recommendations (Griffs et al., 2000) 98
Table 4.7: Al Masane drift dimensions and use (Griffs et al, 2000) 99
Table 4.8: Standard bolting patterns at various drift widths (Griffs et al, 2011) 100
Table 4.9: Summary of geotechnical data for Q' and Intact Rock Strength (WGM, 2007) 101
Table 4.10: Al Masane Stoping Scenarios for stability graph methods (Griffs et al, 2000) 102
Table 4.11: Scenario 1 – Empirical Stope Stability Analysis for Inclined Hangingwall, Slabbing Failure (Griffs et al, 2000) 103
Table 4.12: Scenario 2 – Empirical Stope Stability Analysis for Inclined Hangingwall, Slabbing Failure (Griffs et al., 2000) 104
Table 4.13: Scenario 1 – Hydraulic Radius (Griffs et al, 2000) 105
Table 4.14: Scenario 2 – Empirical Stope Stability Analysis for Inclined Hangingwall, Slabbing Failure (Griffs et al, 2000) 105
Table 4.15: Scenario 2 – Hydraulic Radius (Griffs et al, 2000) 105
Table 4.16: Scenario 2 – Empirical Stope Stability Analysis for Inclined Hangingwall, Slabbing Failure (Griffs et al, 2000) 106
Table 4.17: Summary of parameter values and corresponding distributions used in probabilistic crown pillar design analysis (Griffs et al, 2000). 109
Table 4.18: Summary of parameter values and corresponding distributions used in probabilistic crown pillar design analysis (Griffs et al, 2000). 110
Table 4.19: Laboratory test results for the samples (Testing conducted at 28 days) 114
Table 4.20: Laboratory test results for the samples (Testing conducted at 14 days) 114
Table 4.21: Laboratory test results for the samples (Testing conducted at 7 days) 115
Table 4.22: Geotechnical input parameters obtained from geotechnical mapping, laboratory and Roclab. 117

Chapter 1 : INTRODUCTION

1.1. Research Background

This study evaluates the stability of the open stope with the innovative artificial concrete pillars installed before production drilling, blasting, and loading operations commence. Ground control challenges are experienced in underground mines, especially bulk mining methods with large underground openings (Zaki, 2022). A standard bulk mining method with large underground openings is long hole open-stoping mining method in which long holes are drilled agreeing to a predetermined pattern and cover a range of ore thicknesses from narrow to far-reaching and dips from 0^{o} to 90^{0} (Zaki, 2022). These large underground openings are subjected to high-stress conditions due to bulk mining rates, high field stresses in the high deep mining, and the existence of numerous discontinuities (Martin and Maybee, 2000; Gaede et al., 2014; Zou et al., 2015). Stopes are supported artificially to lighten ground instability in many underground mines (Napa-García et al., 2019). To alleviate ground failure caused by these induced stresses, timber packs are applied for passive temporal support requirements in many underground mines (Deriveries and Bernados, 2017; Sinha and Watton, 2021). Pillars in underground mines can be replaced with timber packs to act as a passive temporal support system (David, 2017; William, 2022). However, timber packs have a negative impact on the natural ecosystem, biodiversity, and climate change. Besides, to have timbers at the mine site is time-consuming and very costly, subject to the location of the mine site (Napa-Garcia et al., 2015). Saudi Arabia is a desert region, and having timber packs is time-consuming and costly. The environmental aspect of cutting down trees most likely affects the ecosystem (Napa-Garcia et al., 2015). Hence, a methodology for designing artificial concrete pillars for temporal support is vital for optimum safety and production in shallow or deep mining operations. In some modern underground mines, concrete pillars are used as a substitute for timber packs (Cougar, 2014; Cougar, 2015; Sahoo et al., 2020).

Various studies have been recorded on testing the strength properties of artificial concrete pillars and evaluating their suitability (Gaede et al., 2014). The most common methodology for evaluating the strength and performance of artificial pillars is through laboratory testing and numerical simulations (Gaede et al., 2014). The mechanical properties of concrete, soil, and other polymeric materials can be obtained by laboratory testing (Zhou et al., 2015; Idriss et al., 2015; Potvin, 2017).

This study takes a comprehensive approach, considering a wide range of factors that influence the stability of the stope and the performance of the artificial concrete pillars. These factors include the mine's stress condition, rock mass condition, experimental exercise for the samples, innovative artificial concrete pillar preparation, stope stability, transportation, and installation of the pillars. The study also thoroughly reviews relevant literature on the empirical, analytical, and numerical concepts of stope stability and pillar design theories. This comprehensive approach ensures that all aspects of the research are thoroughly examined and considered, enhancing the reliability of the study's findings.

This study aims to thoroughly evaluate the stability and effectiveness of artificial concrete pillars when utilized as a support system in active stopes. This investigation holds the potential to

significantly enhance the safety and structural integrity of mining operations. This evaluation considers a range of geotechnical problems, from poor ground conditions to the width of certain portions of the orebody. To achieve this, a framework was developed that combines an empirical rock mass classification system and numerical modelling tools. The stability of the stope was assessed using the adopted numerical modelling code, both before and after installing artificial concrete pillars. The main objective of this study was to evaluate the stability and effectiveness of artificial concrete pillars, ensuring they comply with the principles of support for providing stability and safety of the mine while allowing recovery of ore in wide sections of the orebody at low cost. This underscores the importance and relevance of the research in the field of mining engineering.

Daily underground trips and inspections were made to the selected sections where the study was conducted for seven continuous months from the time of backfilling, data collection, support design, support preparation, artificial concrete pillar installation, drilling, blasting, etc. Various geotechnical instruments were used the rock mass was surveyed using visual diagrams and photographic methods, and the following rock mass parameters were measured: uniaxial compressive strength of intact rock mass, orientation of the discontinuities, joint properties, joint spacing, geological structures, etc.

After compiling the geotechnical data from the field visits, geotechnical mapping, and geotechnical core logging, statistical representation of geotechnical information was performed using various geotechnical software. This was done to represent the case studies using empirical rock mass classification systems. The stability assessment was then evaluated by using the adopted numerical modelling code. The numerical modelling codes considered for this study are the explicit and dynamic code FLAC3D. Chapter Four explains this process in detail with case study examples. The stages of construction for artificial concrete pillars have been highlighted and elaborated on in Chapter Four. The process of installing artificial pillars has also been explained in detail. Chapter Four underscores the paramount importance of quality assurance/quality control (QA/QC) as the primary focus of this support system. The numerical results are succinctly summarized and effectively presented in Chapter Four. In Chapter Five, the results are meticulously compared to other recent studies on stope and pillar stability assessments. Additionally, the study explores various strategies for enhancing innovative artificial concrete pillars, as highlighted in Chapter Six within the recommendations.

1.2. Problem Statement

Ground instability challenges in stope panels are common in underground mines, ranging from highly stressed conditions to adverse ground conditions involving swelling, squeezing, spalling, etc. This manifests from the number of rockfalls experienced before, during, and after mining. Stope stability challenges can lead to major or minor fall of ground which can cause the loss of production, equipment damage, loss of life, and an increase in dilution. A reliable and suitable methodology for evaluating stope stability will be adopted to enhance safe production. This will require evaluating the stope stability using either an empirical or a numerical approach. The

methodology must consider all geotechnical factors that govern the stability or instability of the stope and the support system to be applied.

The major geotechnical problem experienced at the mine site used as a case study is stope instability in the wider section of the orebody. In sections where two limbs of the orebody are intercepted, after mining is completed for the bottom blocks, the two orebodies usually get connected due to the collapse of the middle pillar, making a single wide stope. In this case, the critical dimension or the hydraulic radius is exceeded when plotted against the stability number. Innovative artificial concrete pillars have been adopted and installed to mine such stopes safely to prevent major ground collapse. Therefore, the problem must be evaluated from the initial to the final stage, where the innovative artificial concrete pillars are installed.

1.3. Main Objective

The main objective of this study is: -

To evaluate the stability and suitability of the innovative artificial concrete pillars in stopes with various geotechnical ground conditions using a numerical design method in FLAC3D code.

1.3.1. Secondary Objectives

The secondary objectives of the research project are: -

i. To develop the most appropriate and reliable method of designing artificial concrete pillars.
ii. To create a database of geotechnical data through underground mapping, laboratory sample testing and field measurements.
iii. To determine rock mass quality for various stress environments of the site used as case studies.
iv. To determine the material properties that can be used as geotechnical input parameters in the numerical model.
v. Develop the numerical code that can aid in evaluating the stability and suitability of artificial concrete pillars.
vi. Apply the developed numerical modelling code to analyse and compare the results with those of other studies.

1.4. Benefit of the Study

The following are the benefits of this study.

a) Climate Change Impacts.

Using timber elements as an underground support system has some limitations (Anderegg et al., 2020). Increased timber use can lead to deforestation and unsustainable forest management, and we see the realistic effects of climate change (Anderegg et al., 2020). Another environmental impact of the increased use of timber is its effect on the ecosystem (Anderegg et al., 2020). Therefore, replacing timbers with innovative artificial concrete pillars as temporal support systems will help eliminate the impact of climate change.

b) Economic Impacts

Besides the above on the climate impact, the study site is in the desert region, where having timbers on site would be very costly. This can have an economic impact on the operation of the mine. Despite the cost aspect not being considered, having timbers at the mine site can still be uneconomical and time-consuming.

c) Rock Engineering Research Impact

The principles adapted in the methodology to evaluate the stability to ensure the producing stopes are fully supported with the proposed innovative artificial concrete pillars can be applied to other places. The methodology can be applied to other related rock engineering projects and studies, especially in countries or regions where timbers are scarce to have them.

d) Alternative Ground Support System

The evaluated support system in the form of innovative artificial concrete pillars can be used as an alternative to other existing support systems that are time-consuming and uneconomic, like timber packs, steel arch sets, etc.

1.5. Research Approach

The following outlines the research approach adopted in this study. Reviewing literature relevant to stope stability and pillar design concepts, collecting geotechnical data through underground visits and geotechnical mapping, reviewing external geotechnical reports for the mine site, laboratory testing, and actively participating in constructing innovative pillars, field measurements, etc. The collected data was evaluated using rock mass classification systems such as rock mass rating, Q-system, Mathews-Potvin stability assessment, and mining rock mass rating system. The study also highlights the critical stope spans and hydraulic radius in wider portions, which must be addressed in most geotechnical designs. This empirical evaluation was conducted on a small scale as the main scope was more on numerical modelling. Numerical modelling was undertaken to evaluate stability in the two scenarios given as examples. Then, numerical modelling results were presented and analyzed separately.

1.6. Research Framework

Stope stability could be defined as one or more of the following: -

i. Local instability due to poor support or incorrect support installed.
ii. Regional instability over a large span is mainly due to poor rock mass condition or structural controlled instability driven.
iii. Pillar instability, which is mainly due to poor design
iv. Stope stability due to time of exposure or stand-up time

However, this study focuses on conducting a numerical analysis of the adopted support system in the form of innovative artificial concrete pillars and evaluating the stability, effectiveness, and efficiency of using this support system.

1.7. Thesis Structure

This thesis consists of six chapters, from the introduction to the presentation of results, recommendations, and conclusions. This is outlined as follows: -

Chapter One: This pivotal Chapter sets the stage for the study, providing the necessary context and outlining the problem statement, objectives, benefits, and research methodology that underpin the investigation.

Chapter Two: This Chapter reviews relevant literature on stope stability and pillar design theories. It delves into empirical designs involving rock mass classification and pillar design concepts, such as the theories for determining pillar strength and stress. The other literature reviewed is the beam and plate theory and the kinematic concept. This Chapter also provides a comprehensive review of numerical modelling theories for continuum and discontinuum, establishing a solid foundation for the research.

Chapter Three: This Chapter describes the study's detailed methodology that has been adopted. This Chapter presents the numerical code adopted in this study. The numerical code presented steps involved in the simulation and other principles in FLAC3D. The constitutive models adopted in this study have also been given in detail.

Chapter Four: This Chapter applies the methodology to a case study. This involved a comprehensive understanding of the mine study site and the geotechnical design principles crucial for the mine, support, stope, and crown pillar design. The geotechnical data, presented in a practical and useful manner, aids in visualizing the mine site and its potential challenges. The methodology employed for collecting geotechnical data is also presented in this Chapter. The Chapter also presents the results obtained in FLAC3D numerical modelling in graphical and pictorial views.

Chapter Five: This Chapter discusses the results of numerical modelling presented in Chapter Four by summarizing the essential contents. This Chapter also compares the results that have been obtained from other studies of a similar nature.

Chapter Six: This Chapter presents this study's key findings from the study objectives, recommendations, and conclusions.

Chapter 2 : LITERATURE REVIEW

2.1. Introduction

This Chapter reviews the literature on stope stability assessments and design methodology in rock engineering. The literature reviewed in this Chapter covers topics related to stope stability and pillar design theoretical methods. The topics include analytical, empirical, and numerical concepts for solving rock engineering problems. Empirical concepts are based on experience designs. Empirical concepts are usually estimated based on field data analysis and case studies. Analytical concepts are based on experimental and laboratory tests. They usually involve estimating material strength and applied load using different failure criteria for determining stability. Numerical approaches are based on the simulation of conceptual designs to determine the induced stress effect of mining. Numerical simulations are critical to estimate the stability of underground excavation based on different computer-based approaches. This computer-based software incorporates different failure criteria to simulate the underground excavations to determine stability.

2.2. Analytical Methods

The analytical concept describes the failure mode in three types: gravity, stress, and combination (Hoek et al., 2000). In determining the stability of an open stope, failure can occur due to stress, gravity, or a combination referred to as relaxation.

2.2.1. Stress-Driven Failure

When the applied load is more than the strength of the rock mass, failure is likely to occur, referred to as stress-driven failure. Stress can be in compression or tension. Tension failures are common in shallow mines and are reviewed in the next section. Failures in compression are caused by high-stress concentration; this is common in stope edges, remnants, under-designed pillars, etc. Most design criteria for estimating stress around the opening consider rock mass properties and in situ stress field input parameters. Various failure criteria have been used to estimate stresses. These failure criteria base their concept on estimating intact rock mass strength (Hoek et al., 2002). A high safety factor estimates the weak and robust intact rock mass. Most failure criteria used in rock engineering are limited to estimating compressive stresses only (Hoek et al., 2002). Hoek and Brown's failure is the most common failure criterion for estimating rock mass properties (Hoek et al., 2002), while Mohr-Coulomb is widely used in estimating soil properties (Hoek et al., 2002). These two failure criteria are reviewed in detail in the proceeding sections under constitutive models. The earliest method of estimating stresses was using the Kirsch Equations (Hoek et al., 2002). Stresses around openings can also be estimated using numerical simulation. Different numerical simulations are adopted depending on the problem being evaluated. Numerical modeling type, concept, and specific examples are discussed in the proceeding Section 2.5.1.

1) Kirsch Equations for Estimating Stresses

Kirsch's (1898) Equations are the earliest approach to determining the stresses around the excavation in 2D for an elastic body. Kirsch Equations have been used to estimate stresses for simple cross-sectional circular holes forming in an infinitely long tube within an infinite medium (Kirsch, 1898). The polar coordinate system was to express the equations relatively. Stresses are defined as forces acting perpendicular to the face of an element, located at a radius of r and a polar coordinate and an angle of θ (Goodman, 1989). Kirsch Equations are expressed below (Equations (2.1, 2.2 and 2.3).

$$\sigma_{rr} = \frac{\sigma_v}{2}\left[(1+K)(1-a^2) - (1-K)\left(1+\frac{3a^4}{r^4}-\frac{4a^2}{r^2}\right)cos2\theta\right] \quad (2.1)$$

$$\sigma_{\theta\theta} = \frac{\sigma_v}{2}\left[(1+K)\left(1+\frac{a^2}{r^2}\right) + (1-K)\left(1+\frac{3a^4}{r^4}\right)cos2\theta\right] \quad (2.2)$$

$$\sigma_{r\theta} = \frac{\sigma_v}{2}(1-K)\left(1-\frac{3a^4}{r^4}+\frac{2a^2}{r^2}\right)sin2\theta \quad (2.3)$$

Where: -

σ_{rr} - Radial stress
$\sigma_{\theta\theta}$- Tangential stress,
$\sigma_{r\theta}$- Shear stress,
σ_v - Vertical stress,
σ_h- Horizontal stress,
K - Ratio of horizontal stress to vertical stress (K=σ_h/σ_v),
θ - Polar angle measured counter-clockwise from positive x-axis,
a - Radius of the hole, and
r - Distance from the hole centre

Stress magnitude around the opening is related to the magnitude of the far-field stress, and this is expressed as a ratio of horizontal to vertical stress, geometry size, and distance from the opening (Brady and Brown, 2004). Radial and shear stresses are defined to be zero on the excavation boundaries (Brady and Brown, 2004). Figure 2.1 below shows that tangential stresses are high on the excavation boundaries. They are perpendicular to the minor principal stress (i.e., at r = a, θ = π/2). In contrast, tensile stresses are low (e.g., when K >= 3) on the excavation boundaries perpendicular to the significant principal stress (i.e., at r = a, θ = 0).

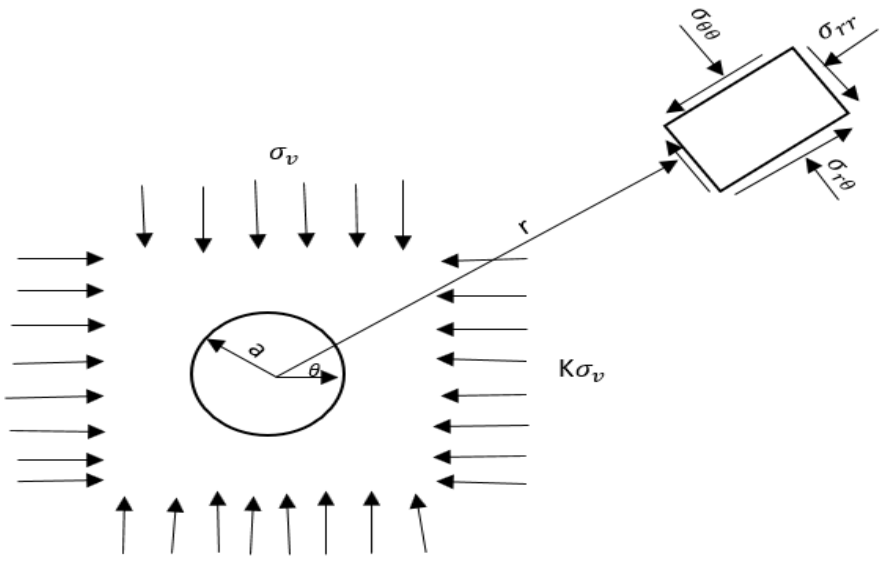

Figure 2.1: Stress estimate by Kirsch's equations defined by the polar coordinates (Kirsch, 1898)

2) Mohr-Coulomb (M-C) Failure Criterion

Shear failure occurs when the rock mass is under compression because of the external applied load (Sofiano and Nomikos, 2006). Shear strength is defined by two factors in the rock mass: cohesion and normal stress (Sofiano and Nomikos, 2006). The increased rock mass strength under confinement defines shear failure. M-C failure criterion basic concept with a tensile cut-off is shown in Figure 2.2. The M-C failure criterion envelope line in the tension cut-off concept is extended to the tensile region where the minor principal stress (σ_3) equals the Uniaxial Tensile Strength of the intact rock mass. M-C failure criterion envelope Equations (2.4 and 2.5) are expressed as follows:

$$\tau = \frac{1}{2}(\sigma_1 - \sigma_3)sin(\frac{\pi}{2} + \Phi) \qquad (2.4)$$

Or

$$\tau = \frac{1}{2}(\sigma_1 - \sigma_3)sin2\beta \qquad (2.5)$$

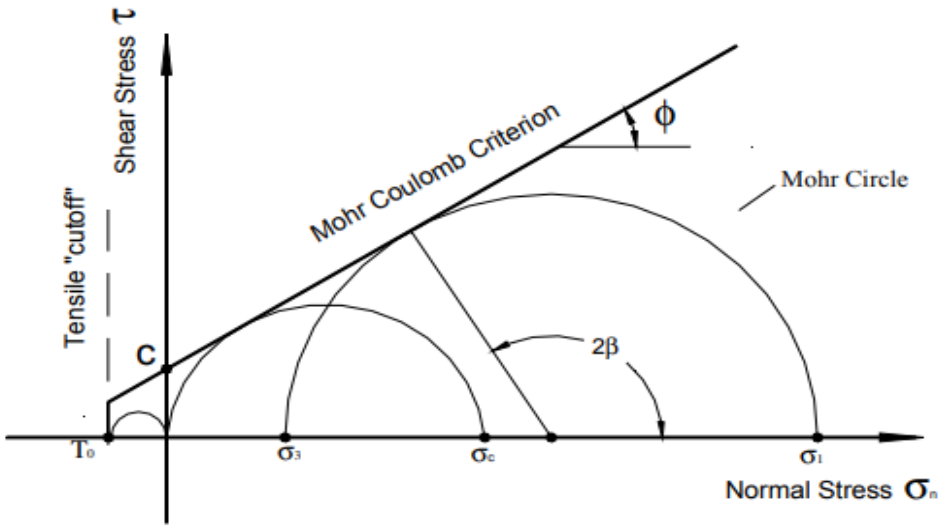

Figure 2.2: Basic concept of M-C failure criterion envelope (Sofiano and Nomikos, 2006)

Where: -

T= Shear Strength
σ_1 = Major Principal Stress
σ_3 = Minor Principal Stress
φ = internal friction angle.
$\beta = 45^o + \varphi/2$

M-C failure criterion envelope in compression state can also be expressed as the maximum principal stress (σ_1) by the following formulation below.

$$\sigma_1 = \sigma_c + \sigma_3 \left(\frac{1+sin\phi}{1-sin\phi}\right) \qquad (2.6)$$

Where:

σ_c= Unconfined Compressive Strength

The M-C failure criterion envelope is discussed in detail in Section 2.5.2 under constitutive models in numerical modeling.

3) Hoek and Brown Failure Criterion

The Hoek-Brown (H-B) is a failure criterion to estimate peak failure points at different confinement stress levels (Hoek and Brown, 2000). The criterion considers two constants, m and s, to account for rock mass strength properties. The constants, m and s are parameters in the Hoek and Brown that depends on the rock mass strength characteristics. Rock type, rock mass characterization, and classification systems are used to determine constants m and s. The H-B failure criterion formulation is expressed as shown below in Equation (2.7).

$$\sigma_1 = \sigma_3 + \sqrt{m\sigma_3\sigma c + s\sigma c^2} \qquad (2.7)$$

Where:

σ_1 = *Maximum Principal Stress*
m and s = Empirical constant

Figures 2.3 below show the H-B failure criterion curve with constant values of m and s (Hoek and Brown, 2019). H-B failure criterion has the advantage of incorporating the rock mass classification values, Q-system, and other rock mass classifications into the system according to the rock mass properties. H-B failure criterion is more applied to the rocks than soils, hence limiting its application, and the concept is purely based on empirical rather than experimental.

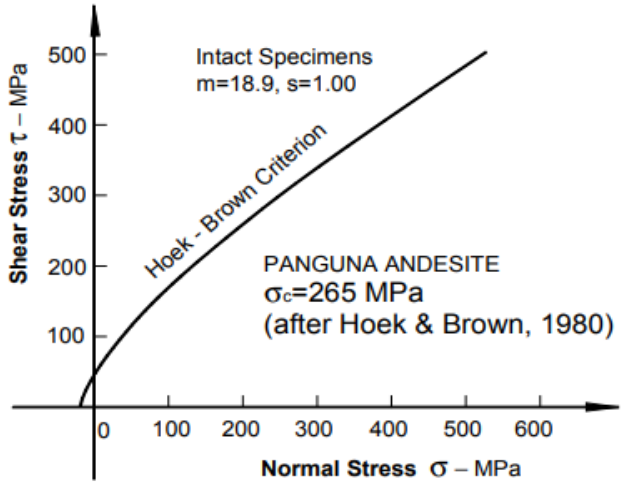

Figure 2.3: Basic concept of H-B Failure Criterion (after Hoek et al., 2004)

Stress concentration is high in pillars, footwall and hangingwall abutments, wide open stopes, etc. Failure is expected to occur in these areas if stress concentration exceeds the strength of the rock mass. High stress concentration can cause instability in open stopes (Hoek and Brown, 2000). In open stope geometry with low compressive and high tensile stresses, the estimate for tensile zones is usually unreliable because the H-B concept was developed from the compressive experiments (Hoek and Brown, 2000). The hanging wall of the stope usually consists of jointed rock masses with lower tensile zones and high compression zones (Hoek and Brown, 2000). Tensile zones loosen the rock mass, making it more susceptible to gravity-driven induced instability than stress-related failures. More details of the H-B failure criterion are discussed in Section 2.5.2 under constitutive models in numerical modeling.

2.2.2. Gravity Driven Failure

Gravity-driven related failures around an opening occur due to the dead weight of the material surrounding the rock mass (Sofiano and Nomikos, 2006). This theoretical concept of dead weight is considered in rock engineering theories of kinematic failure, beam theory, and plate theory. However, civil engineering originated the plate and beam theories (Sofiano and Nomikos, 2006). Kinematic concepts consider the rock mass properties, size, and number of wedges formed from the rock mass. Both underground and open pit mining use the idea of gravity-induced failures to analyze stability. These failures are discussed in detail below.

1) Kinematic Failure

Kinematic failure is sometimes called structurally controlled or wedge failure (Goodman, 1989). This failure analysis is prevalent in underground and open pit mines. The wedge or block formed from the roof or sidewall of the excavation is necessary for the formed wedge to be separated from the surrounding rock mass and at least intersect three structural discontinuities. The study by Goodman (1989) states that wedge failure can occur by sliding along one or more planes on a wall or back. Discontinuous properties such as frequency, condition, orientation, and size of the excavation will determine the number and size of wedges to be produced (Goodman, 1989). Induced stress around the tunnel and discontinuity conditions can also influence the stability of the formed wedge. Detailed mapping and understanding of a particular rock mass can determine potential wedges in a tunnel. Mapping data will assist in analyzing potential wedges by using numerical modeling codes such as Unwedge or stereonet analysis (Brady and Brown, 2004). Kinematic design methods offer more reliable estimates of wedges in tunnels. Scan line or window mapping can be conducted at a scale of tunnel excavation for wedge analysis. It is always a challenge to collect realistic joint property data in an open stope; therefore, for this reason, kinematic design is usually not used for estimating the stability of the stope (Brady and Brown, 2004).

2) Beam Failure

This theory is presented as an approximation of estimating the stability of the flexure beams and is shown in Figures 2.4 and 2.5 based on the following assumptions (Zhang et al., 2018).

i. *The beam has a longitudinal plane of symmetry and is in the form of a prismatic shape*
ii. *The material of a beam is linear, elastic, continuous, isotropic, and homogeneous.*
iii. *The beam must be straight and in length dimensional (either thicker or width) ratio larger than 8.*
iv. *Force is usually applied perpendicular to the longitudinal axis of the beam at a symmetrical state.*
v. *A plane section will remain planar during flexure failure in an unloaded beam.*
vi. *Deflection of the beam is assumed to be a circular arc of radius R. The deflection and slope are slight enough to express the curvature C as Equation (2.8) below.*

$$C = \frac{1}{R} = \frac{\left(\frac{d^2u_2}{dx_1{}^2}\right)}{\left(\left[1+\left(\frac{du_2}{dx_1}\right)^2\right]\right)^{\frac{3}{2}}} = -\frac{d^2u^2}{dx^{12}} \qquad (2.8)$$

Where: -

R = beam deflection circular arc radius

dx_1 = distance increment in x_1 direction

du_2 = *displacement increment in* x^2 *direction*

C = Curvature of the beam deflection

From the above expression, the curvature of the beam deflection C, with deflected slope θ (x_1) and applied load, can be estimated using the following Equations (2.9 and 2.10).

$$Deflection\ Curvature\ C = \frac{1}{R} = \left(\frac{d^2u_2}{dx_1{}^2}\right) = \left(-\frac{M_{13}}{EI_{33}}\right) \qquad (2.9)$$

$$Deflection\ slope\ \theta(x_1) = \frac{du_2}{dx_1} \qquad (2.10)$$

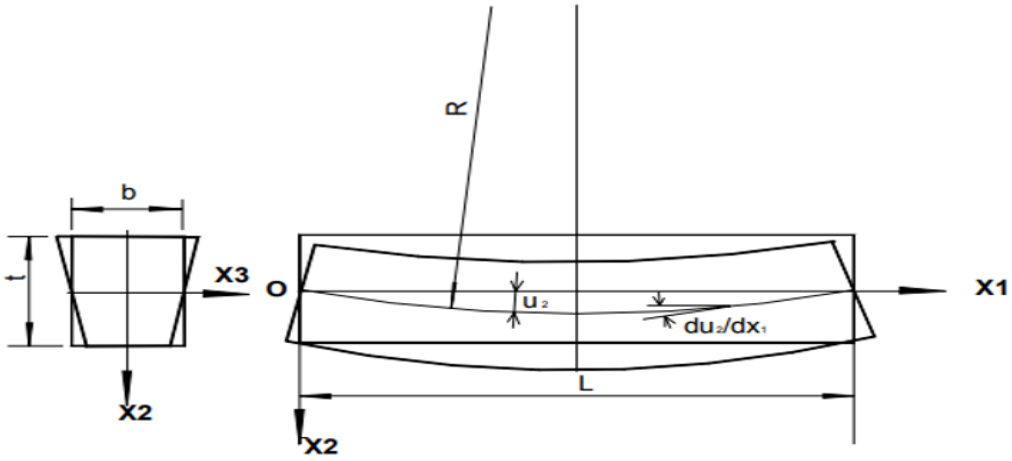

Figure 2.4: Concept of the beam deflection (after Obert and Duval, 1967)

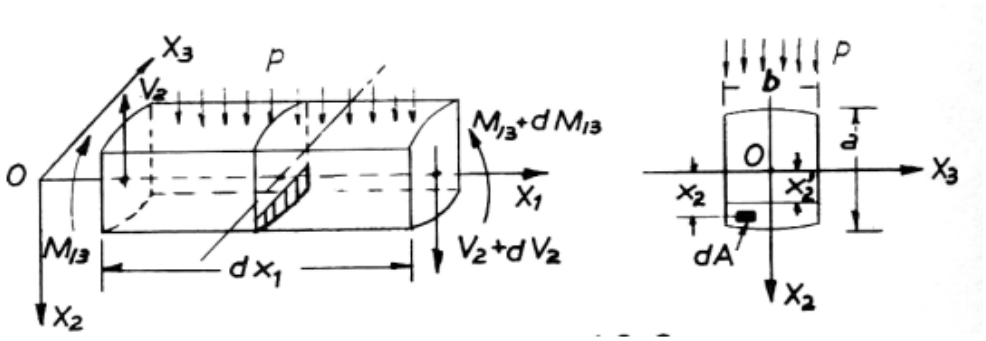

Figure 2.5: Parameters in the beam deflection concept (after Duval and Obert, 1967)

$$\sigma_{11} = \sigma_{11}(x_1 x_2) = M_{13} x_2 / I_{33} \quad (2.11)$$

$$\sigma^{12(x^1,x^2)} = \frac{V^2}{I^{33} b} \int_x^{\frac{a}{2}} x_2 \, dA = \frac{V_2 Q_3}{I_{33} b} \quad (2.12)$$

$$\sigma_{22} = \sigma_{33} = \sigma_{13} = \sigma_{23} = 0 \quad (2.13)$$

Where:

M_{13} = moment of bending about the OX_3 axis to the face normal to OX_1
E = Young Modulus of the material
I_{33} = moment of inertia of the section about the OX_3 axis
Θ (x_1) = deflection slope in OX_1 direction
Q_3 = static moment of the area A about the OX_3 axis
σ_{11}, σ_{12}, σ_{22}, σ_{33}, σ_{13} and σ_{23} are stresses.
V_2 = shear force in X_2 direction.

Whereas the thickness of the beam is determined according to the spacing of the laminations or beddings (Zhang et al., 2018). Maximum deflection is determined to be at the middle of the beam when under loading conditions. However, the compression zone is calculated by considering the beam's stress and deformation of allowable beam strength. The rock strength of the beam and material properties of a beam, such as Young's modulus (E) and Poisson's ratio (v), can be used to determine the allowable deformation range of the beam (Zhang et al., 2018). The disadvantage of this theoretic concept is that it assumes the rock mass can activate tensile stresses (Zhang et al., 2018). The lamination or bedding planes, which are parallel within the rock mass, will usually make tensile stress develop due to the breaks in the continuity of the rock mass (Zhang et al., 2018). This theory is not commonly used in stability designs.

3) Plate Failure

The plate failure theory is described with the following concepts and assumptions (Zhang et al., 2018). In this theory, a plate is defined as a straight or flat rectangular surface whose width is at least more than four times the thickness and whose length is equal to or greater than its width (Zhang et al., 2018). The following are considered in the plate failure theory.

i. Rock mass must be linearly elastic, isotropic, and homogenous.
ii. The plate is less than half its thickness for the maximum deflection.
iii. The applied force is always normal to the plate.
iv. When the plate is deflected, the central plane remains de-stressed.
v. Vertical lines remain straight and inclined after flexure failure.

In the theoretical concept, the rectangular plate length is denoted as b, plate width as a, and plate thickness as t, with built-in edges on all four sides and loaded by its weight (Zhang et al., 2018). The concept of plate theory is expressed as follows in Equations (2.14 and 2.15) to determine the maximum stress and deflection.

$$Maximum\ Deflection(n)\ Max = \frac{\alpha.\gamma.a^4}{Et^2} \quad (2.14)$$

$$Maximum\ Stress\ (\sigma_{max}) = \frac{6\beta.\gamma.a}{t} \quad (2.15)$$

Where: -

α and β = coefficients based on the plate length and width ratio for a Poisson's ratio of 0.3
γ = unit weight of the plate material
a = width of the plate material
E = Young's modulus
t = thickness of the plate material

The ratio of the strength of the plate material to the maximum induced stresses is used to determine the stability of the plate material (Zhang et al., 2018). This theory also assumes that the plate material can exhibit tensile stresses. However, the availability of cross joints makes it difficult for tensile stresses to be developed.

2.2.3. Combination of Gravity and Stress Driven

Instability due to stress relaxation is pervasive around the surface of the excavation opening (Martin and Martino, 2000). This is the case where the tensile stress is nearly zero. The pre-mining stresses' magnitude and orientation will change after every excavation stage. When the excavation is created below the surface, the above rock mass will be under a de-stressing state or relaxation state. This de-stressed zone will develop the state referred to as the tensile or relaxation zone. The intact rock and the discontinuities at this state have low or no tensile strength, making it difficult

for the tensile stress to build up in the rock mass. The tensile stress will induce an open tension crack in the rock mass joints and create relaxation zones. The individual blocks inside the relaxation zone are unconfined, with more movement freedom, and will be sensitive to gravitational forces (Brady and Brown, 2004). The blocks created in the relaxed zone of the back and walls of the excavation within the jointed rock mass may fall due to gravity. This combination of stress and gravity failure within excavation is related to the relaxation zone of failure (Kaiser et al., 1997; Martin et al., 2000; Clark, 2002; Diederichs and Kaiser, 1999). This instability problem is typical in shallow underground mines (Martin and Martino, 2000). The zone of relaxation can be analyzed using different numerical modeling methods. The numerical modeling methods to analyze the zone of relaxations in a particular opening are discussed in Section 2.5. The section discusses the empirical design methods employed in analyzing the stability of stopes and various pillar design theoretical concepts.

2.3. Empirical Stability Design Methods

This section describes different empirical methods for assessing the stability of the stope and various empirical methods for pillar designs. Empirical methods have been successfully employed in underground stope stability designs in Canada, Australia, South Africa, Zambia, the United States, and other parts of the world (Potvin and Milner, 1989). Mathew's Stability Graph is one of the earliest empirical methods developed for open stop stability design (Mathews et al., 1981). In the initial design, the Mathews stability graph had few case studies or histories. However, several modifications have happened to the Mathews Stability graph to suit a particular area. The first modification of Mathews's stability graph was by Potvin and Milner (1989). Potvin and Minlner (1989) added more case studies and redefined the factors. A recent modification of the Mathews Stability design graph is those studies of Nickson (2002), Purwanto et al. (2013), etc. The Geomechanical Classification system or ***Rock Mass Rating (RMR)*** by Bienswiaski (1989), the ***Modified Rock Mass Rating (MRMR)*** by Laubscher (1993), and the ***Norwegian Geotechnical Institute (NGI)*** or ***Q-system*** by Barton and Grimstad (1990) are some of the empirical designs that are used in stope design. The following sections describe different rock mass classification systems that can be applied to stope stability designs and briefly describe pillar design theoretical methods.

2.3.1. Geomechanics Classification System

The classification system, also called the Rock Mass Rating (RMR), was developed by Bieniawski (1973). Most case histories in the RMR were based on civil engineering background. This classification system has been modified recently as more case histories were included and examined from the mining engineering perspective (Swart, 2005). However, the RMR classification has been revised several times by assigning different parameters. The first modification of the geomechanics classification was version 1989 (Bieniawski, 1973). Despite that, Bieniawski's (1989) Rock Mass Rating classification (RMR89) is the most frequently used in rock engineering designs. The RMR classification system has been used extensively and applied by many authors worldwide and has stood the test of time (Swart, 2005). RMR considers six

parameters to quantify the Rock Mass Rating system: very good, good, fair, poor, and very poor (Swart, 2005). The following are the six parameters.

a) *Rock Quality Designation (RQD)*
b) *Joint Spacing (JS)*
c) *Joint Conditions (JC)*
d) *Uniaxial Compressive Strength (UCS)*
e) *Groundwater Condition*
f) *Joint Orientation*

The RMR classification system divides the rock mass into different domains, each with a different rating. Boundaries of each domain may coincide with a significant structural feature, such as a fault or a change in rock type. In situations with a substantial change in the joint spacing or condition with the same rock type, this will require dividing the rock mass into small domains. Some of the authors who modified the RMR classification system are Swart (2003), Laubscher and Page (1990), Laubscher (1977, 1984, 1990, and 1993), etc. The basic parameters considered in the modification are joint orientation, blast damage, mining-induced stress, and rate of weathering. This rock mass classification is known as the Mining Rock Mass Rating (MRMR) or Modified Rock Mass Rating (MRMR) system. The mining industry uses the classification system for stability design purposes (Swart, 2005).

MRMR classification system by Laubscher (1993) originated from the block-caving mining setup. For this reason, its application may be limited to specific mining environments. However, several other case histories were added to the database in recent years to make the application suitable. The different studies that showed the modification of the RMR are those of Swart (2005) and Palmström (1995). These modifications of the RMR are called the Modified Basic RMR (MBR) system for mining. MBR classification system was developed in the US specifically for block cave mining setup. The adjustment of RMR to produce the MBR is the structural features, the distance from the cave front, and the size of blocks to undergo caving and mining-induced stress field. The MBR classification system can be used to estimate support systems for tunnels.

The study of Bieniawski (1993) presented a graph that can be used to estimate the stability of a non-stope in terms of stand-up time and RMR value, as shown in Figures 2.6. This theory of evaluating the stand-up time of the open stope was initially developed by Lauffer (1958). This theory is unreliable due to the influence of factors such as extraction technique, durability, and pre-mining state stress, which are not considered in the classification system (Swart, 2005).

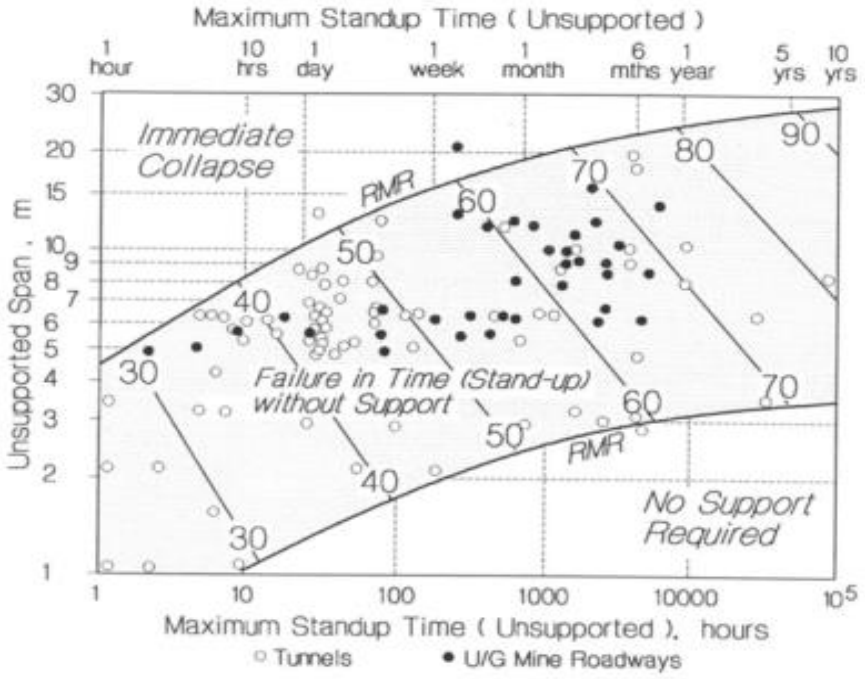

Figure 2.6: Stand-up time estimate using excavation span and RMR (Bieniawski,1993)

Therefore, the stand-up time should be used only for comparative purposes (Swart, 2005). This classification has advantages and disadvantages but will not be presented as it is outside the scope of this study.

2.3.2. Modified Rock Mass Rating (MRMR)

Laubscher (1977, 1984), Laubscher and Taylor (976), and Laubscher and Page (1990) modified the RMR to develop the Modified Rock Mass Rating (MRMR). The in-situ rock mass rating assigns the MRMR based on the rock mass properties and geological conditions. A total rating of 100 is adopted in the system and weighed according to the geological parameters. In situ rock mass rating, in this case, is referred to as RMR, and it must not be confused with the RMR of Bieniawski (Laubscher et al., 1990). Laubscher's (1992) RMR essentially described the same parameters as Bieniawski's (1989) RMR classification system. However, the rating weighting is different (Swart, 2005). Laubscher's (1992) in situ RMR is adjusted according to the rock mass condition of that mining environment to come up with the Mining Rock Mass Rating (MRMR) classification. The MRMR classification system considers the following adjustments: i) blasting, ii) weathering, iii) joint orientation, and iv) mining-induced stresses. MRMR classification system can be successfully used for stope stability design (Swart, 2005). The classification can also be utilized for support design using tables incorporating rock mass rating class and support technique recommendations (Swart, 2005). MRMR classification is a versatile empirical design method that can provide excellent design guidelines (Swart, 2005). This classification stipulated that different

geotechnical domains must be related separately, as average ratings can be misleading (Swart, 2005). These ratings are described below in Table 2.1.

Table 2.1: Description of the rating systems for RMR (Bieniawski, 1989) and in situ RMR (Laubscher, 1992).

No.	Parameters	Maximum Rating (In situ RMR)	Maximum Rating (RMR)
1).	Uniaxial Compressive Strength (UCS)	20	15
2).	RQD	15	20
3).	Joint Spacing	25	20
4).	Joint Condition and Groundwater	40	30-40

In most cases, the weak zone, regardless of size, may determine the response of rock mass to mining. The Rock Mass Strength (RMS) can be defined by considering the value of Rock Mass Rating (RMR) and Intact Rock Strength (IRS) values of a particular rock mass. It is critical to point out that rock mass strength cannot be more than that rock mass zone's corrected average intact rock strength. The IRS can be determined by testing rock specimens, and the values are rated at 80% as the strength of large specimens is weaker than that of small specimens. This reduction of IRS does not relate to the influence of joints on the strength of the rock mass and is expressed as follows in Equation (2.16):

$$RMS = \left(\frac{A-B}{80}\right) x\ C\ x \left(\frac{80}{100}\right) \qquad (2.16)$$

Where: -

A = Total RMR rating
B = IRS rating
C = IRS in MPa

The Design Rock Mass Strength (DRMS) is the design parameter used for stability purposes and considers the strength of unconfined rock mass at a particular site. DRMS is defined as the rock mass strength, which has been adjusted considering groundwater, joint orientation, weathering, and the effect of blasting in the design (Laubscher et al., 2001). These adjustments are like those considered in Laubscher's MRMR. DRMS offers advantages over the classification system in that it deems strength in the design and relates to in situ stresses. Most of the case studies used in the MRMR stability graph came from South Africa, Canada, the USA, and Zimbabwe (Swart, 2005). The MRMR stability graph is shown in Figure 2.7.

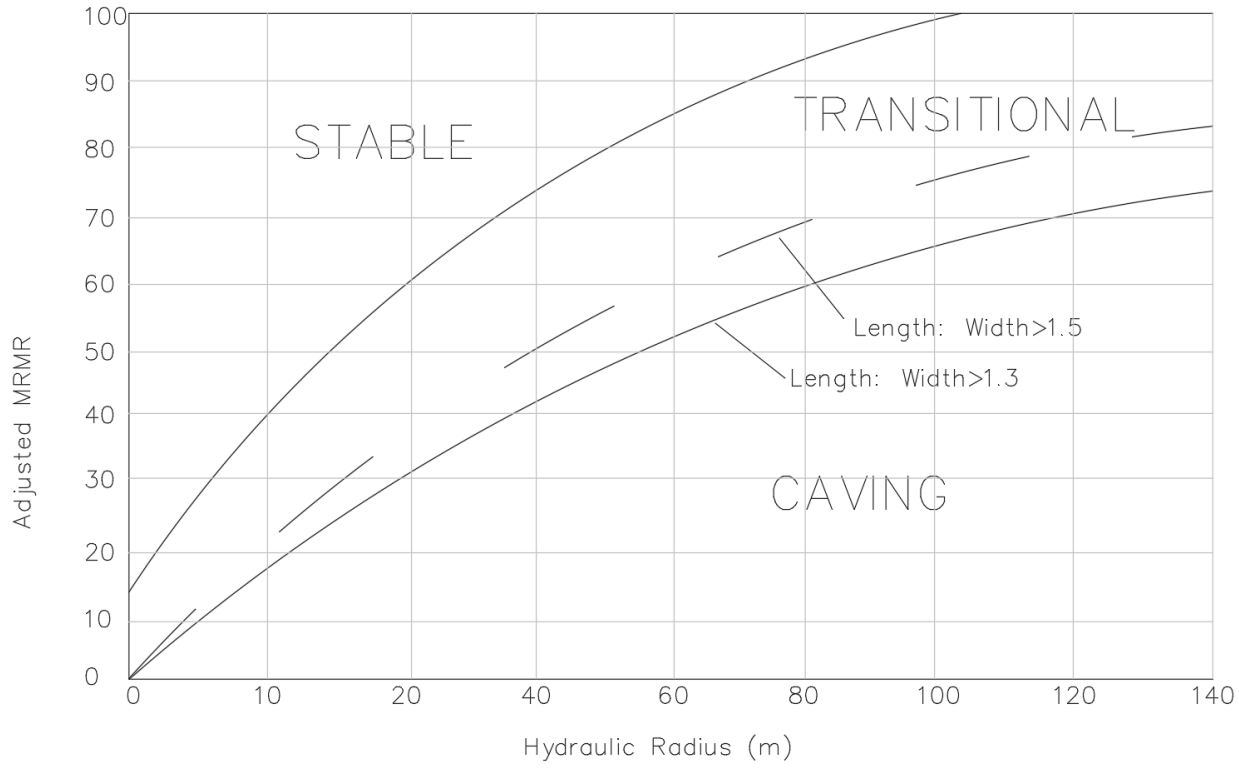

Figure 2.7: MRMR Stability graph (Laubscher, 2001)

Laubscher's (2001) stability graph estimates the stope stability using the MRMR and Hydraulic Radius (HR). As earlier explained in the previous section, the adjusted parameters in the MRMR are blasting, stress, weathering, and joint orientation. MRMR can also calculate the Design Rock Mass Strength (DRMS). The DRMS empirical method is widely used for stope design in South Africa and the Democratic Republic of Congo (Swart, 2005). Although the technique was developed from the caving mines, it provides very reliable approaches for evaluating the stability of stopes. Although two parameters of joint orientation and stress effect are considered in this empirical method, a certain level of experience in using this classification system is needed, especially in adopting and applying them (Swart, 2005).

For this reason, it makes it difficult to use other empirical designs. The influence of groundwater on the stability of the rock mass is always considered regardless of the condition of the joint strength being applied. This is not used in an arid environment.

2.3.3. Modified Stability Number

Mathew et al.'s (1981) Stability Number (N) and Potvin's (1988) modified Stability Number (N') are used to quantify the rock mass and conditions for stope stability design methods. These two classification systems are based on the same Equation. Still, the only difference is the weighting factors for A, B, and C. Potvin et al. (1988), Potvin and Nickson (1992), and Swart (2005) use the modified stability number (N') for stability design estimates. Stress Reduction Factor (SRF)

parameter becomes redundant if the classification system is used to estimate the rock mass properties in the analytical and numerical designs. Induced stresses are considered in this design process calculation. The modified stability number allows a separate assessment of stress conditions, as shown in Equation 2.17 below.

$$Q' = \frac{RQD}{Jn} x \frac{Jr}{Ja} x\, Jw \qquad (2.17)$$

SRF=1 (Clamped but not over-stressed rock mass) is considered in the design. Most deep mining environments are relatively dry (transient mine drilling water is not considered). Joint water (Jw), therefore, can also be 1.0. The modified Q' system classification is expressed in Equation (2.18) below.

$$Q' = \frac{RQD}{Jn} x \frac{Jr}{Ja} \qquad (2.18)$$

The modified Q' system considers the rock mass initially divided into geological or geotechnical district zones (e.g., hangingwall, footwall, ore formation, etc.). Each geotechnical district must be classified separately. The Modified Q' system must also consider other critical factors such as stress, gravity, joint conditions, and joint spacing to estimate the stability number, N', used in different classification systems for stability assessment. These stability assessment classification systems include Potvin and Nickson (1992) and Swart (2005). The modified stability expression is defined by the following Equation (2.19).

$$N' = Q' \; x \; A \; x \; B \; x \; C \qquad (2.19)$$

Where: -

N' = modified stability number
Q' = modified tunnelling quality index (NGI), with SRF = 1 (Barton, 1974)
A =Rock Stress Factor
B = Joint Orientation Adjustment Factor
C = Gravity Adjustment Factor

The values for A, B and C are determined by an empirical approach, as shown in Figure 2.8 below. The value for A is determined by dividing uniaxial compressive (UCS) with maximum induced compressive stress (σ_{max}), as shown in Figure 2.8 (a). Based on the site rock mass characterization data mapped in the stope, the dominating joint sets can be obtained. The dominating structural sets are determined using DIPS 7.0 (Rocscience Inc.), and the results can be summarized as plotted in Figure 2.8 (b). The value of gravity adjustment factor (C) can be estimated using a graph in Figure 2.8 (c), based on the inclination of each stope's surface (α)

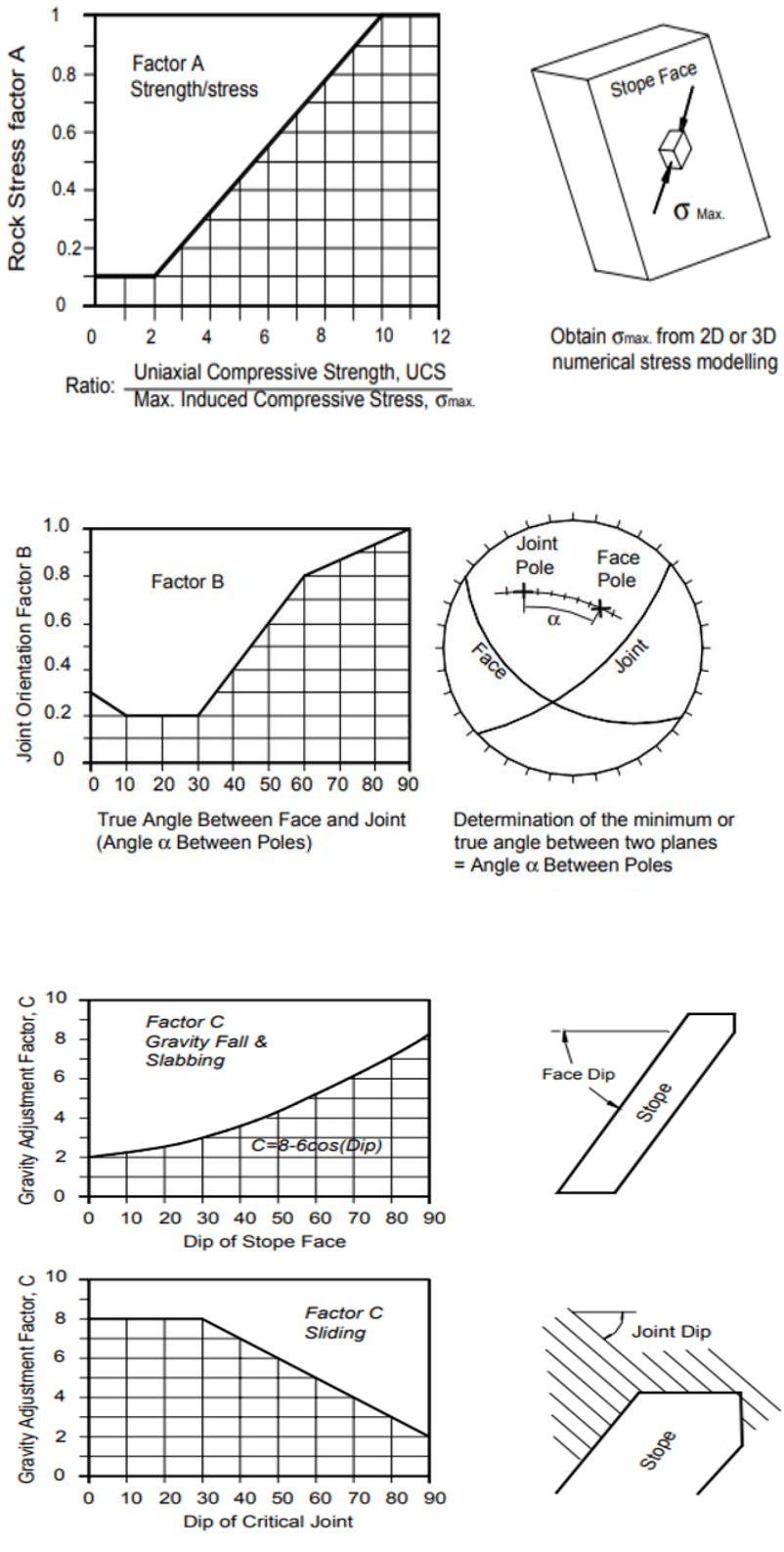

Figure 2.8: Mathew's stability factors (after Potvin, 1988)

1) Hydraulic Radius and Radius Factor

Hydraulic Radius (HR) or Shape Factor (SF) is used in the mining industry to define the excavation surface geometry. Initially, the term hydraulic radius was used in fluid mechanics to relate fluid flow in square pipes to circular pipes. Since then, it has been employed in the mining industry for empirical design purposes (Swart, 2005). The adopted empirical design formula is expressed as the area of a stope surface divided by the perimeter of that same surface, as shown in Equation 2.20.

$$HR = \frac{Area}{Perimeter} \qquad (2.20)$$

The hydraulic radius has been successfully used to evaluate the stability of stopes (Potvin and Milner, 1992). The stability number, N' value, and the HR are used together to define the stability in the stability graph. Hydraulic Radius (HR) or Shape Factor (SF) is plotted against the stability graph's N value. This empirical design method employs the graphical technique of estimating the stability of the walls of the underground openings based on the surface geometry, induced stresses, and other rock mass properties. The initial stability was presented with three zones: potentially stable, unstable, and caving (Potvin and Milner, 1992). The stability was later modified by Potvin and Milner (1992) by adding more case histories and redefining the adjustment factors, which led to a modified stability number, N'. Again, the stability graph was modified by Potvin and Milner (1992) by adding more case histories, in which the influence of cable bolt support was concluded. Further, the stability graph was modified by Nickson et al. (1992) to make it more practical and applicable to the mining environment in evaluating stope stability. The stability was delineated as stable, unsupported transition, stable with support, supported transition, and caved zones, as shown in Figure 2.9. This method has been used recently in most mines' stope stability design approaches.

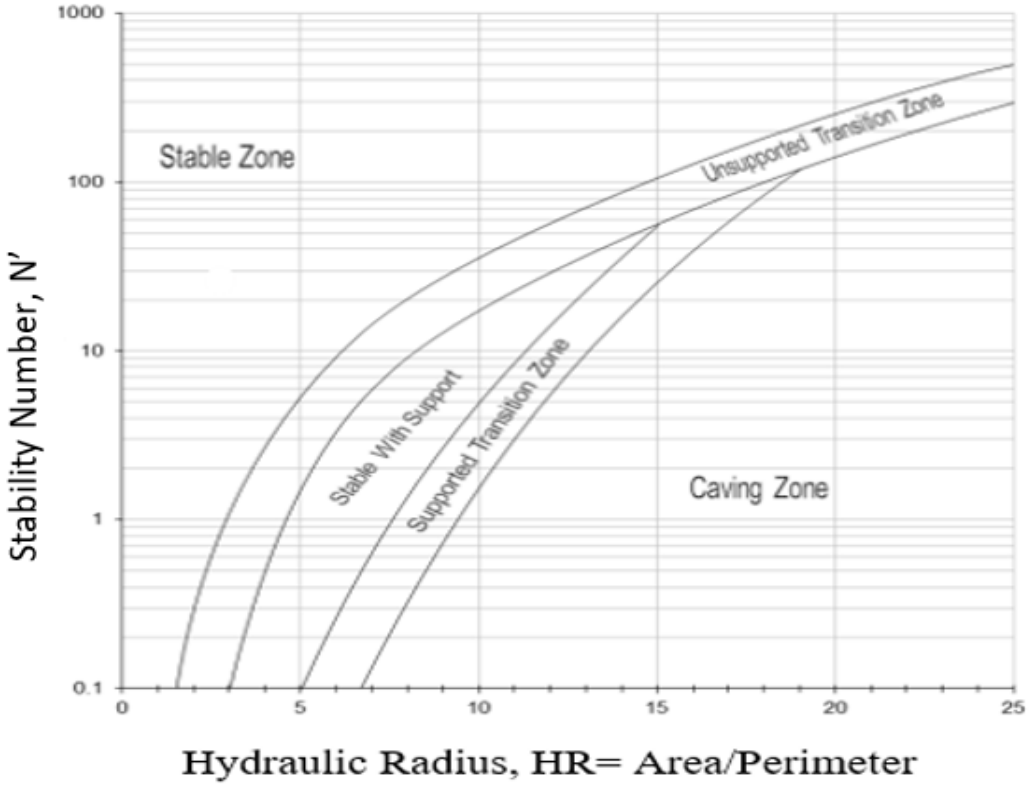

Figure 2.9: Modified Stability Graph with Support (after Nickson, 1992)

This empirical classification system has limitations, such as the qualitative description of the stope stability. Some critical factors in the stope stability design approach are not considered which doesn't make the system reliable. The anticipated failure mode is not considered in the analysis. Also the zone extent of failure expected is not considered as opposed to the numerical modelling in which the yield and relationship zones are considered. The other ignored factors include stope undercutting of the walls, drilling and blasting effects are poorly counted for.

2.4. Pillar Design Methods

This study aims to enhance the stability of the wide sections of the stope by ensuring that an adequate artificial concrete pillar is installed. Therefore, assessment of the pillar design system is briefly considered, though it's not the main aim of this study. The author saw it necessary to include an empirical pillar design approach in the literature review. The brief topics considered are pillar stress and pillar strength methods.

2.4.1. Pillar Design Theories

Many studies have been done on pillar designs for metalliferous and coal mines worldwide. Still, more needs to be done on artificial concrete pillar designs to be used as temporary or permanent support in underground mines. Some of the different pillars in underground mines are Rip Pillars, Regional Pillars, Sill Pillars, Crown Pillars, Bracket Pillars, Dip Pillars, Shaft Pillars, etc. Spencer

(2010) defined pillars in underground mines to be Non-Yield, Yield, and Crushed. Generally, these pillars are classified into three main types: Support Pillars, Protective Pillars, and Control Pillars (Salamon, 1983). The support pillars are a system of pillars usually laid out systematically to offer support to the undermined hangingwall strata (Zvarivadza, 2012). The most used pillars in shallow metal mines are non-yield, yield, barrier, and crushed pillars (Zvarivadza, 2012). Several formulas determine the pillar strength (Coates, 1981). The area tributary theory is used to calculate the pillar stress and applied to regular mining layouts (Zvarivadza, 2012). The most common parameters adopted in shallow mines for pillar design are strength, stress, and width-to-height ratio (Zvarivadza, 2012). Typically, the width-to-height ratio is generally used as the first step to determine the strength of the pillar (Salamon, 1983). A numerical design approach has recently been utilized for the pillar design of underground mines. The numerical approach is more holistically oriented in solving geotechnical problems than the empirical design method. The following literature has been reviewed for pillar design.

1) Pillar Stress Theories

There are various theories regarding Pillar Stress determination. Below are the list of pillar stress theories.

a) Area Tributary Method (ATM)

The pillar's stress can be determined using the area tributary method (Ozbay et al., 1995). The area tributary method is used in regular mining layouts with a large lateral extension of several mining panels, which are greater than the depth of the mine under consideration (Zvarivadza, 2012). In the pillar design concept, each pillar in the layout provides an equal load to the surface (Zvarivadza, 2012). The area tributary method considers the concept of the Average Pillar Stress (APS) as the primary factor and is expressed by Equation 2.21.

$$APS = \frac{\sigma_v}{1-e} \qquad (2.21)$$

$$\sigma_v = \rho g h$$

Where: -

APS = the Average Pillar Stress (MPa)
σ_v =Vertical Stress (MPa)
e = extraction ratio
ρ = Rock Density (Kg/m^3)
g = Acceleration due to gravitational acceleration (m/s^2)
h = Depth of below surface where the design is being considered

The Area tributary method by Ozbay et al (1995) was simplified by Zvarivadza (2012) in which he explained the calculation of extraction ratio (**e**) as (**a=b** for square pillars and **a ≠ b**) for rectangular pillars as shown in Figure 2.10.

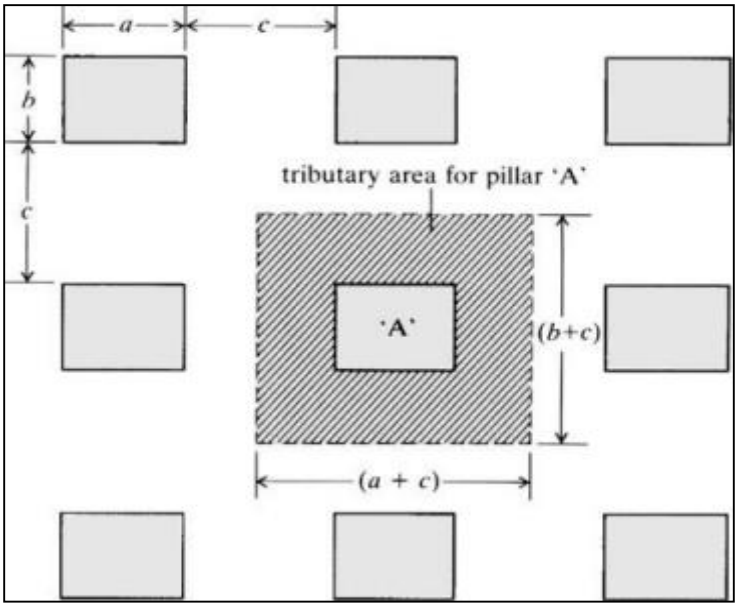

Figure 2.10: Plan view simplification of the area tributary method (Brady and Brown, 2004)

The extraction ratio was also defined in a different way as expressed in Equation 2.22 (Brady and Brown, 2004).

$$e = \frac{a+cb+c-ab}{a+cb+c} \qquad (2.22)$$

The above equation 2.22 is rephrased as shown in Equation 2.23.

$$e = \left[\frac{pillar\ base\ area}{pillar\ base\ area+pillar\ tributary\ area}\right] \qquad (2.23)$$

Another consideration for pillar design is the study of Ryder and Jager (2002), which suggests that the cross-sectional view can be used to calculate the extraction ratio, as shown in Figures 2.11.

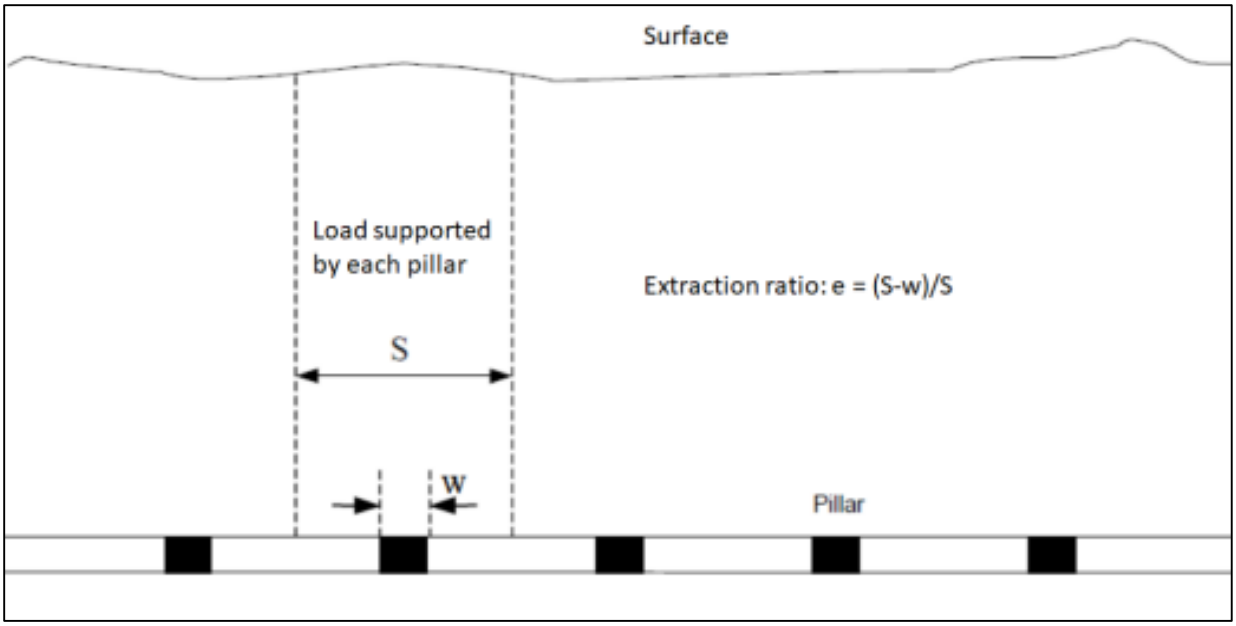

Figure 2.11: Vertical Cross Section for extraction ratio estimation (after Rydee and Jager, 2002)

Hoek et al. (2002) also conducted a study to determine stress for square pillars using the area tributary theory. The formula calculation was based on the diagram shown in Figures 2.12.

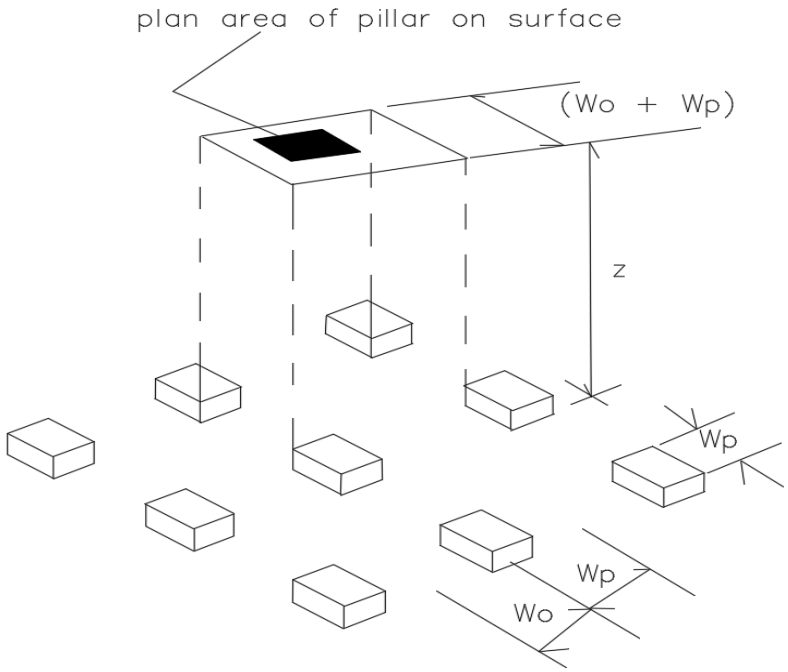

Figure 2.12: Concept of the area tributary for pillar design (Hoek et al., 2002)

From this layout they deduced the formula for calculating average pillar stress as:

$$APS = \sigma_v \, 1 + \frac{W_0^2}{W_p} \qquad (2.24)$$

Where

APS = Average Pillar Stress (Mpa)
σ_v *= vertical Stress (Mpa)*
$W_0 = Excavation\ width$
W_p *= Pillar Width*

b) Coates (1981) Method

The study of Coates (1981) led to the discovery of the formula for calculating load after the inefficiency of the area tributary method. Geometrical and rock property parameters are not considered in the area tributary pillar design formula (Zvarivadza, 2012). However, in the study of Coates (1981), these two parameters were considered to discover the formulation. This pillar design method was adapted to the central part of the mine, which is not disturbed and in cases where the span of the mine doesn't exceed half of the depth. This concept applies to pillar design in deep mining environments and mining zones with long sections (Coates, 1981). The formulation is presented below in Equation 2.25.

$$APS = \sigma_v \, x \, 1 + \frac{2e\ 1+h_s-kh_s\left(1-w+w_p n\right)}{h_s n+2\ 1-e\ 1+h_s+\frac{2eb(1-w)}{\pi}} \qquad (2.25)$$

$$e = \frac{B_o}{B_o + B_p}, k = \frac{\sigma_h}{\sigma_v}, w = \frac{v}{1-v}, w_p = \frac{v_p}{1-v_p}, n = \frac{E\left(1-v_p^2\right)}{E_p 1-v^2}, b = \frac{B_p}{L}, h_s = \frac{H}{L}$$

Where :

APS = Average Pillar Stress (Mpa)
σ_v = Vertical Stress (Mpa)
e = Extraction ratio
H= Height of stope (m)
σ_h= Horizontal Stress (Mpa)
k = ratio of Vertical to Horizontal stress
h_s= Stope height
v = Poisson ratio for abutments
v_p= Poisson ratio for Pillars
E = Young's Modulus for abutment
E_p= Young's Modulus for Pillars
B_o= Room width (m)
B_p = Pillar Width (m)
L = Width of extraction span (m)

However, both studies by Ozbay et al. (1995) and Zvarivadza (2012) for pillar design acknowledge that they need to consider the stiffness of the rock mass and the overburden properties. The pillar for Coates's (1981) method modified the area tributary method and considered L infinity, as shown below in Equation 2.26.

When L → infinity, b = 0 and h_s = 0 such that

$$APS = \sigma_v \; x \; 1 + \frac{2e \; 1+h_s-kh_s \; 1-w+w_p n}{h_s n+2 \; 1-e \; 1+h_s+\frac{2eb \; 1-w}{\pi}} \qquad (2.26)$$

$$APS = \sigma_v \; x \; 1 + \frac{2e \; 1 + 0 - 0}{0 + 2 \; 1 - e \; 1 + 0 + 0} = \sigma_v \; x \; 1 + \frac{2e}{2 - 2e} = \frac{\sigma_v(2 - 2e + 2e)}{2 - 2e}$$

$$APS = \sigma_v \frac{2}{2(1-e)} = \frac{\sigma_v}{1-e} \textit{ (This is the same as equation (2.25))}$$

As shown above, in Coates's (1981) formula, the geometry and rock mass characteristics are considered. However, in this method, the rock mass properties are expected to be similar for the pillar and abutment (Zvarivadza (2012). Abutments have sharp edges on their corner, which are highly stressed. The difference in the stresses acting on the abutment and pillars led to a significant difference in their elasticity properties (Zvarivadza (2012).

2) Pillar Strength Theories

Most methods for determining the strength of the pillars are based on empirical background. The theories relating to pillar strength were conducted from different case histories involving failed pillars. Pillar Strength is defined either in powder form or linear form; however, they have similar expressions of considering width to height ratio of a pillar (Salamon and Munro, 1967). Below is the pillar strength design expression, either Power or Linear forms, as shown in Equations 2.27 and 2.28.

$$Power \qquad \sigma_s = Kw^{\alpha}/h^{\beta} \qquad (2.27)$$

$$Linear \qquad \sigma_s = KA + B\frac{w}{h} \qquad (2.28)$$

Where:

σ_s = Pillar Strength (Mpa)
h = Height of Pillar (m)
w = width of Pillar (m)
K = Strength of Rock Mass or adjusted unit cube of pillar strength, can be determined either statistically or through laboratory tests.
α, β, A and B are constants.

Several pillar strength design formulas and studies have been presented widely from metalliferous and coal mines. Some of these formulations for determining the pillar strength are shown below.

$$Holland\ and\ Graddy\ (1956)\ \sigma_s = K\frac{w}{h} \quad (2.29)$$

$$Salamon\ and\ Munro\ (1967)\ \sigma_s = K\frac{w^{0.46}}{h^{0.66}} \quad (2.30)$$

$$Bunschinger(1876)\ \sigma_s = K\ 0.778 + 0.22\frac{w}{h} \quad (2.31)$$

$$Bunting\ (1911)\ \sigma_s = 1000\ 0.70 + 0.30\frac{w}{h} \quad (2.32)$$

$$Bieniawski\ (1968a)\ \sigma_s = K\ 0.64 + 0.36\frac{w}{h} \quad (2.33)$$

The other critical factors to consider in determining the strength of the pillar are rock mass strength, shape, and size of the pillar (Stacey and Page, 1986). The study of Stacey and Page (1986) considered the width, height, and gross structural features such as clay, faults, and joints to define the size and shape of the pillar. Most formulations for designing the pillar strength either overestimate or underestimate the strength, resulting in the wrong design. The study of Martin and Maybee (2000) proposed that this formulation was developed empirically and should not be used for a width to height (w/h) ratio exceeding 2. This means that the formulation should not apply to barrier pillars. Barrier pillars are non destructive, and their width-to-height ratio must exceed 10. Stacey and Page (1986) also conducted a study in which it was pointed out that the pillar confinement will increase with the increase of w/h ratio such that when the w/h exceeds 5, the pillar strength will increase rapidly due to confinement of the pillar.

a) Salamon and Munro (1967)

Most of the formulas used in calculating the strength of the pillar were derived from Salamon and Munro's (1967) theoretical concept. Based on the study of Solomon and Munro (1999)'s explanation, the formulation was developed after the collapse of the CoalBrook North Colliery in 1960. They also studied 125 case histories of pillars in South African coalfields, represented by the following pillar strength formula as shown in Equation 2.34.

$$\sigma_s = Kw^{\alpha}/h^{\beta} \quad (2.34)$$

Where:

σ_s= Pillar Strength (In coal mine)
K = Strength of Material (UCS) by one third
w = Width of the pillar
h = height of pillar

α, β= empirical constants

The pillar strength formula is only applicable to pillars of square in shape. To determine the pillar strength formula for rectangular shape, effective width, W_e is incorporated and has been used to place W. Therefore, the expression for effective width is as follows (Wagner, 1980).

$$W_e = \frac{4A}{C} m \qquad (2.35)$$

Where

A= Area of the pillar

C= Circumference of the Pillar

From the database used, the study of Wagner (1980) came up with the empirical constant values 0.46 and 0.66 for the empirical constants α and β respectively.

b) Hedley and Grant (1972)

The authors adopted the concept of Salamon and Munro's (1967) pillar design and came up with the formulation widely used in hard rock mines for pillar designs. The database used for the design had statistical pillar failure analysis for Eliot Lake Uranium Mines in Canada based on hard rock mining. Another study was conducted by Ozbay et al. (1995) in which the orebody was classified as a stratified conglomerate, with the hangingwall and footwall consisting of layered quartzite, argillite, and limestone formations. In their study, 28 pillars were used in the analysis, covering a depth range from 150 to 1040 meters. In their research, three pillars were crushed or failed, while two were taken to have failed partially. The 23 remaining pillars were considered to be stable. Therefore, their study recorded the values of 0.5 and 0.75 as empirical constants for α and β, respectively. Their study concluded that the exponential constants (0.5 and 0.75) for a narrow range of w/h ratio were 0.7 to 1.5, respectively. The value of k was also estimated as the strength of a unit cube of the hard rock measured at 133MPa (Hedley and Grant, 1972). Hedley and Grant's (1972) pillar strength design method became so popular after it was influenced by the study of Wagner and Salamon (1979). The pillar strength determination using Hedley and Grant (1972) is shown in Equation 2.36 below: -

$$\sigma_s = 133 \frac{w^{0.5}}{h^{0.75}} \qquad (2.36)$$

Despite the Hedley and Grant (1972) pillar strength formula being specifically for square shaped pillars, it was also later used for rectangular shaped pillars. The relationship between pillar performance and factor of safety for the pillar was developed as shown in Figure 2.13 (Hedley and Grant, 1972). Different pillar strength and empirical data were represented in Figure 2.13. The relationship between pillar strength and pillar width to height ratio are used as visualization in formulating pillar stability graphs. These pillar stability graphs are presented as stable, unstable, or failed, depending on the level of rock mass deformation. Stable pillars are referred to as intact

and capable of withstanding the load; unstable pillars have undergone deformation to the extent that they can fail unexpectedly.

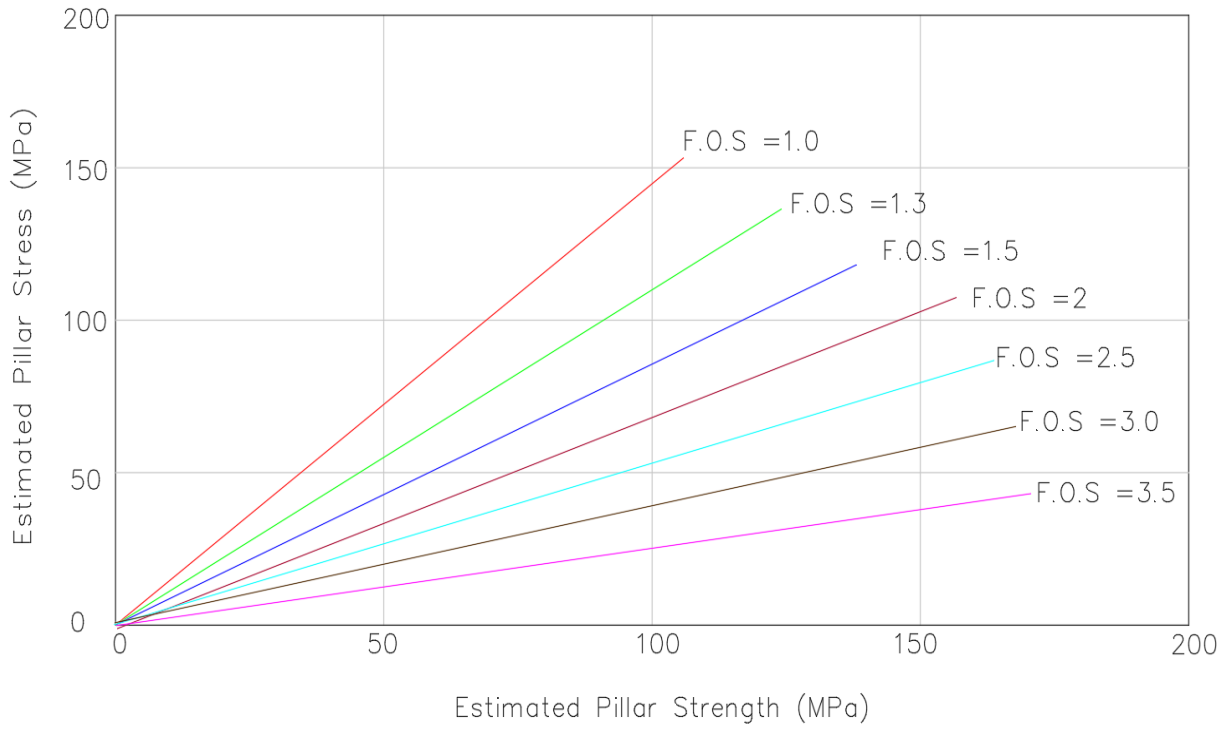

Figure 2.13: Pillar stability graph relating pillar strength to pillar stress (after Hadley and Grant, 1972)

Those pillars that cannot withstand the load are called failed pillars (Hedley and Grant, 1972). The pillar stability graph for determining stable, unstable, and failed pillars is below in Figure 2.14 (after Hedley and Grant, 1972).

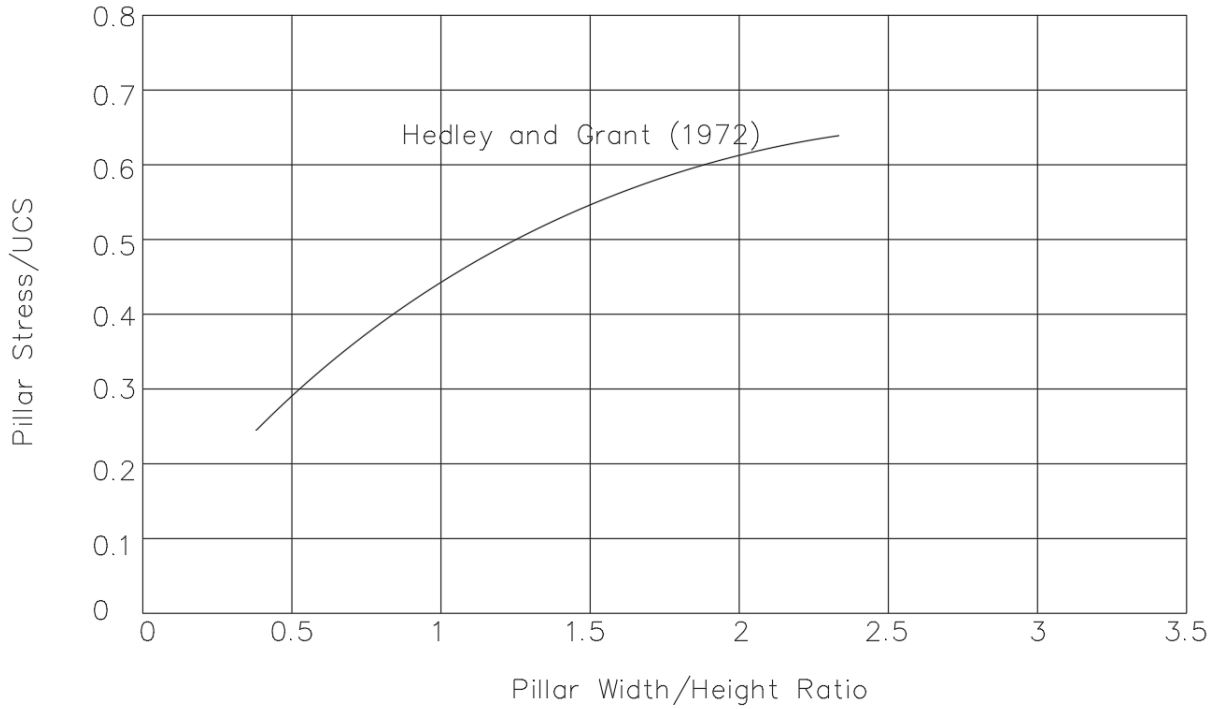

Figure 2.14: Pillar stability graph relating pillar width/height ratio to pillar stress (after Hedley and Grant, 1972)

c) Potvin et al (1989)

The study of Potvin et al. (1989) for open stopes in Canada proposed an empirical design for rip pillars. The initial pillar design proposed by Hedley and Grant (1972) incorporated only smaller pillars (less than 5m width); however, due to this, Potvin et al. (1989) considered this method to be conservative (see Figure 2.15). To provide accuracy in the design, Potvin et al. (1989) had to modify the value of K by increasing the number of case histories in the database. Therefore, they devised the following formulation in Equation 2.37.

$$\frac{\sigma_s}{UCS} = 0.4162\frac{w}{h} \qquad (2.37)$$

Where:

UCS is the Uniaxial Compressive Strength of the Intact Pillar Rock Mass

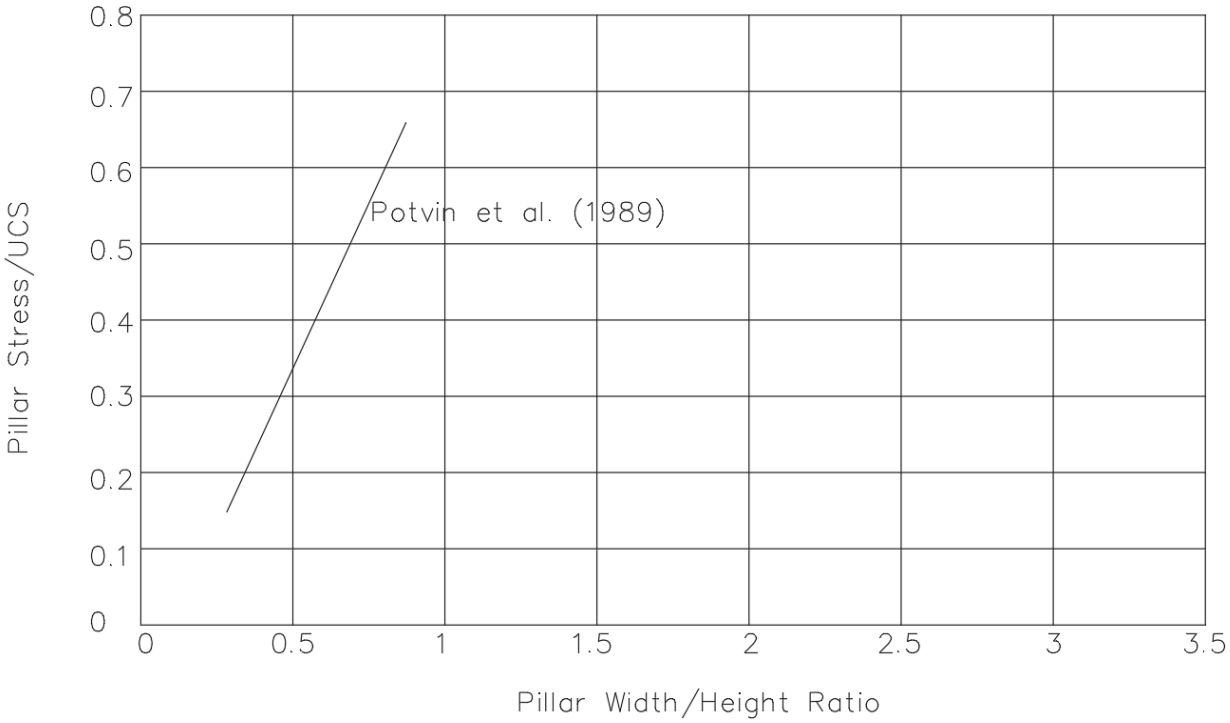

Figure 2.15: Pillar Stability graph for Potvin et al (1989)

d) Krauland and Soder (1987)

Another study by Krauland and Soder (1987) modified Obert and Duvall's (1967) equation and came up with the Equation 2.38 below.

$$\sigma_s = \sigma_{pl} 0.78 + 0.22 \frac{w}{h} \qquad (2.38)$$

Equation 2.37 is differentiated from Equation 2.38 by the difference in the value of σ_{pl}. Plotting their results, Krauland and Soder (1987) found that the value of 35.4 MPa gave the best curve fit for the database. The UCS for the rockmass in which the study was conducted was 100 MPa. The pillar stability graph for Krauland and Soder (1987) is given as shown in Figure 2.16 below.

Figure 2.16: Pillar stability graph for Krauland and Soder (1987)

e) Lunder and Pakalnis (1997)

Lunder and Pakalnis (1997) combined a database of different authors to develop the new pillar design formula. The increased number of case histories in the database gave a perfect statistical representation of the field observation. Some of the authors that were included in the new database are Hedley and Grant (1972), Brady (1977), Von Kimmelman et al. (1984), Krauland and Soder (1987), Hudyrna (1988), Sjoberg (1992b), Lunder (1994), etc. Lunder and Pakalnis (1997) formulated an expression in Equation 2.39 to determine the pillar strength considering the pillar confinement.

$$\sigma_s = K * UCS * C1 + C2 * kappa \qquad (2.39)$$

Where:

K= rock mass strength size factorand averaged at 44%

UCS = Pillar material for Unconfined Compressive Strength (Mpa)

C1, C2 = Empirical constants determined to be 0.68 and 0.52 respectively.

The pillar friction term is called Kappa and is expressed as follows in Equation 2.40

$$Kappa = tan\, Cos^{-1} \frac{1-Cpav}{1+Cpav} \qquad (2.40)$$

Where:

$Cpav$ = average pillar confinement defined as the ratio of average minor stress to average major principal stress at the mid height of the pillar. The formula for calculating $Cpav$ is as follows below.

$$Cpav = 0.46\, log\frac{w}{h} + 0.75 \quad 1^{\frac{1.4}{w\,h}} \qquad (2.41)$$

Lunder and Pakalnis (1997) developed some pillar stability graphs for designing pillars by relating the average pillar confinement and the average pillar stress to UCS, as shown in Figure 2.17 below.

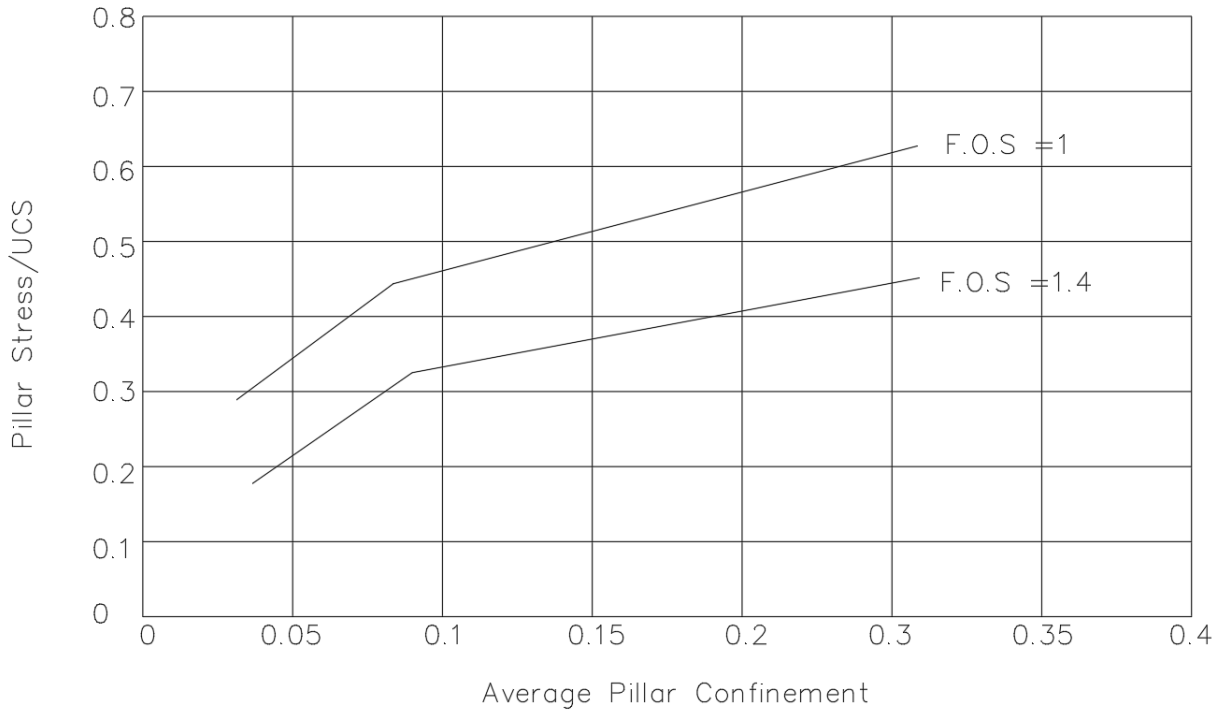

Figure 2.17: Pillar Stability Graph relating average pillar confinement and average pillar stress to UCS (after Lunder and Pakalnis, 1997)

Lunder and Pakalnis (1997) developed another pillar stability graph using the relationship between pillar width-to-height ratio and the average pillar stress or UCS, as shown in Figure 2.18 below.

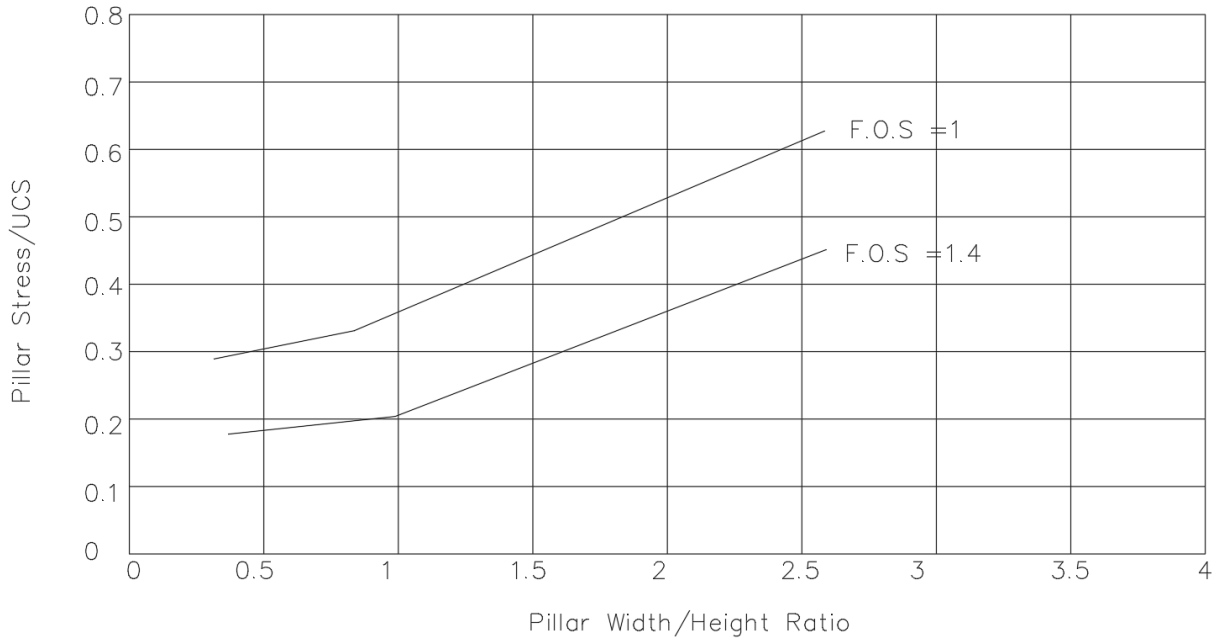

Figure 2.18: Pillar Stability Graph relating Pillar width to height ratio and the average pillar stress to UCS (after Lunder and Pakalnis, 1997).

f) Salamon (1982)'s extended formula

The empirical pillar design formula of Salamon (1982) developed from the coal mine was later modified by Maaden (1991) to design pillars in the metal mines. This was motivated by the need to expand the capacity of pillars to carry more load when the width-to-height ratio is increased. The concept was extended by determining the strength of the pillar as follows below:

$$\sigma_s = K\frac{R_0^b}{V^a}\ x\ \frac{b}{\varepsilon}\ x\ \frac{R^\varepsilon}{R_0} - 1 + 1\ (MPa) \qquad (2.42)$$

$$V = W_{eff}^2\ x\ h,$$

$$R = \frac{W_{eff}}{H}$$

$W_{eff} = 4\frac{A}{C}$ (Defined according to Wagner (1980)'s definition of squat-pillar width)

$$= 4\frac{Pillar\ Plan\ area}{Pillar\ Plan\ Circumference}$$

Where:

R_0 = Critical width-to-height ratio (R_0=5)
ε = rate of strength increase (2.5)
a = 0.0667 (as determined by Madden, 1991)
b = 0.5933 (as determined by Madden, 1991)
V = Pillar volume (width-w_1 x length-w_2 x height-h), m^3
R = Pillar effective width to height ratio
σ_s = Pillar Strength (Mpa)
K = Design rock mass strength (Mpa)
W_{eff} = Effective width (m)
h = Height of pillar (m)
A = Pillar area (m^2)
C = Pillar perimeter

The above literature reviewed the empirical design for determining the average pillar stress and pillar strength, which are the critical aspects of pillar design stability. Depending on the pillar's purpose, the safety factor can vary from temporary to permanent pillars. However, the purpose of this current study is to evaluate the stability of concrete artificial pillars by applying the numerical simulation that will be appropriate. Therefore, reviewing all the empirical pillar design formulations will not be necessary, but a brief review of the above literature is sufficient.

2.5. Numerical Modeling Methods

Stress-strain relationships are the concept used to simulate the mechanical behavior of rock mass when the load is applied to it (Brady and Brown, 1985). This concept varies from small to large volumetric scale of intact rock being analyzed, as shown in Figure 2.19. When load or force is applied to intact rock mass, it will behave elastically by departing from its linear state as the represented sample size increases (Brady and Brown, 1985). This is critically observed near the opening of an excavation where the stress concentration is low, and the linearity of the rock mass decreases, such that the slip dominates the joint surface. When applied with the load, the rock mass's mechanical response at any scale will depend on factors such as the aperture of joints, joint filling, spacing, orientation, weathering, and stress magnitude (Brady and Brown, 1985). This describes two common modeling approaches in rock engineering designs (Itasca, 2022).

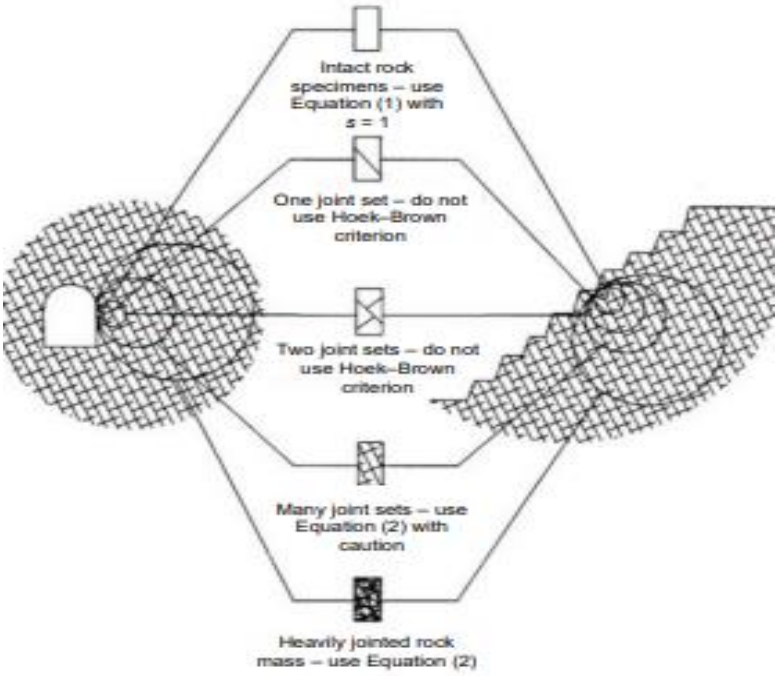

Figure 2.19: Intact rock mass response when load is applied at different geometric scale (Brady and Brown, 1985).

The first concept is where the rock mass is treated as a discontinuum material consisting of individual wedges or blocks interacting with each other via plasticity and stiffness (Itasca, 2021). The second concept is where the rock mass is regarded as a continuum material with non-linearity and is considered as the state in the model (Hoek, 2007).

2.5.1. Model Types

Two typical numerical modeling approaches in rock engineering are commonly used today and are as follows:

1) Discontinuum Modeling

Trollope (Stagg and Zienkiewiz, 1968) was the first to introduce the discontinuum modeling concept; later, Cundall adopted and modified the idea in 1971. The earliest modeling concept consisted of rigid blocks with interacting joint surfaces directed by the Mohr-Coulomb failure criterion. The concept was further modified and led to the discovery of the Universal District Element Code (UDEC) for the Itasca (2022) in two dimensions and another recent three-dimensional distinct element code (3DEC) that was developed by Itasca (2021), Lemon (1987) and CICE (Hocking et al., 1985). UDEC and 3DEC incorporated the automatic generation of joint statistical analysis, constitutive laws for joints, discretization of blocks, rigid and deformed blocks, etc. (Itasca, 2021). Despite having this theoretical concept in the distinct element method, some continuum modeling codes may also include elements or joint interfaces upon which slip can occur

(Itasca, 2021). However, these concepts are limited to only a tiny interface that cannot interact (Hoek, 2007). In the continuum modeling codes, interfaces are usually restricted; this is only applied to a small number of discrete elements such as faults or sheared zones (Itasca, 2021). The basic concept in the distinct element method is that a rock mass consists of a series of blocks that interact with each other across the joint planes (Cundall, 1971). The joint constitutive laws in discontinuum modeling represent the rock mass properties of joint stiffness, friction, dilation, and cohesion. The Mohr-Coulomb model explained in the later sections below is the most straightforward joint constitutive law. When applied, block accelerations, translations, and rotations are determined using the law of motion equations (Hoek, 2007). The internal block deformation can be calculated from any incorporated joint constitutive model using the internal discretization approach (Cundall, 1971).

With the discontinuum numerical modeling approach, non-linearity and possible structurally controlled related failure mechanism of the rock mass response can be simulated explicitly, provided that the geometrical and joint properties are known (Hoek, 2007). The problem with this modeling concept is determining the level of necessary details in the discretization stage to define the prominent failure mechanism of that rock mass (Hoek, 2007). The other challenge when modeling this concept is that it becomes unpractical over a large scale of complete rock mass structure with a highly jointed rock mass in a distinct state (Hoek, 2007). Even though a high-speed computer can be used in the modeling, reasonable run times may still limit the problem size to several thousand blocks (Hoek, 2007). Discontinuum modeling is also efficient and applicable in evaluating simple problems such as the stability of a single excavation and borehole or a fault plane intersecting a repository horizon, which can be simulated very effectively and efficiently with the Distinct Element Modelling Codes (Brown, 1970).

2) Continuum Modeling

The concept of continuum modeling is defined as numerical techniques that base their equations on continuum mechanics. They assume that the holes in a body do not open or slip, and separation does not occur on a discrete joint plane (Hoek, 2007). The non-linear behavior of the fractured rock mass is primarily due to slipping along the joint plane. This behavior of non-linear rock mass in the continuum modeling is incorporated into the constitutive laws. The typical representation of the continuum modeling is the Finite Element Method (FEM), Finite Volume Method (FVM), and Boundary Element Method (BEM). The sections below describe the brief background of the continuum modeling concepts.

2.5.2. Constitutive Models in Numerical Modeling

The most common practice of estimating rock properties is laboratory testing, primarily based on the representative sample taken from the intact rock mass. This approach of testing rock samples from the laboratory setup can only be assumed valid for some blocks of the intact rock mass (Marinos and Hoek, 2001). Therefore, some modification to the parameters obtained is required. Various forms and methods have been adopted in rock mechanics for testing the strength of intact rock mass. Some methods involve testing a rock with a single natural or saw-cut joint (Brady and

Brown, 1992). The strength of a rock sample with a single joint will depend mainly on the orientation. In highly jointed rock masses, there are often enough joints oriented in different directions, making the rock mass homogeneous (Brady and Brown, 1992). Applying numerical approaches to evaluating rock engineering problems faces several challenges when adapting and implementing the available constitutive models to obtain the correct geotechnical parameters (Hoek and Brown, 1992). These three common problems presented in the numerical processes are instability due to physical state, path dependency of non-linear materials, and non-linearity of the stress-strain response.

These problems faced in numerical rock engineering simulations can be addressed using explicit and dynamic solution schemes such as FLAC3D, 3DEC, etc. The explicit and dynamic numerical codes will allow the analysis to follow the evolution of a geological system realistically, without concerns about numerical instability problems (Itasca, 2022). The formulation includes all dynamic equations of motion in the explicit, dynamic solution (Itasca, 2022). Using this approach, numerical solutions will be stable and eliminate physical instability. It is important to note that with non-linear rock mass material, physical instability is always expected to occur (e.g., pre-mature collapse of the open stope). The numerical approach should be viewed as a tool for evaluating a particular problem, not a black box that will give a solution (Marinos and Hoek, 2001). FLAC3D and 3DEC can follow the explicit and dynamic approach to solve a problem in a numerical simulation (Itasca, 2022). The mechanical constitutive models available in continuum and discontinuum range from linear elastic to highly linear plastic models. The basic constitutive models with a brief theoretical background are presented below. The constitutive models are grouped as null, elastic, and plastic.

1) Null Model Group

This constitutive model represents the material removed or excavated from the rock mass (Hoek, 2007). This model sets the stresses to zero; forces are not considered to act on these zones. The following expression in Equation 2.43 represents the null model.

$$\sigma_{ij}^{N} = 0 \qquad (2.43)$$

Null modeling can be used to simulate backfill material.

2) Elastic Model Group

Elastic Model Group can be divided into three: isotropic, orthotropic, and anisotropic elastic modeling. The characteristics of this modeling include reverse deformation when loaded, the law of stress-strain, etc.

3) Plastic Model Group

The plastic constitutive model group consists of simulations involving path-dependent or permanent deformation and considering the non-linearity relationship of stress-strain in the model process (Marinos and Hoek, 2001). Plastic constitutive models consider the yield function, hardening/softening functions, and flow rule in the model process. The yield function in the model involves defining stress in which plastic flow can occur (Itasca, 2022). These solutions are presented by one or more limit surfaces in a generalized stress space, with points below or on the surface characterized by an incremental elastic or plastic rock mass behavior. The plastic flow in these constitutive models depends on the basic assumption of the plasticity theory, which states that the total strain increment is decomposed of elastic and plastic parts, in which the elastic part is the only factor contributing to the increment of stress using an elastic law (Itasca, 2022). In principle, both increments in plastic and elastic strains can be co-axial with the existing principal axes of the stresses (Mostyn and Douglas, 2000). The direction of the plastic strain increment vector, which is expected to the potential surface, defines the flow rule; this is referred to as the associated potential and yield functions (Itsaca, 2022). Below is the list of models under the plastic group: -

a) Mohr-Coulomb Model

The Mohr-Coulomb (M-C) failure criterion remains one of the earliest constitutive models for estimating rock mass failure when compressive stresses are applied (Itasca, 2022). The M-C constitutive model can be used to calculate the stability of the rock mass. It is also a simple or easy operation method, giving accurate results when applied correctly (Brady and Brown, 1992). As earlier stated, the stress point in this failure envelope criterion is controlled by the non-associated flow rule for shear and tension failure associated rule, which incorporates the three generalized stress vector components σ_1, σ_2 and σ_3 for the model $(n = 3)$. the corresponding generalized principal strain components are $\in_1, \in_2$ and $\in_3$. Incremental Elastic law according to Hooke's law for generalized stress and stress increments in the M-C is represented in Equation (2.44) below.

$$\Delta\sigma_1 = \alpha_1 \Delta\epsilon_1^e + \alpha_2(\Delta\in_2^e + \Delta\in_3^e) \qquad (2.44)$$

$$\Delta\sigma_2 = \alpha_1 \Delta\epsilon_2^e + \alpha_2(\Delta\in_1^e + \Delta\in_3^e)$$

$$\Delta\sigma_3 = \alpha_1 \Delta\epsilon_3^e + \alpha_2(\Delta\in_1^e + \Delta\in_2^e)$$

Where, α_1 and α_2 are material constants defined in terms of the shear modulus, G, and bulk modulus, K, defined as follows in Equation 2.45.

$$\alpha_1 = K + \frac{4}{3}G \qquad (2.45)$$

$$\alpha_2 = K - \frac{2}{3}\mathrm{G}$$

This equation is compared to the expression on S_i in terms of increments presented in Equation 2.46 below.

$$S_1(\Delta\epsilon_1^e, \Delta\epsilon_3^e, \Delta\epsilon_3^e) = \alpha_1 \Delta\epsilon_1^e + \alpha_2(\Delta\epsilon_2^e + \Delta\epsilon_3^e) \quad (2.46)$$

$$S_2(\Delta\epsilon_1^e, \Delta\epsilon_2^e, \Delta\epsilon_3^e) = \alpha_1 \Delta\epsilon_2^e + \alpha_2(\Delta\epsilon_1^e + \Delta\epsilon_3^e)$$

$$S_3(\Delta\epsilon_1^e, \Delta\epsilon_2^e, \Delta\epsilon_3^e) = \alpha_1 \Delta\epsilon_3^e + \alpha_2(\Delta\epsilon_1^e + \Delta\epsilon_2^e)$$

The other failure criterion and rule considered in the M-C constitutive model is the tension cutoff composite failure, defined by three principal stresses, as shown in Equation 2.47 below.

$$\sigma_1 \leq \sigma_2 \leq \sigma_3 \quad (2.47)$$

Failure composite with compressive stress is represented as negative in the plane $(\sigma_{1,}\sigma_3)$ as shown in Figure 2.20. The M-C failure criterion defines failure envelope as $f^s(\sigma_{1,}\sigma_3)$ =0, in which from point A to B is defined as $f^s = 0$

$$f^s = -\sigma_1 + \sigma_3 N_\emptyset - 2_C\sqrt{N_\emptyset} \quad (2.48)$$

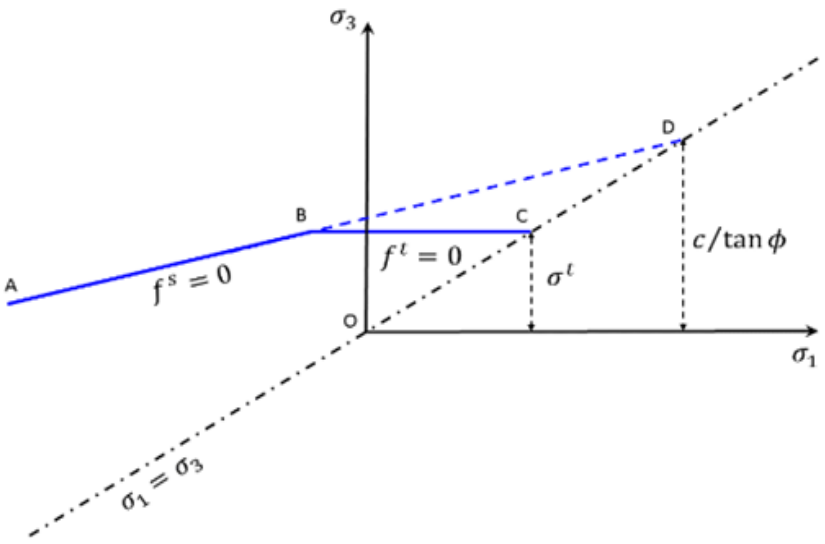

Figure 2.20: Mohr-Coulomb failure criterion (Itasca, 2022)

Tension failure criterion in M-C is defined from B to C as $f^t = 0$, and is expressed as shown in Equation 2.49 below:

$$f^t = \sigma_3 - \sigma^t \quad (2.49)$$

Where σ^t is defined as shown in Equation (2.50) below, with friction angle (∅) and cohesion (C) in place.

$$N_{\emptyset} = (\frac{1+sin\emptyset}{1-sin\emptyset}) \quad (2.50)$$

Tensile strength in the rock mass cannot exceed the value of corresponding minor principal stress (σ_3) at a point which intersect the straight lines $f^s = 0$ and σ_1=σ_3 in the $f(\sigma_1, \sigma_3)$ plane. The maximum tensile value in M-C is defined by Equation 2.51 below.

$$\sigma_{max}^{t} = \frac{c}{tan\emptyset} \quad (2.51)$$

Shear plastic flow and tensile plastic flow can be defined as shown in Equation 2.52 below and they are denoted $g^s and\ g^t$ respectively.

$$g^s = -\sigma_1 + \sigma_3 N_{\psi} \quad .(2.52)$$

Dilation angle is denoted by ψ and is defined as shown in Equation 2.53 below

$$N_{\psi} = \frac{1+sin(\psi)}{1-sin(\psi)} \quad (2.53)$$

The associated flow rule is denoted by g^t and is expressed as shown in Equation 2.54 below.

$$g^t = f^t = \sigma_1 - \sigma^t \quad (2.54)$$

Figure 2.21 below shows a presentation of the planes dividing the domain where elastic is guessed to be violating the composite yield function into two domains, which are domains 1 and 2. Shear failure is defined when the stress point falls within domain 1, and the stress point is placed on the curve as f^s = 0. Tensile failure occurs when the point falls within domain 2, and the new stress point confirms to be f^t= 0 using a flow rule of g^t.

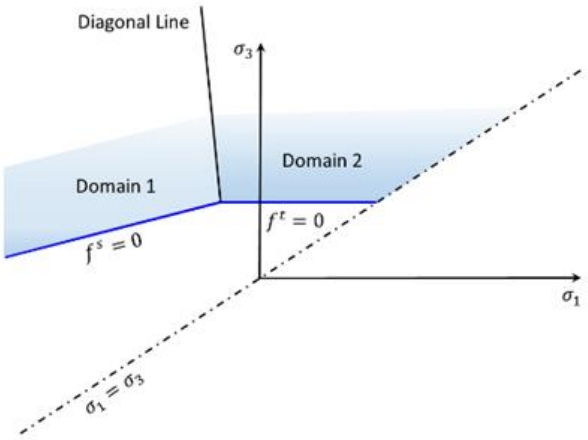

Figure 2.21: Mohr-Coulomb model-domains used in the definition of the flow (Itasca, 2021)

The shear plastic correction partial differential equations in M-C failure criterion as expressed as follows in Equations 2.55 and 2.56 below.

$$\frac{\partial g^t}{\partial \sigma_1} = -1 \qquad (2.55)$$

$$\frac{\partial g^s}{\partial \sigma_2} = 0$$

$$\frac{\partial g^s}{\partial \sigma_3} = N_\psi$$

Substitution of $\frac{\partial g^t}{\partial \sigma_1}, \frac{\partial g^s}{\partial \sigma_2}$ *and* $\frac{\partial g^s}{\partial \sigma_3}$ *for* $\Delta\epsilon_1^e, \Delta\epsilon_2^e$ *and* $\Delta\epsilon_3^e$ *respectively in Equation 2.56 gives*

$$S_1\left(\frac{\partial g^t}{\partial \sigma_1}, \frac{\partial g^s}{\partial \sigma_2}, \frac{\partial g^s}{\partial \sigma_3}\right) = -\alpha_1 + \alpha_2 N_\psi \qquad (2.56)$$

$$S_2\left(\frac{\partial g^t}{\partial \sigma_1}, \frac{\partial g^s}{\partial \sigma_2}, \frac{\partial g^s}{\partial \sigma_3}\right) = \alpha_2(-1 + N_\psi)$$

$$S_3\left(\frac{\partial g^t}{\partial \sigma_1}, \frac{\partial g^s}{\partial \sigma_2}, \frac{\partial g^s}{\partial \sigma_3}\right) = \alpha_1 N_\psi - \alpha_2$$

Using $f = f^s$ *(see Equation (s))*

$$\sigma_1^N = \sigma_1' + \lambda^s(\alpha_1 - \alpha_2 N_\psi) \qquad (2.57)$$

$$\sigma_2^N = \sigma_2' + \lambda^s \alpha_2 (1 - N_\psi)$$

$$\sigma_3^N = \sigma_3' + \lambda^s(-\alpha_1 N_\psi + \alpha_2)$$

$$\lambda^s = \frac{f^s(\sigma_1', \sigma_3')}{(\alpha_1 - \alpha_2 N_\psi) - (-\alpha_1 N_\psi + \alpha_2) N_\phi} \qquad (2.58)$$

In the tension place corrections, the partial differential equations in the M-C failure criterion is expressed as follows in Equation (2.59) below.

$$\frac{\partial g^t}{\partial \sigma_1} = 0 \qquad (2.59)$$

$$\frac{\partial g^t}{\partial \sigma_2} = 0$$

$$\frac{\partial g^t}{\partial \sigma_3} = 1$$

Using Equation 2.59, other expression for Equation 2.60 can be obtained as shown below.

$$S_1(\frac{\partial g^t}{\partial \sigma_1}, \frac{\partial g^t}{\partial \sigma_2}, \frac{\partial g^t}{\partial \sigma_3}) = \alpha_2 \quad (2.60)$$

$$S_2(\frac{\partial g^t}{\partial \sigma_1}, \frac{\partial g^t}{\partial \sigma_2}, \frac{\partial g^t}{\partial \sigma_3}) = \alpha_2$$

$$S_3(\frac{\partial g^t}{\partial \sigma_1}, \frac{\partial g^t}{\partial \sigma_2}, \frac{\partial g^t}{\partial \sigma_3}) = \alpha_1$$

This can be repeated presented as follows in Equation 2.61 below.

$$\sigma_1^N = \sigma_1' - \lambda' \alpha_2 \quad (2.61)$$

$$\sigma_2^N = \sigma_2' - \lambda' \alpha_2$$

$$\sigma_3^N = \sigma_3' - \lambda' \alpha_1$$

The other expression for the above is presented in Equation 2.62 below.

$$\lambda^l = \frac{\sigma_3^l - \sigma^t}{\alpha_1} = \frac{f^t}{\alpha_1} \quad (2.62)$$

Substitution of Equation 2.62 for λ^l in Equation 2.63 gives: -

$$\sigma_1^N = \sigma_1' - (\sigma_3' - \sigma^t)\left(\frac{\alpha_2}{\alpha_1}\right) = \sigma_1' - (\frac{\alpha_2}{\alpha_1}) f^t \quad (2.63)$$

$$\sigma_2^N = \sigma_2' - (\sigma_3' - \sigma^t)\left(\frac{\alpha_2}{\alpha_1}\right) = \sigma_2' - (\frac{\alpha_2}{\alpha_1}) f^t$$

$$\sigma_3^N = \sigma^t$$

From the above equations, this can be evaluated into two principal stresses in tension failure as follows in Equation 2.64.

$$f_z^t = g_z^t = \sigma_3 - \sigma^t > 0 \quad (2.64)$$

$$f_y^t = g_y^t = \sigma_2 - \sigma^t > 0$$

Partial differentiation of Equation 2.65 gives: -

$$\frac{\partial g_z^t}{\partial \sigma_1} = 0, \frac{\partial g_y^x}{\partial \sigma_1} = 0 \tag{2.65}$$

$$\frac{\partial g_z^y}{\partial \sigma_z} = 0, \frac{\partial g_y^t}{\partial \sigma_z} = 1$$

$$\frac{\partial g_z^t}{\partial \sigma_3} = 1, \frac{\partial g_y^t}{\partial \sigma_3} = 0$$

Therefore is expressed as Equation 2.66

$$\sigma_1^N = \sigma_1^l - (\lambda_y^t + \lambda_z^t)\alpha_2 \tag{2.66}$$

$$\sigma_2^N = \sigma_2^l - (\lambda_y^t \alpha_1 + \lambda_z^t \alpha_2)$$

$$\sigma_3^N = \sigma_3^l - (\lambda_z^t \alpha_1 + \lambda_y^t \alpha_2)$$

From Equation (2.70), after plastic correction, we can get Equation 2.67 below

$$\lambda_y^l + \lambda_z^l = \frac{\sigma_2^l - \sigma^l + \sigma_3^1 - \sigma^l}{\alpha_1 + \alpha_2} = \frac{f_y^t + f_z^t}{\alpha_1 + \alpha_2} \tag{2.67}$$

Substitution of Equation 3.81 in Equation 2.68 gives.

$$\sigma_1^N = \sigma_1^l - \frac{\alpha_2 (f_y^t + f_z^t)}{\alpha_1 + \alpha_2} \tag{2.68}$$

$$\sigma_2^N = \sigma^t$$

$$\sigma_3^N = \sigma^t$$

The three principal stresses in tension failure are finally obtained as follows.

$$f_z^t = g_z^t = \sigma_3 - \sigma^t > 0 \tag{2.69}$$

$$f_y^t = g_y^t = \sigma_2 - \sigma^t > 0$$

$$f_x^t = g_x^t = \sigma_1 - \sigma^t > 0$$

This is like Equation 2.70

$$\frac{\partial g_z^t}{\partial \sigma_1} = 0, \frac{\partial g_y^t}{\partial \sigma_1} = 0, \frac{\partial g_x^t}{\partial \sigma_1} = 1 \quad (2.70)$$

$$\frac{\partial g_z^t}{\partial \sigma_2} = 0, \frac{\partial g_y^t}{\partial \sigma_2} = 1, \frac{\partial g_x^t}{\partial \sigma_2} = 0$$

$$\frac{\partial g_z^t}{\partial \sigma_3} = 1, \frac{\partial g_y^t}{\partial \sigma_3} = 0, \frac{\partial g_x^t}{\partial \sigma_3} = 0$$

Therefore this will become Equation 2.71

$$\sigma_1^N = \sigma_1^l - \lambda_x^t \alpha_1 + (\lambda_y^t + \lambda_z^t)\alpha_2 \quad (2.71)$$

$$\sigma_2^N = \sigma_1^l - \lambda_y^t \alpha_1 + (\lambda_z^t + \lambda_x^t)\alpha_2$$

$$\sigma_3^N = \sigma_3^l - \lambda_z^t \alpha_1 + (\lambda_x^t + \lambda_y^t)\alpha_2$$

From Equation 2.71, we can obtain Equation 2.72 below: -

$$\lambda_x^t + \lambda_y^t + \lambda_y^t = \frac{\sigma_1^l - \sigma^t + \sigma_2^l - \sigma^t + \sigma_3^l - \sigma^t}{\alpha_1 + 2\alpha_2} = \frac{f_x^t + f_y^t + f_z^t}{3K} \quad (2.72)$$

Remember $f_x^t(\sigma_2^N) = 0, f_y^t(\sigma_2^N) = 0 \; and \; f_z^l(\sigma_3^N) = 0$ after plastic correction, so we get.

$$\sigma_1^N = \sigma_2^N = \sigma_3^N = \sigma^l \quad (2.73)$$

As earlier stated, this constitutive model is straightforward and effective to use and has been widely used worldwide to estimate rock mass parameters that can be utilized in the initial design concept. Due to the model's simplicity, inherent flaws are encountered during the modeling process. The model has also been used effectively to estimate the shear strength. However, this constitutive model needs to explain the tensile strength estimate better. Despite that, this has been considered by engineers as a severe flaw because almost all the constitutive models available focus much on the compressive region, and none of them offer an extension of the tensile zone to give a high level of confidence in the modeling process (Brady and Brown, 2004). The M-C constitutive model is mainly applicable to non-linearity problems.

The shear strength for many rock types was also overestimated with the linear approach of the M-C constitutive model in the region of high-stress concentration.

b) Hoek-Brown Failure Criterion

The Hoek-Brown (H-B) constitutive model is mainly applicable for estimating the failure, which is related to non-linear (Hoek and Brown, 2004). The H-B failure criterion presented a relationship for estimating induced stress incorporating rock mass strength and empirical constants **s** and **m**. Below is the Equation 2.74 for estimating induced stress using the H-B failure criterion. The general condition for the H-B failure criterion is as follows.

i. Can be applied to estimate any stress conditions.
ii. Can handle one or more joints with the sample.
iii. Can accurately provide rock mass response when load is applied to it.

$$\sigma_1 = \sigma_3 + \sqrt{(m\sigma_c\sigma_3 + s\sigma_c^2)} \qquad (2.74)$$

Where, σ_1 is the major principal stress, σ_3 is the minor principal stress, σ_c is the Uniaxial Compressive Strength, and **m** and **s** are empirical constants.

One major challenge of using the Hoek-Brown failure criterion was overpowering the popularity of the Mohr-Coulomb failure criterion. The software packages and closed-form solution then required the Mohr-Coulomb constants, c and φ, as input parameters. A few years after introducing the Hoek-Brown, the relationship with the Mohr-Coulomb failure criterion was presented by incorporating empirical constants of **m** and **s**. The relationship between the two constitutive models was derived, as shown in Equations 2.75 and 2.76.

$$\emptyset = \arctan\left(4hcos^2\left(\frac{\pi}{6} + \frac{1}{3}\arcsin\left(h^{\left(-\frac{3}{2}\right)}\right)\right) - 1\right)^{-\frac{1}{2}} \qquad (2.75)$$

Where $\emptyset$ is defined as the internal friction angel and h: -

$$h = 1 + \frac{16\,(m\sigma + s\sigma_c)}{3m^2\sigma_c} \qquad (2.76)$$

This constitutive model was explicitly designed for rock mass that behaves isotropically. Given the appropriate empirical values of **m** and **s**, the model can describe the behavior of the intact rock mass or highly jointed rock mass. However, this criterion is not recommended for describing the rock mass with a single or few joints because such rock mass cannot behave in an isotropic manner (Hoek and Brown, 1992). The authors of this constitutive model acknowledged that an empirical relationship of such equations shown in Equation 2.77 is only as good as those values chosen for the constants m and s. The model was also modified to relate well with the constants and the Rock Mass Rating (RMR) value (Hoek et al., 2002). These values obtained in the empirical relationships can be used to estimate the rock mass behavior. Another modification was made to the model by considering the third fitting parameter (Hoek et al., 2002). Therefore, the H-B constitutive model has remained unchanged, but empirical constant **a** was added to describe the jointed rock mass, which was later expressed as shown in Equation 2.77.

$$\sigma_1 = \sigma_3 + \sigma_{ci}\left\{m_b\left(\frac{\sigma_3}{\sigma_{ci}}\right) + s\right\}^a \qquad (2.77)$$

Where σ_{ci} is the Uniaxial Compressive Strength of the intact rock mass, $and\ m_b$, s, and a are empirical constants and can be related to the Geological Strength Index (GSI). GSI was incorporated into the Hoek-Brown for a quick estimate that applies to intact rock mass (Hoek et al., 2002). H-B constitutive model application to non-linear has been proved to be more realistic than the M-C model (Hoek et al., 2002). When the significant principal stress is in compression, the H-B constitutive model can be used appropriately in a yielding scenario. For numerical implementation, the H-B constitutive model uses a linear approximation, where the non-linear consideration is continuously approximated by the M-C tangent at the current stress level, as shown in Figure 2.22. The Mohr-Coulomb tangent formulation is expressed as shown in Equation 2.78.

$$\sigma_1 = \sigma_3 N_{\emptyset c} + 2C_c\sqrt{N_{\emptyset c}} \qquad (2.78)$$

Where:

$$N_{\emptyset c} = \frac{1+sin\emptyset_c}{1-sin\emptyset_c} = tan^2\left(\frac{\emptyset_c}{2} + 45^o\right) \qquad (2.79)$$

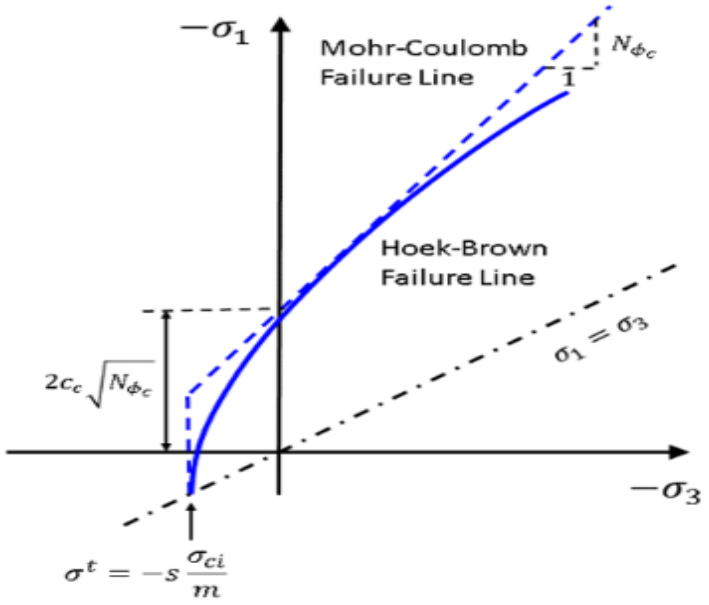

Figure 2.22: Relationship of H-B and M-C constitutive models (Itasca, 2022)

Cohension current value (C_c) and internal friction $(\emptyset_c)$ are calculated as follows in Equations 2.80 and 2.81 below.

$$\emptyset_c = sin^{-1}\left(\frac{N_{\emptyset c}-1}{N_{\emptyset c}+1}\right) \tag{2.80}$$

$$C_c = \frac{\sigma_c^{ucs}}{\sqrt[2]{N_{\emptyset c}}} \tag{2.81}$$

where

$$N_{\emptyset c} = 1 + am_b\left(m_b\frac{\sigma_3}{\sigma_{ci}} + s\right)^{-1} \tag{2.82}$$

$$\sigma_c^{ucs} = \sigma_3(1 - N_{\emptyset c}) + \sigma_{ci}\left(m_b\frac{\sigma_3}{\sigma_{ci}} + s\right)^{a} \tag{2.83}$$

M-C failure criterion extends the tensile stress (σ_3) by considering Equations 2.84 amd 2.85 to derive the value of σ_3. This is a compressive stress and is positive.

$$\sigma_3 = \max(\sigma_3, 0) \tag{2.84}$$

The current M-C flow rule is also adopted to calculate the plastic strain increment for shear yieding and is expressed as follows: -

$$\Delta e_{ij}^p = \Delta e^p\frac{\partial g}{\partial \sigma_{ij}} - \frac{1}{3}\Delta e_{vol}^p\delta_{ij} \qquad i = 1, 3 \tag{2.85}$$

Δe^p is defined as the plastic flow increment intensity where as g is the plastic potential function and this is expressed as shown in Equation 2.86.

$$\Delta e_{vol}^p = \Delta e^p(\frac{\partial g}{\partial \sigma_{11}} + \frac{\partial g}{\partial \sigma_{22}} + \frac{\partial g}{\partial \sigma_{33}}) \tag{2.86}$$

Whereas the plastic potential function is expressed as shown in Equation 2.87 below.

$$g = \sigma_1 - \sigma_3 N_{\psi c} \tag{2.87}$$

However, $\psi_c$is defined as the current value of dilation and expressed as shown in Equation 2.88.

$$N_{\psi c} = \frac{1+sin_{\psi c}}{1-sin_{\psi c}} \tag{2.88}$$

The current tangent M-C yield failure criterion is used to obtain the increment of plastic flow, Δe^{p}. The three choices that are conidered for the flow rule in the constitutive model and these are as follows: -

i. The dilation angle (ψ_c is a constant value) must be specified by the property keyword constant and dilation-flag = 0.
ii. The plastic flow ($\psi_c$is set equal to Φ_c) must be set by the dilation-flag = -1.
iii. The constant friction angle (ψ_c is set to a constant time Φ_c) must be a set dilation function, in which the dilation-flag must be a postive fraction

As explained above, with the H-B constitution model, two choices for the evolution of parameters are considered: the plastic shear strain or the plastic strain. Plastic shear strain is when the property keyword flag-evolution is set to 1, which is only accumulated when the shear yielding occurs. The plastic strain, in the direction of the minor principal stress, is considered when the property keyword flag-evolution is set to 0. The strain-plastic property can be used to monitor the evolution parameters. A simple regular technique can be selected to address the issue of grid dependency on the softening behavior. To activate this process, the grid zone used to calibrate the model properties with experimental data can be assigned to the property length calibration, Lc referred to as the calibration length.The input softening rate is then automatically adjusted by a factor of $\frac{L_c}{\sqrt[3]{V_z(V_z}}$, which is used to account for the different zone sizes used in the dynamic and explicit modeling software (Hoek, 2007). This is an experimental way of calibrating the model, and precautional measures must be considered during its usage (Itasca, 2021).

c) Other models in Plastic Model Group includes;

Drucker-Prager Model, Ubiquitous-Joint model, strain-hardening/softening model, bilinear strain-hardening/softening ubiquitous-joint model, Double-Yield Model, Modified Cam-Clay Model, time-dependent (creep) models, etc.

2.6. Conclusions

This Chapter has represented literature on the stopes' stability and pillar designs. However, the literature must be summarized to conclude the key learning points. The following conclusions are drawn from the reviewed literature above, starting from Sections 2.2 to 2.5 of this Chapter. The literature covered stability design methods in rock engineering, which included analytical, empirical, and numerical methods. The analytical design methodology reviewed three failure modes: stress, gravity, and a combination driven. In the section under the stress-driven failure concept, the literature discusses the interaction between induced stress and intact rock mass strengths presented in Section 2.2. The literature assumes that when the stress magnitude applied to the rock mass exceeds the inherent strength of the rock material, failure is expected to happen. Mohr-Coulomb failure criterion for intact rock mass and Hoek-Brown failure criterion for rock

masses have been presented critically with examples to understand the basis of the stress drive-related failure design approach. For stope stability assessments, sources of high-stress concentration are in abutments, pillars, and remnants left between hangingwall and footwall. The other areas with high-stress concentrations are the crown, sill, rib pillars, etc. The ancient methodology for estimating the stresses around the excavation used the Kirsch equations. Kirsch's equation calculations revealed that the stress magnitude around the excavation is directly related to the far field stresses, presented as the ratio of horizontal to vertical stress, geometry size, and the distance from the opening.

The literature revealed that this method could be used to estimate the pre-mining state stress and as design input parameters to evaluate stope stability. The literature also reviewed further presented that failure mechanisms in shallow mines are influenced by gravity. The gravity mechanism involving the beam, plate, and kinematic analyses were briefly reviewed in this Chapter to understand their backgrounds. Kinematic analysis is mainly used for structural control evaluation of the available wedges. A kinematic mechanism can be utilized to determine the wedge failure analysis in underground or open-pit mining. However, in stope stability, the approach has limits to its application. Therefore, this should be used carefully but must be supported with other analytical methods. Plate and beam theories were developed from a civil engineering background. Due to this reason, the literature for these theories has only been reviewed. However, the author is aware that presenting such literature in detail will not have any purpose in the scope of this study. Empirical methods have been used widely in stope stability designs. The empirical stope design accounts for rock mass properties, gravity, geometry, and the effect of stress. In most cases, empirical designs ignore some essential factors in the design methodology. Some of the critical factors that the empirical needs to consider from the above literature review are the influence of stope undercutting, blasting, curvature of the hanging wall, etc. The empirical design methods reviewed in this study are the rock mass classification systems involving Rock Mass Rating by Bieniwski, Modified Rock Mass Rating by Laubscher, NGI or Q-tunneling system, and Mathew's modified stability number for stope stability design. The literature reviewed revealed that some rock mass classification systems are unreliable and need to be used for verification with other classification systems.

The literature reviewed on pillar stability design entails adopting a robust design system to determine the accuracy of the factor of safety (FoS). The overall geotechnical input parameters for estimating the factor of safety reviewed above are the pillar strength and pillar stress using various methods such as the area tributary method, Coates method, numerical modeling, etc. The area tributary method states that it can be utilized in regular mining layouts of large lateral extents, several times greater than the mining depth. It assumes that each pillar is the same size and provides an equal load to the surrounding surface area. The literature also explained that the area tributary method needs to consider the geometrical and rock properties in its theoretical concept. However, the study of Coates incorporates such a gap in the area tributary method. The Coates method also does not consider the overburden stiffness and seam stiffness, which play a significant role in determining the pillar stress as reviewed above in Section 2.4 of this Chapter. Numerical modeling

has been pointed out as another method that can be used to determine the pillar stress, which also considers the depth and span of the excavation. The concept of assessing the strength of the pillar is grouped as either linear or power form. The focus of this study is to review the design methodology for pillar stability evaluation, which are weight to height ratio, pillar stress, and strength of pillar material, which can be determined by either statistical or laboratory means, as pointed out in the literature reviewed above. This study has examined some critical pillar design methodologies to act as a basis for evaluating the effectiveness of the proposed artificial concrete pillars.

The reviewed numerical methods are the continuum and discontinuum approaches. Numerical, more explicit, and dynamic simulations can be used to evaluate geotechnical complex problems. The discontinuum type includes a universal distinct element (UDEC) and a three-dimensional distinct element (3DEC). In contrast, Finite Element Method (FEM) and boundary element methods (BEM) are the most common methods for continuum analysis.

In the literature, it was revealed that FEM implement the solution by using differential equations, which involves dividing the main problem domain into small finite "elements" of different shapes (triangular or rectangular in 2D cases and tetrahedron or bricks in 3D cases) held together at the "nodes," which are the cornerstone of the elements. The problem may then be solved based on approximations of the connectivity of elements, continuity of displacements, and stresses between elements, together with their boundary conditions, and to the satisfaction of compatibility and equilibrium constraints. It is also worth mentioning, as discussed in the literature that the FEM can easily accommodate non-linear and heterogenous material properties. The major problem that has been highlighted with the FEM is that the outer boundary of the problem domain is defined arbitrarily, and discretization errors occur throughout the main domain. The boundary element method solves a problem regarding surface values of the traction and displacement field variables. FEM is very efficient and less time-consuming during model computing. The disadvantage is that its application is restricted to applications involving linear and homogeneous materials. Overall, it has been reviewed that modeling accuracy depends upon the geotechnical input parameters. Therefore, numerical modeling can be used to evaluate the stopes' stability accurately.

The next chapter describes the adopted numerical modeling code used to conduct the numerical simulation to evaluate the stability and suitability of artificial concrete pillars to be used as temporal support systems in active stopes. The adopted numerical code is a finite volume method (FVM); steps and model-derived input parameters are also described in the next Chapter.

Chapter 3 : METHODOLOGY

3.1. Introduction

This Chapter focuses on the methodology adopted for this study. A numerical modelling approach was adopted to evaluate the stability and suitability of the innovative artificial concrete pillars. As explained earlier in Chapter One, this study aims to evaluate the suitability of innovative artificial pillars. This Chapter also briefly describes the empirical aspect of rock mass classification employed to quantify the ground condition deemed poor or wider. Two case studies, carefully selected to represent different scenarios, have been used as typical examples of numerical modelling. The approach employed to investigate the stability and suitability of the artificial pillar is numerical modelling using a continuum analysis called FLAC3D.

3.2. FLAC3D Background

The FLAC3D numerical code of the Itasca consulting group can be used for design prediction and a laboratory test (Itasca, 2021). In that situation, it is more of a field situational than a computer-based program. FLAC3D and other numerical modelling software can be used to give predictions if correct geotechnical data are available and of high quality. Table 3.1 below shows the recommended geotechnical steps in numerical modelling.

Table 3.1: Geotechnical numerical modeling steps recommended in FLAC3D

STEPS	DESCRIPTION
1	Set up the Objectives
2	Conceptual picture
3	Create and Run a Simple Model
4	Assemble Specific-data Problem
5	Run a Series of Detailed Models
6	Performing Numerical Calculations
7	Interpretation of the Results

Step 1: Defining the Model Objective

This step involves setting up the model's objective to define the numerical simulation's intended purpose (Cai, 2008). For example, suppose the objective of the simulation is to decide between two conflicting types of failure mechanisms in the analysis. In that case, a clear objective must be defined and provided in the study (Cai, 2008). It is always necessary to avoid complexity when setting up model objectives. Complex features must always be avoided to prevent influencing the model's purpose. It is always essential to start and refine a global model if necessary. Therefore, the main objective of this study is to evaluate the stability and suitability of the artificial concrete pillars so that they can be used as a support system in the wider section of the orebody.

Step 2: Conceptual picture

Constructing a conceptual picture of a problem is essential to provide an estimated rock mass behavior under the imposed conditions (Carranza-Torres etal., 1999). Various questions may be imposed during conceptual pictorial creation. This includes questions such as, is it expected that the design could become unstable? Is the rock mass behavior linear or non-linear? Is the rock mass movement anticipated to be large or small compared to the size of the set objectives, or does the rock mass behave in a discontinuum or continuum? Is there an influence of groundwater in the analysis? Are the boundary conditions fixed or extended to infinity? Is there any geometric symmetry in the physical state of the system? These conceptual considerations can dictate the gross characteristics of the simulation. These include model geometry, material type, boundary conditions, initial state of equilibrium, etc. Conceptual pictorial analysis helps determine whether a two-dimensional or three-dimensional model is required in the analysis, considering the advanced physical condition of the model (Cai, 2008).

Step 3: Create and Run a Simple Model

Constructing and running a simple test model in the numerical simulation is more efficient than building a detailed model (Itasca, 2021). It is essential to consider creating a simple model at the earliest possible stage of the simulation analysis to generate a more comprehensive understanding. Simple model results can provide insight into the conceptual model of the system. Simple models can also anticipate the expected shortcomings in the model that can be worked on before conducting a sizeable numerical system (Cai, 2008). For instance, do the material properties in the model sufficiently represent the anticipated rock mass behavior? Do the boundary conditions influence the model response? The results obtained in a simple model can also guide geotechnical data collection planning by identifying the critical parameters affecting the model results in the analysis.

Step 4: Assemble Specific-data Problem

The specific data that is required for a model analysis to be successful include the following:-

a) Geometry details (excavation profile, surface topography, soil/rock mass structure, etc).
b) Geological structural location (e.g., joints, faults, dykes, bedding planes)
c) Rock mass behaviors in terms of elastic, plastic, and post-failure)
d) Initial state condition of the model (e.g., in-situ state stress, pore pressure, saturation)
e) External loading conditions (e.g., explosive loading, pressurized cavern).

Significant uncertainties related to specific conditions are expected due to a reasonable range of parameters required for investigation. Therefore, the results from the simple model runs can help determine this range.

Step 5: Run Series of Detailed Models

When preparing a set of model runs for calculations, several numerical simulation aspects must be considered, and these are as follows: -

a) Time required to perform a model calculation. Would obtaining enough information to arrive at a conclusive decision be challenging if model runtimes are more than enough? Care and consideration must be given to various parameters on multiple computers to reduce the total computation time frame.
b) The model state at each stage must be saved so that the entire run does not have to be repeated for each parametric variation. For instance, if the model involves several loading/unloading stages, the user must be able to return to any stage, modify a parameter, and then continue the simulation from that stage.
c) The maximum unbalanced forces in the simulation must constantly be monitored to check for equilibrium and if there is any failure at each state in the model.

Step 6: Performing Numerical Calculations

Creating or building two runs, separated into sections, is crucial before launching a series of complete model runs (Itasca, 2021). The model run must always be checked at each stage to analyze the expected outcome. Once the analysis shows good direction that the model is correct, several data files can also be linked together to run a complete model calculation in series (Itasca, 2021). At any stage during a sequence of model runs, it is possible to interrupt the model calculations, view the results, and then continue or modify the model as required (Carranza-Torres, 1999).

Step 7: Interpretation of the Results

Interpreting the results is the final stage of any numerical simulation (Cundall et al., 2003). Results are analysed by plotting or directly copying them as output from the computer device and displaying them in graphical form. It is recommended that the results be presented in a format that can be compared with field measurements and observations (Hoek, 2007). The displayed plots should clearly show the area of interest in the region, such as regions of high-stress concentration, high displacement zones, convergence zones, etc. Numerical values are also displayed in the model's result interpretation for detailed analysis.

The seven steps above are the recommended processes to solve geoengineering problems effectively and efficiently (Itasca, 2021). The following sections present the application of FLAC3D to meet the above-described steps, which have been adopted for this study.

3.3. Material Properties

FLAC3D considers two categories of material rock properties to be used as input parameters in the numerical simulation (Itasca, 2021). The two main rock mass material properties are;

a) Elastic deformability properties
b) Rock Mass Strength Properties

In addition to the two primary rock mass material properties in FLAC3D, the definitions of post-failure properties, extrapolation of the laboratory to fieldwork, spatial variation of properties, and randomness of the property distribution are also considered.
When generating a numerical model, the most challenging part is the selection of properties due to high uncertainty in the available material property database (Ford et al., 2007). Another expected problem during a geomechanical analysis is having limited data in the system, in which the field data is always only known partially (Ford et al., 2007). However, regardless of the above, with a selection of the best material properties from the available database, an insight into the physical problem can be obtained (Itasca, 2021).
Conventionally, material properties are always obtained from various laboratory testing methodologies (Itasca, 2021). The laboratory material properties of various rocks are grouped in FLAC3D.

3.3.1. Intrinsic Deformability Properties

The intrinsic deformability properties are grouped as follows;

1) Isotropic Elastic Properties

Isotropic material exhibits the behavior of elasticity ranging to describe two elastic constants: **bulk modulus (K)** and **shear modulus (G)**. This is exceptional for orthotropic and transversely isotropic elastic models. Young's modulus (**E**) and Poisson's raio (**υ**), the isotropic elastic properties are preferred and described with the bulk modulus (K) and shear modulus (G). FLAC3D preferably uses K and G constants rather than E and υ contants to describe material elastic properties due to the expression corresponding to more fundamental aspects of material behavior. Therefore, FLAC3D recommends using **K, G** in describing elastic material properties rather than **E, υ**, respectively.
Young's modulus (E) and Poisson's ratio (υ) can be expressed in terms of Bulk Modulus (K) and Shear Modulus (G) as shown in Equations 3.1 and 3.2, respectively below.

$$K = \frac{E}{3(1-2v)} \tag{3.1}$$

$$G = \frac{E}{2(1+v)} \tag{3.2}$$

The above-expressed Equations 3.1 and 3.2 must be used with precautionary measures if the value is near 0.5. This is because unrealistic convergence values of **K** will cause the solution to be slow in the numerical simulation (Itasca, 2021). According to the study of Goodman (1980), it is recommended in FLAC3D to first use the value of bulk modulus, **K** (this can be estimated from the isotropic compaction test), then shear modulus (**G**) can be computed from the bulk modulus (**K**) and Poisson's ratio (**υ**). Table 3.2 below summarizes the elastic constant values of different rock types.

Table 3.2: Selected elastic constants (laboratory-scale) for Rocks (Goodman, 1980)

	Dry Density (Kg/m^3)	E (GPa)	υ	K (GPa)	G (GPa)
Sandstone	-	19.3	0.38	26.8	7.0
Siltstone	-	26.3	0.22	15.6	10.8
Limestone	2090	28.5	0.29	22.6	11.1
Shale	2090-2570	11.1	0.29	8.8	4.3
Marble	2700	55.8	0.25	37.2	22.3
Granite	-	73.8	0.22	43.9	30.2

2) Anisotropic Elastic Properties

The nine constants represent the anisotropic elastic material properties in the model, and these are E1, E2, E3, V12, V13, V23, G12 and G13. These constants are defined also in the Orthotropic Elastic Model.

3) Transversely isotropic elastic

The transversely isotropic elastic model is linked with the uniform jointed or laminated rock mass condition. Various investigations have been conducted to develop the elastic constants in the transversely isotropic model, which defines the joint stiffness and spacing of the discontinuities

The transversely isotropic elastic model is linked with the uniform jointed or laminated rock mass condition. Various investigations have been conducted to develop the elastic constants in the transversely isotropic model, which defines the joint stiffness and spacing of the discontinuities. The anisotropic values for various rock specimens are presented in Table 3.3 below.

Table 3.3: Elastic constant values for transversely isotropic rocks (Batugin and Nirenburg, 1972)

Rock	E_x **(GPa)**	E_y **(GPa)**	V_{yx}	V_{zx}	G_{xy} **(GPa)**
Siltstone	43.0	40.0	0.28	0.17	17.0
Sandstone	15.7	9.6	0.28	0.21	5.2
Limestone	39.8	36.0	0.18	0.25	14.5
Gray granite	66.8	49.5	0.17	0.21	25.3
Marble	68.6	50.2	0.06	0.22	26.6
Sandy Shale	10.7	5.2	0.20	0.41	1.2

4) Fluid elastic properties

Groundwater modeling analysis usually requires the Bulk Modulus (K_f) parameter for water, which involves more calculations for incompressible grains or compressible grains for Biot modulus (M). 2GPa is the physical value of pure water at room temperature. Therefore, any value selected in the analysis must have a purpose. A low physical value (K_f) must be used in the steady-state flow or distribution of an initial pore pressure not to disturb the physical process. High physical value (K_f) still also affect the mechanical convergence of the process due to the time step, which will be very insignificant. FLAC3D numerical code has adopted the time step for fluid delta

(Δt_f,) which is directly related to porosity (η) and permeability (K' and K_f). This relationship is expressed as shown in Equation 3.3 below.

$$\Delta t_f \propto \left(\frac{n}{K_f K'}\right) \tag{3.3}$$

The consolidation coefficient (C_v) for fluid in a deformable state can be expressed by considering the effect of changing the physical value of permeability (K_f), as shown in Equation 3.4. Most rock engineering books, however, assume that the fluids are incompressible (Hoek, 2007).

$$C_v = \frac{K'}{m_v + \frac{n}{K_f}} \tag{3.4}$$

The expression in Equation 3.4, m_v can be defined as follows in Equation 3.5

$$m_v = \frac{1}{K + \frac{4G}{3}} \tag{3.5}$$

The value of, K, can also be defined as follows in Equation 3.6.

$$K = K'\gamma f \tag{3.6}$$

The following symbols are also denoted as: -

K'= Permeability used in FLAC3D

$K = hydraulic\ conductivity\ in\ velocity\ units\ \left(e.g., \frac{m}{sec}\right), and$

γf= the unit weight of water

Consolidation coefficient (C_v) is also defined as a direct relationship to the proportion of the consolidated time constant.It is seen as the error brought in by removing it from its original of $2\ x\ 10^9 Pa$. Fluid bulk modulus affects the rate of convergence in the model with no flow, considering the generation of mechanical pore pressure. The pore pressure is usually slow if the value of (K_f) can be compared with the mechanical moduli, even though reducing the value of (K_f) without affecting the rock mass behavior is possible. The bulk modulus in the drained saturated is expressed as shown in Equation 3.7 below.

$$K_u = K + \frac{K_f}{n} \tag{3.7}$$

However, Poisson's ratio in the undrained is expressed as shown in Equation 3.8 below

$$v_u = \frac{3K_u - 2G}{2(3K_u + G)} \tag{4.8}$$

To evaluate the actual effect of the convergence rate, it is important to compare the drained constant values of K and v to the above values. FLAC3D combines the drained properties with mechanical

flid-flow to perform calculations (Itasca, 2021). On the convergence rate for the compressible grains, the fluid bulk modulus is similar to the influence of BiotModulud (M).

3.3.2. Intrinsic Material Strength Properties

FLAC3D mainly considers the intrinsic material strength properties for the M-C failure criterion relationship, which is expressed as follows in Equation 3.9 below.

$$f_s = \sigma_1 - \sigma_3 N_\emptyset + 2C\sqrt{N_\emptyset} \quad (3.9)$$

The above symbols are denoted as follows: -

$N_\emptyset = (1 + sin\emptyset)(1 - sin\emptyset)$;
σ_1= major principal stress (compressive stress in negative)
σ_3= minor principal stress
$\emptyset$ = friction angle; and
C= cohesion.

Shear can be detected only if $\mathbf{f_s}$ is less than **zero**. The triaxial compressive tests can be used to obtain the constant values of cohesion and internal friction angle. If the normal stress becomes tensile, the M-C failure criterion loses its physical strength, though, for simple expression, it will be extended beyond the region of the tensile strength to achieve a point at which the minor principal strength is equal to the uniaxial tensile strength as shown in Equation 3.10 below. This expression entails that the minor principal stress cannot exceed the tensile strength value.

$$f_t = \sigma_3 - \sigma^t \quad (3.10)$$

Tensile yield is detected only if $\mathbf{f_s}$ is more than 0. The tensile strength of rock and concrete can be derived using the Brazilian test (Itasca, 2021). The tensile strength value cannot exceed the minor principal stress value corresponding to the apex limit for the M-C relationship. Equation 3.11 can be used to estimate the maximum value of the tensile strength, as shown below.

$$\sigma^t_{max} = \frac{C}{tan}\emptyset \quad (3.11)$$

Table 3.4 below lists the typical cohesion, tensile strength, and friction angle values for a presentative rock specimen. Rock mass strength is usually described as the Unconfined Compressive Strength (UCS). The relationship between friction angle, cohesion (C), and Unconfined Compressive Strength (q_u) can be expressed as shown in Equation 3.12.

$$q_u = 2\ c\ tan\left(45 + \emptyset\frac{1}{2}\right) \quad (3.12)$$

Table 3.4: Selected strength Properties (laboratory-scale) for Rocks (adapted from Goodman, 1980)

	Friction Angle (degrees)	**Cohesion (MPa)**	**Tensile Strength (MPa)**
Berea sandstone	27.8	27.2	1.17
Repetto siltstone	32.1	34.7	-
Muddy shale	14.4	38.4	-
Sioux quartzite	48.0	70.6	-
Indiana limestone	42.0	6.72	1.58
Stone Mountain granite	51.0	55.1	-
Nevada Test Site basalt	31.0	66.2	13.1

Cohesion and friction angle properties can be used to estimate the **Drucker-Prager Strength** parameters for FLAC3D.
For instance, an assumption of the Drucker-Prager failure criterion circumscribes the M-C failure criterion, the Drucker-Prager parameters of $q_{\emptyset}$ and $k_{\emptyset}$ are related to $\emptyset$ and c by Equations 3.13 and 3.14.

$$q_{\emptyset} = \frac{6}{\sqrt{3(3-sin\emptyset)}} sin\emptyset \qquad (3.13)$$

$$k_{\emptyset} = \frac{6}{\sqrt{3(3-sin\emptyset)}} c\, cos\, \emptyset \qquad (3.14)$$

The strength properties for the planes of weakness are also required in the ubiquitous-joint models. Laboraboratory testing is conventionally used to derive the joint properties (e.g., triaxial and direct shear tests). These laboratory tests can help to drive at physical properties for tensile strength, cohesion, dilation angle, friction angle, etc. Jaeger and Cook (1999), Barton et al. (1990), and Kulhawy (1975) have published some of the properties of joints. Internal friction angle differs for different joints; smooth joints in weak rocks, such as tuff, are less than 10^{o}, while rough joints, such as granite, can have more than 50^{o}. The cohesion values for joints can also vary from zero to values corresponding to the compressive strength of the surrounding rock mass. It is important to state or note that the measured joint properties in the laboratory tests are typically not a true representative of field joint properties. The primary question in rock mechanics is the scale dependence of joint properties. The only way to guide the appropriate choice is to compare similar joint properties derived from the field tests. However, getting field observation tests is usually very rare (Kulhawy, 1975).

3.3.3. Extrapolation to Field-Scale Properties

Material properties to be used in FLAC3D simulation should correspond as closely as possible to the actual values of the physical problem. In particular, the laboratory-measured properties of rocks should not be used directly in the FLAC3D model for simulation to analyze a full-scale problem. However, these rock mass properties must be scaled to account for the availability of the present discontinuity and heterogeneities. Several empirical approaches have been proposed and developed to derive the field-scale properties. Modulus of deformation (E_m) is generally used to define a rock mass's deformability. The deformation modulus can be estimated by treating the rock mass as the equivalent transversely isotropic continuum if the rock mass contains a set of parallel, uniform, and continuous spacing. The relationship below in Equation 3.15 can be used to estimate (E_m) in the direction average to the joint.

$$\frac{1}{E_m} = \frac{1}{E_r} + \frac{1}{K_n S} \tag{3.15}$$

Where:

$E_m = rockmasYoung'smodulus;$
$E_r = intactrockYoung'smodulus;$
$K_n = jointnormalstiffness; and$
$s = jointspacing$

Another expression which is similar is for shear modulus:

$$\frac{1}{G_m} = \frac{1}{G_r} + \frac{1}{K_s S} \tag{3.16}$$

Where:

$G = rockmassshearmodulus$
$G_r = intactrockshearmodulus; and$
$K_s = jointshearstiffness$

The equivalent continuum can be expressed by the following relationship in equations 3.17 and 3.18 below when extending the three orthogonal joint sets.

$$E_i = \left(\frac{1}{E_r} + \frac{1}{K_{si} S_i}\right)^{-1} (i = 1, 2, 3) \tag{3.17}$$

$$G_{ij} = \left(\frac{1}{G_r} + \frac{1}{S_i K_{si}} + \frac{1}{S_j K_{sj}}\right)^{-1} (i, j = 1, 2, 3) \tag{3.18}$$

Various expressions have been developed in two- and three-dimensional characterization of multiple joint sets (Sinha, 2020). However, in practice, rock mass structure is usually too irregular, or data needs to be more sufficient to use the approach. The deformation modulus can be determined from the force-displacement curve in the in-situ compression tests. These tests include

the plate-bearing, dilatometer, and flatjack tests. Bieniawski (1978) developed an empirical relationship for E_m based on the field test results at different sites worldwide. The Rock Mass Rating (RMR) has been adopted to relate to the deformation modulus, as shown in Equation (3.19) below. The test data fits well for rocks with a rating higher than 55.

$$E_m = 2(RMR) - 100\ (GPa) \tag{3.19}$$

Serafim and Pereira (1985) discovered that the modulus of deformation (E_m) values from 1 to 10 GPa is better represented by the following relationship in Equation 3.20.

$$E_m = 10^{\frac{RMR-10}{40}} \tag{3.20}$$

The studies of Goodman (1980) and Brady and Brown (1985) have provided an additional discussion on the methods described above. However, the most commonly accepted approach for estimating the rock mass strength was proposed by Hoek and Brown (1980). Equation 3.21 below shows the generalized Hoek-Brown failure criterion, defined explicitly for the jointed rock masses (Hoek and Brown, 1997).

$$\sigma_1' = \sigma_3' + \sigma_{ci}\left(m_b \frac{\sigma_3'}{\sigma_{ci}} + S\right)^a \tag{3.21}$$

Where

σ_1'= Maximum effective stress at failure

σ_3'= Minimum effective stress at failure

Note: that compressive stresses are positive

m_b= Hoek-Brown constant m for the rock mass,

s and a are constants that depend upon the characteristics of the rock mass, and

σ_{ci}= Uniaxial Compressive Strength of the intact rock pieces.

Hoek and Brown's (1997) failure criterion can also be used to estimate the rock mass's tensile strength, which is expressed as shown below in Equation 3.22.

$$\sigma_m = \frac{\sigma_{ci}}{2}(m_b - \sqrt{(m_b^2 + 4S)} \tag{3.22}$$

To use the Hoek-Brown failure criterion, three properties are required, as shown in Equations 3.23 below: -

1) The uniaxial compressive strength, σ_{ci}, for intact rock material
2) The Hoek-Brown constant, m_i, for the intact rock material
3) Geological Strength Index (**Appendix 4**), GSI, for the rock mass material provides an estimate for the Hoek-Brown constants, s, m_b, and a.

Therefore, the intact rock strength material becomes as shown in Equation 3.23 below

$$\sigma_1' = \sigma_3' + \sigma_{ci}\left(m_i \frac{\sigma_3'}{\sigma_{ci}} + 1\right)^{0.5} \quad (3.23)$$

The statistical analysis of the results from a set of triaxial tests can be used to determine the constant values of (σ_{ci}) and (m_i).

The recommended procedures for conducting these tests are outlined in a report by Hoek and Brown (1997). This study also presents the estimates of constant values for,σ_{ci},and,m, to be used in the preliminary design calculations in case laboratory tests are unavailable. Estimates for reducing rock mass strength can also be conducted using the Geological Strength Index (GSI) as shown in **Appendix 4**. Estimate GSI using Figures 4.24 and 4.25 for Hoek and Brown (1997).

Hoek and Brown (1997) relates the values of **GSI** and $\boldsymbol{m_b}$, **s** and **a** as follows below: -

$$m_b = m_i \, exp\left(\frac{GSI-100}{28}\right) \quad (3.24)$$

For GSI > 25,

$$s = exp\left(\frac{GSI-100}{9}\right) \quad (3.25)$$

and

$$a = 0.5$$

For GSI < 25,

$$s = 0$$

and

$$a = 0.65 - \frac{GSI}{200} \quad (3.26)$$

To facilitate the tables for GSI, Hoek and Brown (1997) also provide Equations for the estimates. The cohesion and friction angle can also be estimated using the Mohr-Coulomb and the Hoek-Brown criteria, as shown in Equation 3.27.

$$\sigma_1' = N_\emptyset \sigma_3' + \sigma_c^M \quad (3.27)$$

Where

$$N_\emptyset = \frac{1+sin\emptyset}{1-sin\emptyset} = tan^2(\frac{\emptyset}{2} + 45^o) \quad (3.28)$$

By substitution, σ_c^M is.

$$\sigma_c^M = \sigma_1 - \sigma_3 N_\emptyset = \sigma_3 + \sqrt{((\sigma_3 \sigma_c m + \sigma_c^2 s))} - \sigma_3 N_\emptyset = \sigma_3(1 - N_\emptyset) + \sqrt{(\sigma_3 \sigma_c m + \sigma_c^2 s}} \quad (3.29)$$

σ_c^M= apparent uniaxial compressive strength of the rock mass for that value of σ_3.

The tangent to Equation 4.31 is defined by Equation 3.32.

$$N_{\emptyset}(\sigma_3) = \frac{\partial \sigma_1}{\partial \sigma_3} = 1 + \frac{\sigma_c m}{2\sqrt{\sigma_3.\sigma_c m + s\sigma_c^2}} \quad (3.30)$$

The values of cohesion (c) and friction angle ($\emptyset$) can be estimated from from $N_{\emptyset}$ and σ_c^M in Equations 3.31 and 3.32.

$$\emptyset = 2\ tan^{-1}\sqrt{N_{\emptyset}} - 90^o \quad (3.31)$$

$$c = \frac{\sigma_c^M}{2\sqrt{N_{\emptyset}}} \quad (3.32)$$

3.4. Boundary Conditions

FLAC3D model defines the boundary conditions to have values of field variables (e.g., displacement and stress) prescribed at the numerical grid's boundary (Itasca, 2021). These boundaries are of two types: artificial and natural boundaries. FLAC3D defines actual boundaries as those in which physical objects are modelled, e.g., ground surface or tunnel surface. In contrast, artificial boundaries are defined as those that do not exist in reality but can be introduced in the model to enclose the chosen number of zones (Itasca, 2021). The conditions imposed on each of the above boundaries are similar. In artificial boundaries, suggestions concerning the location and choice of artificial boundaries and their effect on the derived solution are considered. In artificial conditions, the applied boundaries are of two main types: stress and displacement. The described stress boundary is the particular case for the free surface. Stress and displacement boundary conditions are the two types of mechanical conditions presented.

3.4.1. Stress Boundary Condition

In FLAC3D, by default, the grid boundaries are free of stress and any constraints. The zone face apply command is used to apply for stresses or forces around the boundary or part of the boundary. The stress tensor for individual components in FLAC3D is specified with the keywords Stress-yy, zz, and xx. The critical command words used in the FLAC3D model to define stress boundary conditions are: -

$$Zone\ face\ apply\ Stress\text{-}zz - 1e5\ range\ position\text{-}Z\ 0$$
$$Zone\ face\ apply\ Stress\text{-}xz - 5e4\ range\ position\text{-}Z\ 0$$

These stress components in a stress tensor's x, y, and z directions can be applied to all boundary face zones, with centroids failing within the range from -0.1 to 0.1. The other stress components can be set to zero. The stresses can be applied in either the x, y, and z directions of a model or in a direction normal and tangential to the local face boundary. FLAC3D uses keywords such as stress-normal to be applied to the face, whereas stress-dip and stress-strike can be applied to shear stress of the face. The stress component applied in the dip direction of the local face is called stress dip, whereas the stress component applied to the strike direction is called strike stress. Figure 4.1

below shows the orientation of the local face axes in FLAC3D. The global stress orientation (x, y, z) and local stress orientation (d, s, n) axes cannot be applied in the same face.

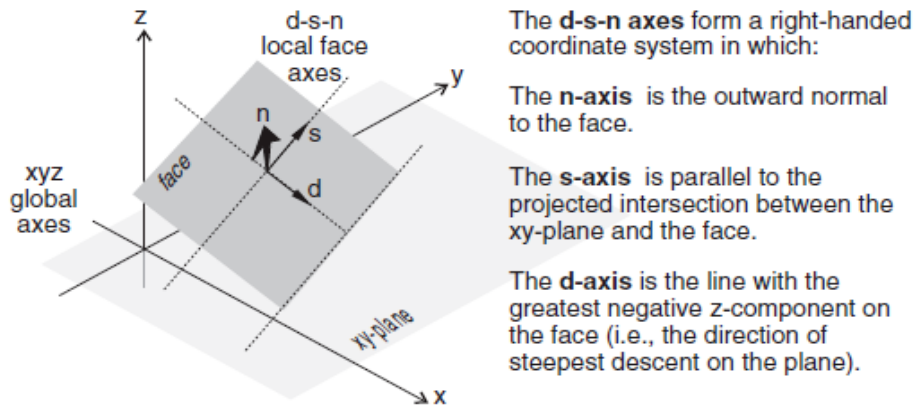

Figure 3.1: Local face axes defined by (d) dip direction, (s) strike direction, and (n) normal direction (Itasca, 2021)

Several considerations must be taken about using the ***zone face apply command***. The first consideration is that the zone face apply command will affect the faces inside the defined range. In contrast, the face selection range of geometry will select only the centroid face location. FLAC3D considers the second reason that the compressive stresses in the model have a negative sign in line with the general sign convention for internal stresses. The stress component is usually applied as forces or traction in FLAC3D, resulting from a stress tensor acting on a boundary plane. At the same time, the tractions are also computed whenever the model solve command is issued, which happens after every tenth step in the large-strain model.
Zone gridpoint fix command, ***force-applied-x***, ***force-applied-y***, and ***force-applied-z*** keywords can be used in FLAC3D to be applied to individual forces. The x-, y-, and z- components of an ***applied force vector*** (the force applied can be used to specify all the troops at once). In this situation, no account for the boundary face area can be taken. However, the specified forces are applied to the given grid points.

1) Applied Stress Gradients

The applied stresses or forces tend to vary linearly over the specific range, and the keyword gradient may be used for the ***zone face apply command.*** The following parameter for gradient, v, specifies the x-, y-, and z- components for the stress- or - force- component. The value varies linearly with distance from the global coordinate origin at (x = 0, y = 0, z = 0) as defined by the Equation 3.33 below.

$$S = S^{(o)} + g_x x + g_y y + g_z z \qquad (3.33)$$

In which $S^{(o)}$ is the value at the global coordinate origin at (x = 0, y = 0, z = 0), and g_x, g_y andg_z specify the variation of the value in the x-, y-, and z- directions. This is presented by the following expression.

$$zone face apply stress\text{-}xx \text{-}10e6\ gradient(0,0,1e5)\ range\ position\text{-}z \text{-}100\ \ 0$$

The equation for the Z-variation in stress-component σ_{xx} is calculated as follows

$$\sigma_{xx} = -10\ x\ 10^6 + (10^5)\ z \qquad (3.34)$$

The stress gradient is typically used to reproduce the effects of stress increase with depth caused by the force of gravity. The applied gradient must be compatible with the stress gradient, and the ***zone initialize-stresses comman***d is adapted.

2) Changing Boundary Stress

It is necessary to change the values of applied stresses in the FLAC3D numerical simulation (Itasca, 2021). The load on the footing, for instance, may be changed. A new ***zone face apply command*** can be used to effect a sudden change in the existing stress or force, with the stress range component specified precisely as in the original command, however, with the variation in the value. FLAC3D can detect and replace the conflicting conditions already applied in such a situation. The ***face apply commands*** will replace existing values with new ones for overlapping zones. Before updating the boundary stress state in the model, it is necessary first to remove the boundary conditions (use the command zone face-remove). In several situations, changing the boundary stress gradually will be required for the model (Itasca, 2021). Suppose the "path-dependence" of the solution is critical in the model (as presented in Chapter Three under physical and path-dependence). In that case, reducing the shock to a sensitive system may be often essential. To make the gradual application (or removal) of the boundary conditions simple in FLAC3D, the zone ***face apply command*** must be adopted. The servo keyword from the ramp option can be adopted to increase the applied load or force, for instance, while incrementally maintaining the quasi-equilibrium.

$$\boldsymbol{zone\ face\ apply}\ stress\text{-}xx\ \text{-}1e5\ \boldsymbol{servo\ ramp}\ range\ group\ 'East'\ position\text{-}z\ \ 0,2$$

3.4.2. Excavation Command in FLAC3D

To achieve static convergence in the model, FLAC3D uses physics to inform the path, which results in sudden changes to the model and can have quasi-inertial effects that may artificially exaggerate the damage in the area (Itasca, 2021). To mitigate this condition, the approach is to excavate regions gradually, which will cause the zone removal to be less damaged. To activate this purpose, the zone relax excavate commands must be adopted. The ***zone-based apply*** condition can gradually reduce the zone's stress, stiffness, and density. This can be done until they affect the model and are usually defined to be in the ***null constitutive model***. ***The zone relax command*** uses a servo by default to maintain the quasi-equilibrium automatically. However, This command has various options for controlling the exact method of eliminating the influence of zones tagged in the excavation.

The total number of steps in the model to achieve equilibrium is usually lower when the relaxation command is used. This is very uncommon in FLAC3D. The relaxed versions not only show less damage but entirely lack tensile failure indicator identification according to the examination of the state flag for the zones surrounding the excavations. It is possible to apply stresses around the

body's boundaries with no displacement constraints in FLAC3D (Other finite-element programs will require some constraints to apply stresses around the boundaries). The body in the model will react the same way as the natural body (i.e., if the boundary stresses are not in equilibrium, it will result in the entire body moving).
Similarly, the effect will arise if the material is excavated from the body supported by the stress boundary condition; the body is usually under gravity. However, the removal of the material will reduce the weight. The body will tend to start moving upwards (Itasca, 2021).

3.4.3. Displacement Boundary

FLAC3D does not directly control displacement boundary; instead, it does not play any part in the calculation process. To describe the boundary's velocity for a given number of steps, it is necessary to apply displacement to a given boundary. However, if the given displacement is a velocity V over N, the number of steps (where N = D/V) can be applied in FLAC3D. In practice, V should be kept small and N large to minimize shocks to the system that is being modeled. To specify velocities or gradients, commands such as the zone ***face-apply command*** or the ***zone gridpoint fix*** and ***zone gridpoint initialize commands*** can be used in FLAC3D.

3.5. Initial Conditions

Before any excavation is initiated in the ground, an in-situ state of stress exists in almost all mining engineering projects. An attempt is usually made to reproduce this in situ state by setting initial conditions in the FLAC3D model. Usually, the information about the initial stress state will come from field measurements. However, when this is unavailable, the FLAC3D model can still run for various conditions. Despite this, the range is potentially infinite, and many constraining factors (e.g., the system must be in a state of equilibrium, and the selected yield criterion must not be violated anywhere). The vertical stresses in the uniform layer of soil or rock for a free surface can be defined as follows in Equation (3.35) below.

$$\sigma_v = \rho g z \qquad (3.35)$$

In the equation above the symbols denotes the following:

g= gravitational acceleration,

ρ= the mass density of the material,

z= the depth below surface.

In rock mechanics engineering, estimating the in-stu horizontal stresses at a particular point is always more complicated. The standard and erroneous expression for the ratio of horizontal stress to vertical stress is presented in Equation 3.36 below.

$$\frac{v}{1-v} \qquad (3.36)$$

*w*here,

v is the poisson's ratio.

The above relationship of horizontal stress to vertical stress is assumed to have been derived from the expression that gravity is the sudden applied force to a mass in the elastic material where lateral movement is prevented. Due to a repeat of the tectonic movements, material failure, overburden removal, and locked-in stresses due to faulting and localization, this condition is hardly ever practical (Itasca, 2021). The model can be conducted to simulate the whole process numerically to arrive at the initial stress condition for the planned engineering works, primarily if enough knowledge about the history of that particular material volume is known. However, there might be other options than this approach. A set of stresses is typically installed compromised, and the FLAC3D model is run until an equilibrium state is achieved. It is essential to state that in FLAC3D, an infinite number of equilibrium states can be used in the system (Itasca, 2021).

3.5.1. Uniform Stresses without Gravity

In deep underground excavations, the gravity variation of stresses from the top to the bottom of the excavation can be ignored because the variation is very small when compared to the stress magnitude acting on the volume of the whole rock mass being modelled (Itasca, 2021). To default the ***gravitational acceleration*** to zero, the model ***gravity command*** may be omitted in the system. The ***zone initialize command*** can be installed to define the initial uniform stresses. To ***initialiaze*** the entire stress tensor at once in the model, the keyword stress can be adopted. This can be done only for the uniform stress field orientation in FLAC3D model.

3.5.2. Stresses with Gradients/Uniform Material

The variation in stress with depth cannot be ignored near the ground surface. To inform FLAC3D about the gravitational acceleration on how the grid operates, the ***gravity command*** is used in the model. It is very critical to understand that the gravity command in the model does not directly cause the stresses to show in the grid; however, it simply cause the body forces to act on all the gridponts. The weight of material surrounding each gridpoint corresponds to the body forces. The force will cause the material to move in the direction of the forces until an opposite and equal forces are generated in the zone stresses with no initial stresses present in FLAC3D model. With the given appropriate boundary conditions (e.g., fixed bottom, roller boundaries) of the model, FLAC3D will generate its own gravitational stress around the boundary that are compatible with the gravity that was applied. This process may be insufficient and ineffective because many of the hundreds steps will be necessary to reach equilibrium. It is important initialize the internal stresses in the model such that they can satisfy both gravity gradient and reach equilibrium state. To automatically initialize the stress field due to gravity, the ***zone initialize-stresses command*** is used in FLAC3D model. The first command to be given is the ***model gravity command*** and then the ***density command*** must be assigned to all other zones. To calculate stresses for any irregular

geometry in the model, the ***zone initialize-stresses*** command is adopted. This works very well by finding all the variations in values that may affect gravitational loading and pursuing which one would come across as you move from the given zone against gravity direction.

3.5.3. Initial Stress State with gravitational gradient

To determine the stresses in xx and yy direction, the keyword ratio is used to specify horizontal stress ratio K_0 is used which are equal. The stress boundary condition if they are used they need to be compatible with the calculated stresses using the ***zone initialize-stresses.*** To make stress and gradient calculations very simple and clearly, in line FISH is used in FLAC3D numerical modelling. The maximum compressive vertical stress in FLAC3D model is defined as the height **x** density **x** gravity **x** ratio and whereas the gradient is deined as density **x** gravity **x** ratio.

3.6. Reaching Equilibrium

The model must reach "equilibrium" after setting up initial conditions and probably during multiple intermediate model stages. The "model solve" command is used to achieve the equilibrium in FLAC3D. Now, the question is how to know if the model has reached equilibrium. The second question is how to see if you have performed more cycles than required in the model or if some portion of the model would require more computational time.

The model calculation cycles in FLAC3D are usually performed manually using the commands for a model cycle or model step. This is useful in instances where velocity is prescribed at the boundary, and there is a need for a step to reach the specific total displacement in the model. However, in some instances, it would be desirable to cycle the process to get a particular condition; in the FLAC3D model, dynamic simulation modelling could be used until a certain amount of time passes (Itasca, 2021). To allow cycling to continue in the model until one or more limits (using keywords) are met, the model solve command is used in FLAC3D. The most common limit of interest in the static model is the command "until the model is in equilibrium."

To reach static equilibrium, FLAC3D uses an iterative procedure based on physics. Therefore, equilibrium means fully converged to a static solution. FLAC3D provides various ways to visualize and measure convergence or equilibrium in the model, as presented below. It is essential to be aware of the issues involved during the process to achieve the efficiency and accuracy of the model in FLAC3D.

3.6.1. Criteria for Determining Convergence

FLAC3D defines five different criterias for equilibrium calculation or determination and these are Maximum Out-of- Balance Force, Local Force Ratio, Average Force Ratio, Maximum Force Ratio, and Convergence.

1) Maximum Out-of-Balance Force

This is the first and simplest tool for measuring convergence. Though not usually used, it is still available for both as a model solve criteria and the zone of unbalance (Itasca, 2021). In the model, every point grid (structural node) receives forces from zones, gravity and elements (Itasca, 2021).

These forces are added together to form the net forces actin on a gridpoint. The maximum absolute value of any one component of the remaining forces after all forces are summed up together is called the maximum out-of-balance force. This force can drive the gridpoint in the direction of the equilibrium. The gridpoint can be thought of converged or at equilibrium if the force is zero.
The major disadvantage with the maximum out-of-balance force is that is it not a unit less measure for overall convergence measurement. The model size, zone size, material properties and stress magnitude are the appropriate dependant target values. To use a rule of thumb as a single value provided is practically impossible. Due to this reason, it is no longer commonly used as a solve criteria.

2) Local Maximum Force Ratio

This is the unitless measure for local convergence at the gridpoint. The concept is to divide the out-of-balance remaining components after adding the forces by the measured total forces at the gridpoint. Because of this reason, FLAC3D uses the "Manhattan norm" or "Taxicabnorm" For performance purposes, we use the "Manhattan norm" or "Taxicab norm" of a vector, defined in Equation (3.37):

$$\langle v_i \rangle = |v_x| + |v_y| + |v_z| \qquad (3.37)$$

The components of the vector are calculated as sum of absolute values

Therefore, the Local Force Ratio can be defined as shown in Equation 3.38 below.

$$\frac{\langle \sum_i f_i \rangle}{\sum_i \langle f_i \rangle} \qquad (3.38)$$

Where f_i is the equation denotes force vectors that are added to the gridpoint.

The maximum Local Ratio at the model's gridpoint is defined as the local maximum force ratio. This measure of convergence in the model is very conservative. However, it becomes a weakness when less than two forces are applied to the gridpoint or when all forces are applied in the same direction. In such instances, only equilibrium values are the possibility for the model's denominator and numerator to converge to zero. Therefore, the ratio between the two will be 1.

3) Average Force Ratio

The sum of all out-of-balance force components at every gridpoint divided by the total sum of all forces applied at the gridpoint is called the average force ratio. The Average Force Ratio is expressed as shown in Equation 3.39.

$$\frac{\sum_j^{\bar{n}} \langle \sum_i f_i \rangle}{\sum_j^n \sum_i \langle f_i \rangle} \qquad (3.39)$$

This measure is very reliable for the overall convergence in the system. This is good for relatively uniform models. This is the bulletproof evidence enough for default convergence criteria for solving the model, and the average ratio used is 1e-5.

4) Maximum Force Ratio

The maximum out-of-balance force divided by the average total force that is acting on all the gridpoints is referred to as Maximum Force Ratio. Therefore, the average total force is defined as follows in Equation 3.40 below.

$$\frac{\sum_j^n \sum_i \langle f_i^j \rangle}{N} \qquad (3.40)$$

Where: -

N is denoted as the total number of gridpoints in the model

5) Convergence

For the user to have more control over the convergence criteria that is desired and by overcoming the possible disadvantages of depending on the local force ratio, the convergence solve was created. Convergence is unimaginatively quantity which is defined as the ratio of the *current* local force ratio to the *target* local force ratio. A volue of 1.0 is considered to be "converged". However, the **Maximum Convergence** is defined as the measure of the overall model convergence tied to keywords of convergence in the model solve.

3.7. Result Interpretation

Interpreting the results in the FLAC3D model can be difficult because it uses a nonlinear system rather than a conventional finite-element program that solves at the end of the calculation phase. Several indicators can be used to evaluate the state of the numerical model (e.g., stable, unstable, or steady-state plastic flow of the model). Various result interpretation indicators are described below.

3.7.1. Unbalanced Force and Convergence Results

The zones that contribute to the forces around the gridpoint are connected to each gridpoint. The algebraic sum of gridpoint forces is almost zero at the equilibrium state (i.e., forces acting on one side of the gridpoints are nearly balanced to those acting on the other hand). The failure and plastic flow will occur within the model if the unbalanced forces approach a constant non-zero value. As mentioned earlier, five methods of determining model convergence in FLAC3D exist. The above convergence model determination is based on the out-of-balance force that acts on the gridpoint. The convergence model results can be saved in historical form and then viewed in graphical form. It is essential to use the convergence criteria to assess the model state.

The average force ratio of 1e-5 is the rule of thumb value for the average force ratio. In contrast, the value for the local force ratio is 1e-4, or 1.0, which is used for convergence to indicate the overall convergence value. However, depending on the size or specificity of the model and the degree of precision required, values of 10 or higher can be used to represent the acceptable design

criteria (e.g., an adopted higher value may be good enough for an intermediate stage in the model process or sequence).

3.7.2. Gridpoint Velocity Results

Plotting out the whole field velocities can help to assess the grid (plot of item "***zone-vector***" and set a value of "Velocity), or by selecting certain key points in the grid and tracking history velocities (e.g., zone history velocity-x, velocity-y, velocity-z, or velocity). Both vector and velocity plots are very useful. When the velocity histories shows horizontal traces in the final stages, the condition will show steady-state. The absolute equilibrium will occur if they all converge to nearly-zero (comparing to the starting values); then the steady plastic-flow will occurif the history has converged to a nonzero value at the gridpoint corresponding to history. The system is likely to be in transient situation if one or more velocity plots indicates fluctuating velocities. The units of measure for velocities is displacement divided by the number of steps.

3.7.3. Plastic Indicator Results

The FLAC3D plasticity models, with their intricate stress plots, present a fascinating challenge. Stresses that satisfy the yield criterion can be plotted in the zone plot item by setting "ColorBy" to "Label" and then setting "Label" to "State." These indicators typically denote that plastic flow is occurring. However, it's possible for an element to "sit" on the yielding surface without any significant flow. To truly grasp the mechanism developed in the model, it's crucial to examine the entire pattern of plasticity indicators in FLAC3D.

A standard Mohr-Coulomb plasticity state plot, which is a graphical representation of the stress and strain states of a material, can indicate the two types of failure mechanisms, which are tensile and shear failures. A different color on the plot will show each type of failure in the model. This plot will also indicate whether the stress within the zone is on the yielding surface (i.e., the zone is positioned at the active failure, -n) or that the zone failed before the model was run and has now failed below the yielding surface (i.e., the zone failed in the past, -p). At the beginning of the simulation in the model, initial plastic flow is always expected to occur. However, the subsequent redistribution of stresses will unload the yielding elements so that the stresses within can no longer satisfy the yielding criterion, indicated by shear-p or tension-p (on the state plot of plasticity). If a continuous line of active plastic zones (either tensile-n or shear-n) joins two surfaces in the model, a failure mechanism will be in the plot. If the plot's velocity shows motion corresponding to the exact mechanism, then diagnosis will be verified in the model in FLAC3D. Two patterns must be compared before and after the execution of roughly about 5000 steps if there was no contiguous line or band of active zones between boundaries. At this point, the question is whether the active yielding region is decreasing or increasing. If the active yielding is decreasing in the model, the system is heading to equilibrium; if it is increasing, it is headed for ultimate failure.

Another question to ask if the condition of continuing plastic flow has been identified in the system is: Is the 'active floe band a continuous line or band of active plastic zones, including those adjacent to the 'artificial boundaries '? Artificial boundaries are those boundaries that do not correspond to the physical entity. However, they exist to minimize the size of grids used in the model. For instance, in a model of a building, the artificial boundaries could be the edges of the floor slabs. The solution will be non-realistic if the plastic flow occurs along the model's boundary due to the influence of the failure mechanism of the non-physical entity. This analysis only applies to the

final steady-state solution and the intermediate stages in the model that may exhibit the flow along the boundaries.

3.8. Case Study

Two case studies were considered in this study. The two case studies involved the mining pillars above (Sill and Crown pillars). The Saadah (SA) ore deposit has been experiencing rock mass-related failures, mainly on SA-1498 North and SA-1575 South levels (Figure 3.2). These failures have primarily been attributed to the interaction of structural geological features with mined-out excavations in the form of drives, cross-cuts, and stops. The most prominent geological structures contributing to failures are the central fault zone parallel to the main orebody formations, inclined parallel to the orebody footwall, and hangingwall contacts. However, the failure mechanism will not be discussed in this study. This study aimed to evaluate the stability and suitability of artificial pillars using numerical code in FLAC3D.

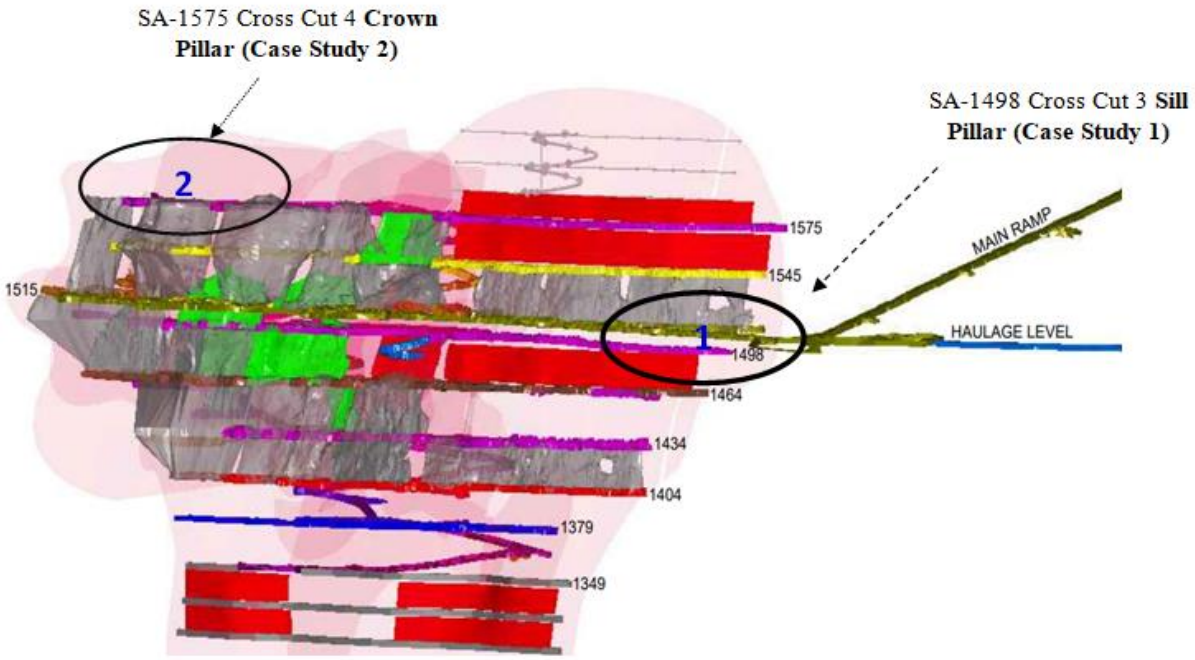

Figure 3.2: Section of the mine where the study was conducted

3.8.1. Case Study 1: Mining a Sill Pillar

Case study 1 considered the SA-1498 stope, in which innovative artificial concrete pillars were installed before stope drilling, blasting, and production. Above the stope is a 10 m Sill Pillar, in which above is 40 m void.

1) Location of SA-1498 Stope

The stope used as a case study 1 is in the Saadah section of the mine, located less than 250 m below the surface. The stope width was wide, with more than 20 m length, and adverse ground

conditions were encountered, posing a geotechnical risk (as shown in Figure 3.3 (a) and (b)). The footwall and orebody are in fair rock mass condition. In contrast, according to geotechnical mapping and core logging results, the hangingwall is in good rock mass condition (this is presented in Chapter Four). Little or no geological structures were mapped in the stope to pose a significant geotechnical challenge. The stope geometry of the block prepared for artificial concrete pillar installation is 20m wide, 10m high, and 50 m long (as shown in Figure 3.3 below). Above this stope is a void with more than 40 m back length (as shown in Figure 3.3 (a)).

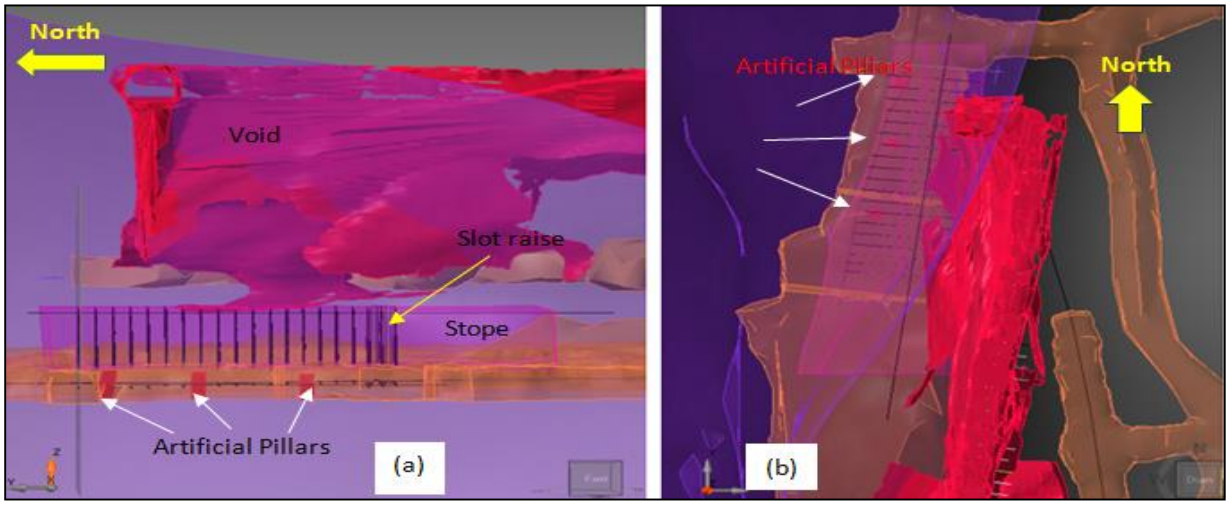

Figure 3.3: Longitudinal section (a) and plan long hole drilling pattern (b) of the SA 1498 stope, respectively (Designed using i-ring Aegis software)

Figure 3.4: Saadah 1498 C23 Stope before ground support reinforcements were installed

3.8.2. Case Study 2: Mining a Crown Pillar

Case study 2 considered the SA-1575 Cross Cut 4 Crown Pillar stope, in which innovative artificial concrete pillars were installed before stope drilling, blasting, and production. Above the stope is a 40 m Crown Pillar, and above or on the surface is a left valley or depression, in which when it rains, water accumulates on the surface. The accumulated water on top of the crown pillar has caused to affect the stability of the rock mass in the SA-1575 Stope.

2) Location of SA-1575 Stope

The stope used in case study 2 is also in the Saadah section, less than 80 m below the surface. The stope width was wide, with more than 40 m, and adverse ground conditions were encountered, posing a geotechnical risk (as shown in Figure 3.5). According to geotechnical mapping and core logging results, the footwall and orebody are in poor rock mass condition, whereas the hanging wall is in fair rock mass condition. Shear zone was intercepted along the footwall contact according to the mapping conducted and the structural geotechnical model available at the mine site. The stope geometry of the block prepared for artificial concrete pillar installation is 40m wide and 50 m long (as shown in Figures 3.6 and 3.7 below). Above this stope is the crown pillar, which is more than 40 m high up to the surface. The stope was planned to be mined in a longitudinal retreat using the Long Hole Open Stoping (LHOS) mining method, as shown in Figure 3.5 below. Below, the stope was mined and backfilled with waste from development. The ground support system in the form of installed split sets and cable bolts has deteriorated due to corrosion, as shown in Figures 3.6 and 3.7 below.

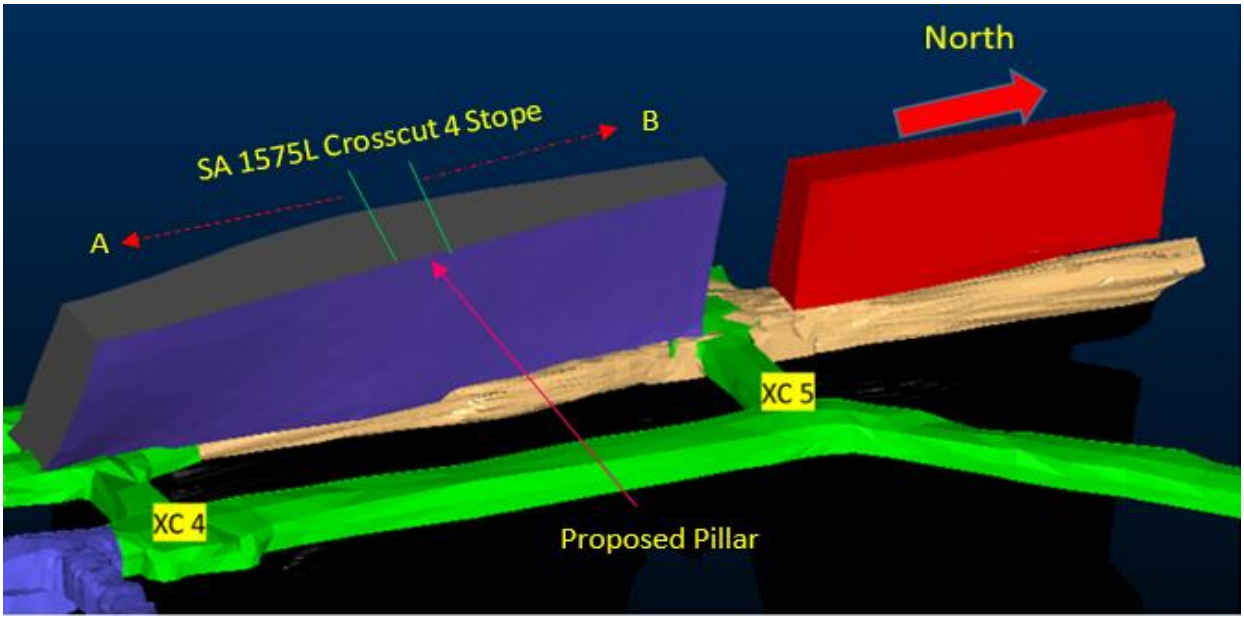

Figure 3.5: Longitudinal Section of the SA 1575 Cross Cut 4 North Crown Pillar Stope

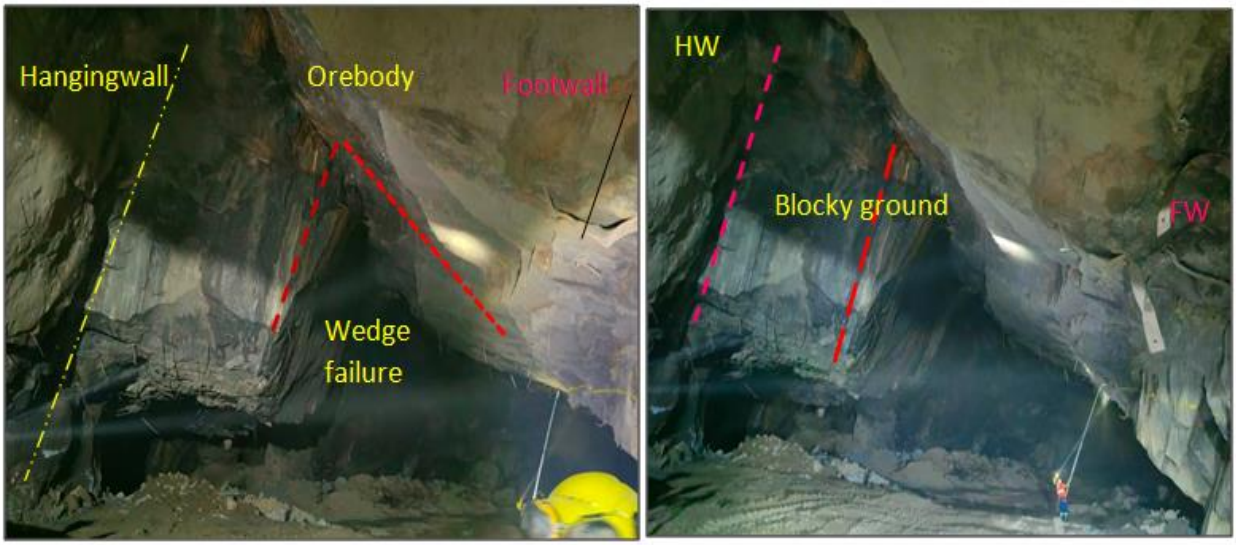

Figure 3.6: Status of the SA 1575 Cross Cut 4 Crown Pillar stope before artificial pillars were installed

Figure 3.7: Status of the SA 1575 Stope before artificial pillars were installed

3.8.3. Rock Mass Condition for Case Studies

The rock mass condition for the two sections of the mine site used as a case study was determined by mapping the exposed development and drilled boreholes. Rock Mass Rating (RMR), Q-system, and Mathews-Potvin Stope Stability method are the rock mass classification systems for geotechnical designs. The mine has seven geotechnical domains, which are Ore zone, proximal footwall (0.5 to 3 m thickness), distal footwall (0.5 to 3 m from ore contact m), middling (Waste rock that is located between two orebodies), proximal hangingwall (2 to 3 m thickness), distal hangingwall (2 to 3 m from ore contact), diabase, dyke, faults and Crown Pillar. The rock mass

condition for the Footwall (FW), Orebody, and Hanging wall (HW) for the two sections used as case studies were summarized below (as shown in Table 3.5).

3.8.4. Empirical Stope Stability Assessment

Stability assessment for the two stopes used as case studies was also conducted using the empirical design based on the Mathews et al. (1981) modified stability number (N'). This design method aimed to quantify the stability of the stope in which artificial pillars were installed.

Table 3.5: Rock Mass Condition for two sections used as case studies

Section	Mining Level	Proximal to Orebody	Q - value Range	RMR (Value)	RMR (Class)
Sa'adah (Case Study 1)	SA-1575 (Point 1)	Footwall	3.0 - 10.2	40 – 80	Poor to Good
		Ore	2.5 - 25.0	40 - 60	Poor to Good
		Hangingwall	0.8 - 10.0	20 - 60	Very Poor to Fair
	SA-1575 (Point 2)	Footwall	5.0 - 10.0	50 - 70	Fair to Good
		Ore	4.3 - 6.4	41 - 60	Fair
		Hanging wall	5.0 - 7.2	41 - 55	Fair
	SA-1575 (Point 3)	Footwall	8.0 - 14.0	60 - 70	Fair to Good
		Ore	4.0 - 12.0	55 - 70	Fair to Good
		Hanging wall	5.0 - 8.0	50 - 60	Fair
Sa'adah (Case Study 2)	SA-1498 (Point 1)	Footwall	4.0 - 10.0	41 - 60	Fair
		Ore	4.0 - 10.0	41 - 60	Fair
		Hanging wall	4.0 - 10.0	41 - 60	Fair
	SA-1575 (Point 2)	Footwall	7.5 - 12.0	50 - 70	Fair to Good
		Ore	7.0 - 12.0	60 - 80	Fair to Good
		Hanging wall	7.5 - 12.0	60 - 80	Fair to Good

The study of Lang (1994) on stope span design states that the critical span curve is developed to evaluate stope roof stability in the open stoping underground mines based on the 172 data sets classified with Bieniawski's (1976) RMR classification system (RMR76) for the rock mass rating from 60-80 or good rock. In 2003, the database was updated with 292 data sets: more than 69% of the databases consisted of good rock, and less than 10% and 20% with RMR76 below 40 and 55, respectively (Potvin et al., 2017). Figure 3.8 illustrates the span design curve for the stope stability where, at an RMR89 value of 55 and span of 20 m, the SA-1498 and SA-1575 stopes were in the potentially unstable zone.

Therefore, the mine needs to adopt measures of stabilizing the stopes when utilizing the empirical design tools for the actual design, considering the variation in the field conditions and existing support system. The stability graph is an empirical design tool regularly used to estimate the stability of underground stopes (Potvin, 2017). Mathews et al. (1981) developed the initial stability graph based on 50 case histories, which have since been modified several times. The stability graph proposed by Nickson (1992) is widely used to determine the stope stability in underground mines.

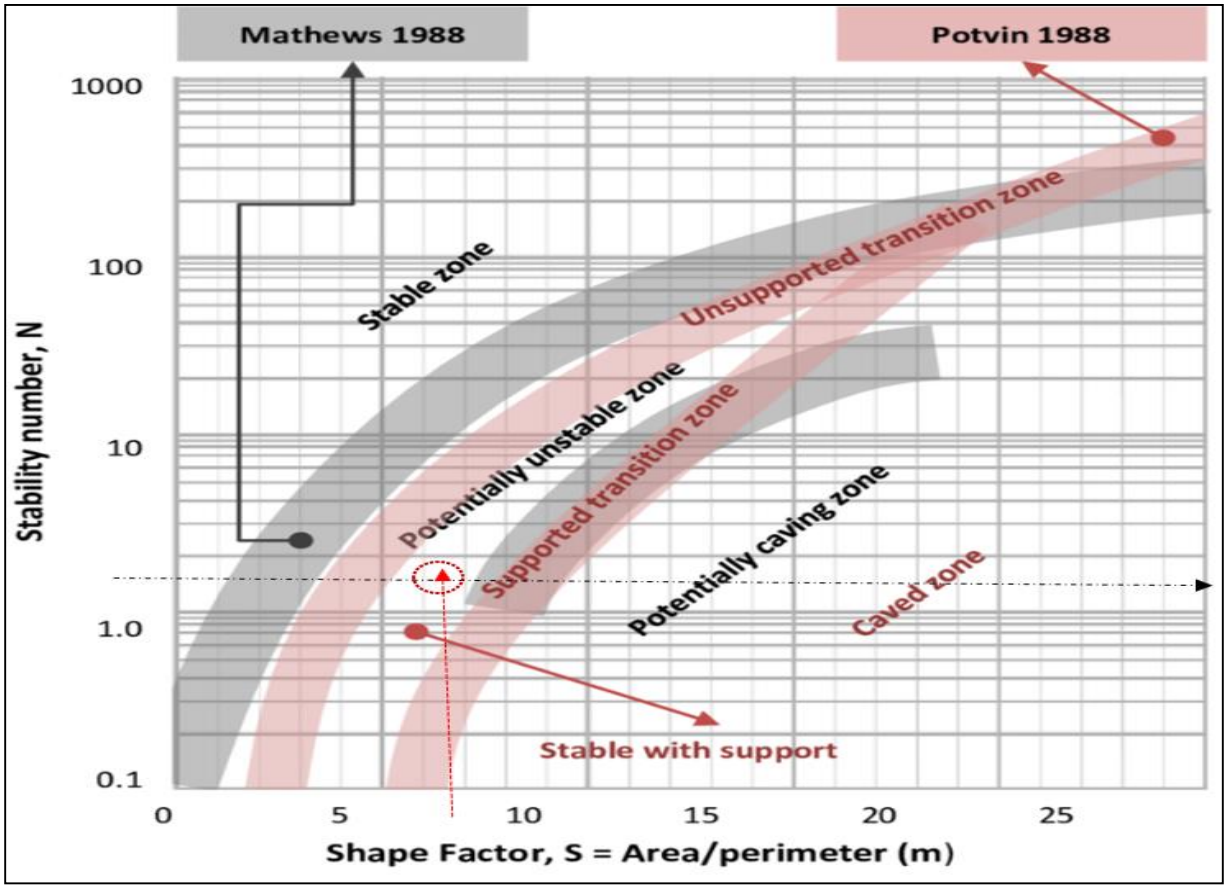

Figure 3.8: Stope stability assessment using the Potvin (1998) Stability Graph for two stopes used as case studies

3.8.5. Installation of Artificial Concrete Pillars

The artificial concrete pillars were prepared and installed according to the following stages and procedures;

1) Artificial Concrete Pillar Preparation

Concrete innovative artificial pillars were constructed using the material composition of quarry aggregate (limestone material), Ordinally Portland Cement (OPC), and reinforced wires. A mold measuring 1.4 m wide, 0.4 m high, and 1.4 m long is used to make the concrete pack (Figure 3.9 (a)). Each concrete pack is designed with some cubical lifting "spaces" at the base for easy lifting by the telehandler (Front End Loader), as shown in Figure 3.9 (b). The concrete pack can cure over 28 days to achieve a minimum allowable compressive strength (UCS) of 24 Mpa and above.

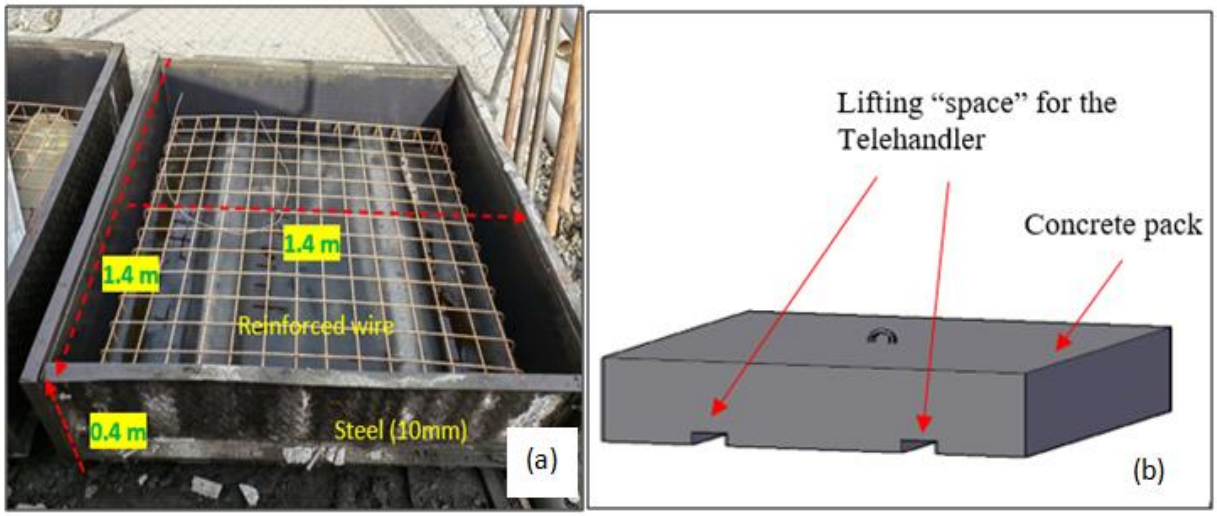

Figure 3.9: Artificial Concrete mold with reinforced wire (a) and concrete design for easy lifting by telehandler machine (b)

a) Stage 1 is Mold Preparations

The following section describes the dimensions of mold and reinforcement wire used to construct the artificial concrete pillar at the mine site.The mold comprises 10 mm thick steel and angle bars, 1.4 m Long, 1.4 m Wide, and 0.4 m high (as shown in Figure 3.9 (a)).

i. *Before construction, reinforced wire is placed in the mold and waits for concrete placement (Figure 3.9 (a) above).*
ii. *The front-end loader is used for mixing aggregate and cement, then pouring it into the mold, and the operator compresses the material using the shovel to ensure it's evenly distributed. Mixing was done at the mixing bay with the loader.*

b) Stage 2 is Material Mixing

The following describes the stages which are involved;

i. *Ordinally, Portland Cement (OPC) is extracted from the silos at the batch plant using a mixer or agitator truck with a capacity of $5m^3$. Water to Cement ratio should be at 0.5. Then, cement slurry is poured on aggregate, and the front-end loader mixes the material. The front end loader is used for mixing material (cement slurry and aggregate) at the mixing bay. The water must be clean and free from any chemicals that can affect the strength of the concrete packs.*

ii. *When adequately mixed, the material is transported to the concrete construction site and poured into the prepared mold. Mixed material is transported by using a front-end loader. The front-end load is also used for pouring mixed material into the mold. The mold is made of thick steel iron sheets.*

iii. *When the material is complete in the mold, the operator uses the shovel to compact the concrete surface and ensure the concrete material is evenly distributed in all corners as shown in Figure 3.10 below.*

Figure 3.10: Pouring of the mixed concrete into the mold (a) and operator distributing the concrete (b)

c) Stage 3 is Concrete Pack Curing

The curing stage is critical to ensure the constructed concrete packs achieve ultimate strength (UCS) of at least 24 MPa. The concrete is only removed from the mold after 24 hours.

i. *After three to four hours, the operator must pour water on top of the concrete and allow it to flow.*

ii. *Another cycle after 12 hours is to pour additional water on top of the constructed concrete and allow water to flow and float on top of the concrete.*

iii. *When the concrete is hard and strong enough, usually after 24 hours, it is generally removed from the mold and taken to the storage facility on the surface (as shown in Figure 3.11). The concrete pack will be stored, and curing will continue until it is transported underground.*

iv. *The concrete packs are transported underground using dump trucks. Telehandler machine is used when loading and unloading the packs from the dump trucks.*

Figure 3.11: Concrete pack constructed before being removed (a) and constructed concrete pack ready to underground.

d) Stage 4 is Site Preparations

This stage involves preparing the site before artificial pillars are installed. The preparation consists of cleaning, lashing out, barring down, and installing the ground support system. The sites used as case study before artificial concrete pillars were installed are shown in Figure 3.12 for the SA-1498 Stope.

e) Stage 5 is Installation of Artificial Pillars

The following briefly outlines the steps for artificial pillar installation. Figure 3.12 (a) presents the packing of the concrete pack, whereas Figure 3.12 (b) shows the fully installed artificial pillars before drilling commences.

i. *The ground must be level flat by scrapping the floor using a loader and then applying concrete on the floor.*

ii. *Each concrete pack must be erected one at a time and aligned in the same direction as the previous (as shown in Figure 3.12 (a)).*

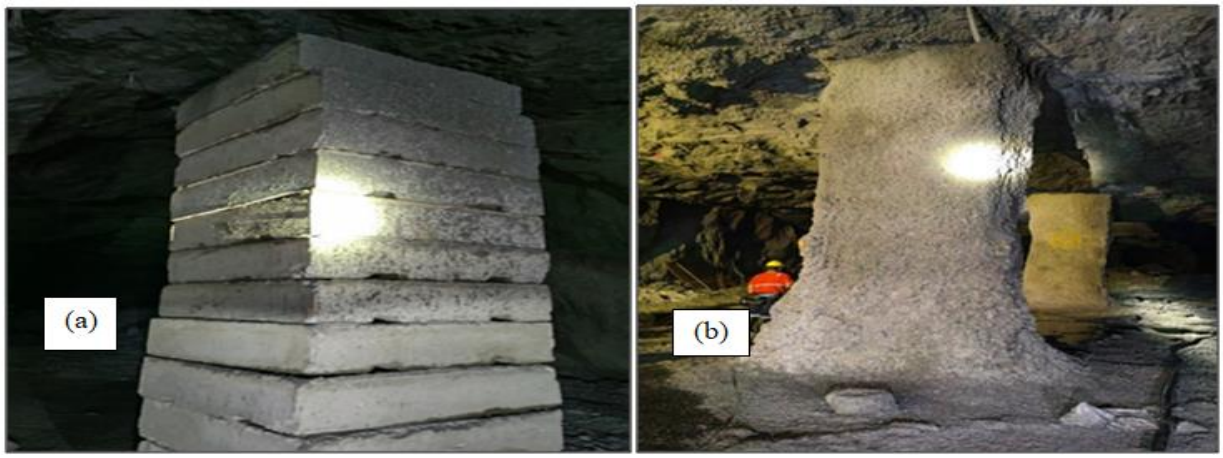

Figure 3.12: Artificial pillar installation after packing (a) and after shotcreting the pillars (b)

iii. *Artificial concrete pillars are installed up to the roof and pre-tensioned before welded wire mesh is applied around the pillar. Then, a 75-100 mm thick shotcrete is applied to avoid further displacement.*

f) Stage 6 is During Longhole Drilling

Figure 3.13 shows the condition of the artificial concrete pillars during stope drilling. The artificial pillars are monitored by visual inspection to note any changes or deformation around the pillar. The pillars have provided a perfect support system, leading to an improved drilling of the production holes. The innovative artificial concrete pillars gave the operator confidence to improve the drilling operation.

Figure 3.13: Condition of the artificial concrete pillars during longhole drilling

g) Stage 7 is During Loading from the Draw Points

Figures 3-14 show the condition of artificial concrete pillars during stope blasting and loading. The artificial concrete pillars are remarkably intact after the slot opening, with no signs of deterioration. Lashing is conducted by retreating from the supported area.

Figure 3.14: Condition of the artificial pillars during production loading from draw-points (a) and the condition of the artificial pillar after the last blast (b)

2) Concrete Parameters Requirements

The backfilling concrete has anelastic-plastic behavior for which the Mohr-Coulomb drained material model can be used. As discussed by Ardiaca (2009), the elastic modulus (E), cohesive strength, and angle of internal friction of concrete can also be estimated by the following relations:

$$E = 8500\sqrt[3]{f_{ck}} + 8\ [Mpa] \quad (3.41)$$

$$C = \beta . f_{ct.d} \quad (3.42)$$

$$\mu = tan\ \varphi \quad (3.43)$$

$$f_{ct.d} = 0.3.(f_{ck})^{(2}/3)\ /1.5\ [Mpa] \quad (3.44)$$

Where:

$(f_{ck}) = Compressive\ Strength(MPa)$;

$f_{ct.d} = Design\ value\ of\ Concrete\ tensileStrength\ (MPa)$;

$C = Cohesive\ Strength\ (MPa)$

φ = angle of internal friction (degree).

The coefficients μ and β depend on the roughness of the joint surface (Table 3.6).

Table 3.6: Values of $\boldsymbol{\beta}$ amd $\boldsymbol{\mu}$ (adopted from Ardiaca, 2009).

Parameters	Low roughness Surface	High roughness Surface	Average Value
β	0.2	0.4	0.3
μ	0.6	0.9	0.7

The above requirement for concrete strength is critical and must be used to design concrete strength and quality control/Assurance. Quality control assurance is the primary concern in constructing artificial pillars, as presented in Figure 3.15.Therefore, the mix design must be adequate for at least Cement at 18.2%, Sand at 27.3%, and Aggregate at 54.5%; this equals the ratio 1:1.5:3, respectively (ACI, 2016). This will achieve a concrete strength of more than 24 Mpa in 28 days (ACI, 2016).

Figure 3.15: Crushing of the poorly constructed concrete packs

3.9. Conclusion

This Chapter provides a concise overview of the methodology and steps involved in evaluating the stability of artificial pillars, with a specific focus on the role of the numerical modelling code FLAC3D. FLAC3D, a finite volume method (FVM), is not merely a 'Predictive Model' but also a 'Numerical laboratory' capable of testing ideals. It's critical to emphasize that FLAC3D, when high-quality geotechnical data are available, plays a paramount role in providing remarkably precise predictions. This precision instills a strong sense of trust in the method's reliability, enhancing the audience's confidence in the results.

The most critically important factor in FLAC3D numerical code is understanding the material properties as input in the model. The material properties required in FLAC3D are generally categorized into elastic deformability and strength properties. This Chapter presents a detailed overview of the properties of deformability and strength. Special considerations of defining post-failure properties, extrapolation of laboratory-measure properties to the field scale, spatial variation of properties, and randomness of properties are also presented in this Chapter. Boundary conditions in the FLAC3D numerical model code consist of field variable values prescribed at the

numerical grid's boundary, such as stress and displacement. In FLAC3D numerical codes, the boundary conditions can be natural or artificial. FLAC3D has also attempted to reproduce the in situ state of stress by setting initial conditions. The FLAC3D model performs calculation cycles manually with the model step or model cycle command. These calculation cycles involve [specific steps or processes]. FLAC3D model is a nonlinear system as it evolves, which adds a layer of complexity to the interpretation of the results. This complexity underscores the depth of the research and the thoroughness of the analysis.

This Chapter also presents the precise steps in constructing artificial concrete pillars. The process, which includes concrete construction, artificial concrete pillar installation, and experimental laboratory testing, is detailed and aided by the pictorial views presented in the sections. This process, which involves [specific steps], is important for creating the physical structures that is simulated in the FLAC3D numerical model. The geotechnical parameters used in the FLAC3D numerical model, which are presented in the next Chapter, were based on empirical charts. The RocLab has been used to define material parameters for the footwall, orebody, and hangingwall formations for input into the numerical model of FLAC3D. The laboratory testing for the concrete samples was also used to define material input parameters for the numerical model in FLAC3D. Chapter Five presents the geotechnical data collection and brief summary of the input parameters in the FLAC3D numerical model. Also, the model setup and results obtained before and after artificial pillars were installed is presented in the Chapter. The other information presented in Chapter Five is detailed discussion of the results obtained in FLAC3D. These results, which [specific effects or findings], provide valuable and comprehensive insights into the stability of artificial pillars, equipping the audience with a deeper understanding of the subject matter. A comparison with other studies that have conducted similar research using FLAC3D have also been included in this study. The next Chapter presents application to a case study mine site.

Chapter 4 : APPLICATION TO A CASE STUDY – AL MASANE MINE

4.1. General Information about the Study Site

4.1.1. Location

The Al Masane Property ("the Property" or "Al Masane Project") is in southwestern Saudi Arabia, approximately 640 km southeast of Jeddah at latitude 18°08'N and longitude 43°51'E (Figure 4.1). The elevation is approximately 1,620 m above sea level. Najran is the principal town in the area and is serviced by air from Jeddah and Riyadh. Access to the project site from Najran is by paved road to Sifah, which is 130 km from Najran. From Sifah, access to the site is by a 20 km improved asphalt roadway. As of February 2009, the road from Sifah had a short gravel section and was under construction through the project site. There are scheduled flights from Jeddah to Abha and Najran.

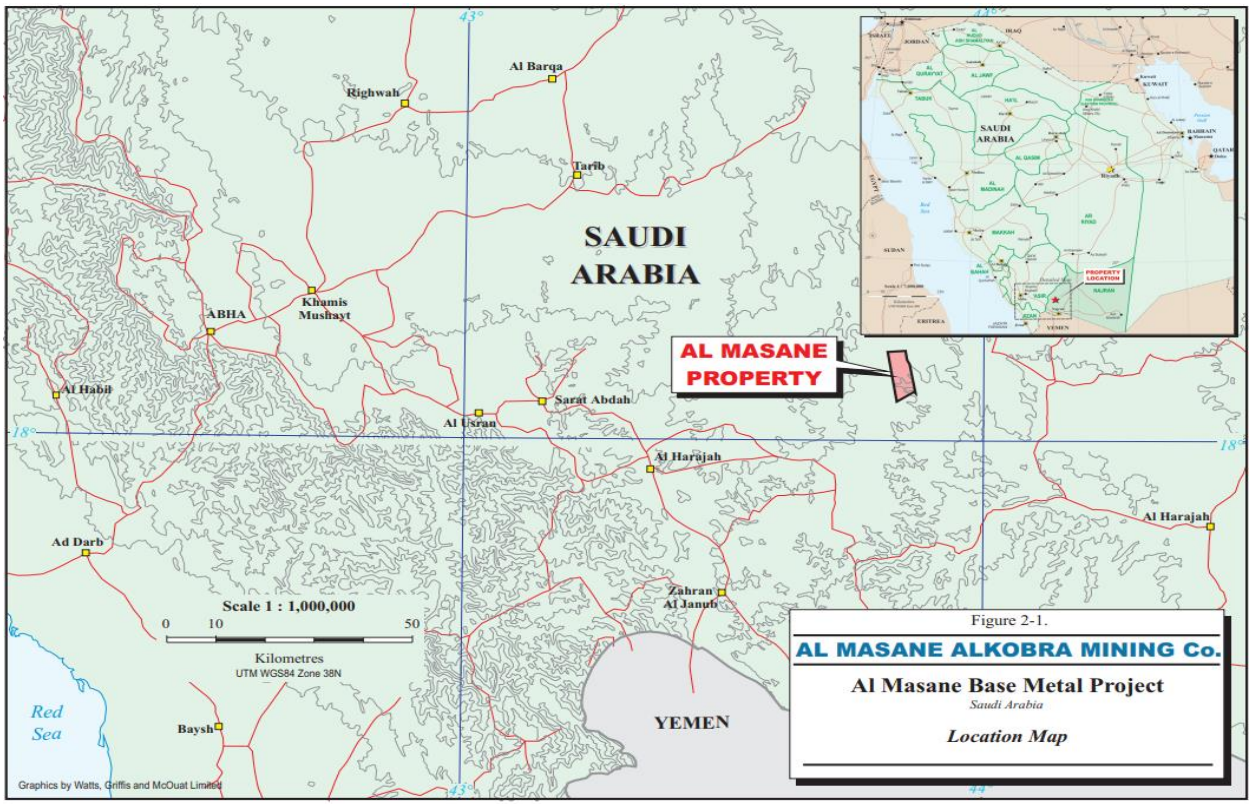

Figure 4.1: Location of the Al Masane project (source: WGM, 2007)

4.1.2. General Geology

While the basic framework of the geology of the Al Masane region is understood, the details, particularly of the structure and stratigraphy, are less so (Smith, 1981). This is especially true in the Al Masane region (Smith, 1981). The stratigraphy was first studied by Jackaman (1972) in the Wadi Wassatt-Qatan areas, where he was the first to point out the island arc affinities of the rocks (Greenwood et al., 1976) established a regional stratigraphic framework during his reconnaissance geologic mapping. Riofinex (1978) challenged this framework. C.E. Smith of the USGS attempted to synthesize the regional stratigraphy based on his extensive detailed work on mineral deposits in the region (Smith, 1981). Work conducted by Greg Fernette and Edward Neczkar of WGM was confined mainly to the Al Masane mine and the immediate area, except for work at other prospects mentioned previously. Fernette and Neczkar (1981) compiled a regional geologic map of the ASDC exploration license areas to aid continued exploration.

In general terms, the layered rocks of the Al Masane region consist of a volcanic assemblage and a metasedimentary assemblage(Smith, 1981). These outcrops are in a series of north-trending belts. Greenwood recognized two regional formations: the Wassatt Formation, composed of volcanic rocks, and the younger, predominantly sedimentary Qatan Formation. Riofinex divided the volcanic rocks into two units above and below a middle sedimentary-volcanic unit (Smith, 1981). The study of Smith (1981) recognizes a felsic volcanic unit separate from the mafic volcanic and a single metasedimentary unit. Fernette and Neczkar (1981) largely followed Greenwood and Smith in their compilation of regional geology because their work more accurately reflected the stratigraphic and structural picture understood at the time. Five lithologic units of layered rocks were outlined (Heyer, 1989). Intrusive rocks are grouped into five groups, of which two groups exist in the area surrounding the Al Masane deposit, as shown in Figure 4.2.

Intermediate Volcanic Breccias and Lapilli Tuff are common throughout the region and comprise one or more regionally mappable units (Lawrence, 1984). The predominant rock types are feldspathic wacke, lithic wacke, phyllite, conglomerate, and lapilli tuff. Some graywackes appear to be turbidities (Fernette and Neczkar, 1981). Volcanic breccias and tuffs predominate in parts of the unit, notably west of Al Masane (Fernette and Neczkar, 1981).

Basalt Flows and Basaltic Agglomerate are andesitic to basaltic and include pillow lava, flow breccia, amygdaloidal to scoriaceous lavas, substantial amounts of andesitic to dacitic tuff, lithic tuff, and agglomerate, and thin interbeds of carbonaceous shale, and marble (Fernette and Neczkar, 1981).

Rhyolite Flow and Felsic Crystal Tuff Felsic volcanic rocks occur in three areas associated with the western three volcanic belts in the region. Quartz—plagioclase crystal tuff, crystal—lithic tuff, and some felsic flows are the predominant lithologies (Fernette and Neczkar, 1981).

Felsic Lapilli tuff is dark brown to gray, and weathers are light brown, formed by the accumulation and welding of semi-molten lapilli. Lapilli are mainly flattened (fiamme) pumice platelets and minor fragments of felsic tuff and black shale (Chapman, 1994).

Black and Grey Shale Carbonaceous is in depositional contact with felsic and mafic volcanic rocks east of Al Masane. Rocks in this area include black siliceous shale, siltstone, and gray aluminous shale, with interbeds of mudstone, graywacke, and marble (Fernette, 1982).
Diabase and Gabbro Sill are intermediate volcanic breccias of Al Masane. To a lesser extent, the basalt flow is extensively intruded by diabase sill ranging from one to 30 meters in width (Heyer, 1989). The most prominent concentration of sills is in a zone along the contact between volcano-sedimentary rocks and the mafic volcanic rocks of the Al Masane volcanic belt (Heyer, 1989).

1) The sills are dark gray to black, fine-grained diabase, and fine- to medium-grained gabbro (Stoesser and Elliot, 1979). Locally, the sills are vascular and show a crude layering, which is believed to be related to successive intrusions (Conway, 1985). The sills are concordant to slightly discordant but locally undergo sharp U-shaped bends, which appear to be primary features (Stoesser and Elliot, 1979).

2) Quartz Monzonite and Granodiorite Numerous circular stocks and ring plutons with steeply dipping sides intrude the layered rocks and older plutons (Sabir and Pouit, 1982). These are composed of granodiorite, monzogranite, and riebeckite-bearing quartz monzonite. At Al Masane, these rocks are restricted to the northeast corner of the property (Sabir and Pouit, 1982).

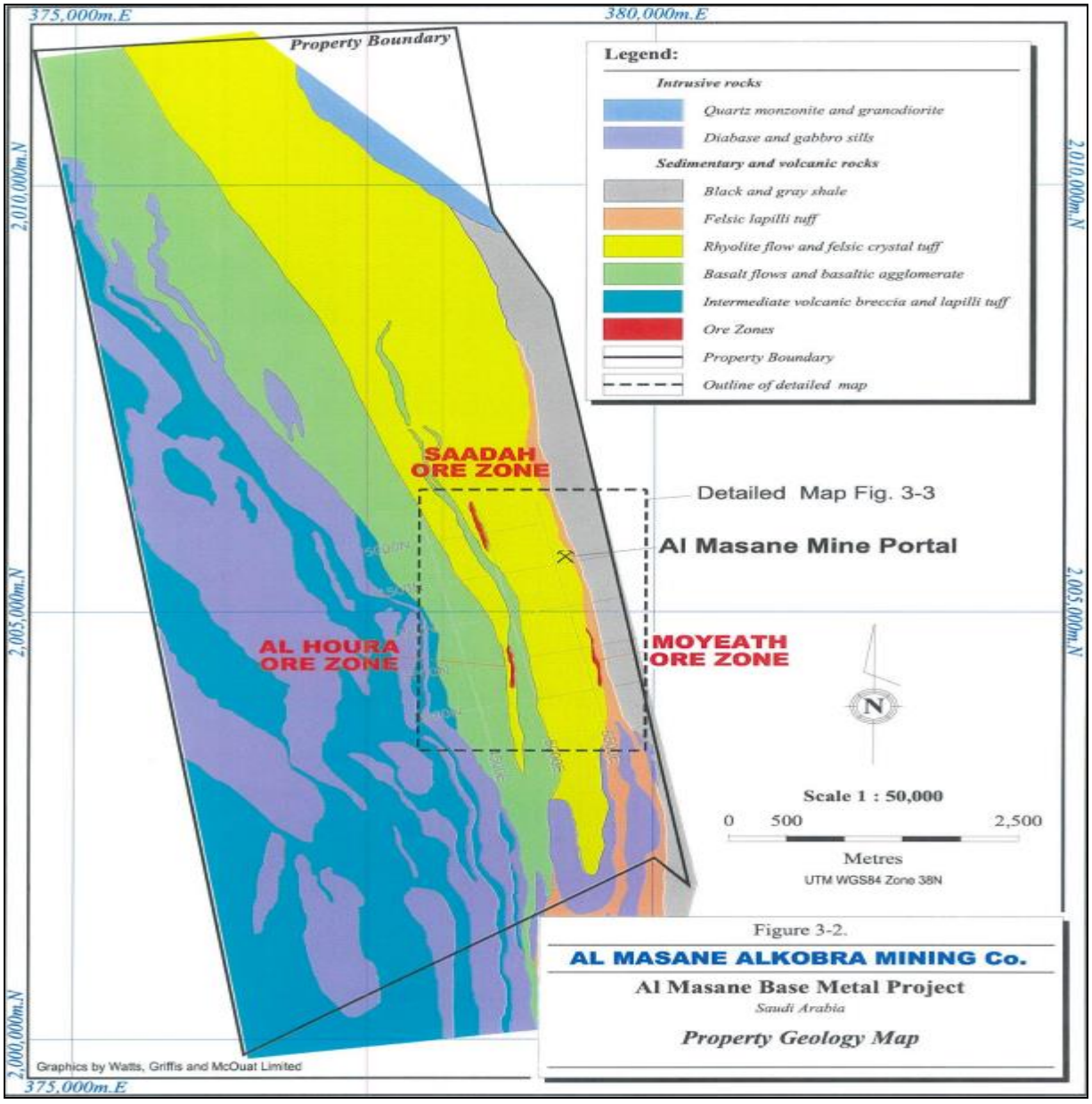

Figure 4.2: Main geology for Al Masane Al Kobra mine (after Sabir and Pouit, 1982)

4.1.3. Al Masane Geotechnical Units

Approximately 24 rock types are observed within the Al Masane resource area (Lawrence, 2007). The reviewed geological discontinuity data from the surface and underground and the rock mass characterization of the Saadah and Al Houra ore zones show no obvious structural domain boundaries at Al Masane (Lawrence, 2007). According to study by Challiner (2009), the geologic structural orientations were consistent within and between the two ore zones (Saadah and Al Houra). Geotechnical domains were developed for design purposes by grouping some of the principal rock types into broadly similar geotechnical units based on their hardness grade, point

load index, and mean RMR values (Griffs et al., 2000). Defining the rock mass in this manner results in nine geotechnical units on site, six of which are of greater importance when less abundant intrusive and hybrid rock types are excluded (Griffs et al., 2000).

4.1.4. Al Masane Rock Mass Characterization

BGC Engineering Ltd (BGC) completed rock mass classification and characterization work using the field and laboratory data from the 2009 Al Masane geotechnical investigation program (Griffs et al., 2000). A summary of the results of this work is presented in the following sections

1) Al Masane Structural Geology

Structural discontinuity data from surface and underground mapping was analyzed to develop a preliminary understanding of the dominant structural orientations present at Al Masane (Griffs et al., 2000). Contoured stereonet plots were developed from discontinuity data using the commercial software DIPS (Hoek and Brown, 2004). Major discontinuity orientations were identified based on Terzaghi weighted pole concentrations (Griffs et al., 2000). The mapping data was further analyzed to determine quantitative descriptions of joint characteristics and conditions (Griffs et al., 2000). A summary stereonet is provided in Figure 4.3. Note that the dip direction orientations on the streets concern 'True North,' which is located 15° east of Mine Grid North (Griffs et al., 2000). Table 4.1 below presents the rock code, lithology, and geotechnical group to describe al masane geotechnical units in this chapter.

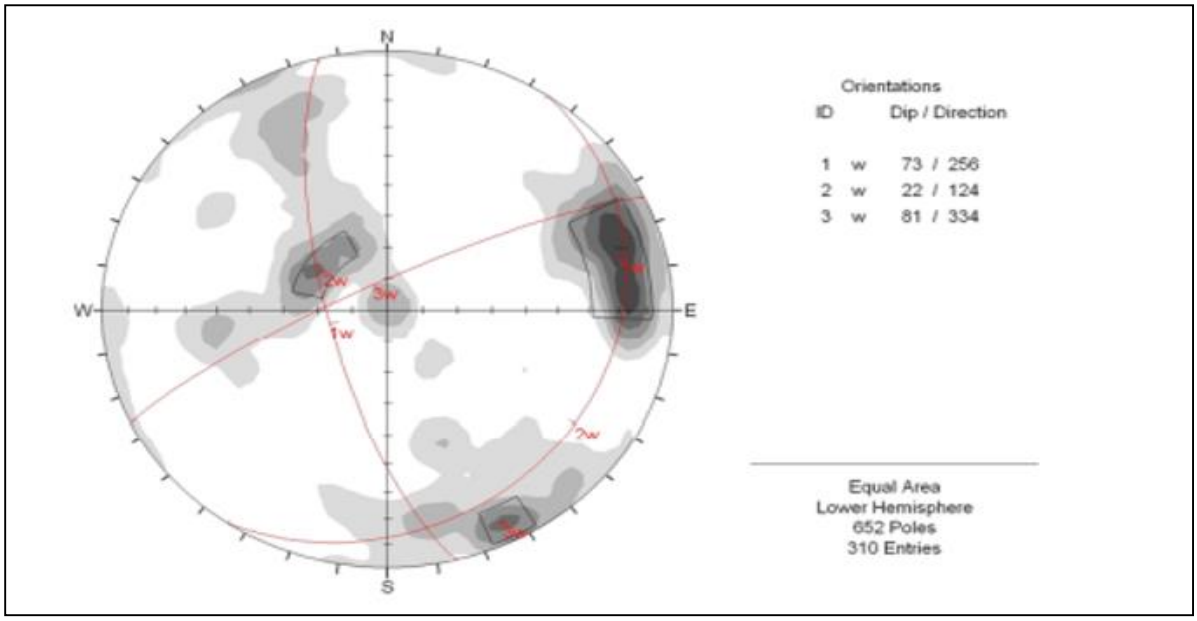

Figure 4.3: Joint character and condition data for the three main sets (Griffs et al, 2000)

Table 4.1: Summary of lithological and geotechnical units observed at Al Masane (WGM, 2007)

Rock Code	Lithology	Lithological Group	Geotechnical Group
FV1	Rhyolite Porphyry	Felsic Volcanics	FV/MV
FV2	Felsic Tuff and Crystal Tuff		
FV3	Laminated Cherty Rh		
FV4	Micaceous Felsic Tuff		
FV5	Lapilli Tuff		
FV6	Bedded Felspathic Chert		
MV1	Andesitic Tuff and Agglomerate	Mafic Volcanics	
MV2	Andesitic Lava		
MV3	Basalt/Andesitic Dike		
C	Chloritite	Sedimentary Rocks	
QTZ	Vein Quartz		
SH	Black Shale		SS/SH
SS	Sandstone		
D	Dolomite Breccia		D
T	Talc		T
G	Gossan	Massive Sulphide	MS
MS1	Thin Bedded Massive Sulphide		
MS2	Massive to Bedded Massive Sulphide		
MS3	Sulphide Breccia		
PY	Pyrite		
DB	Diabase Sill	Intrusive Rocks	DB
B	Basalt Dikes		B
D/T	Dolomite Breccia/Talc	Hybrid Rock Types	D/T
MS/T	Massive Sulphide/Talc		MS/T

As indicated, three discontinuity sets were identified (Griffs et al, 2000). Joint character and condition data for the three main sets is included in Table 4.2.

Table 4.2: Summary of mean structural discontinuity orientations (Griffs et al, 2000).

Data Group	Dip (º)	Dip Direction (º)	Mean True Spacing (m)	Mean Continuity (m)	Mean JRC
ALL DATA	-	-	0.31	3.29	10.21
SET 1	73	256	0.23	4.11	9.68
SET 2	22	124	0.61	5.07	9.52
SET 3	81	334	0.53	1.29	8.05
Note: 1. Dip Direction is with respect to truth north					

2) Al Masane Rock Mass Classification

According to the geotechnical study by Lawrence (2007), the Rock mass ratings (RMR ’76) were determined from diamond drill core, underground line mapping, and surface outcrop exposure in both the Saadah and Al Houra ore zones (Table 4.3). Individual plots of calculated RMR ’76 values vs. depth for each drill hole logged are presented in Table 4.3. Histograms of RMR 76’ calculated from diamond drill core and grouped by geotechnical unit are presented in Table 4.3.

Table 4.3: Summary of RMR ’76 Data (Griffs et al, 2000)

Geotechnical Unit	Mean RMR '76 Rating		
	Drillcore Logging	Underground Mapping	Surface Mapping
FV/MV	62.4	75	80
MS	56.5	76	-
D	62.7	87	-
DB	73.6	78	-
T	48.9	51	-
SS/SH	60.8	62	-

The NGI-Q parameter was calculated from diamond drill core, underground line mapping, and surface outcrop exposure in the Saadah and Al Houra ore zones, as shown in Table 4.4 (Griffts, 2000).

Table 4.4: Summary of NGI-Q Data (Griffs et al, 2000)

Geotechnical Unit	Mean Q-System Rating		
	Drillcore Logging	**Underground Mapping**	**Surface Mapping**
FV/MV	*14.0*	*18.0*	*11*
MS	*14.0*	*25.0*	-
D	*16.0*	*23.0*	-
DB	*22.1*	*63.0*	-
T	*5.0*	*2.0*	-
SS/SH	*15.0*	*13.0*	-

3) Al Masane Rock Strength Determination

Intact rock strengths for the various geotechnical units were determined using the industry standard International Society Rock Mechanics (ISRM) R0 to R6 hardness scale (ISRM, 1978), point load test data, and Uniaxial Compressive Strength (UCS) and triaxial test data. Forty-four UCS tests were completed on samples from Al Masane drill core, representing three of the six principal geotechnical units (Griffs et al, 2000). Hardness and point load test estimates of UCS were available for all units as shown in Figure 4.4. To calibrate the more widely available point load test data, results from the laboratory UCS tests were compared to results from point load testing to develop a linear correlation factor between $I_s.50$ (MPa) and UCS (MPa) was followed (Griffs et al, 2000): $UCSEST = 21^{*}I_s(50)$.

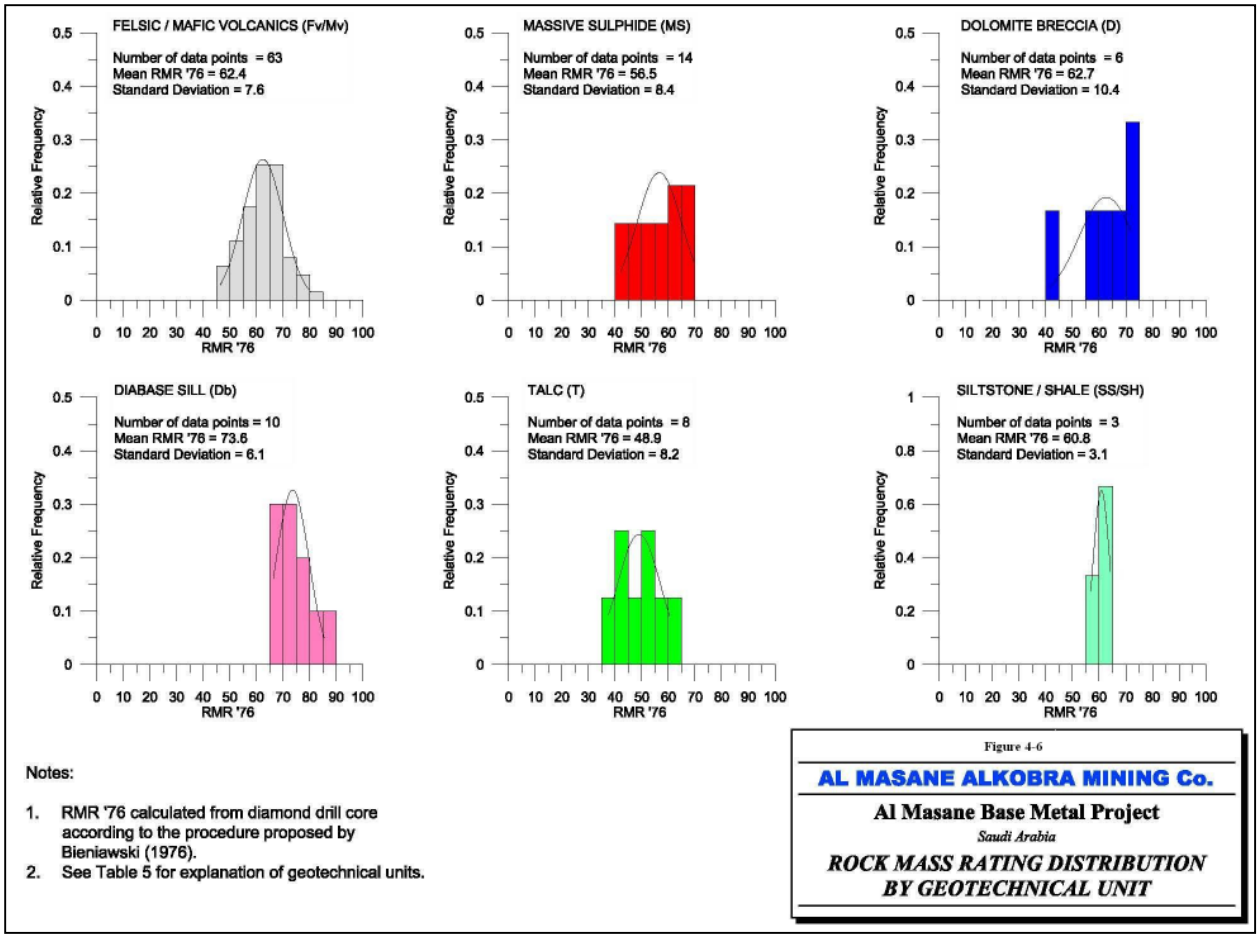

Figure 4.4: Rock Mass rating distribution by Geotechnical Unit (WGM, 2007)

This correlation agrees well with the 20 – 25 x I_s (50) suggested by the ISRM (1978). A design UCS value for each geotechnical group within the resource area has been estimated using this correlation between $I_s(50)$ (MPa) and UCS (MPa).

For consistency, the intact rock strength determined from the calibrated point load strength test data is recommended for design purposes as it is more reliable than hardness data, covers all types, and is generally more conservative than the laboratory determined UCS (Nickson et al, 1992).

Table 4.5: Summary of Al Masane rock strength data (WGM, 2007)

Lithology	From Hardness Grade ("R")			From $I_s(50)$	From Lab Testing	
	UCS (Mpa) Lower	UCS (Mpa) Upper	UCS (Mpa) Avg	UCS (Mpa) Avg	UCS (Mpa) Intact Avg	UCS (Mpa) Global Avg
Db	50	100	75	92	115	120
FV/MV	50	100	75	82	79	82
SS/SH	50	100	75	77	65	71
Db	25	50	38	64	-	-
MS	25	50	38	59	-	-
T/D	5	25	15	32	-	-
T	5	25	15	26	-	-
Notes: 1)	UCS estimated using the average I_s (50) value for each lithology and common/average correction multiplier of 21					
2)	Only Db, FV/MV and SS/ST units laboratory tested					
3)	Intact and Global average UCS values determined from valid UCS and triaxial laboratory test results using the Hoek-Brown Failure Criterion (2002)					

4) Al Masane In Situ Stress Measurement

There have been no direct or indirect measurements of in-situ stress orientation or magnitude at Al Masane, and little external information is available on the stress regime for the area (Griffs et al., 2000). The World Stress Map's (Heidbach et al., 2016) web-based HTML form CASMO was used to create a stress map of Saudi Arabia, North Africa, and surrounding areas (Figure 4.5) to assist in characterizing the regional stress regime at Al Masane. The map includes a borehole breakout measurement within 200 km of the project site, which indicates the potential principal stress direction (Heidbach et al., 2016). This measurement aligns closely with the principal joint set identified during the surface and underground mapping programs and correlates well with the tectonic setting of the Arabian plate (Vita-Finzi and Saadi, 2001). Based on this information, the foliation observed is assumed to have formed under an earlier stress regime than that observed

from breakout and focal mechanism measurements in the northeastern tip of Oman (Vita-Finzi and Saadi, 2001).

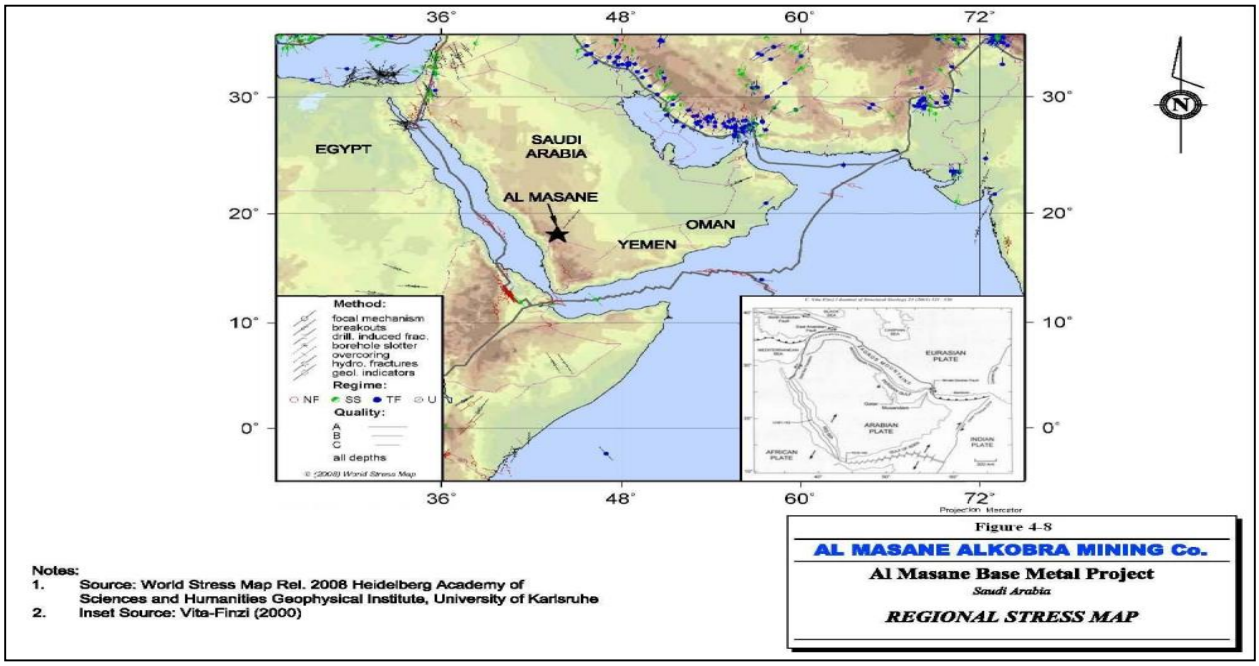

Figure 4.5: Regional Stress Map (Vita-Finzi and Saadi, 2001)

Vita-Finzi and Saadi (2001) note that although instantaneous strain energy release at a compressive plate boundary (Zagros Mountains) is periodic, it is felt only close to the boundary (Eurasian/Arabian plate boundary), and the plate (Arabian) interior acts purely as a reservoir for strain energy. He quotes that gravity data suggest that "elastic flexure of a relatively stiff continental plate over an inviscid fluid layer may distribute vertical stress associated with the Zagros orogeny as far…as the Persian Gulf" (Heidbach et al., 2016). In conjunction with data from the World Stress Map, these statements suggest that the Al Masane mine site sits within an elevated horizontal stress regime, possibly 1-2.5 times the primitive vertical stress (Griffs et al., 2000).

For design purposes, the vertical stress is calculated by the following Equation 4.1:

$$\sigma_v = \rho g H \qquad (4.1)$$

Where: -

σ_v = *Primitive Vertical Stress (pa)*
$\rho = Rock\ Mass\ Density\ of\ 2{,}700 Kg/m^3$
$g = Gravity of\ 9.81 m/sec^2$
$H = Depth of cover of\ 250\ m$

Horizontal stress (σ_H) is subsequently calculated by multiplying (σ_v) by a k factor (ratio of σ_H: σ_v). Based on the results from our interpretations of the World Stress Map information, a k value of 1.5 appears to be reasonable, and has been used in subsequent geotechnical design calculations (Challiner, 2009).

5) Al Masane Geotechnical Design

The previous sections determined and estimated the rock mass strength and stress conditions. They were used for various aspects of mine design, including stope dimensioning, ground support requirements, and a stability assessment of the crown pillar (Griffs et al., 2000). Due to the uncertainties inherent in this stage of the design process, empirical design methods have been used; these methods are based on experience obtained from mining in a range of ground conditions (Lawrence, 2007). More elaborate design methods, such as the use of numerical stress analysis, are not warranted due to the quality of the supporting geotechnical data and would be more appropriate once more detailed observations and measurements are made, such as during the early stages of mining (Griffs et al., 2000).

a) Al Masane Ground Support Pattern

Ground conditions in access drifts and ramps are likely unfavorable, as seen in the existing exploration drift (Challiner, 2009). However, constant man entry, stress changes due to nearby mining, and the vibrations associated with production blasting make it prudent to recommend a standard bolting pattern to reduce the risk of falling ground (Lawrence, 2007). The support recommendations are based on several industry-standard empirical design methods and would be expected in access drifts in North American Mines (Griffs et al., 2000). Once local conditions have been adequately monitored for stability and support performance, these - 104 - patterns should be adjusted to suit local conditions (Challiner, 2009). No rock bolt type or grade recommendation has been made at this time, although a bolt with an ultimate tensile strength of at least 100 kN was assumed for calculation purposes (Griffs et al., 2000). This capacity could be provided by a range of products, including various grades of friction stabilizers, Swellex support elements, or resin rebar (Griffs et al., 2000). Application of any product to the densities provided (Table 4.6) should be carefully reviewed at the final design stage (Lawrence, 2007).

Table 4.6: Al Masane Drift Support recommendations (Griffs et al., 2000)

Excavation Type	Main Entry	Pattern	Bolt Length (m)	Bolt Spacing (m)	Coverage (%)	Mesh (%)
Permanent	Yes	Standard	1.8	1.3	100	50
Temporal	Yes	Standard	1.8	1.3	50	25
	Yes	Spot	1.8	2.6	50	-
Production	No	None	-	-	-	None
Note: Coverage (%) refers to the percentage of that excavation type that is supported, i.e., 50% of all temporal excavations are supported with a bolt spacing of 1.3 m						

For this thesis, 'permanent' excavations are defined as all ramp and primary access drifts, while 'temporal ' excavations would be those used to access stopes (crosscuts). 'Production' excavations, such as slots and some ventilation openings, are not accessed by personnel at any time. Although there are no specific guidelines for the requirement to use mesh, the following principles have been applied (Lawrence, 2007):

i. Exposure of personnel and equipment is greater in main ramps. Installation of mesh (estimated 50% coverage) will prevent loose from falling out, reducing risk, inspection, and support maintenance requirements and
ii. The detailed geological conditions will be known once more detailed drilling has been carried out in planned permanent excavations or during development. Weak rock types (talc and sedimentary units) may require this additional level of support, and a cost allowance should be made to incorporate mesh usage (25% estimated for temporal excavations).

Table 4.7 shows the drift dimensions to vary considerably depending on the purpose, lifespan, and ore zone geometry (Griffs et al., 2000). To deal with this variation, standard bolting densities (average bolt spacing) have been provided (Table 4.8), which will apply to all drifts between 3 and 5 m wide (Griffs et al., 2000). Other drift dimensions are dealt with case-by-case as operational experience is attained (Griffs et al., 2000). All drifts are assumed to be formed using drill and blast methods, and all support is installed at the face as mining advances (Lawrence, 2007).

Table 4.7: Al Masane drift dimensions and use (Griffs et al, 2000)

Type	Ore Width (m)	Drift Width (m)	Drift Height (m)
Ramp	n/a	5	4.5
Drift and Crosscut (trucks)	>5	5	4.5
Drift and Crosscut (No trucks)	>5	4	4
Pilot Drift in Ore	>5	4.5	4.5
Slashed Drift in Ore	>5	<13	4.5
Narrow Vein Drift and Crosscut	<5	3	3
Narrow Vein Ore Drift	<5	3	3
Vent Raises with Ladders	n/a	2.4	n/a

Average bolt spacing (or density) can be challenging to apply to pattern bolting in drifts of a set span (Griffs et al., 2000). Table 4.8 provides some indicative bolting patterns for the four potential drift spans (up to 5 m) proposed for Al Masane (WGM, 2007). These patterns satisfy the average bolt spacings provided in Table 4.8. Bolts per row and row spacing can be adjusted to suit production requirements, providing the average bolt spacing is maintained (Griffs et al., 2000). However, it is recommended that the bolt row spacing does not exceed 1.5 m (Griffs et al., 2000). According to the feasibility study conducted by Lawrence (2007), to maintain an adequate support system, the spacings (see Table 4.7) and patterns (Table 4.8) must also apply to the top half of the sidewall, extending down to approximately 1.5 m from the invert (floor).

Table 4.8: Standard bolting patterns at various drift widths (Griffs et al, 2011)

Parameter	Drift Span (m)		
Dimension	3.0	4.0	5.0
Bolts/Row	3	4	5
Row Spacing (m)	1.3	1.3	1.3
Bolt Length (m)	2.1	2.1	2.1
Average Bolt Spacing (m)	1.3	1.3	1.3

b) Al Masane Stope Design

Geotechnical data collected during the 2009 investigation program determined stable stope dimensions using the industry standard empirical 'Stability Graph' method (Hutchinson and Diederichs, 1996; Nickson, 1992). The method considers a combination of geological, geotechnical, and stope geometry data to determine a unique 'Stability Number' (N') for a given stopping scenario. The Stability Number is defined by N' = Q' x A x B x C, Where Q' is a rock mass classification parameter (NGI-Q parameter with Jw / SRF = 1), A is a measure of the ratio of intact rock strength to applied stress, B is a measure of the relative orientation of dominant jointing concerning the excavation surface, and C is a measure of the influence of gravity on the stability of the face being considered. Once determined, the Stability Number is compared graphically to an empirical dataset of stable and unstable case histories to determine acceptable stopping dimensions (Nickson, 1992). The empirical dataset consists of more than 350 case histories collected from various mining environments, including hangingwalls, footwalls, endwalls, and backs (Challiner, 2009). Based on this comparison with stable and unstable stope data, the maximum opening size can be determined, expressed as a hydraulic radius (defined as the area divided by the perimeter of the face being assessed). For reference, the Stability Graph is shown in Figure 4.6.

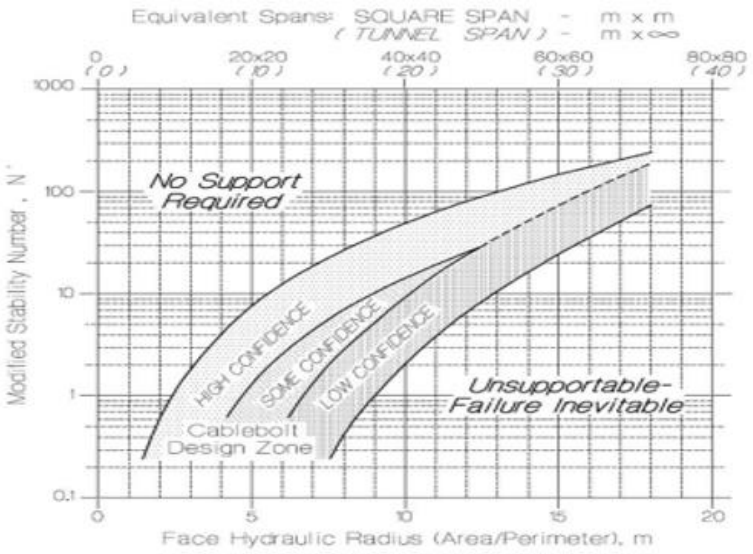

Figure 4.6: Stability Graph chart used to determine Stable spans (after Hutchinson and Diederichs, 1996)

Table 4.9 summarizes the rock mass classification and strength values used in the Stability Graph analysis (WGM, 2007). According to the feasibility study by Griffs et al. (2000) for the al Masane mine, all six of the principal geotechnical units identified in Table 4.9 were evaluated for stability, intact rock strengths derived from point load testing were also used in the analyses (as opposed to intact strengths determined from laboratory testing, which exist for only three of the six principal geotechnical units).

Table 4.9: Summary of geotechnical data for Q' and Intact Rock Strength (WGM, 2007)

Geotechnical Unit	Q'	Point Load Test (Mpa)
FV/MV	18	82
MS	25	59
D	23	64
DB	63	92
T	2	26

Stable stope dimensions were determined based on the considered mining layouts (Griffset et al., 2000). These are (i) longitudinally mined stopes in narrow vein zones and the potential to use (ii) transversely mined stopes in broad zones of the orebody (Griffs et al., 2000). The Stability Graph (SG) analysis places bounds on the dimensions of stopes in both layouts (Nickson, 1992). Due to economic considerations, an emphasis is placed on determining geotechnical design recommendations that will enable longitudinal mining to take place in preference transverse mining (Griffs et al., 2000). Details of the analysis parameters determined for the three critical stope faces for these scenarios are shown in Table 4.10.

Table 4.10: Al Masane Stoping Scenarios for stability graph methods (Griffs et al, 2000)

Stope Scenario	**Scenario 1 (Longitudinal Hangingwall)**	**Scenario 2 (Longitudinal Hangingwall)**	**Scenario 3 (Transverse Hangingwall)**
Depth Below Surface to Stope Midpoint (m)	250	250	250
K-ratio (horizontal: vertical stress)	1.5	1.5	1.5
Dip of Stope Face (^{o})	70	0	0
Dip/Dip Direction of Critical Joint Set ($^o/^o$)	73/256	22/124	22/124
σ_{max} Orientation wrt Stope Face	Tangential	Tangential	Tangential
σ_{max} (Mpa)	1	20	10.5

As indicated, for each scenario, the stope was assumed to be 250 m below the surface (Lawrence, 2007). According to the current mine plan, the bulk of mining in the first few years of operation will occur at or above this depth (Griffs et al., 2000). As previously indicated, a k ratio value (horizontal: vertical stress) of 1.5 has been assumed. This value is considered reasonable given the geologic and tectonic conditions at Al Masane (Vita-Finzi and Saadi, 2001). Stress conditions at the midpoint of the stope face under consideration, required for the Stability Graph analysis, have been determined at this 250 m depth using linear finite element analysis (Griffs et al., 2000).

In the Stability Graph chart (see Figure 4.6), there is a transition zone between the region of spans and rock mass condition in which no support is required, and some failure will occur even with support (Griffs et al., 2000). The boundaries of this zone represent conditions where there was a mix of stable and unstable cases in the original database of case histories (Lawrence, 2007). These boundaries are not fixed and may be calibrated to local site conditions once mining advances to deeper levels (Lawrence, 2007). Therefore, for conservative design purposes, the span for stable supported conditions has been taken as the boundary between the "high confidence" and "some confidence" region (Griffs et al., 2000).

Maximum allowable 'unsupported' and 'supported' stope surface dimensions have been determined for each scenario and each geotechnical unit (Griffs et al., 2000). For the Stability Graph method, 'supported' refers to installing a regular pattern of cable bolt elements to enhance stability (Nickson et al., 1992). Cable bolt spacing and length recommendations for 'supported' cases have been determined using semi-empirical charts developed in conjunction with the Stability Graph method (Challiner, 2009). The results of the Stability Graph analysis are presented in Tables 4.11 to 4.16.

A graphical representation of a typical longitudinal stope is provided in Figure 4.7. The inclined span of the hangingwall for the proposed 25 m mining level interval (30 m vertical floor to roof) was 32 m (a fixed dimension resulting from the proposed mining geometry). Note that the hangingwall span dimension was taken from the bench's vertical face to the backfill slope's midpoint (Griffs et al., 2000).

It was assumed that rock fill would be sufficient to prevent loose slabbing-type failures expected to occur at large hangingwall spans (Lawrence, 2007). The stability graph results indicated a degree of flexibility in maintaining the rock fill face near the mining face, depending on the

hangingwall rock type (Lawrence, 2007). As shown in Tables 4-11 to 4-16, the maximum unsupported open span length maintained in the 'FV/MV' geotechnical unit is 26 m (Griffs et al., 2000). The study by Lawrence (2007) also presented that with support in the hanging wall, the open span length along the strike can be increased to a maximum length of 74 m, provided cable bolts are applied with an adequate density (Table 4.11). Less dense cable bolting patterns could be applied, provided the open span lengths are adjusted lower accordingly (Lawrence, 2007). Calibration and back analysis of the above results were recommended as mining progresses at Al Masane, as more detailed geotechnical data becomes available, to improve long-term stope performance and assist with future mine planning and design (Lawrence, 2007).

Table 4.11: Scenario 1 – Empirical Stope Stability Analysis for Inclined Hangingwall, Slabbing Failure (Griffs et al, 2000)

Unit	N'	Maximum Supported	Allowable HR Unsupported	Inclined Span (m)	Maximum Open Supported	Open Portion (m) Unsupported
DB	75.6	15.0	11.6	32.0	480.0	84.0
DB	27.6	12.1	7.9	32.0	114.0	31.0
MS	30	12.5	8.3	32.0	99.0	34.0
FV/MV	21.6	11.2	7.3	32.0	74.0	26.0
SS/SH	15.6	10.0	6.4	32.0	53.0	21.0
T	2.4	5.9	3.3	32.0	17.0	8.0

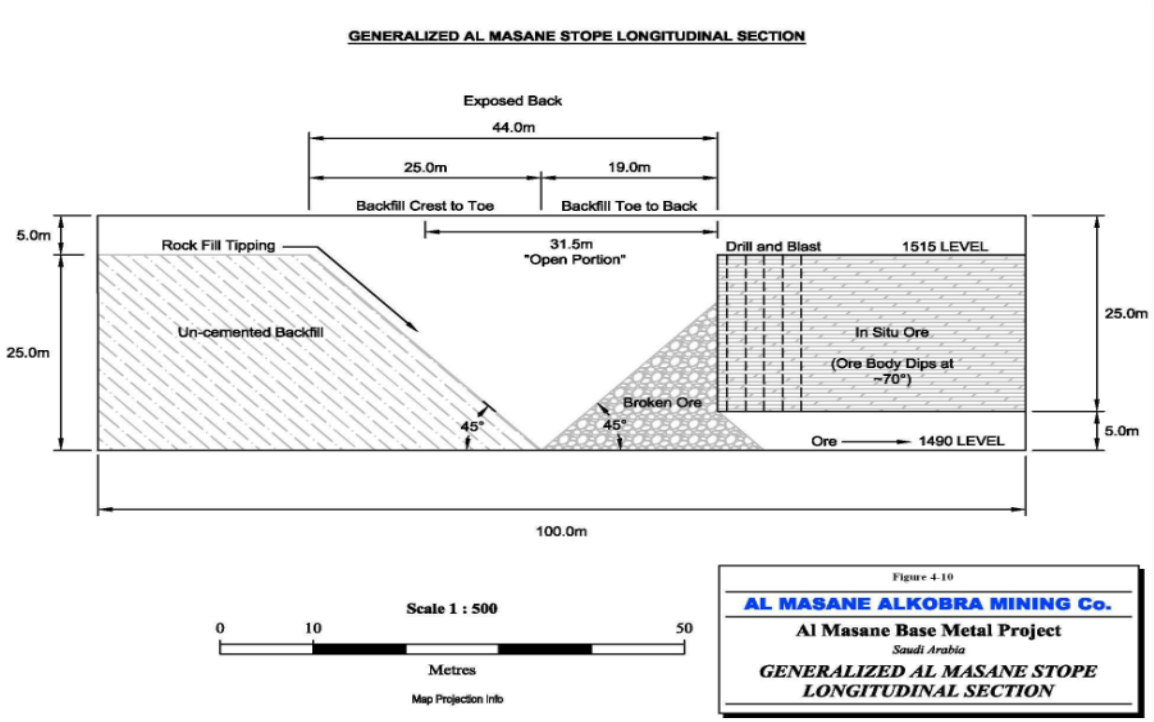

Figure 4.7: Al Masane Al Kobra stope longitudinal section (Griffis et al., 2000)

Table 4.12: Scenario 2 – Empirical Stope Stability Analysis for Inclined Hangingwall, Slabbing Failure (Griffs et al., 2000).

Geotechnical Unit	**FV/MV**	**MS**	**D**	**DB**	**T**	**SS/SH**
Single Strand Cable Spacing (m) for Equivalent						
Square Pattern	1.50	1.50	1.50	-	1.00	1.00
Minimum Cable Bolt Density (Cables/m2)	0.44	0.44	0.44	-	1.00	1.00
Cable Length (m)	9.00	9.00	9.00	-	18.00	13.00

Table 4.13: Scenario 1 – Hydraulic Radius (Griffs et al, 2000)

Unit	N'	Maximum Supported	Allowable HR Unsupported	Stope Length (m)	Maximum Supported	Stope Width (m) Unsupported
DB	11.3	9.3	5.8	100	22	13
FV/MV	2.5	6	3.4	100	13	7
D	2.2	5.9	3.3	100	13	7
MS	2.1	5.8	3.2	100	13	6
SS/SH	1.6	5.2	2.9	100	11	6
T	0.1	3	1.2	100	6	2

Table 4.14: Scenario 2 – Empirical Stope Stability Analysis for Inclined Hangingwall, Slabbing Failure (Griffs et al, 2000).

Geotechnical Unit Single Strand Cable Spacing (m) for Equivalent	FV/MV	MS	D	DB	T	SS/SH
Square pattern	2.00	2.00	2.00	-	1.00	2.00
Minimum Cable Bolt Density (Cables/m^2)	0.25	0.25	0.25	-	1.00	0.25
Cable Length (m)	9.00	9.00	9.00	-	113.00	9.00

Table 4.15: Scenario 2 – Hydraulic Radius (Griffs et al, 2000)

Unit	N'	Maximum Supported	Allowable HR Unsupported	Stope Width	Maximum Supported	Stope Length (m) Unsupported
DB	21.4	11.4	7.50	25	259.0	37.0
FV/MV	5.3	7.4	4.4	25	36.0	13.0
D	5.2	7.4	4.4	25	36.0	13.0
MS	5.1	7.3	4.3	25	35.0	13.0
SS/SH	3.6	6.6	3.9	25	27.0	11.0
T	0.1	3.0	1.2	25	7.0	2.0

Table 4.16: Scenario 2 – Empirical Stope Stability Analysis for Inclined Hangingwall, Slabbing Failure (Griffs et al, 2000)

Geotechnical Unit Single Strand Cable Spacing (m) for Equivalent	**FV/MV**	**MS**	**D**	**DB**	**T**	**SS/SH**
Square pattern	1.50	1.50	1.50	-	1.00	1.50
Minimum Cable Bolt Density (Cables/m^2)	0.44	0.44	0.44	-	1.00	0.44
Cable Length (m)	9.00	9.00	9.00	-	18.00	9.00

Table 4.15 shows that the maximum conservatively determined span for longitudinal mining with cable bolt support was 13 m (Lawrence, 2007). In those zones where the orebody width exceeds 13 m, transverse stoping could be considered up to spans indicated in Table 4.15. As mentioned, the boundaries between stable and unstable regions of the Stability Graph are site-dependent, and to determine the feasibility of adopting the more cost-effective longitudinal mining throughout, the conservative approach can be relaxed (Griffs et al., 2000). By adopting spans corresponding to the limit of the cable bolt support region, spans that can be mined using longitudinal stoping can be increased (Griffs et al., 2000). These revised estimates indicated that the stope back (roof) span is the limiting factor, but an open stope length (along strike) of 60 m could be achieved in orebody spans up to 30 m wide, and an open strike length of 100 m could be achieved in stope widths of up to 25 m (Griffs et al., 2000). These dimensions refer to stope backs. Backfill support of stope hangingwalls, as previously described, was still required. In cases where the width of the ore zone was mined to these limits, the strike length of the top heading must be limited by tight filling to the stope backs or using support such as shotcrete pillars (Griffs et al., 2000). Increased cable bolt density would also be required, with the possibility that mesh and bolts may be needed as supplementary support in localized areas (Griffs et al., 2000). While the advantages of longitudinal mining may warrant the additional support requirements, it was emphasized that there was an increased risk of ground control problems in the wide span zones, and careful evaluation of in situ performance was required to verify that these spans can indeed be adopted (Lawrence, 2007).

6) Al Masane Crown Pillar Assessment

The feasibility study conducted by Griffs et al (2000) also included the crown pillar geotechnical assessment to evaluate the stability of 25 m thick crown pillar located in the northern retreat of the Sa'adah section, in which the orebody protrudes to the ground surface (as shown in Figure 4.8). A crown pillar was required at this location to prevent interaction of the mine workings with the

overlying Wadi Saadah, and particularly to limit the potential for water inflow in the event of surge-type flooding typical for the region (Griffs et al, 2000).

Back analysis of crown pillar stability was undertaken by Carter and Milner (1995) as an initiative to examine methods for design of surface crown pillars. Based on that study, an expression for 'scaled span' required for crown pillar stability was developed (Carter, 2000). Although this empirical approach implicitly excludes site-specific features of rock masses, it is representative of a broad range of geological conditions typical of hard rock mines (Carter, 2000). As such, it provides a means for assessing crown pillar stability based on the collective experience embodied in a database of over 300 case histories (Carter et al, 2005).

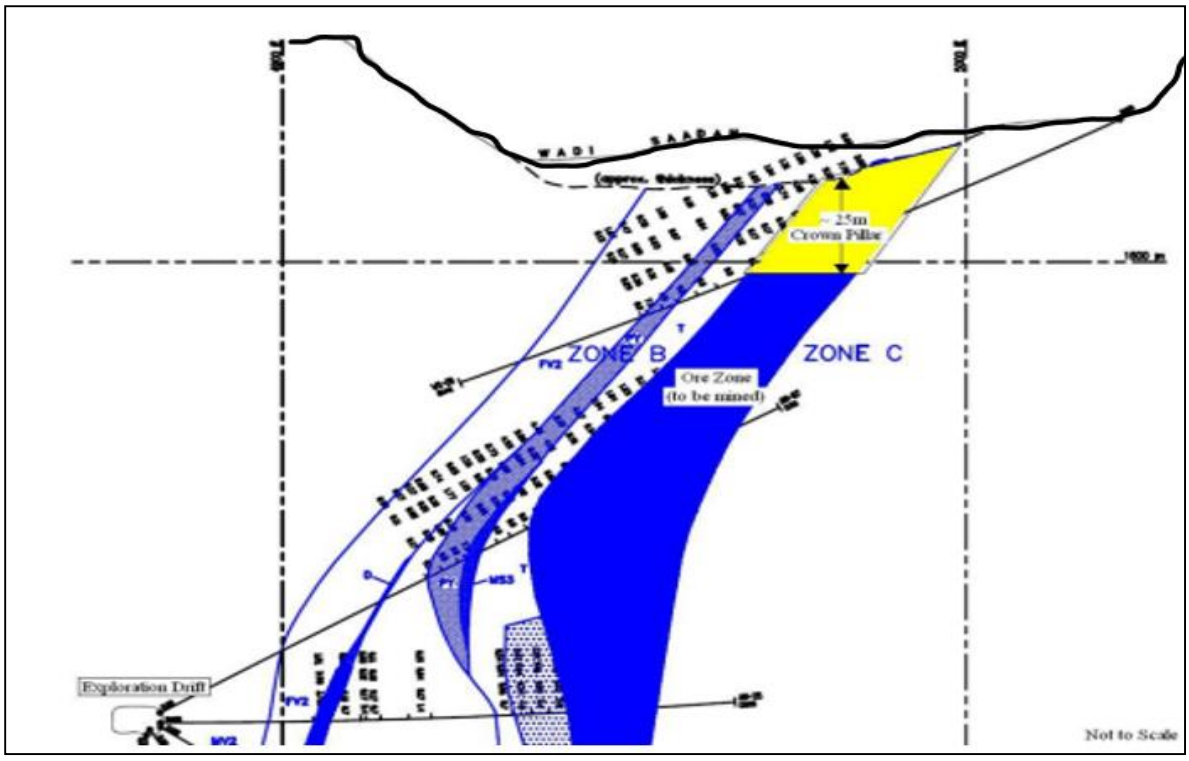

Figure 4.8: Crown pillar thickness design for Saadah section (Griffs et al., 2000)

The scaled span expression is defined by Equation 4.2 below: -

$$T_{calculated} = \frac{S^2.\gamma}{C_S^2\left(1+\frac{S}{L}\right)(1-0.4cos\theta)} \qquad (4.2)$$

Where: -

$T_{calculated}$ = required crown pillar thickness (m)
S = Span of stope beneath pillar (m)
L = Strike Length of stope beneath pillar (m)
θ =Dip of orebody (degrees)
γ =Unit weight of the rock mass composing the pillar ($\frac{tones}{m^3}$)

Compiling numerous crown pillar case histories and plotting scaled span values as a function of rock mass quality, Equation (4.3) separated the data into failed and stable (Carter and Milner, 1995).

$$\textit{States: } 43.0S = 3.3QC \qquad (4.3)$$

where: -

$C_S = Critical\ span\ (m)$
$Q = The\ NGI\ Q\ rock\ mas\ classification\ number$
(With $\frac{J_w}{SRF} = 1$)

The critical span function is presented graphically in Figure 4.9. The empirical data points that define the function have been removed from the graph for clarity (Carter, 2000).

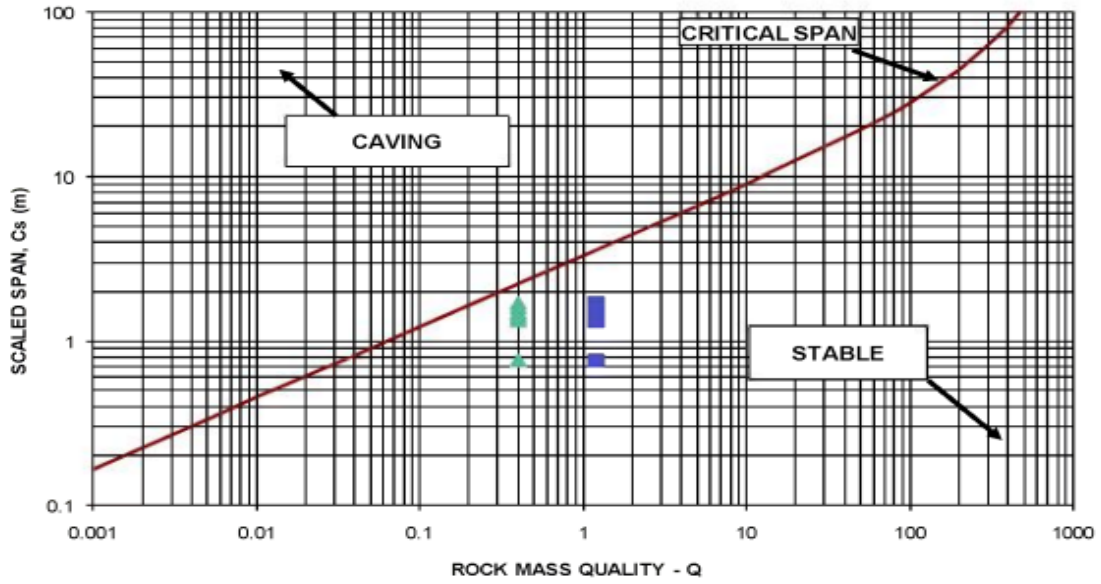

Figure 4.9: Crown Pillar Analysis C_s vs.Q (Carter and Milner, 1995)

Once the required crown pillar thickness has been determined, a 'Factor of Safety' can be defined as the ratio of the proposed pillar thickness (25 m) to the calculated or required pillar thickness (Griffs et al., 2000).
It was recognized that due to the complexity and variability of rock mass characteristics, a single deterministic analysis cannot portray the range of possible stability (Nickson et al., 1992). Thus, Griffs et al. 's (2000) study combined probabilistic analysis with the empirical relationship for crown pillar size, as shown in Equation 4.4.

$$\boldsymbol{FoS} = \frac{T_{proposed}}{T_{calculated}} \qquad (4.4)$$

It was recognized that due to the complexity and variability of rock mass characteristics, a single deterministic analysis cannot portray the range of possible stability (Griffs et al., 2000). Thus, the approach that was taken in their study was to combine probabilistic analysis with the empirical relationship for crown pillar size (Griffs et al., 2000).

Recognizing that individual parameters can represent a range of possible values by a probability distribution, the scaled span expression can be solved discretely for combinations of parameter values selected from the respective probability distributions (Carter, 2000). To obtain a representative output distribution of $T_{calculated}$ and Factor of Safety, the scaled span equations were solved repeatedly using a Monte Carlo analysis (Griffs et al, 2000). The commercially available software package at RISK was used to conduct this analysis in conjunction with a spreadsheet model (Griffs et al., 2000). According to Carter (2000), on crown pillar stability assessment, certain input variables are to remain fixed, such as strike length (100 m), rock mass unit weight (2.7T/m^3), and proposed thickness (25 m).

The normal distribution is generally used for probabilistic studies in geotechnical engineering and was chosen for their research to determine the stability of the crown pillar (Griffs et al., 2000). The survey of Griffs et al. (2000) also presented the normal distributions that defined several input geotechnical parameters using data collected during the 2009 site investigation program for the three geotechnical units likely to exist in the Saadah crown pillar (FV/MV, MS, and T) as shown in Figure 4.17 below.

Table 4.17: Summary of parameter values and corresponding distributions used in probabilistic crown pillar design analysis (Griffs et al, 2000).

	Input Variable	**RQD**	**J_r**	**J_a**	**J_n**
FV/MV	*Average*	*69.9*	*1.4*	*1.3*	*6*
	St. Dev.	*27.1*	*0.3*	*0.5*	*0*
	Weighted	*68.1*	*1.4*	*1.3*	*6*
	Maximum	*100.0*	*3.0*	*4.0*	*6*
MS	*Minimum*	*4.1*	*1.0*	*1.0*	*6*
	Average	*67.8*	*1.3*	*1.7*	*6*
	St. Dev.	*16.4*	*0.2*	*1.3*	*0*
	Weighted	*68.2*	*1.3*	*1.6*	*6*
	Maximum	*93.0*	*1.5*	*4.0*	*6*
	Minimum	*39.2*	*1.0*	*1.0*	*6*
T	*Average*	*59.8*	*1.3*	*3.5*	*6*
	St. Dev.	*27.8*	*0.3*	*0.9*	*0*
	Weighted	*60.4*	*1.3*	*3.8*	*6*
	Maximum	*88.9*	*1.5*	*4.0*	*6*
	Minimum	*14.2*	*1.0*	*2.0*	*6*

The study by Griffs et al. (2000) for the probabilistic scaled span analysis is summarized in Table 4.18. As indicated, mean Factor of Safety values of 7.8, 5.6, and 3.0 were calculated for the FV/MV, MS, and T units, respectively, indicating likely stable crown pillar conditions for the proposed 25 m thick pillar (Griffs et al., 2000). The results also suggest a near negligible likelihood for Factor of Safety (FoS) values to be less than one (Griffs et al., 2000).

Table 4.18: Summary of parameter values and corresponding distributions used in probabilistic crown pillar design analysis (Griffs et al, 2000).

Geotechnical Unit	Scaled Span Analysis Output	Min	Mean	Max	5%	95%
FV/MV	*Q*	*0.7*	*10.5*	*29.3*	*3.6*	*19.3*
	Cs	*2.9*	*8.8*	*14.1*	*5.7*	*11.8*
	$T_{calculated}$	*1.2*	*4.2*	*36.2*	*1.9*	*8.9*
	F of S	***0.2***	***7.8***	***22.2***	***2.9***	***13.4***
MS	*Q*	*2*	*7.5*	*20.1*	*3.5*	*13.5*
	Cs	*4.5*	*7.7*	*12*	*5.7*	*10.1*
	$T_{calculated}$	*1.8*	*5.1*	*15.9*	*2.5*	*9*
	F of S	***1.6***	***5.6***	***16***	***2.6***	***10.2***
T	*Q*	*0.8*	*3.7*	*9*	*1.4*	*6.4*
	Cs	*3*	*5.6*	*8.5*	*3.8*	*7.3*
	$T_{calculated}$	*3*	*9.7*	*33.2*	*4.8*	*19.5*
	F of S	***0.7***	***3***	***10.3***	***1.3***	***5.0***

4.1.5. Mining Methods

1) Mining Method Selection

WGM (1982) conducted the first feasibility study for the al Masane Al Kobra mine by considering different mining methods.

a) Horizontal Cut-and-Fill
b) Shrinkage Stoping
c) Open Stope Blasthole Mining
d) Sub-Level Retreat Blasthole Stoping
e) Vertical Retreat Blasthole Stopin

In 1982, open-stope blast hole mining was selected as the most suited to conditions at Al Masane (Lawrence, 2007). In the WGM feasibility study 2007, horizontal cut-and-fill was chosen for Al Masane (WGM, 2007). In the WGM feasibility study 2007, horizontal cut-and-fill was selected for mining below the crown pillar at Wadi Saadah (WGM, 2007). In other mine areas, open-stope blast hole mining was chosen with the hanging wall supported by permanent triangular pillars (Challiner, 2009). As a result of the geotechnical program undertaken during this study, the analysis of stable spans indicates that all stope openings should be filled after ore production (Lawrence, 2007). A review of the modeled deposit grades and financial information available at the commencement of this study indicated that low-medium cost bulk mining methods must be used for profitability (WGM, 2007). This conclusion led to the following decisions:

a) The expensive horizontal cut-and-fill method was unsuited for productive extraction of the large orebodies to be mined below the crown pillar below Wadi Saadah and
b) Uncemented fill was used for filling completed stopes. Cement content in a 5% rockfill was around $3.70/t fill (WGM, 2007).

This study conducted by WGM (2007) selected a form of bench and fill, combining reasonable productivity and medium cost with the added security of ground control by filling stopes with uncemented rockfill as mining advances.

i) Bench and Fill Mining Method

The designed sub-level interval was 25 m (Griffs et al., 2000). For the first bench, a top slice is mined on the upper and lower levels longitudinally along the strike, 4.5 m high, for the entire deposit width (WGM, 2007). The waste hangingwall may be supported by Cable Bolts installed from these levels as necessary to control dilution (Lawrence, 2007). The top slice width for drilling is limited to 13 m (WGM, 2007). WGM plans included Cable Bolt support of the top slice back (WGM, 2007). Where the deposit is more than 13 m wide, separate development is mined along the hangingwall and footwall contacts (Lawrence, 2007). Parallel 64 mm blast holes are drilled from the upper level, holing in the level below. Some angled holes will be necessary where a full-width top slice is not mined (WGM, 2007).

A central slot raise is developed by long hole raising (Lawrence, 2007). From this raise, a slot is blasted across the entire width of the deposit to create two bench production faces one on either side of the slot (Lawrence, 2007). Both bench production faces are blasted to retreat from the slot (Lawrence, 2007). Blasting is controlled to minimize the throw of the broken ore, seeking to achieve a slow heave from the blast hole lines (WGM, 2007).

Mucking is undertaken from the level below, using a remote control where the ore is in the open stope beyond the brow (Lawrence, 2007). As mining progresses, development waste and rockfill from the surface is backfilled into the open hole such that the rill of the waste and rockfill follows a few meters behind the bottom of the blasted face (Lawrence, 2007). The backfill adopted is uncemented but fills the stope opening, hangingwall to the footwall, providing control against dilution and preventing caving (Griffs et al., 2000). This style of placement of fill behind the

retreating production face is termed the “Avoca” style, named after the mine in Eire, where this system was first used (WGM, 2007). The method progresses upwards in a series of 25 m lifts (Lawrence, 2007). After extracting the first bench, the top of the backfill was used as the mucking floor for the above lift. The method is illustrated in Figure 4.10.

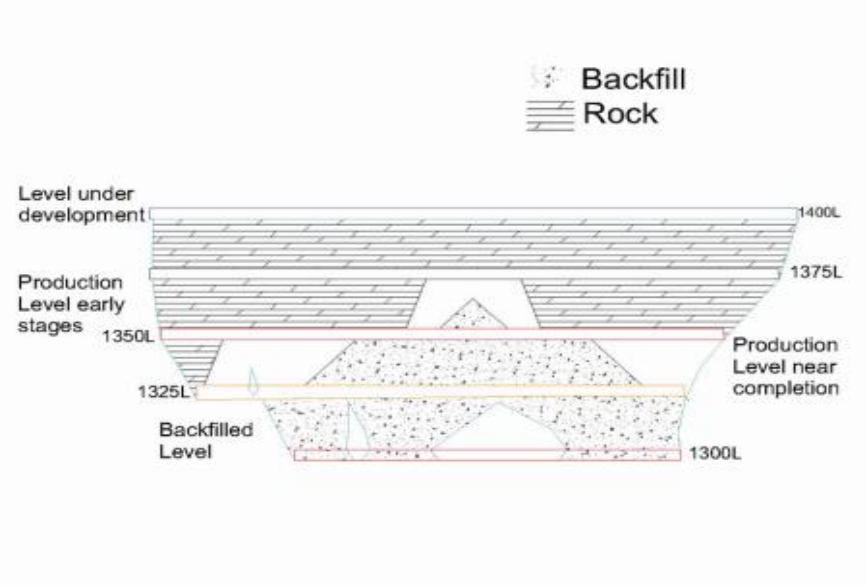

Figure 4.10: Longitudinal bench and fill (WGM, 2007)

ii) Longitudinal Bench and Fill Method

The longitudinal bench and fill method was adopted where the deposit width was less than 5 m (Griffs et al., 2000). Where the deposit was less than 5 m wide and above a minimum in situ ore width of 1.2 m, smaller equipment was used to develop 3 m x 3 m (WGM, 2007). A smaller drill hole diameter was used to tighten up the bench drilling pattern to improve the blasting of the tighter production face and minimize blasting damage to the waste foot and hangingwalls (Lawrence, 2007). Dilution control in narrow stopes is very critical (Lawrence, 2007). Irregularity of the vein between the mining levels was to be checked by delineation drilling to ensure that the ore was within the planned stope outlines (Griffs et al., 2000). Some blast holes can be drilled upwards from the lower level (Lawrence, 2007). There is a risk that loss of ore within the stope outlines combined with dilution from the waste walls could significantly reduce the planned production grades from these areas (Griffs et al., 2011). In these circumstances, there is flexibility to reduce the sublevel interval or adopt a horizontal cut-and-fill method if this is considered economical at that time (WGM, 2007).

Two stopes were mined on the same level in some areas, separated by a waste/low-grade pillar (Griffs et al., 2000). WGM (2007) assumed that a minimum thickness of the waste pillar of 8 m to be left. Narrow pillars are considered in danger of failure (Lawrence, 2007). Typically, the hanging wall stope was mined first. However, local conditions indicate reversing this sequence (Griffs et al., 2011).

All stopes were planned at 30 m or less. However, there was a 100 m to 200 m strike length of the northern portion of the Saadah deposit where the stopes are in the 20 m to 30 m range (WGM, 2007). As the width of the bench undercut increases, it is necessary to fill the central area of the undercut tightly or install concrete packs to limit the span (Griffs et al., 2011). The geotechnical analysis suggests these measures can be required in the few stopes expected to be between 25 m and 30 m wide (WGM, 2007).

4.2. Geotechnical Data Collected

4.2.1. Introduction

Two stopes were used as case study trials for the experimental works in which the artificial concrete pillars were installed. Geotechnical data were collected to derive the material input parameters in FLAC3D numerical simulation. As earlier introduced in Chapter One, the actively mined zones are Sa'adah and Al houra, which occur in a volcanic sequence that consists of two mafic-felsic sequences with interbedded cherts and meta-sedimentary rocks. The numerical and experimental case studies considered are located in the Sa'adah section of the mine. These two stopes were situated on different levels or depths of the mine. During the stoping in the Al Houra and Sa'adah sections of the mine, a major geotechnical problem encountered was the collapse of production stopess in a wide portion of the orebody. This has been aided by increased hydraulic radius and reduced stability number due to the change in rock mass condition and high-stress change. The condition is more frequent in sections with three or two limbs of the orebody. The pillar dividing the two limbs (orebodies), during or after mining, one stope usually collapses and forms a single wide stope, increasing the Hydraulic radius.

4.2.2. Data Collection Methodology

The geotechnical data collection involved in this study includes laboratory test works, geotechnical mapping, and field displacement monitoring. This is described in the later section below;

1) Laboratory Tests

Random samples were taken from the mixed concrete material for testing to obtain the material properties of the artificial concrete pillars, as shown in Figure 4.11 (a). Almehwar Civil Engineering and Construction, a local laboratory, was used to test the concrete strength of the samples. Each cubic mold is 150 cm x 150 cm x 150 cm as per the International Society for Rock Mechanics (ISRM) Standards for strength tests (as shown in Figure 4.11 (a)). During the loading of the samples, a photograph was taken to verify the laboratory test works carried out for this study (as shown in Figure 4.11 (b)).

Figure 4.11: Sample preparation (a) and concrete strength testing (b)

The tests were conducted on different samples with various curing times, from 7 days, 14 days, and 28 days. The concrete test results for density and strength were conducted at the Al-Mehar Construction Engineering (as shown in Table 4.19 to 4.21 below).

Table 4.19: Laboratory test results for the samples (Testing conducted at 28 days)

Sample #	Age (Days)	Weight (gm)	Density (gm/cm^3)	Area (cm^2)	Volume (cm^3)	Load (KN)	Strength (Kg/cm^3)	Strength (Mpa)
1	28	7980	2.36	225	3375	586.85	266.04	26.08
2	28	7940	2.35	225	3375	532.92	241.59	23.69
3	28	8050	2.39	225	3375	597.11	270.69	26.54
4	28	7930	2.35	225	3375	634.14	287.48	28.18
5	28	7920	2.35	225	3375	585.26	265.32	26.01
Average		**7964**	**2.36**	**225**	**3375**	**587.26**	**266.22**	**26.10**

Table 4.20: Laboratory test results for the samples (Testing conducted at 14 days)

Sample #	Age (Days)	Weight (gm)	Density (gm/cm^3)	Area (cm^2)	Volume (cm^3)	Load (KN)	Strength (Kg/cm^3)	Strength (Mpa)
1	14	7980	2.36	225	3375	440.14	199.53	19.56
2	14	7940	2.35	225	3375	399.69	181.19	17.77
3	14	8050	2.39	225	3375	447.83	203.02	19.91
4	14	7930	2.35	225	3375	475.61	215.61	21.14
5	14	7920	2.35	225	3375	438.95	198.99	19.51
Average		**7964**	**2.36**	**225**	**3375**	**440.44**	**199.67**	**19.58**

Table 4.21: Laboratory test results for the samples (Testing conducted at 7 days)

Sample #	Age (Days)	Weight (gm)	Density (gm/cm^3)	Area (cm^2)	Volume (cm^3)	Load (KN)	Strength (Kg/cm^3)	Strength (Mpa)
1	7	7980	2.36	225	3375	293.43	133.01	13.06
2	7	7940	2.35	225	3375	266.46	120.77	11.85
3	7	8050	2.39	225	3375	298.56	135.35	13.27
4	7	7930	2.35	225	3375	317.07	143.74	14.09
5	7	7920	2.35	225	3375	292.63	132.66	13.01
Average		**7964**	**2.36**	**225**	**3375**	**293.63**	**133.11**	**13.06**

The test results for 15 samples are below in Figure 4.12. The results showed that 28 days has the ultimate strength for the concrete pack with at least 26 MPa.

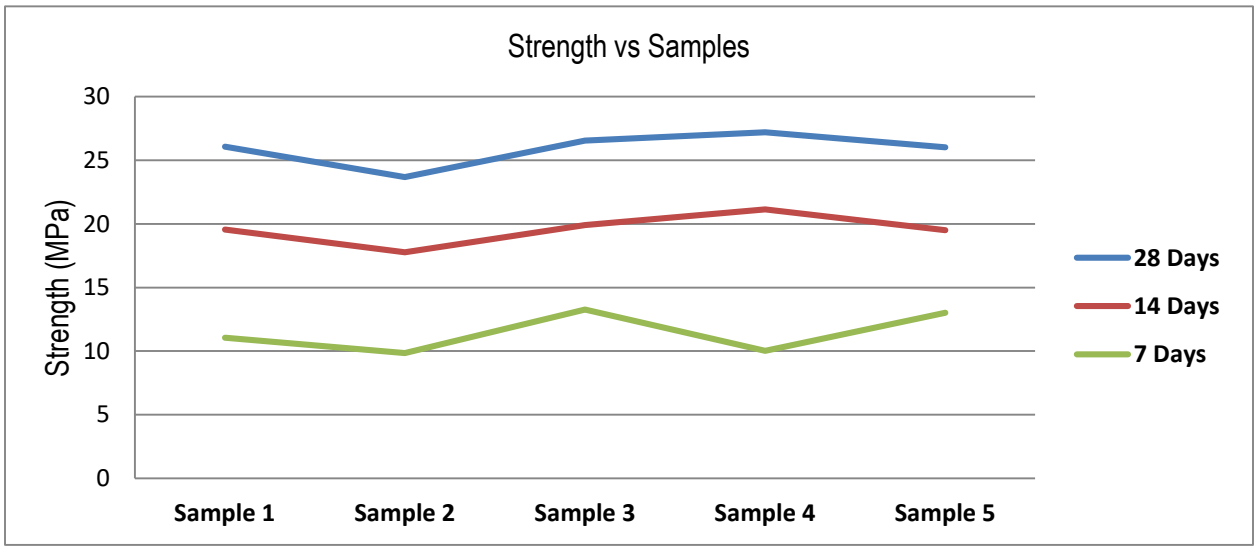

Figure 4.12: Strength comparison with the curing time (days)

2) Geotechnical Mapping

Geotechnical mapping using window and scaling methods were used to collect data for the two stopes used as case studies. This geotechnical data was collected to define the material properties in the two stopes. The rock units in the mapped stopes were the hangingwall, footwall, and orebody. A standard geotechnical form was used to enter the parameters in the field during underground mapping (**Appendix 1**). This aimed to obtain parameters to be used as input in the FLAC3D numerical modeling code. These parameters are uniaxial compressive strength (UCS), Rock Quality Designation (RQD), Joint Spacing (JS), Joint Condition (JC), Groundwater (GW) and Joint Orientation (JO). The output of the geotechnical mapping was used to quantify the rock mass rating (RMR) and the Q-system for quantifying the stope stability assessment. The other

geotechnical parameters that were collected during mapping were dip and dip direction for the intercepted discontinuities. For joint or discontinuity condition; joint surface roughness, aperture, infill, weathering and persistence were collected every joint set.
Rock samples were collected for laboratory testing of rock density, young's modulus, poisson's ratio, friction angle and cohesion. Point Load Testing was conducted on available cores at the site to randomly obtain a rough estimate of the intact rock mass strength (IRS) for the three units (hangingwall, footwall, and orebody). Schmidt hammer was also used during the underground mapping to quantify the strength of the three units in the two stopes used as case studies. The rock mass rating results from the mapping that were calculated for each geotechnical domain were also used to determine geological strength index (GSI). GSI was used as inpout parameter in the roclab (RocScience tool) to help derive the material properties for the three units. The other three parameters that is used in the roclab are uniaxial compressive strength (UCS), m_i and disturbance factor (D) as explained in the previous in Chapter three.

3) Field Measurements

Field measurements were conducted through a conventional approach, in which convergence monitoring points were installed in the roof and sidewalls of the two stopes used as case studies (SA-1498 and SA-1575 Stopes). A tape extensometer measured displacement and convergence in the two stopes before and after installing artificial concrete pillars. Field measurements were conducted using a tape extensometer to obtain field data for displacement and convergence in the roof and sidewalls. The results for convergence and displacement were monitored for five months before installing the artificial pillars. The results were also taken after artificial pillars were installed and compared with those before the pillars were installed. This was done to evaluate the stability of the artificial concrete pillars. The displacement field measurement results before and after artificial concrete pillars were installed in the two stopes are presented in **Appendix 2.**

4.2.3. Geotechnical Input Parameters

The input parameters considered in the FLAC3D numerical modeling code are Uniaxial Compressive Strength (UCS), intact rock constant (mi), Geological Strength Index (GSI), and Disturbance Factor (D), which were used in RocLab to obtain constants for (**s**), (**mb**), (**a**), cohesion (C), internal friction angle (Φ) and young's modulus (γ) input parameters for the numerical model. No stress measurement has been done at the mine. World stress map was considered for the pre-mining state stress as input into the numerical model (as described in Section 4.1.4 of this Chapter). The geotechnical parameters used in the model are listed below in Table 4.22.

1) Material Properties for SA-1498 and SA-1575 Stopes

This section defines the model input parameters for SA-1498 Sill Pillar stope and SA-1575 Crown Pillar Stope. These parameters were obtained from the mapping data and laboratory experiment, as presented above. The four units considered in the numerical model are the Footwall, Orebody, Hanginwall, and Concrete. The input parameters considered in the numerical modeling codes (FLAC3D) are Uniaxial Compressive Strength (UCS), rock density, Mi, GSI, and Disturbance

Factor (D) were used in RocLab to obtain values (s), (mb), (a), cohesion (C), internal friction angle (Φ) and young's modulus (E) as input parameters for the numerical model. Bulk Modulus (K) and Shear Modulus (G) parameters for material properties used in the model were obtained by using Equations 3.1 and 3.2 as presented in Chapter Three. As mentioned earlier, in FLAC3D numerical modeling, it is better to use Bulk and Shear modulus properties to define the material's elastic properties. Different Constitutive models have been explained under numerical model Section in Chapter Three (Elastic, Mohr-Coulomb, Hoek-Brown, etc). However, this Chapter aims to present input material parameter results and the steps involved in collecting geotechnical data. Table 4.22 below summarizes the model input parameters for the four units used in the FLAC3D for the two case studies.

Table 4.22: Geotechnical input parameters obtained from geotechnical mapping, laboratory and Roclab.

No.	Parameters	Footwall	Orebody	Hangingwall	Concrete
1	Sigc (MPa)	150	100	84	23
2	Density (gm/cm^3)	2.9	2.8	2.7	2.36
3	GSI	55	50	55	46
4	m_i	20	25	20	12
5	Disturbance Factor (D)	0	0	0	0
6	Young Modulus (MPa)	56,250	47,000	31,500	10,574
7	m_b	4.009	5.991	4.009	1.744
8	Poisson Ratio	0.25	0.23	0.21	0.20
9	s	0.067	0.012	0.007	0.002
10	a	0.504	0.503	0.504	0.508
11	Internal Friction Φ (°)	62.6	57.92	60.15	35.56
12	Cohesion (Mpa)	1.44	1.94	0.956	0.786
13	Bulk Modulus (K)	37,500	29,012	18,103	5,874
14	Shear Modulus (G)	22,500	19,105	13,016	4,404

2) In Situ Stress levels for SA-1498 and SA-1575 Stopes

As explained in the above sections, there is no stress measurement that has been conducted at the mine site. World stress map was considered for the pre-mining state stress as input into the numerical model (as presented in Section 4.1.4). The K-ratio of 1.5 was adopted based on the world stress map to define in situ stresses and use them as input in FLAC3D numerical simulation. The above presented geotechnical material input paramters were validated with the mine site's geotechnical database for rock strength, rock mass rating and Q-values for each geotechnical unit. Therefore, the geotechnical input parameter results presented in this Chapter reflect the material properties of the above rock units. The author also acknowledges that a particular portion of the orebody had undergone rock mass deterioration, signifying that some values are less than those presented in the input geotechnical parameters in Table 4.22. However, the author is also aware of calibrating the model by comparing field measurements with the numerical modeling results in FLAC3D. This can be achieved by collecting accurate geotechnical data through stress measurement, laboratory testing of rock samples, and rigorous underground mapping, which can be used as geotechnical input parameters in the model. Then, field measurements can be done by installing reliable and accurate geotechnical instruments such as real-time multiple borehole extensometers (MPBX) that can be used to measure convergence and displacement results. Then, numerical modeling results can be compared with the field measurements. As stated earlier, no stress measurement has been conducted at the mine site, and the world stress map was used to estimate the in situ stress. Stress measurement is one of the most expensive activities that most mines shine away from undertaking. Therefore, the field measurements of stress will help evaluate the expected deformation for the stope stability analysis. FLAC3D numerical code aids in simulating stability issues, mainly if the correct and sufficient geotechnical input parameters are used in the model. Such parameters will help simulate the actual displacement and be coupled with field measurement using geotechnical instruments such as MPBX. The next Section present the results from the numerical simulation using the FLAC3D model.

4.3. Numerical Modeling

4.3.1. Introduction

This Section presents the numerical modeling results that were obtained in FLAC3D. The results presented are before and after artificial concrete pillars were installed in the two stopes used as case studies for SA-1498 and SA-1575 Stopes, respectively. All the case studies are simulated for the proposed model, and the suitability of the artificial concrete pillars is evaluated based on the defined failure criterion and material properties employed in the model. The Failure criterion used in each model is an Elasto-Plastic Mohr-Coulomb, as explained in the previous Chapter Three. This Section consists of three sub-sections: numerical model setups, model results, and conclusion. The results presented in this Section using the FLAC3D model will be discussed further, with a comparison of similar studies of other authors in the next Chapter Five. This Section explicitly presents numerical model results conducted in FLAC3D to evaluate the stability and suitability of the artificial concrete pillars.

4.3.2. Model Setup for SA-1498 Stope in FLAC3D

The model setup in FLAC3D for S-A1498 stope is as follows: The Footwall, Hangingwall, and Orebody are defined in the model (as shown in Figure 4.13). The model setup is before any mining commences, in which the numbers (1 to 5) are according to the modeling stages. Number 1 is the bottommost levels, which are mined and then backfilled. Number 2 is the actual stope (7 m height x 20 m width x 50 m Length) being considered for modeling before and after the innovative artificial concrete pillars are installed. Number 3 is the sill pillar (10 m), which will be mined after innovative artificial concrete pillars have been installed. Number 4 is the already mined zone; instead, it is void above the sill pillar without any backfill (40 m high). Number 5 is the in situ or unmined zone. The simplification of the above explanation is presented in a graphical view in Figure 4.13 below. The results will be shown in the preceding sections. The model is set on the 200 m x 200 m x 50 m grid.

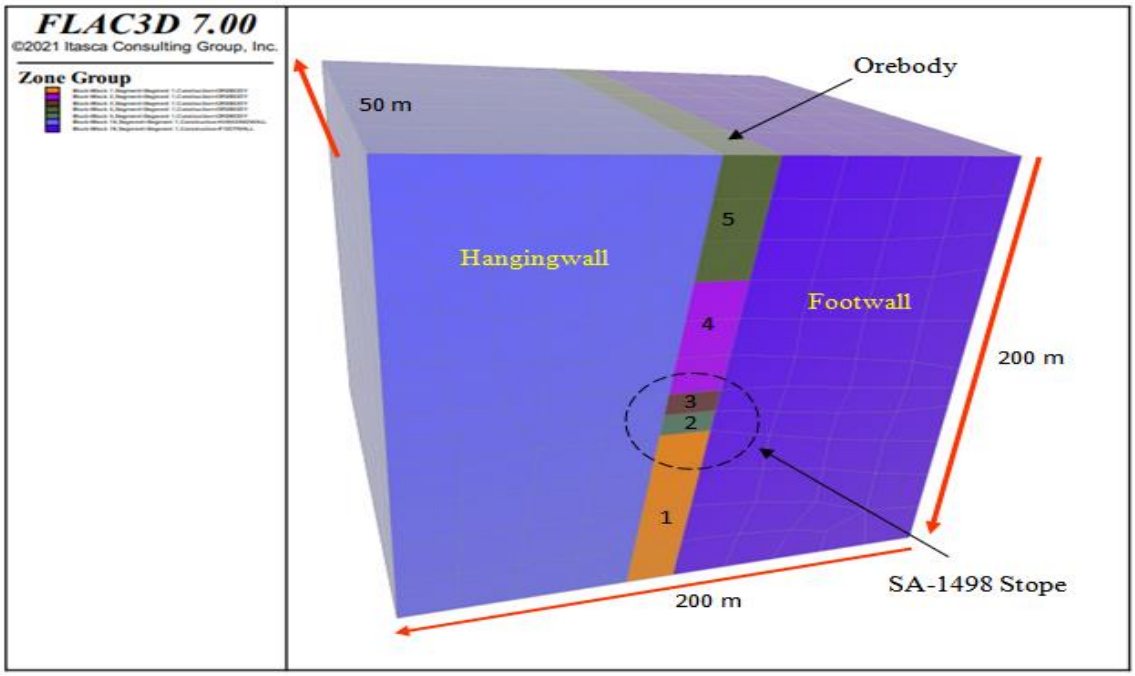

Figure 4.13: Model setup for SA-1498 Stope in FLAC3D.

4.3.3. Model Setup for SA-1575 Stope in FLAC3D

The model setup in FLAC3D for SA-1575 stope is as follows: the Footwall, Hangingwall, and Orebody are defined in the model as different rock units (as shown in Figure 4.14). The model setup is before any mining commences, in which the numbers (1 to 3) are according to the modeling stages. Number 1 is the bottommost levels, which are mined and then backfilled. Number 2 is the actual stope (10 m height x 30 m width x 100 m Length) being considered for modeling before and after the innovative artificial concrete pillars are installed. Number 3 is the crown pillar (40 m), which will be mined after innovative artificial concrete pillars have been installed.

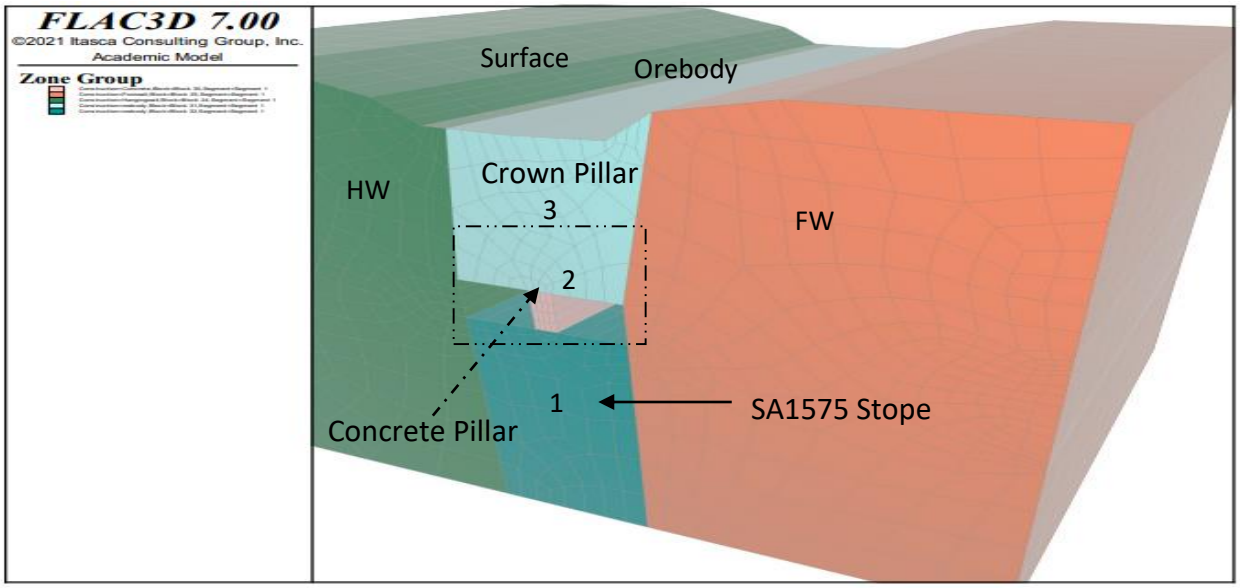

Figure 4.14: Model Setup for SA1575 Stope

4.3.4. Numerical modelling Results

1) Numerical Results for SA-1498 Stope

The results are presented for SA-1498 stope with and without installed artificial concrete pillars. The results considered for comparison are for Displacement Magnitude, State Failure by Average (plastic indicator), Convergence, and Local Force Ratio. These results have been presented in each case study for thorough analysis and comparison. A typical model setup is briefly presented in **Appendix 3**.

a) Zone Displacement Magnitude for SA-1498 Stope

This section presents Zone Displacement Magnitude results for the numerical modeling in SA-1498 stope using FLAC3D. Results presented in Figures 4.15 and 4.16 compare displacement zones before and after artificial pillars were installed, respectively. The roof of this stope is more susceptible to displacement due to the current condition of the stope, which is arranged from poor ground to the wideness of the orebody drive.

The displacement zone was relatively high in the roof (18 mm) of the ore drive before artificial pillars were installed, whereas in the sidewalls (4 mm), the displacement was very insignificant. Displacement zones decreased by 97% relatively in the roof (0.5 mm) of the ore drive after artificial pillars were installed, as shown in Figure 4.16. The results further reveal that the displacement is more on the footwall side than the hanging wall for the mined-out stope (void) above.

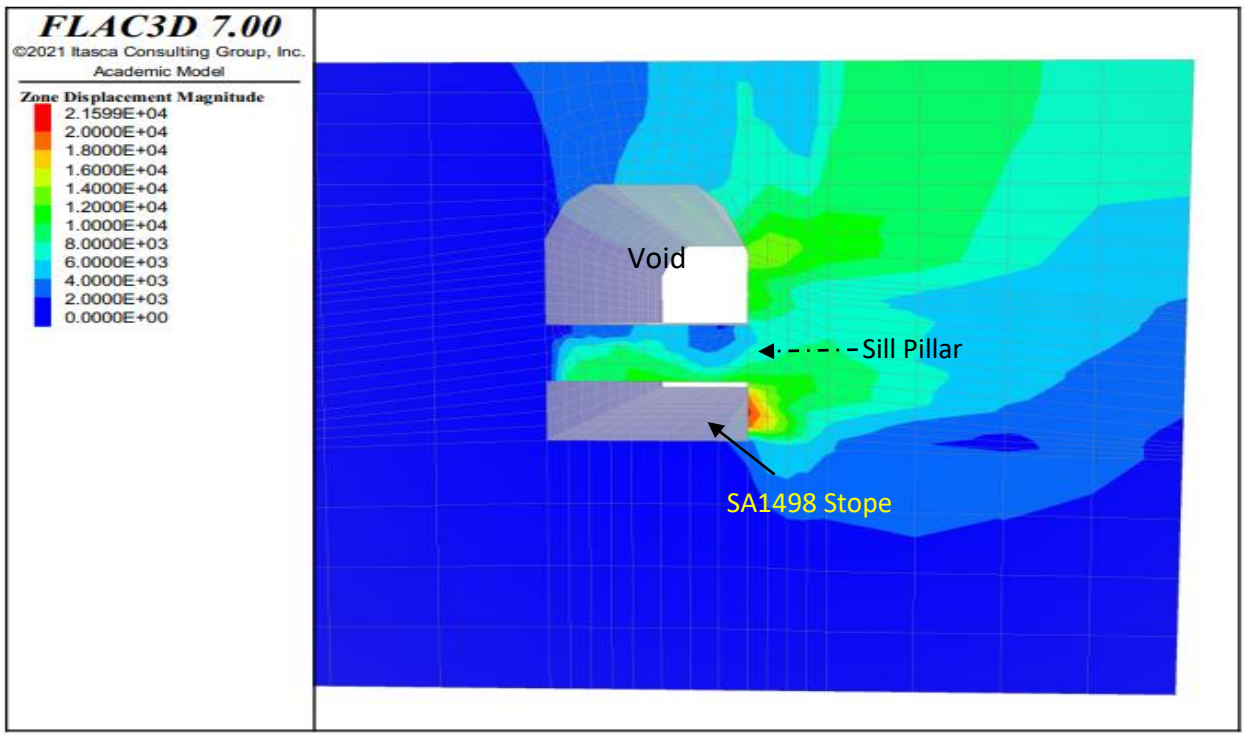

Figure 4.15: Zone Displacement Magnitude results before artificial concrete pillars were installed for SA1498 stope

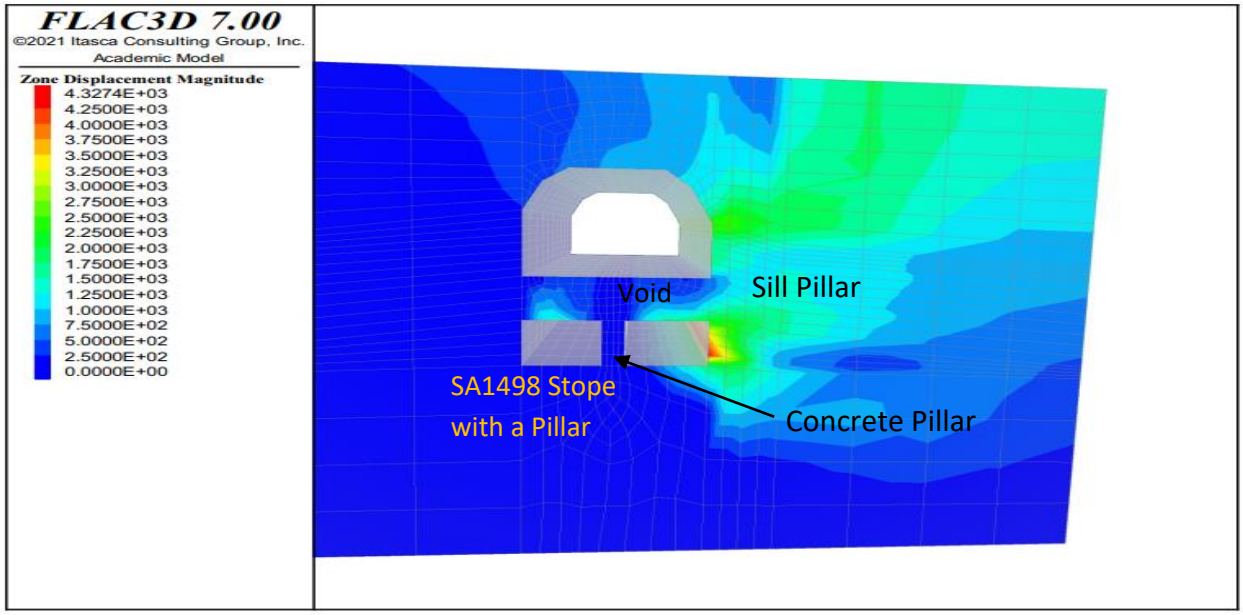

Figure 4.16: Zone Displacement Magnitude results after artificial concrete pillars were installed for SA1498 stope

b) Zone Local Force Ratio for SA-1498 Stope

This section presents Zone Local Force results for the numerical modeling in SA-1498 stope using FLAC3D. Zone Local Force Ratio results were compared before and after artificial pillars were installed as shown in Figure 4.17 and 4.18. The Zone Local Force Ratio was relatively high on the roof (1.0 x 10^+00) compared to the sidewalls (1.0 x 10^-01) of the ore drive before artificial pillars were installed as shown in Figure 4.18.

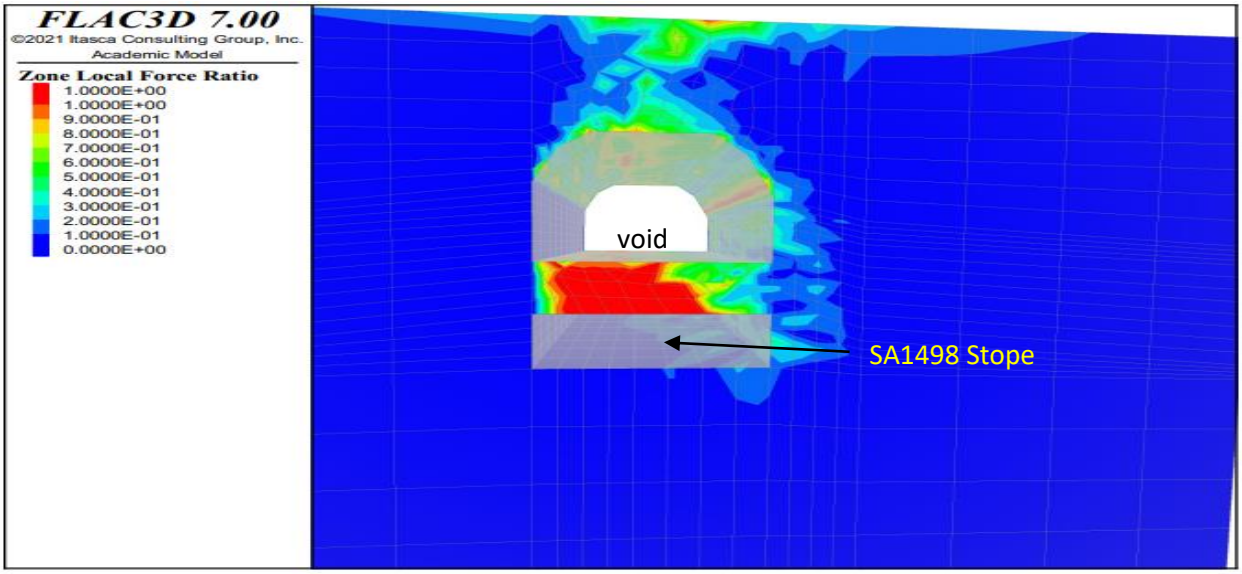

Figure 4.17: Zone Local Force Ratio results before artificial pillars were installed for the SA1498 stope.

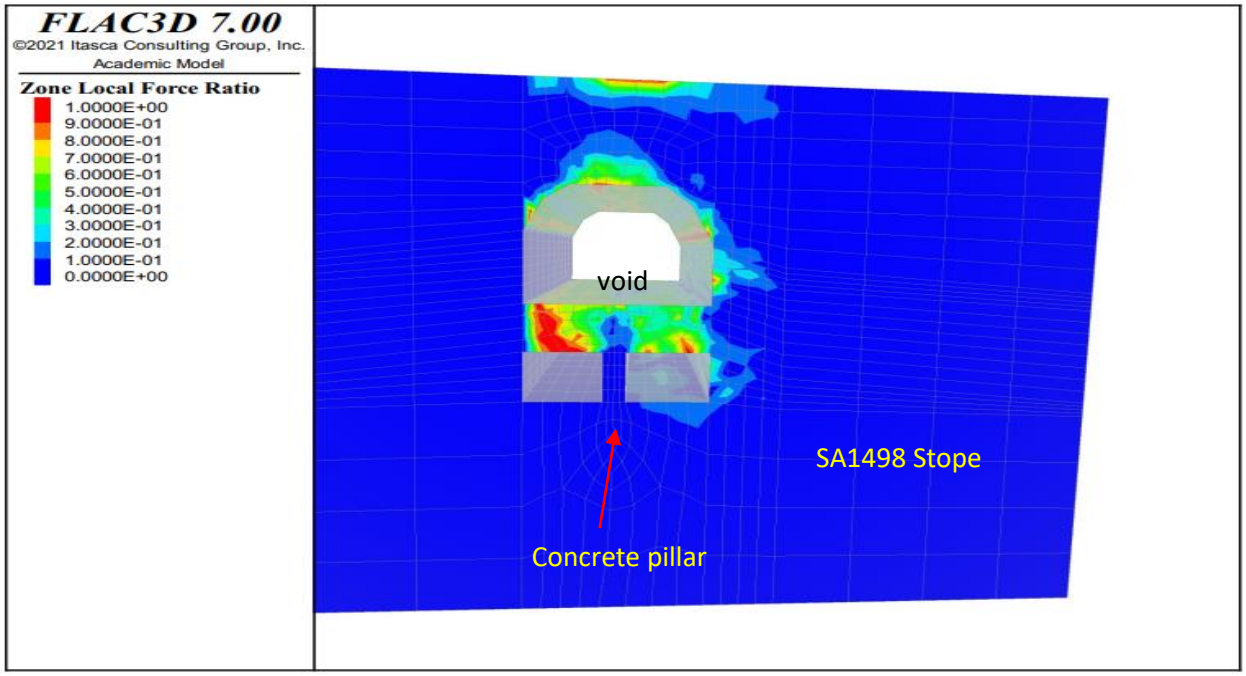

Figure 4.18: Zone Local Force Ratio results after artificial pillars were installed for the SA1498 stope

However, the sidewall deformation is relatively low (before and after artificial pillars were installed). After artificial pillars were installed, the simulation revealed 85% reduction of the Local Force Ratio in the roof (1.5 x 10^-01) of the excavation (as shown in Figure 4.18).

c) Zone State By Average for SA-1498 Stope

This section presents Zone State By Average (Plastic) results for the numerical modeling in SA 1498 stope using FLAC3D as shown in Figures 6.5 and 6.6. The Zone State By Average results were relatively high on the roof compared to the sidewalls of the ore drive before artificial pillars were installed as shown in Figure 4.19. After artificial concrete pillars were installed, the results showed a reduction in the zone of failures as shown in Figure 4.20. The numerical modeling results have verified that the innovative artificial concrete pillars are suitable for underground support systems.

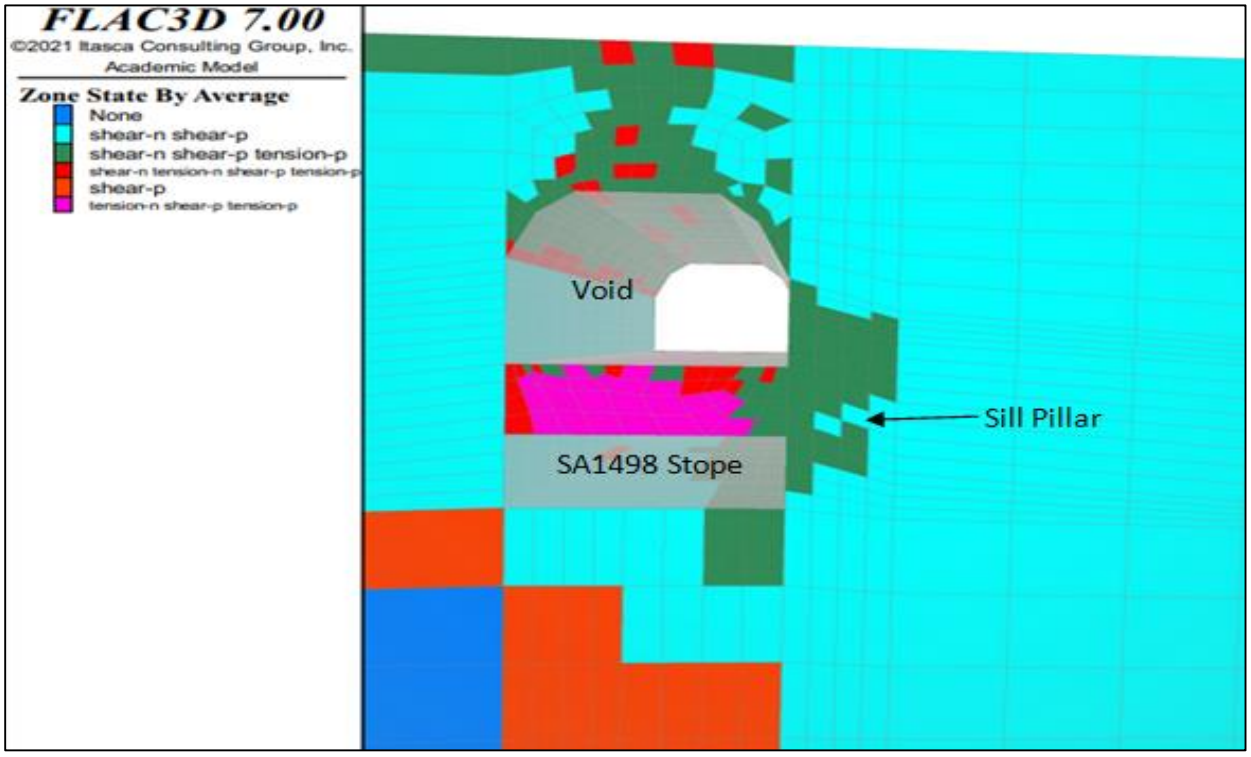

Figure 4.19: Zone State By Average results before artificial pillars were installed for the SA1498 stope

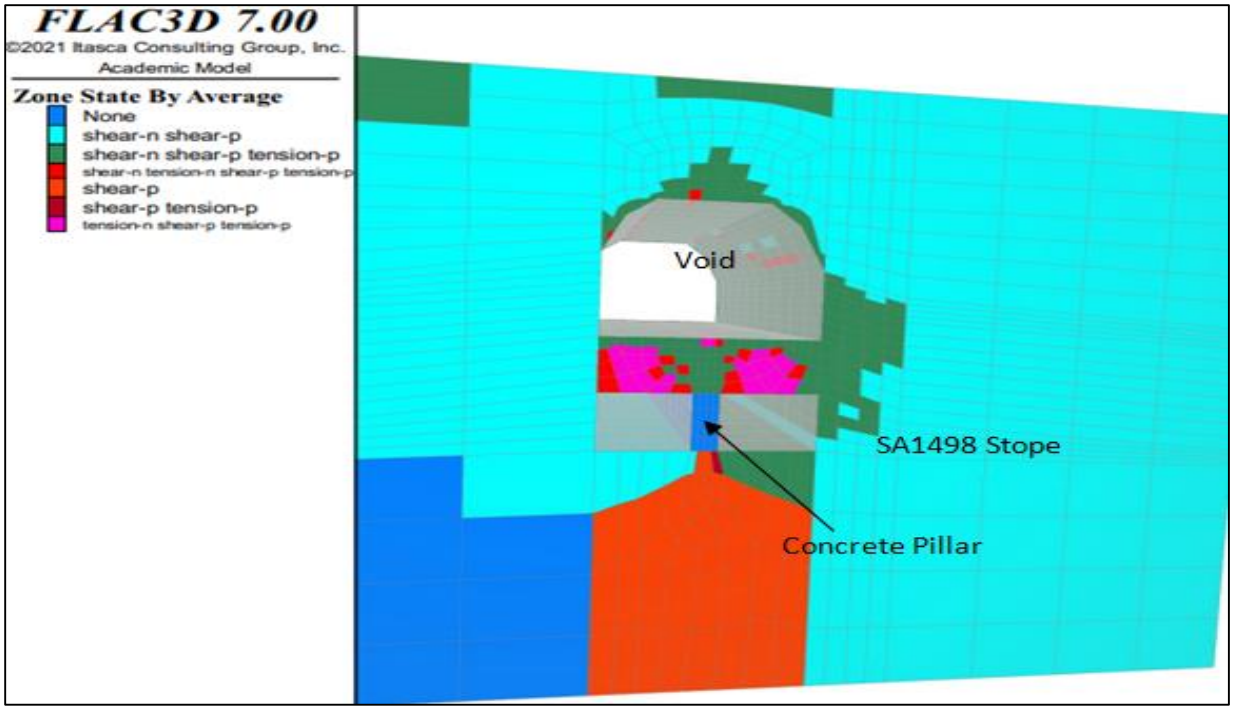

Figure 4.20: Zone State By Average results after artificial concrete pillars were installed in SA1498 stope.

The results presented in this sections above in the analysis involved before and after artificial concrete pillars were installed suggest that there is a need to introduce a robust support system to reinforce the roof of the stope. The results in both Displacement and Local Zone Force Ratio showed a reduction of 85% and 97%, respectively after artificial concrete pillars were installed.

d) Zone Convergence for SA-1498 Stope

The zone convergence results are also compared for conditions before and after artificial concrete pillars were installed, as shown in Figures 4.21 and 4.22. Zone Convergence results for both cases in the sidewall and floor of the stope are relative high. However, the results are relatively high in the roof (10 mm) for the case without artificial pillars in place, while in the case in which the artificial pillars are in place, the results are low, signifying little roof (2 mm) instability as shown in Figure 4.22 below. The red zone is a sill pillar intercepted with different geotechnical challenges, from exceeding critical dimensions to poor ground conditions.

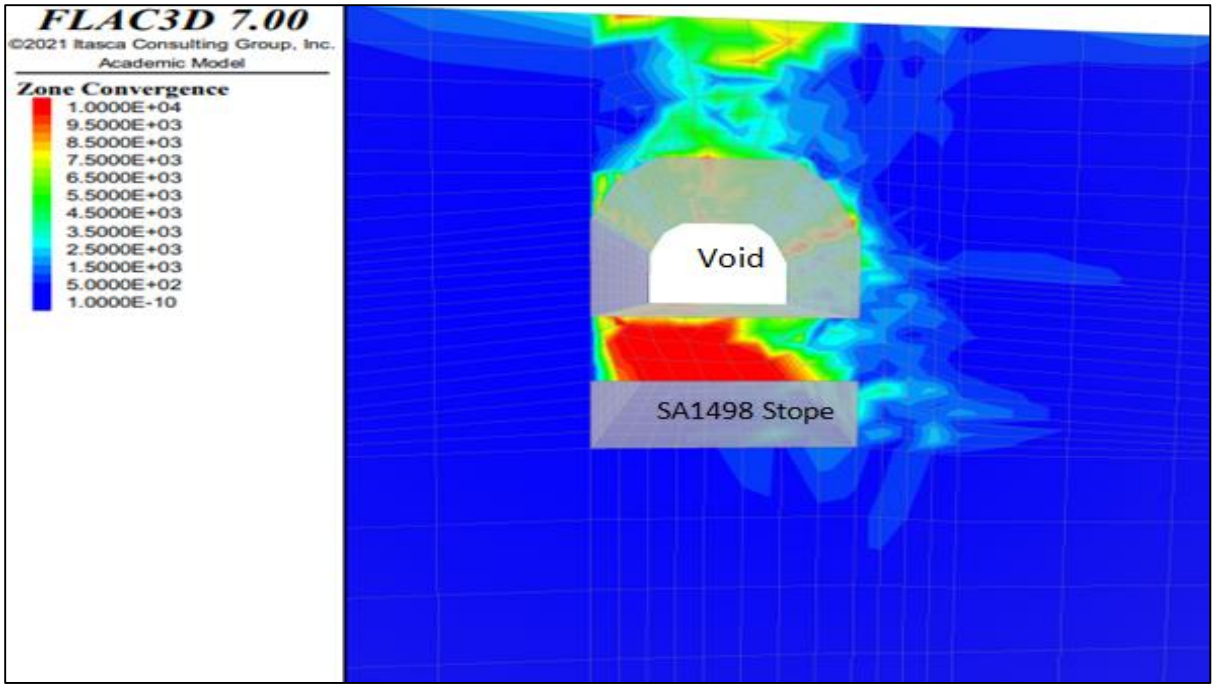

Figure 4.21: Zone Convergence results before artificial concrete pillars were installed in the SA1498 stope

After artificial concrete pillars were installed in the 1498 stope, the convergence results showed a further decrease by 80% as shown in Figure 4.22 below. The footwall side produced a slightly higher convergence compared to the hangingwall due to the intercepted poor ground condition and the sheared zone.

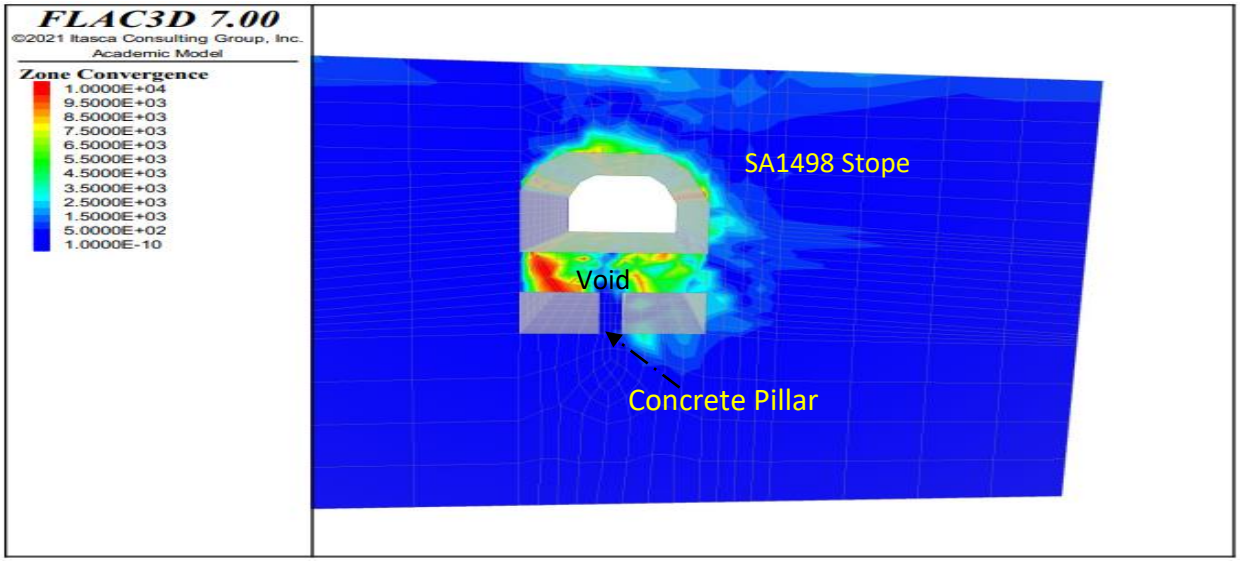

Figure 4.22: Zone Convergence results after artificial concrete pillars were installed in the SA1498 stope

2) Numerical Results for SA-1575 Stope

The results are presented for SA-1575 stope with and without installed artificial concrete pillars. The results considered for comparison are for Displacement Magnitude, State Zone Failure by Average, Convergence, and Local Force Ratio. These results have been presented in each case study for thorough analysis and comparison.

a) Zone Displacement Magnitude for SA-1575 Stope

This section presents Zone Displacement Magnitude results for the numerical modeling in SA-1575 stope using FLAC3D. Results for the Zone Displacement Magnitude are presented in Figures 4.23 and 4.24, comparing before and after installing artificial concrete pillars, respectively. The results are similar to those in the SA1498 stope, where displacement zones are high in the roof at 16 mm before artificial pillars and 0.15 mm after artificial concrete pillars were installed. After artificial concrete pillars were installed, the results showed a further reduction by 99% the roof as shown in Figure 4.24.

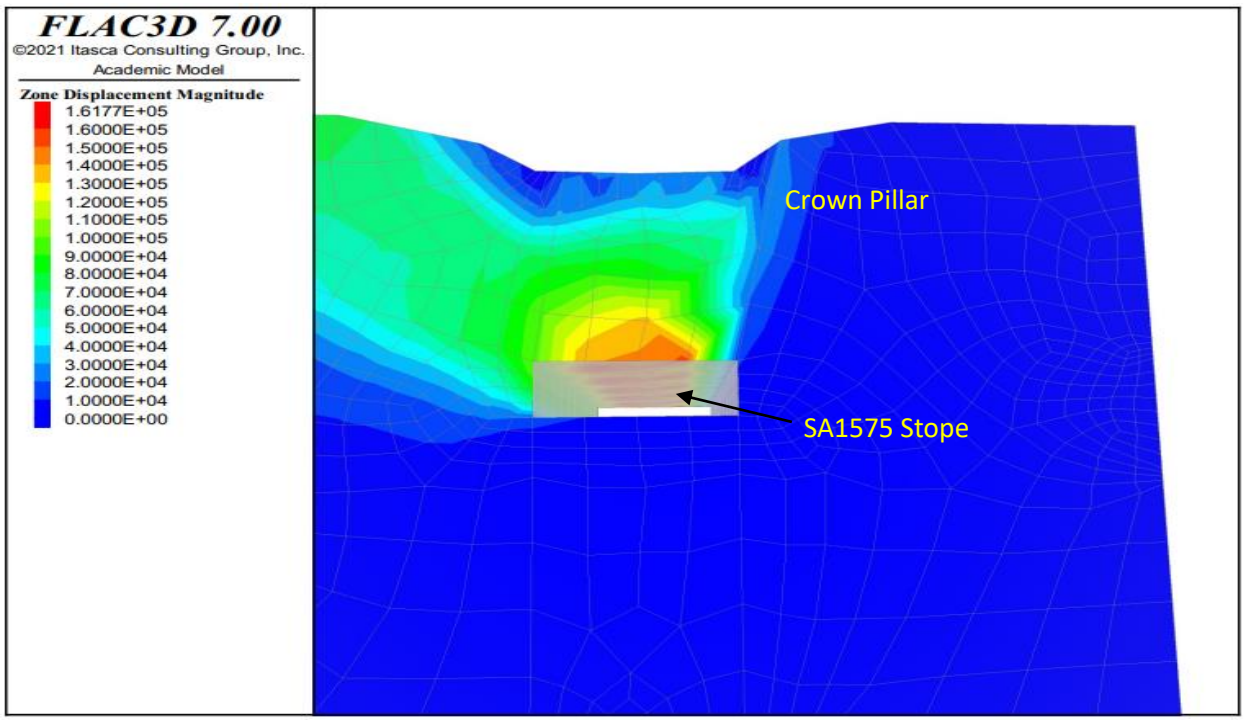

Figure 4.23: Zone Displacement Magnitude results before artificial concrete pillars were installed in SA1575 Stope

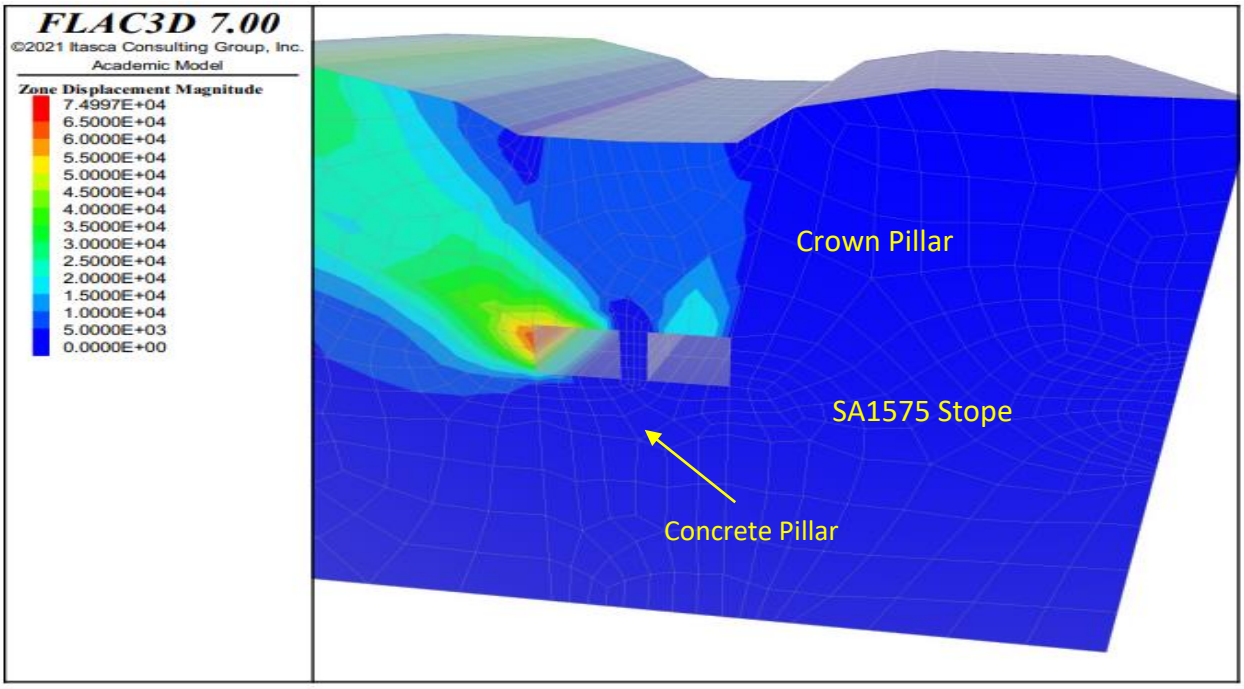

Figure 4.24: Zone Displacement Magnitude results after artificial concrete pillars were installed in SA1575 Stope

b) Zone Local Force Ratio for SA-1575 Stope

This section presents Zone Local Force Ratio results for the numerical modeling in SA 1575 stope using FLAC3D. Zone Local Force Ratio results were compared before and after artificial pillars were installed as shown in Figure 4.25 and 4.26. The Zone Local Force Ratio was relatively high in the roof (7.0 x10^-01) compared to the sidewalls (1.0 x10^-01) of the ore drive before artificial pillars were installed (as shown in Figure 4.26). Therefore, the roof's tensile stress is higher than the sidewalls before concrete pillars were installed. The results for the local force ratio were reduced to 2.5 x 10^-01, showing signs of stability (a further reduction by 71%).

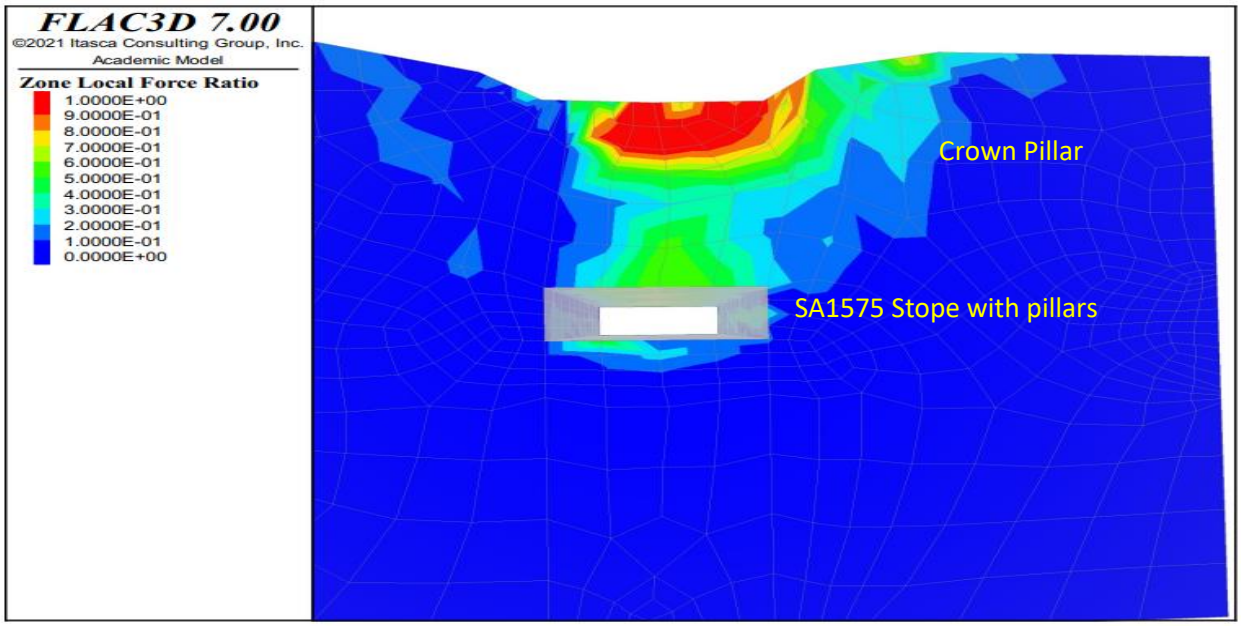

Figure 4.25: Zone Local Force Ratio results before artificial concrete pillars were installed in the SA1575 stope

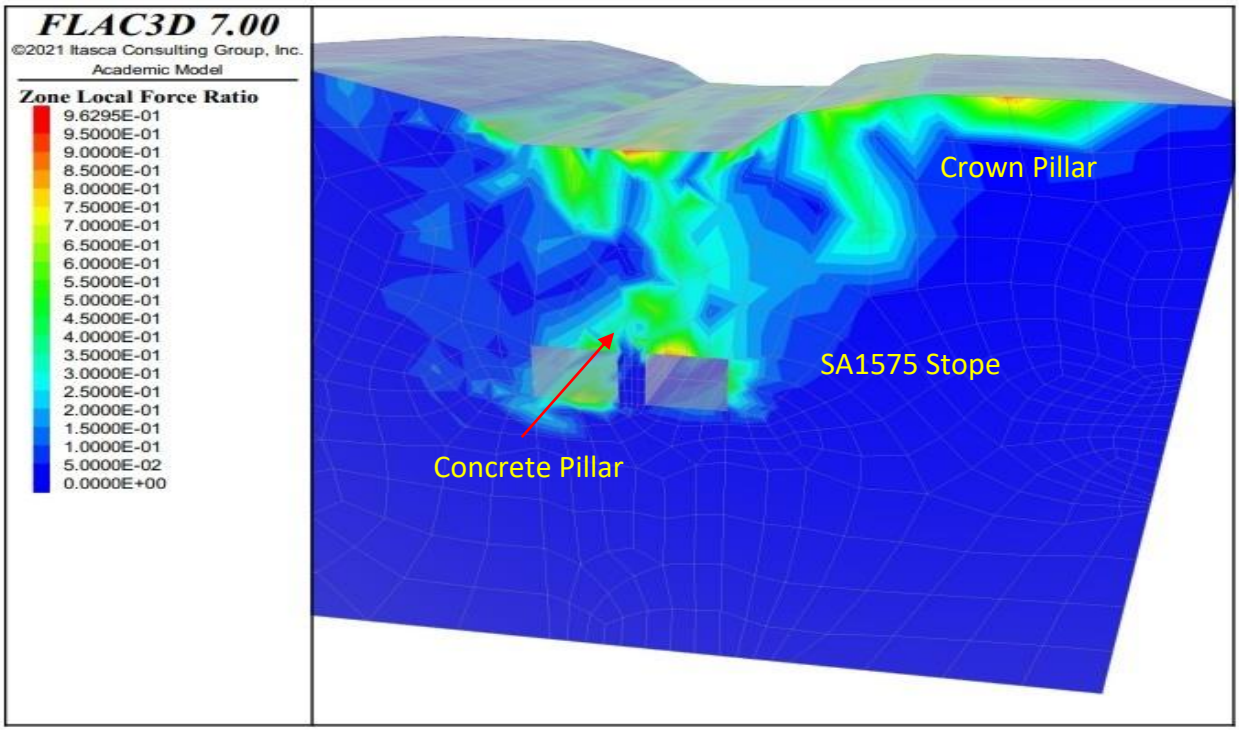

Figure 4.26: Zone Local Force Ratio results after artificial concrete pillars were installed in SA1575 stope

c) Zone State By Average for SA-1575 Stope

This section presents Zone State (plastic) by Average results for the numerical modeling in SA1575 stope using FLAC3D. The Zone State by Average results were relatively high in the roof compared to the sidewalls of the ore drive before artificial pillars were installed, as shown in Figure 4.27 and 4.28. Figure 4.28 shows a reduction in the zone of failures after artificial pillars were installed.

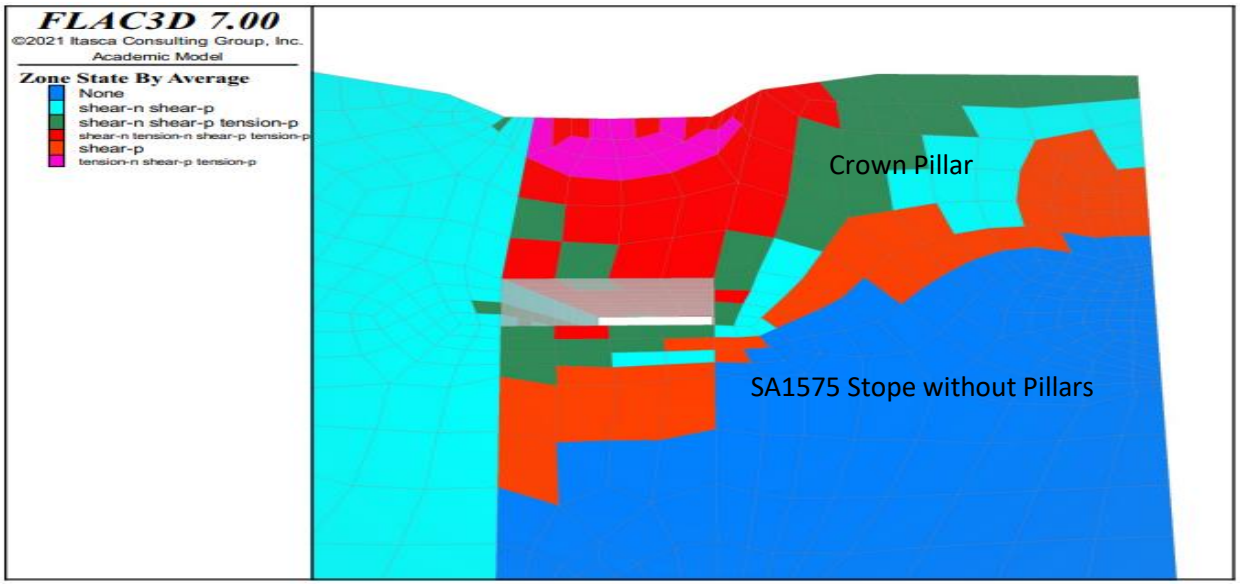

Figure 4.27: Zone State By Average results before artificial concrete pillars were installed in SA1575 stope

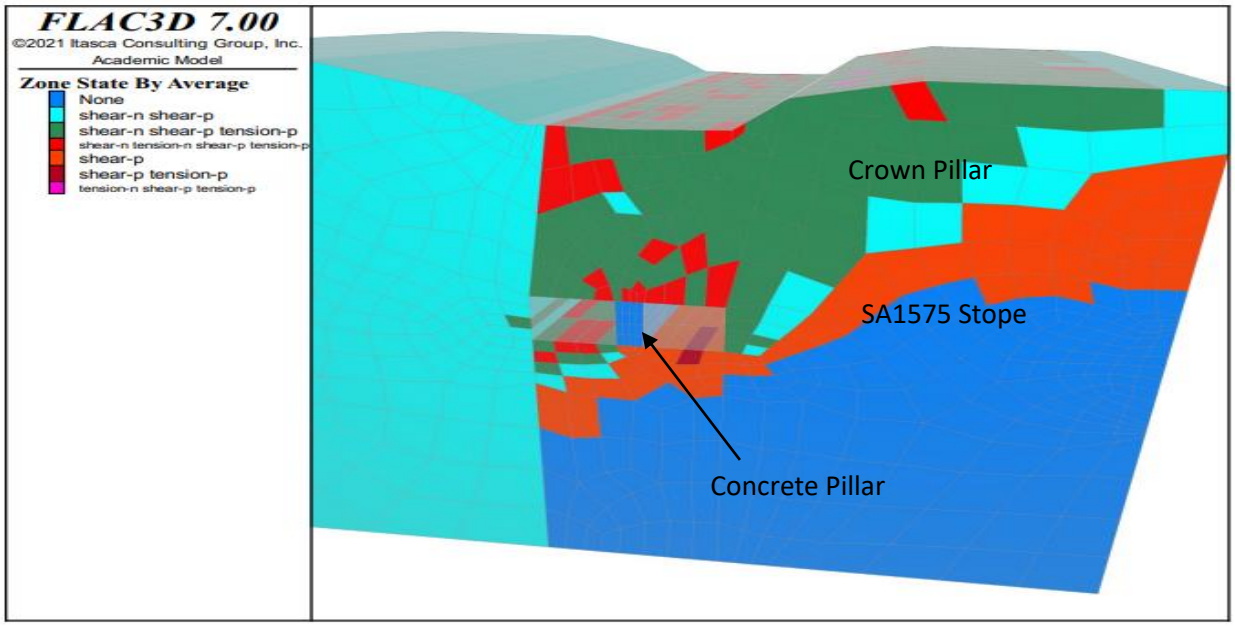

Figure 4.28: Zone State By Average results after artificial concrete pillars were installed in SA1575 stope

d) Zone Convergence for SA-1575 Stope

The zone convergence results are also compared for conditions before and after artificial concrete pillars were installed, as shown in Figures 4.29 and 4.30. Zone Convergence results for both cases in the sidewall and floor of the stope are relative high before artificial concrete pillars were installed, 8.5 mm and 3 mm respectively. The convergence was 8.5 mm in the roof before artificial concrete pillars were installed. The results decreased to 3 mm after artificial concrete pillars were installed (showing a 65% decrease). Further, the ground surface results also decreased convergence results from 10 mm to 3 mm (showing 63% decrease).

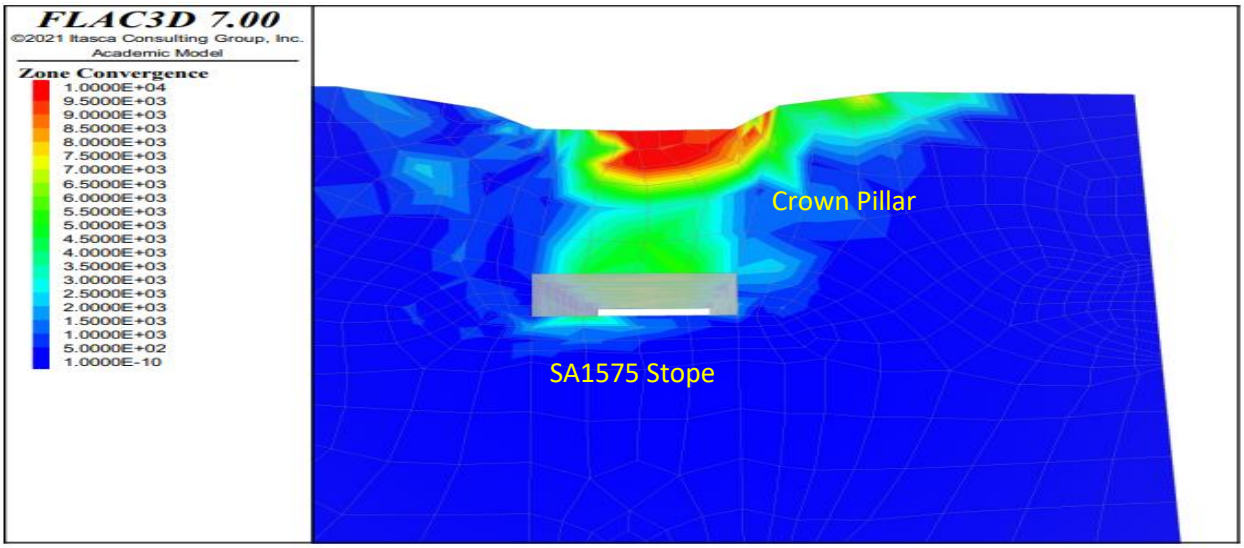

Figure 4.29: Zone Convergence results before artificial cocnrete pillars were installed in SA1575 Stope

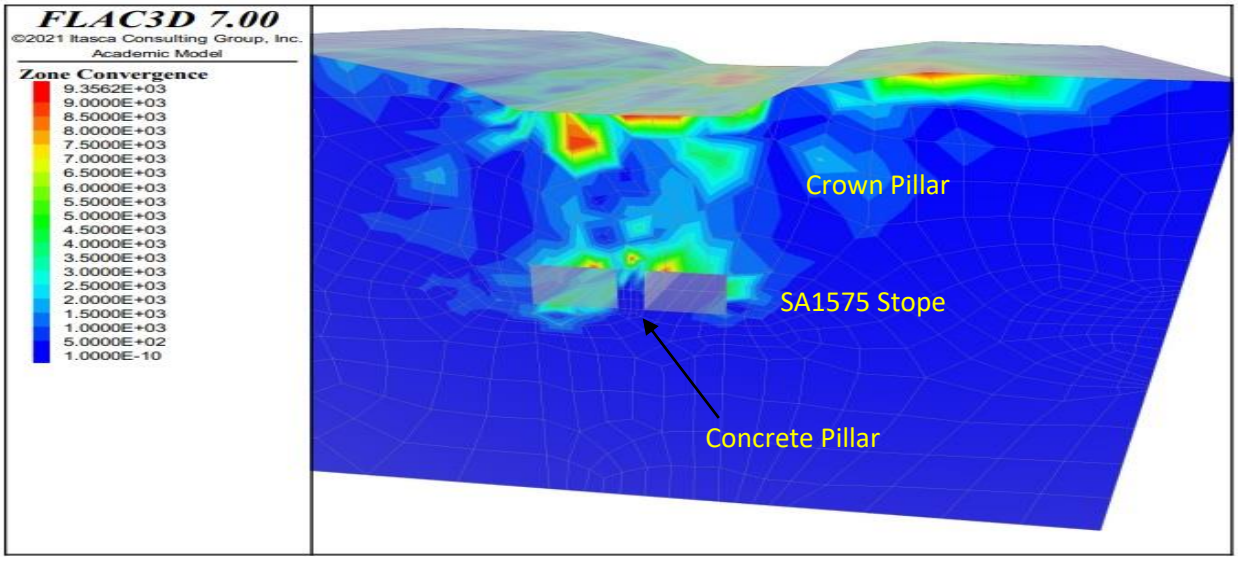

Figure 4.30: Zone Convergence results after artificial concrete pillars were installed in SA1575 stope.

4.3.5. Conclusion

The results of the two case studies have been presented thoroughly and detailed in this chapter, showing a significant decrease in convergence percentage. The results considered for analysis in the two case studies are; State failure zone, Displacement, Local force ratio, Convergence in the FLAC3D numerical model of the Itasca group.

Displacement zone results in both case studies revealed that the stope's roof is very susceptible to instability, which is significant if the stope exceeds the critical stope dimension or increases the hydraulic radius. Both case studies presented wider portions of the orebody (more than 20m wide). The first case study (SA1498 stope) involved mining a sill pillar with the void above. In this instance, the geotechnical instability challenges of mining a sill pillar were very significant. However, the second case study involved mining in the crown pillar. In both case studies, similar geotechnical instability problems were encountered, in which the stope's roof was susceptible to displacement and high failure rates, as presented in pictorial views in Chapter Four. In both studies, the displacement rates in the sidewalls were meagre before artificial concrete pillars were installed, 2 mm to 4 mm. In both cases, the sidewalls and the floor presented slight or little displacement and minor failures.

FLAC3D numerical modelling results also showed that the roof in the two stopes had high shearing and tension failures, signifying instability in the roof compared to the sidewalls and floor without artificial concrete pillars in place. Although the mine used as a case study is shallow, instability problems in the stope's roof are always challenging. Care must ensure the stope is adequately supported before mining commences. The other results presented in FLAC3D above in which the stope's roof experiences instability without artificial concrete pillars installed are the Local Force Ratio, Convergence zones, and State Failure By Average. In both cases, the results for the Local Force Ratio were very high on the roof and low on the floor and sidewalls. In both cases, the convergence zone results were very high (18 mm) on the roof and low on the sidewalls and floor (4 mm). Therefore, the two stopes used as case studies presented high rock mass deformation without artificial concrete pillars installed. Geotechnical instability problems are unlikely to be encountered in the sidewalls and floor, as presented in FLAC3D numerical modelling results, especially if the sidewalls were installed with reinforcement bolts during development. However, this study aimed to evaluate the stability and suitability of the artificial concrete pillars using a numerical simulation in FLAC3D. For this reason, reinforcement bolt analysis is not included in this study, but it is worth mentioning as it plays a role in maintaining excavation stability in stopping.

The results presented in both case studies with artificial pillars showed improved stability in the roof of the two stopes. Displacement Zone results showed further reduction stability before mining, 18 mm to 0.5 mm and 16 mm to 0.15 mm, respectively. This represents a 97% and 99% reduction in cases 1 and 2, respectively. The results also showed reduced or improved convergence stability after installing artificial pillars, which were 10 mm to 2 mm and 8.5 mm to 3 mm, respectively. This represents an 80% and 63% reduction in cases 1 and 2, respectively. The Convergence Zone results further showed improved results in the sidewalls and floor of the stope.

FLAC3D simulation results for Local Force Ratio results also revealed a further reduction in the simulation of the artificial concrete pillars, which was 1.0 x 10^+00 to 1.5 x 10^-00 and 7.0 x 10^-01 to 2.5 x 10^-01, respectively. Both cases present an 85% and 71% reduction for cases 1 and 2, respectively. The local force ratio results in the FLAC3D numerical model have made the roof stable after installing artificial concrete pillars in the stope.

As stated earlier, the failure state zone in FLAC3D numerical modelling results presented high shear zones and tensile failures in the roof before installing artificial concrete pillars. However, after installing artificial concrete pillars, the numerical simulation presented a different picture. The results presented after installing artificial concrete pillars showed further or improved stability in the roof of the two stopes. The roof in the two stopes improved stability with reduced tensile failures and shear zones.

Therefore, the results presented above for the two case studies showed further improvement in conditions before and after installing artificial concrete pillars. The FLAC3D numerical model has been used successfully to evaluate the suitability and stability of the artificial concrete pillars as temporal support systems in active stopes. The artificial concrete pillars simulated above in FLAC3D can support ground strata in adverse stopes. practical and experimental aspects of installing artificial concrete pillars are presented in Chapter Three, the primary challenge of which is quality control and assurance. This assertion is to meet the required concrete strength of more than 24MPa per guidance from the American Concrete Institute (ACI). Therefore, to achieve this maximum concrete strength, the material used for construction and the mixing design must be according to recommendations by the American Concrete Institute.

The results presented above have revealed that artificial concrete can be used as temporary support in active stopes. This is supported by the results presented before and after artificial concrete pillars were installed, as presented above, under Convergence Zones, Displacement Zones, Local Force Ratios, and State Failure Zones. Chapter Five discusses the results obtained in Chapter Four and compare them to other studies that have used FLAC3D numerical modelling to simulate stopes and pillars.

Chapter 5 : DISCUSSION OF THE RESULTS

5.1. Introduction

This Chapter discusses the results that have been presented in Chapter Four. This Chapter compares the results obtained in this study to other studies that used FLAC3D for the analysis. Empirical analysis has been used to evaluate the stability of open stopes and pillars. However, this study uses the numerical approach to evaluate the stability and suitability of artificial concrete pillars as a temporal support system in the active stope. The results presented in Chapter Four revealed that the innovative artificial concrete pillars can be successfully used as temporal support in active stopes. This Chapter discusses the following results for Displacement, Convergence, State Failure By Average, and Local Force Ratio globally.

5.1.1. Displacement Results

Displacement results in both case studies (SA-1498 and SA-1575 Stopes) without artificial concrete pillars were revealed to be high in the roofs of the two stopes, representing 18 mm and 16 mm, respectively. The results have also been compared to other studies for roof and sidewall displacement in the stopes. This study was compared to the study of Bali (2014) for the three-dimensional (3-D) numerical modelling encompassing the roof's stability in FLAC3D. In his study, various three-dimensional numerical models were developed using the FLAC3D program and calibrated against actual gase failure in displacement, as cited in Dean-Pelikan (2021). Similar results showed high displacement (25 mm) in the broader portion of the vertical gas well. He discovered that the clay layer between two strong strata induced high stresses on the gas well casing and caused high compressive strain at the gas well failure horizon (Bai, 2014). The study of Wang et al. (2022) on the evaluation of stope stability and displacement in a subsidence area using FLAC3D coupling was also compared to this study. The results showed that the roof of the roadway is more prone to rupture and deformation, and there is a particular hidden danger of instability (Wang et al., 2022). Based on the numerical prediction and analysis of the displacement and stress after excavation of the stope, it is known that the roof displacement (39 mm) of the analyzed stope is significantly larger (than that of the sidewall with the maximum displacement (Wang et al., 2022). This is a pronounced stress concentration at the maximum displacement point (Wang et al., 2022). However, the horizontal displacement results in the stopes presented are less and are also lower than the roof failure tendency (Wang et al., 2022). This is expressed in other words, the roof is more prone to vertical displacement after stope excavation and is regarded as a roof-falling accident, commonly observed in actual metal deposit mining operations (Wang et al., 2022). The earlier study of Wang et al. (2022) states that the other influence of the collapse area on the stope is mainly reflected in the roof displacement. As the stope is far away from the collapse area, the roof displacement decreases significantly, the maximum displacement is at the roof centre of the stope, and the maximum stress occurs at the corner of the stope (Wang et al., 2022). The study of Zhang et al. (2020) also conducted numerical modelling of shallow abandoned mined working subsidence affecting transport infrastructure. In their studies, the results show that the shear failure along the interfaces and the yield state of the rock mass over the excavation roof where it can be seen that a water table above the excavation floor triggers displacements that

exceed criterion 1 (marked by displacement co-incident with pore pressure of 20kPa in the roof centerline). The specific results of the modelling undertaken for the Dolphingstone collapse were also a result of roof failure in a room width of at least 2 m spans (Zhang et al., 2020).

Displacement results in both case studies (SA1498 and SA1575 Stopes) with innovative artificial concrete pillars installed were revealed to be low or reduced in the two stopes, with 97% and 99% decrease, respectively. The results have been compared with other studies for roof and displacement when pillars are left and improvised in the stopes as a temporal support system. The study of Dean-Pelikan (2021) for the numerical modelling of pillar stress redistribution during the retreat mining process was also compared to this study. This study was performed to understand the influences of model type (elastic vs plastic), pillar width-to-height ratio, and roof properties on the overall retreat mining process. The study discovered that plastic numerical models could capture the yield propagation within a pillar array, allowing for potential pillar failure investigation (Dean-Pelikan, 2021). The study further verified that the FLAC3D numerical model can successfully simulate pillar stability. This has also been aided in evaluating the stability and suitability of innovative artificial concrete pillars using FLAC3D for this study.

5.1.2. Convergence Results

Convergence results in both case studies (SA-1498 and SA-1575 Stopes) without innovative artificial concrete pillars were revealed to be high or prominent in analyzing stope stability, with 10 mm and 8.5 mm, respectively. Convergence is a critical parameter in assessing the stability of an underground opening since it is usually the amount of convergence in the rock mass around an excavation that determines whether or not the excavation is serviceable (Idris et al., 2015). Displacement convergence indices are generally site-specific (Idris et al., 2015). The index depends on the characteristics of rock mass stiffness, the intended use of the underground opening, and the design and code requirement (Zhang et al., 2020). The study of Idris et al. (2015) on stope stability was compared to this study for the convergence analysis. Similar results were noted in which horizontal convergence results were insignificant in causing instability problems. The roof convergence was higher in both studies; 10 mm to 8.5 mm were noted without artificial concrete pillars. The study of Sainsbury (2012) for discrete analysis of open stope also simulated horizontal convergence in the hangingwall access compared well to the observed displacements immediately before stoping. In addition, the study further stated that the area was observed to undergo instability in the toe of the hangingwall drive and the shoulders of the ore drives. The simulated convergence profiles are also consistent with the damage observed before stoping (Sainsbury, 2012).

Convergence results in both case studies (SA-1498 and SA-1575 Stopes) with innovative concrete pillars in place revealed a reduction (80% and 63% were recorded) or little or minor influence on the stability of the stope.

5.1.3. State Failure By Average

The state failure by average results to evaluate the failure mechanism involved in the instance before, and artificial concrete pillars were installed in the two stopes. After installing artificial

concrete pillars, the results verified a minor failure for shearing and tension in the stopes' roof. The results in this section were also compared to related studies. The study of Zhang et al. (2020) on the stability of artificial pillars under a regenerated mechanical environment in China also achieved similar results. Another study by Vishwanath (2019) investigated the performance of complex rock pillars with different width-to-height ratios and the effects of inclination, discontinuity, and blasting operations. He discovered that the factors influencing the failure mechanisms of the pillars include pillar inclinations, discontinuity, blast damage, roof conditions, and water conditions (Vishwanath, 2019). He further pointed out that numerical modelling can be used as a platform to understand the failure mechanisms of the pillars under these factors if adequately calibrated. Laboratory tests and numerical modelling were conducted to understand the failure mechanisms and to determine the pillar strength under the cited conditions (Vishwanath, 2019). FLAC3D numerical modelling has been used explicitly to evaluate the failure mechanism in the stope, in which shear and tension are more prevalent in the unsupported roof of the stopes (Vishwanath, 2019). The study further revealed reduced failure mechanisms where pillars are left as support systems (Vishwanath, 2019).

5.1.4. Local Force Ratio Results

The local force ratio results were in the same state as the convergence and displacement results. This section was also compared to the study of Vishwanath (2019), in which the stress or forces were significantly higher in the roof than in the sidewalls before pillars were considered. Her study further showed a significant reduction in the influence of stresses where pillars were left. Another study by Zhang et al. (2020) verified that pillars could reduce stresses in the stopes, especially in wide stope spans.

Therefore, with the results and comparisons presented above, the innovative artificial concrete pillars can help reduce the influence of the local force ratio in the broad span stopes, as given in the numerical modelling, with 80% and 71% in the two case studies, respectively. This study has typically also verified that the artificial concrete pillars can be used as a support system and can further reduce instability problems in stopes.

5.2. Conclusion

Overall, the displacement deformation of the artificial pillar is small in the sidewalls and floor of the two stopes. In contrast, the roof deformation of the two stopes supported with artificial concrete pillars is in a safe range. The deformation is consistent with the abovementioned plastic zones (Figures 4.19 and 4.27); all structures in the stope are stable, and instability and failure will not occur. This evaluation of the artificial concrete pillars to be used as support systems in active stopes demonstrates that the stability of the mine stope structure supported by artificial pillars and the self-stability of the pillar can meet the requirements of safe production in mines. To compare the above results, the relationship between field measure and numerical simulation at different points in a stope must be measured using displacement instruments or extensometers. The displacement is higher near the roof of the stope while lower in the sidewalls. The displacement in the roof is about 18 mm to 16 mm, close to the numerical simulation presented before artificial

pillars were installed in the two case studies, respectively. After installing artificial pillars, the displacement in the roof of the two stopes reduced to 0.5 mm and 0.15 mm, respectively, close to the maximum field measurement. By comparing the two different settlement curves, the roof's displacement resulted in the overlying strata's instability due to the large span for the stope. The next chapter, Chapter Six, concludes the study by considering the set objectives and recommendations.

Chapter 6 : CONCLUSIONS AND RECOMMENDATIONS

6.1. Conclusions

As Chapter One of this study mentioned, the main objective was to evaluate the stability and suitability of the innovative artificial concrete pillars in stopes in the long-hole open-stoping mining method with various geotechnical ground conditions. This was achieved using the scientifically rigorous numerical code FLAC3D. To accomplish this primary objective, it was necessary to define sub-objectives, which were completed as stated below in the concluding remarks.

The first sub-objective of this study was to develop the most appropriate and reliable methodology for designing the artificial concrete pillars. This has been achieved by identifying suitable locations to install artificial concrete pillars, comprised of wide-span stopes with geotechnical challenges such as weak rock mass. Rock Mechanics empirical methods were employed, which consist of rock mass classification systems of Rock Mass Rating (Geomechanical system), Q-system and Mathews modified stability graph. For the RMR Geomechanical system, the rock mass was deemed poor with a low RMR of less than 40, while the Q-system quantified poor rock mass with a value of less than 4. After that, the construction of artificial concrete pillars was also considered. This approach finds the Quality Assurance and Quality Control systems for concrete construction. According to the American Concrete Institute (2016), reliable and suitable concrete should have a design of aggregate (54.5%), cement (18.2%) and sand (27.3%) ratio to achieve 24Mpa strength after 28 days. The quality of water must be free from chemicals. The standard artificial concrete pillar with the stated design mix was tested with this design mix to determine its effectiveness during the blasting and hauling stages. The designed artificial concrete pillars with the above mix ratios have proven to be highly effective in withstanding blasting impact and stress effects from mining, providing a solid sense of safety and reassurance. This methodology is reliable and appropriate for long-hole open stopping, especially in areas with geotechnical challenges ranging from the wideness of orebodies that increase the hydraulic radius to poor rock mass conditions with low RMR, Q-value, and modified stability number. These values fall in the caving zones when plotting on the stability graph. In such instances, the placement of artificial concrete pillars was to be considered for the stability of stopes before drilling, blasting and hauling, ensuring the safety of men and equipment.

The second sub-objective of this study was to create a geotechnical database in the Excel spreadsheet. The database consisted of the three major identified rock units (footwall, orebody and hangingwall) in the SA1498 and SA1575 blocks, which are significant due to their [specific significance]. Central geotechnical data collected from the mapping are rock quality designation (RQD), uniaxial compressive strength (UCS), joint characteristics and spacing, groundwater condition and orientation. These primary data helped quantify Rock Mass Rating (RMR), Q-values, and Geological Strength Index (GSI). The other information in the database was the stope dimension, historical data regarding falls of ground, the type of support system installed before the stopes below were blasted, and the condition after blasting. A database for concrete samples was

also created, stating the date the sample was placed into the mould up to the due date for testing. The concrete samples were specified at 7 days, 14 days and 28 days. The strength, density, and age were recorded for each test. A database for field measurements was also created, in which a tape extensometer was used to measure convergence or displacement from the installed convergence pins in the two stopes. A comprehensive interval of every month was considered and conducted for up to five months. This thorough approach, conducted with utmost care, was facilitated to determine the convergence rate for comparison with numerical modelling results in FLAC3D.

The third sub-objective was to determine rock mass quality at different depths of the mine. SA1575 stope was located in the crown pillar (40 m below the surface), while SA1498 stope was located in the sill pillar (250 m below the surface). It was stated in Chapter Four that stress measurements have yet to be conducted at the mine site. This is a challenging task, as it is required to understand the magnitude and orientation of the stress fields at the mine site. Some mines shy away from this due to the cost of conducting the tests; it is indeed a costly technique. Therefore, the world stress map was used to estimate the stress field in this region, utilizing the k ratio value from 1 to 1.5. From the geotechnical analysis presented, the failures in the two stopes were different despite both being considered shallow. The shortcomings in SA 1575 were larger wedges or blocks that failed due to gravity; instead, it can be depicted that the blocks or wedges could move freely due to lack of confinement. This entails that the failures were related to tension stress contribution rather than compressive stress. Equally, in SA 1498, the failures observed from onsite were also more structural and some minor stress-related due to the stress loading of the sill pillar.

The fourth sub-objective of this study was to develop a numerical code that can aid in evaluating the stability and suitability of artificial concrete pillars. The numerical method developed for this analysis is a continuum modelling method called FLAC3D. Concrete, being isotropic or homogeneous in nature, is referred to as a continuum. This was achieved by following the numerical modelling steps below:

i. Setting up the objective.
ii. Formulating a conceptual picture of a model.
iii. Creating a simple model.
iv. Assembling specific data.
v. Running a series of detailed models.
vi. Performing numerical calculations and result interpretations.

FLAC3D model that was developed with its precision considered two material properties as input parameters: elastic deformability and rock mass strength properties, was a key component of this research. FLAC3D is a command-driven computer program that incorporates the FISH language. The numerical code, with its role in defining the boundary conditions to have values of field variables (e.g., displacement, and stress) prescribed at the numerical grid's boundary, was a testament to the precision of this research. FLAC3D numerical using commands was consistently used in the model, such as the excavation command, which uses the "zone relax command" that is applied for mining steps.

The fifth sub-objective of this study was to determine the material properties that can be used as geotechnical input parameters in the numerical model. Geotechnical data, collected through meticulous mapping, comprehensive laboratory tests, and precise field measurements, were crucial

in defining the material properties. This thorough data collection process was achieved by defining four units: footwall, orebody, hangingwall, and concrete. The roclab was used to define material properties by inputting the Uniaxial Compressive Strength (UCS), rock density, mi, Geological Strength Index (GSI) and Disturbance Factor (D). The values of s, mb, a, cohesion (C), internal friction angle (Φ) and Young's modulus (E) were obtained. Bulk Modulus (K) and Shear Modulus (G) were obtained using Equations 3.1 and 3.2 relating to Young's Modulus and Poisson's ratio. FLAC3D numerical modelling prefers to use Bulk and Shear modulus properties to define the material's elastic properties.

The final sub-objective of this study was to apply the developed modelling code to analyze the stability and suitability of artificial concrete pillars. After that, the results was compared with similar studies using the same numerical code. The numerical modelling was applied using two case studies of the same mine site but in different locations. Based on the analysis of plastic zone distribution (failure state by average) in the stope profile before and after innovative artificial concrete pillars were installed, it was found that there is a plastic destruction area occurring in the innovative artificial concrete pillars. However, the innovative artificial pillars are in a stable stress state with minor tension and shear failures after completion of the mining in the two stopes used as case studies, revealing that the designed structural parameters for the proposed artificial concrete pillars can effectively prevent the formation and destruction of plastic zones in the overburden rock mass above for both sill and crown conditions. This paves the way for a promising future for the project.

Overall, to define the main objective, it can be agreed that evaluated scenarios before and after artificial concrete pillars are installed in FLAC3D, that the stability and suitability of the artificial concrete pillars to be used as support systems for an underground environment are evaluated, in which the pillar displacement deformation is small. The roof deformation of the two supported stopes is also in safe range. The deformations are consistent with the abovementioned plastic zones; all structures in the two stopes are stable, and instability and failure are unlikely to occur. This demonstrates that the stability of two stopes supported by artificial concrete pillars can meet the requirements for the safe production of the mine, providing reassurance about the safety of the mine production.

6.2. Recommendations

The following are the recommendations that are drawn from this study based on the above findings:

1) Installing a multipoint borehole extensometer (MPBX) within the installed artificial concrete pillars or other field monitoring mechanisms is recommended based on real-time measuring. This will act as the basis for comparing numerical modelling and field measurements for displacement in the roofs of the stopes; field measurements will also help calibrate the simulation in FLAC3D simulation, which can be used for future research in rock engineering. The RAMJACK Rock Movement Monitoring system consisting of real-time monitoring of extensometers that are either active (e.g., instrumented cable bolts) or passive (MPBX – Multipoint Borehole Extensometers) rock support systems can be

adapted (Ramjacktech, 2023) for this purpose. These geotechnical instruments can measure the elastic deformation of the rock mass and any ground movement that occurs beyond the rock breakage. The proposal is to use the active extensometers (instrumented cable bolts), built to the required length (6-7m) and installed on the artificial pillars and shotcrete surfaces. A battery data logger can power the extensometer to capture and transmit the readings wirelessly. Ultimately, the data arrives at a gateway and is transmitted back to the mine's central server via the mine's communications infrastructure (Wifi, leaky feeder, etc). Data is stored in an SQL database.

2) A further methodology would be desirable to consider in monitoring the field stresses around the excavation rather than ignoring the stress change resulting from the excavation. Therefore, the field stress can be readily calculated using the digital MINSIM-D Boundary Element Program.

3) There is a need to increase the mould size to construct the concrete packs. Larger concrete packs will offer or increase the size of the artificial concrete pillar, further decreasing displacement and offering more stability to the stopes.

4) Improving the quality of concrete during the construction of artificial pillars is recommended. The aggregate, cement, sand, and water mixing ratio is critical to manufacturing artificial concrete pillars. According to the America Concrete Institute (ACI), the mixing design for concrete to achieve 24Mpa after 28 days must be cement (18.2%), sand (27.3%), and aggregate (54.5%) equal a ratio of 1:1.5:3, respectively (ACI, 2016). The ratio of water to cement should be maintained at 0.5 before mixing with aggregate and sand.
5) Artificial concrete pillars should be replicated in other places or countries like Zambia, where timber packs are used more extensively for support systems, especially in Vertical Crater Retreat (VCR) Chambers. This will help combat deforestation, which is a fight against climate change.

REFERENCES

ACI Committee 201. (2016). Guide to Durable Concrete (ACI 201.2R-16)," American Concrete Institute, Farmington Hills, MI, 84 pp.

Agar, R. A. (1992). The tectono-metallogenic evolution of the Arabian shield Precambrian Research, v. 58, Issues 1-4, pp. 169-194.

Ardiaca, D. H. (2009). Mohr-Coulomb parameters for modelling of concrete structures. Plaxis Bulletin.

Anderegg WRL, Trugman AT, Badgley G, Anderson CM, Bartuska A, Ciais P, et al.(2020). Climate-driven risks to the climate mitigation potential of forests. Science. 2020;368: eaaz7005–11. pmid:32554569

Bai, Q. S., Tu, S. H., Zhang, X. G., Zhang, C., and Yuan, Y. (2014). Numerical modeling on brittle failure of coal wall in longwall face—a case study. Arabian Journal of Geosciences, 7(12), 5067–5080

Barton, N., Grimstad, E., Aas, G., Opsahl, O.A., Bakken, A., Pedersen, L., and Johanson, E.D. (1990). Norwegian method of tunnelling. World Tunnelling and Subsurface Excavation, August, pp.324-331.

Batugin, S.A, and R. K. Nirenburg, R. K. (1972). J. Mining Sci. (Engl. Transl.) 8(1), 5–9.

Berge, J.W. 1981 Recent Investigations of Two Quartz Eye Porphyroidal Rock - Volcanogenic Massive Sulfide Occurrences in Economic Geology, v. —, pp. 1211-1216.

Bienawski, Z.T. (1976). Rock mass classification in rock engineering, Proceedings Symposium on Exploration for Rock Engineering, Johannesburg, Volume 1, pp. 97-106.

Bienawski, Z.T. (1989). Engineering rock mass classifications. New York: Wiley.

Bieniawski, Z.T. (1973). Engineering Classification of jointed rock masses. Trans. S. Afr. Inst. Civil Engineers 15, No. 12, 335-44.

Brady, B. and Brown, E. (2004). "Rock Mechanics for Underground Mining". George Allen & Unwin Ltd. Herts HP2 4TE, UK

Brady, B. G. and Brown, E. T. (2006). Rock Mechanics for underground mining. 3 ed. Dordrecht: Springer.

Brady, B.H.G. (1977). An analysis of rock behaviour in an experimental stoping block at the Mount Isa Mine, Queensland, Australia. International Journal of Rock Mechanics and Mining Science and Geornechanics Abstracts, pp. 1459 – 1466

Brady, B.H.G., and E. T. Brown. (1992). Rock Mechanics for UnderqroundMininq. London: George Allen & Unwin.

Brady, B.H.G., and E. T. Brown. (1985). Rock Mechanics for UnderqroundMininq. London: George Allen & Unwin, 1985.

Brown, G.F. and Jackson, R.O. 1959 Geologic Map of the Asir Quadrangle, Kingdom of Saudi Arabia. Miscellaneous Geological Map I-217A, scale 1:500,000.

Butler, R., Bruinsma, J.W., Andrews, K., Russell, N. and Spaargaren, F.A. (1975). Preliminary Flotation Investigation from Al Masane, Saudi Arabia. Report No. 3200, 27 p.

Carter, T.G. (2000). An Update on the Scaled Span Concept for Dimensioning Surface Crown Pillars for New or Abandoned Mine Workings. Proc. 4th North American Rock Mech. Conf., Seattle, pp.465-472Cougar, A. 2015.Technical data. HG 610 Blend-Technical data

Challiner, G. (2009). Email dated June 10, 2009 sent from Geoff Challiner to Steve McKinnon (Queen's University), Warren Newcomen (BGC Engineering Inc.) and Eric Harkonen (PEG Mining)

Chapman, C. (1994). Feasibility Study on the Al Masane Project for Arabian Shield Development Company.

Coates, D. (1981). Rock Mechanics principles.4th ed Ottawa: Department of Energy, Mines and Resources Canada

Clark, L. (2002). Minimizing dilution in open stope mining with a focus on stope design and narrow vein longhole blasting, Msc. Thesis, University of British Columbia, Canada, 316p

Clayton, R.H. (1979). Geophysical Surveys, February—March 1979, Wadi Qatan - Al Masane, Kingdom of Saudi Arabia for Arabian Shield Development Co. Private Report, 52 p

Cougar, A. (2014). Strata Jack Technical data. Patent# 2010257264.References for (Room and pillar/ Stopping Mines)

Conway, C. (1985). Geology of the A] Masane Ancient Mine Area, Southeastern Arabian Shield, Kingdom of Saudi Arabia. Open File Report 85-240, 101 p., scale 1:20,000

Cundall, P. A. (1971) "A Computer Model for Simulating Progressive Large Scale Movements in Blocky Rock Systems," Proceedinqs of the Symposium of the International Society of Rock Mechanics (Nancy, France, Vol. 1, Paper No. 11-8).

Daniels, J.R. (1977a). Area Report on Gossans and Fresh Sulfides from Wadi Saadah, Saudi Arabia. Australian Ores and Minerals Report to the Directorate General of Mineral Resources, Saudi Arabia, 29 p

David, W. (2017).Underground Mine Timbering &Supporthttps://www.911metallurgist.com/underground-mines-timbering-support/

Dean-Pelikan, R. (2021). Numerical modeling of pillar stress redistribution during the retreat mining process, PhD, thesis, Colorado School of Mines, United State of America.

Deliveris, V., Benardos, A. (2017). Evaluating performance of lignite pillars with 2D approximation 636 techniques and 3D numerical analyses. Int J Min Sci Technol. 27:929–36

Diederichs, M.S., and Kaiser, P.K. (1999). Tensile strength and abutment relaxation as failure control mechanisms in underground excavations. Int. Journal of Rock Mech. And Mining Sci. 36(1999) pp. 69-96.

Dodge, F.C.W. and Rossman, D.L. (1975). The Zinc-Copper-Silver-Gold Deposits of the Al Masane Area, Kingdom of Saudi Arabia. Arabian Shield Development Co., Private Report, 15 p

Elliott, J.E. (1980). The Tin—Bearing Granite of Jabal Al Gajarra in the Southern Arabian Shield, Kingdom of Saudi Arabia. United States Geological Survey, Saudi Arabian Mission, Technical Record 4, 28 p

Fernette, G. Neczkar, E. (1981). The Geology of the Al Masane Cu-Zn Deposits, Wadi Malaha Quadrangle South-Western Saudi Arabia. Private Report for Arabian Shield Development Co., 67 p.

Fernette, G. (1982). Progress Report on Exploration Activities at the Moyeath Gossan Massive Sulfide Deposit and the Al Aqeeq Gold Deposit, Al Masane Area, Saudi Arabia. Private Report for Arabian Shield Development Co., 44 p.

Fleck, R.J., Coleman, R.G., Cornwall, H.R., and Greenwood, W.R. (1976). Geochronology of the Arabian Shield, Western Saudi Arabia; K-Ar Results in Geological Society of America, Bulletin, v. 87, pp. 9-21

Ford, N.T., Pine, R.J. and Flynn, Z.N. (2007) Discrete fracture network modelling and characterisation of rock masses for block caving design. Proceedings 11th Congress of the

International Society for Rock Mechanics, Ribeiro eSousa, Ollala and Grossmann (editors), Taylor and Francis, Leiden, 1, pp. 231–236.

Gaede O, Schrank C, Canbulat I, Karrech A. (2014). A strain-based failure criterion for pillar stability 563 analysis. In Proceedings AusRock. Third Australasian Ground Control in Mining Conference 564 (pp. 393-398). The Australasian Institute of Mining and Metallurgy

Greenwood, W.R., Fleck, R.J., Coleman, R.G., and Cornwall, H.R. (1976). Geochronology of the Arabian Shield, Western Saudi Arabia; K-Are Results in Geological Society of America, Bulletin, v. 87, pp. 9-21

Greenwood, W.R. (1980a). Reconnaissance Geology of the Wadi Malahah Quadrangle, Sheet 18/43D, Kingdom of Saudi Arabia. Geology Map GM-39, 38 p., scale 1:100,000.

Greenwood, W.R. (1980). Reconnaissance Geology of the Wadi Malahah Quadrangle, Sheet 18/43D, Kingdom of Saudi Arabia. Geology Map GM-39, 38 p., scale 1:100,000

Griffs, A.T., Bates, J.A., Everard, J.F.and Edwards, A.T. (1977). Economic Evaluation of the Al Masane Copper-Zinc Deposits, Southwestern Saudi Arabia, for Arabian Shield Development Co. Private Report, 143 p.

Griffs, A.T., Bates, J.A., Everard, J.F.and Edwards, A.T.(2000). Feasibility study of Al Masane Al Kobra mine, Southwestern Saudi Arabia, for Arabian Shield Development Co. Private Report.

Goel RK, Jethwa JL, Paithankar, AG.(1995). Indian experiences with Q and RMR Systems, Tunnelling and Underground Space Technology, Vol 10, No.1, pp. 97–109

Goodman, R. E. (1989). Rock mechanics. New York: John Wiley & Sons

Hadjigeorgiou, J.,Grenon, M.,andLessard, J.F. (1998). Defining in-situ block size. CIM Bull. 91, 72–75.

Harbaugh, A.W., E.R. Banta, M.C. Hill, and M.G. McDonald 2000 MODFLOW. (2000). The United States Geological Survey Modular Ground-Water Model – User Guide to Modularization Concepts and the Ground-Water Flow Process. Open File Report 00-92, 130 p.

Helaby, A.M. and Dodge, F.C.W. (1976). The Jabal Guyan Ancient Gold Mine, Wadi Malahah Quadrangle (Sheet 18/43D), Kingdom of Saudi Arabia. Saudi Arabian Project Report 215.

Heyer, B. (1989). Review of feasibility study Al Masane project for Arabian Shield Development Company and National Mining Company.

Hoek, E., Kaiser, P. K., &Bawden, W. F. (1993). Support of Underground Excavations in Hard Rock. Vancouver: West Broadway Professional Centre.

https://docs.itascacg.com/FLAC3D700/common/docproject/source/manual/program_guide/program_guide.html?node67

https://ramjacktech.com/category/blogs/

Hedley, D.G.F and Grant F. (1972). Stope-and-pillar design for the Elliot Lake Uranium Mines. The Bulletin of the Canadian Institute of Mining and Metallurgy, vol. 65, pp. 37 – 44

Heidbach, O., Rajabi, M., Reiter, K., Ziegler, M., & Team, W. (2016). World Stress Map Database Release 2016. Retrieved April 15, 2021, from https://doi.org/ 10.5880/WSM.2016.001

Helmstaedt, H. and Scott, D.J. (1992). Proterozoic Crustal Evolution (Chapert 2). The Proterozoic Ophiolite Problem). Kent C. Condie Edition: illustrated, Published by Elsevier, pp. 65-67

Hottin, A.M. (1980). Al Masane, Annexe 1, Petrographic Study of 30 Thin Sections. Bureau De RecherchesGeologiques et Minieres, Open File Report, 14 p

Hoek, E., &Marinos, P. (2000). Predicting tunnel squeezing problems in weak heterogeneous rock masses. Tunnels and Tunnelling International, 32 (11), 45- 51

Hoek, E., Carranza-Torres, C., &Corkum, B. (2002). Hoek-Brown failure criterion2002 edition. In Proceedings of the Fifth North American Rock Mechanics Symposium (p. 267-273). Toronto.

Hoek, E., & Brown, E. T. (2000). Practical estimates of rock mass strength. International Journal of Rock Mechanics and Mining Science, 34 (8), 1165-1186.

Hutchinson, D.J. and Diederichs, M.S. (1996). Cablebolting in underground mines. BiTech Publishers Ltd. pp. 265-273

Hudyrna, M.R. (1988). Rib pillar design in open stope mining. MSc. Thesis, University of British Columbia, Vancouver, Canada.

Hocking, G., G.G.W. Mustoe, and J. R. Williams. (1985). "Validation of the CICE code for Ice Ride-Up and Ice Ridge Cone Interaction," in Civil Enqineerinq in the Arctic Offshore (Proceedinss of the Conference Arctic '85) , pp. 962-970. New York: ASCE.

Idris, M.A., Saiang. D., Nordlund E. (2015). Stochastic assessment of pillar stability at Laisvall mine using 592 Artificial Neural Network. TunnUndergrSp Technol. 49:307–19. 593 [15]

Itasca Consulting Group, Inc. (1989). Universal Distinct Element Code (UDEC), Version ICG1.5 User Manual. Minneapolis, Minnesota: Itasca Consulting Group, Inc.

Itasca Consulting Group, Inc. (1988). FLAC: Fast Laqranqian Analysis of Continua, User Manual, Version 2.1. Minneapolis: Itasca Consulting Group, Inc.

Itasca Consulting Group. (2013). FLAC3D: Fast Lagrangian Analysis of Continua in 3 Dimensions. User's Guide. Minneapolis, MN: Itasca Consulting Group Inc.

Itasca Consulting Group. (2021). FLAC3D: Fast Lagrangian Analysis of Continua in 3 Dimensions. User's Guide. Minneapolis, MN: Itasca Consulting Group Inc

Itasca Consulting Group. (2022). FLAC3D: Fast Lagrangian Analysis of Continua in 3 Dimensions. User's Guide. Minneapolis, MN: Itasca Consulting Group Inc

International Society for Rock Mechanics Commission on Standardisation of Laboratory and Field Tests. (1978). Suggested methods for the quantitative description of discontinuities in rock masses. Int. J. Rock Mech. Min. Sci. &Geomech. Abstr. 15, 319-368

Jackaman, B. (1972). Genetic and Environmental Factors Controlling the Formation of the Massive Sulfide Deposits of Wadi Bidah and Wadi Wassatt, Saudi Arabia. Technical Record TR-1972-1, 243 p

Jaeger, J. C. and Cook, N. G. W. (1999). Fundamentals of rock mechanics, John Wiley and Sons, Inc.

Jager, A.J and Ryder J.A. (1999). A Handbook on Rock Engineering Practice for Tabular Hard Rock Mines. The Safety in Mines Research Advisory Committee (SIMRAC) Publications

Kaiser, P.K., Falmagne, V., Suorineni, F.T.,Diederichs, M., Tannant, D.D. (1997). Incorporation of rockmass relaxation and degration into empirical stope design. CIM AGM , Vancouver.

Kaiser, P.K., McCreath, D.R and Tannant, D.D. (1996). The Canadian Rockburst. Canada.

Kirsch, E. G. (1898). Die Theorie der Elastizit¨at und die Bed¨urfnisse der festigkeitslehre. Zeitschrift des VereinesdeutscherIngenieure, 42 , 797-807.

Kulhawy, F. H. (1975). Geomechanical Model for Rock Foundation Settlement,ll J. Geotech. Engr., 104, 211-227.

Krauland, N and Soder, P.E. (1987). Determining pillar strength from pillar failure observation. Engineering and Mining Journal, vol. 8, pp. 34 – 40.

Lang, B.D.A. (1994). Span Design for Entry-Type Excavations. PhD Thesis, University of British Columbia, Vancouver, BC, Canada.

Laubscher, D.H. (1993). Geomechanics classification of jointed rock mass – mining applications. Trans. Inst. Min. Metall., 86, A1 – A8.

Laubscher, D.M and Page, C.H. (1990). The design of rock support in high stress or weak rock environments. Proceeding of the 92nd Canadian Institute of Mining and MetallurgyAnnual General Meeting, vol. 91. Ottawa: Canadian Institute of Mining and Metallurgy.

Laubscher, D.H. (1990). A geomechanics classification system for the rating of rock mass in mine design. The Journal of The Southern African Mining and Metallurgy, vol. 90, no. 10, pp. 257 – 273.

Laubscher, D.H. (1984). Design aspects and effectiveness of support systems in different mining conditions. Transactions International Journal of Mining and Metallurgy, vol. 93, A70 - A82.

Laubscher, D.H and Taylor, H.W. (1976). The importance of geomechanics classification of jointed rock masses in mining operations. In Bieniawski-ZT (Ed.), Exploration for rock engineering, vol. 1, pp. 119 – 128. Cape Town: Balkema.

Laubscher, DH. (1977). Geomechanics classification of jointed rock masses - mining applications. Trans International Institute of Mining and Metallurgy, vol. 86, pp. A1 – 8.

Laubscher, D.H and Taylor, H.W. (1976). The importance of geomechanics classification of jointed rock masses in mining operations. In Bieniawski-ZT (Ed.), Exploration for rock engineering, vol. 1, pp. 119 – 128. Cape Town: Balkema

Lauffer, H. (1958). Gebirgsklassifizierung fur den stollenbau. geologie und bauwesen, Volume 24, Number 1, pp. 46-51

Lawrence, R.D. (2007). Review of 1982 Feasibility Study Al Masane Project for Arabian Shield Development Company and National Mining Company.

Lemos, Jose. (1987). "A Distinct Element Model for Dynamic Analysis of Jointed Rock with Application to Dam Foundations and Fault Motion," Ph.D. Thesis, University of Minnesota.

Lunder, P.J and Pakalnis, R. (1997). Determination of the strength of hard-rock mine pillars. The Bulletin of the Canadian Institute of Mining and Metallurgy, vol. 90, no. 10, pp. 51 – 55.

Lunder, P.J. (1994). Hard rock pillar strength estimation: An applied empirical approach. MSc thesis, University of British Columbia, Vancouver, Canada.

Madden, B.J. (1991). A re-assessment of coal-pillar design. Journal of The South African Institute of Mining and Metallurgy, vol. 91, pp. 27 – 37.

Martin, C.D and Maybee, W.G. (2000). The strength of hard-rock pillars. International Journal of Rock Mechanics and Mining Sciences, vol. 37, no. 4, pp. 1239 – 1246.

Mathews, K.E., Hoek, E., Wyllie, D., and Stewart, S.B. (1981). Prediction of stable excavation spans for mining below 1000 meters in hard rock, Canada: CANMET, Dept. of Energy, Mines and Resources, DSS Serial No. OSQ80-00081, DSS File No. 17SQ.23440-0-9020.

Martin, C.D., Read, R. S and Martino, J. B. (2000). Observation of brittle failure around a circular test tunnel. International Journal of Rock Mechanics: Mining Science and Geomechanical Abstracts, vol. 34, no. 7, pp. 1065 – 1073.

Napa-García, GF, Câmara TR, Navarro Torres VF. (2019). Optimization of room-and-pillar dimensions 568 using automated numerical models. Int J Min Sci Technol; 29:797–801.

Neczkar, E. (1984). Revised ore reserve estimate Al Masane mine Saudi Arabia.

Nickson, S.D. (1992). Cable support guidelines for underground hard rock mine operations. M.Sc. Thesis, University of British Columbia.

Obert, L and Duvall, W.I. (1967). Rock Mechanics and the Design of Structures in Rock. John Wiley and Sons.

Ozbay, M.U., Ryder, J.A and Jager, A.J. (1995). The design of pillar systems as practised in shallow hard-rock tabular mines in South Africa. The Journal of The South African Institute of Mining and Metallurgy, vol. 84, no. 8, pp. 7 – 18.

Overstreet, W.C., Hubert, A.E., Crenshaw, G.L., and Mosier, E.L. (1976). Petrogenetic Significance of Minor Elements in Pyritic Core from the Wadi Wassatt Massive Sulfide Deposit, Kingdom of Saudi Arabia. Saudi Arabian Project Report 214, 116 p., Open File Report 76-863.

Palmström, A. (1995). RMi – a rock mass characterization system for rock engineering purposes. PhD thesis, University of Oslo, Department of Geology.

Potvin, Y. (2017). Design guidelines for open stope support. Rock Mech Eng Vol 3 Anal Model Des. 610:903–14.

Potvin, Y., Hudyma, M.R and Miller, H.D.S. (1989). Design guidelines for open stope support. The Bulletin of Canadian Mining and Metallurgy, vol. 82, pp. 53 – 62

Potvin, Y., Hudyma, M.R and Miller, H.D.S. (1989). Design guidelines for open stope support. The Bulletin of Canadian Mining and Metallurgy, vol. 82, pp. 53 – 62.

Purwanto, Shimada, H., Takashi, S., Wattimena, R. K., & Matsui, K. (2013). Influence of Stope Design on Stability of Hanging Wall Decline in Cibaliung Underground Gold Mine. International Journal of Geosciences, 4, 1-8

Riofinex Geological Mission (1978). An Investigation of the Geology and Exploration Potential of the Wadi Wassatt-Kutam District, Southeast Asir, Saudi Arabia. Report, RF-1978-3, 130 p

Roberts, R.G. and Reardon, E.J. (1978). Alteration and Ore Forming Processes at Matagami Lake Mine, Quebec. Canadian Jour. Earth Sci., v. 15, pp. 1-21.

Roberts, R.J., Rye, R.0., and Mawad, M.M. (1978. Preliminary Sulfur Isotope Investigations of Mineral Deposits in the Precambrian Shield, Kingdom of Saudi Arabia. Saudi Arabian Project Report 246, 19 p.

Roberts, R..J., Rossman, D.L., Bagdady, A.Y., Conway, C.M., and Healby, A.M. (1981). Iron Sulfide Deposits at Wadi Wassatt, Kingdom of Saudi Arabia. Saudi Arabian Mission, Technical Record 17, 129 p.

Ryder, J.A and Jager, A.J. (2002). A text book on Rock Mechanics for tabular hard rock mines. Johannesburg, South Africa: The Safety in Mines Research Advisory Committee (SIMRAC)

Sabir, H. and Pouit, G. (1982). An Overview of Volcanogenic Massive Sulfide Mineralizations in Saudi Arabia (abs.) in Pan—African Crustal Evolution in Arabia and Northeast Africa. Precambrian Research, v. 16, pp. A55.

Sahoo SK, Singh GSP, Sharma SK, Singh UK. (2000). Numerical Modeling Study of the Influence of 630 Softcover on Strata and Support Behavior in a Bord and Pillar Depillaring Working. Mining, Metall 631. 37:1151–68.

Sainsbury, B. (2012). A model for cave propagation and subsidence assessment in jointed rock masses. Ph.D. thesis. University of New South Wales, Sydney, Australia.

Salamon, M.D.G. (1983). The role of pillars in mining, Rock mechanics in mining practice. (S. Budavari, Ed.) The South African Institute of Mining and Metallurgy, pp. 173 – 200.

Sinha, Sand Walton, G. (2021). Investigation of pillar damage mechanisms and rock-support interaction using 638 Bonded Block Models. Int J Rock Mech Min Sci. 138:104652.

Shaheen and Peaker Limited. (1994). Al Masane Water Supply Alternatives Feasibility Study, prepared for Arabian Shield Development Company c/o Watts, Griffis and McOuat Limited

Smith, C.W. (1981). Preliminary Correlation of Layered Rocks in the Tathlith—Kutam Region, Kingdom of Saudi Arabia, with a Note on Previously Unreported Mineral occurrences in the Tathlith Area. Saudi Arabian Mission, Misc. Document 27, 26 p

Sofiano, A. I., &Nomikos, P. P. (2006). Equivalent Mohr-Coulomb and generalized Hoek-Brown srength parameters for supported axisymmetric tunnels in plastic or brittle rocks. International Journal of Rock Mechanics & Mining Sciences, 43 , 683-704.

Swart, A. H. (2005). Investigation of factors governing the stability of stope panels in hard rock mines in order to define a suitable design methodology for shallow mining operations. MSc Thesis. University of Pretoria, Pretoria, South Africa

Sinha, S. (2020). Advancing continuum and discontinuum models of brittle rock damage and rock-support interation. (Doctoral dissertation, Colorado School of Mines).

Sinha, S., and Walton, G. (2018). A progressive S-shaped yield criterion and its application to rock pillar behavior. International Journal of Rock Mechanics and Mining Sciences, 105, 98–109

Salamon, M.D.G and Munro, A.H. (1967). A Study of the Strength of Coal Pillars. The Journal of the South African Institute of Mining and Metallurgy, vol. 68, no. 4, pp. 56 – 66.

Stacey, T.R and Page, C.H. (1986). Practical Handbook for Underground Rock Mechanics (Series on Rock and Soil Mechanics). Trans Tech Publications

Stacey, J.S., DelevauxM.H., Gramlich, J.W., Doe, B., and Roberts, R.J. (1980). A Lead Isotope Study of Mineralization in the Arabian Shield. Saudi Arabian Mission, Technical Record 8, 30 p.

Salamon, M.D.G. (1982). Unpublished report to Wankie Colliery. Wankie, Zimbabwe.

Stagg, K. G. and Zienkiewicz, OC. (1968). Rock Mechanics in Enqineerinq Practice. New York: John Wiley & Sons.

Stoesser, O.E. and Elliott, J.E. (1979). Post Orogenic Peralkaline and Calc—Alkaline Granites and Associated Mineralization of the Arabian Shield, Kingdom of Saudi Arabia. Saudi Arabian Mission, Project Report 265, 42 p.

Sjoberg, J. (1992a). Failure modes and pillar behaviour in the Zinkgruvan mine. Rock Mechanics. Lulea University, Department of Mining Engineering. Rotterdam: Balkemia.

Spencer, D.A. (2010). Hard Rock Tabular Mining: Regional and Support Pillars. A lecture delivered to GDE (rock engineering) students class of 2010 . Witwatersrand University, Johannesburg, South Africa.

Swart, A.H. (2005). Investigation of factors governing the stability of stope panels in hard rock mines in order to define a suitable design methodology for shallow mining operations. MSc Thesis. University of Pretoria, Pretoria, South Africa

Theim, G. (1906). HydrologisheMethode. Leipzig, Gebhardt

Vermeer, P. A., and De Borst, R. (1984). Non-associated plasticity for soils, concrete and rock. HERON, 29(3), 1984.

Vishwanath, J. K. (2018). Investigating the Performance of Hard Rock Pillars with Different Width to Height Ratios and the Effects of Inclination, a Discontinuity and Blasting. Ph.D. Thesis, Curtin University, Australia.

Vita-Finzi, C and A. Saadi, A. (2001). Pliocene-Quaternary fault control of sedimentation and coastal plain morphology in NE Brazil, J. South Am. Earth Sci., 14, 61–75

Von Kimmelmann, M.R., Hyde, B and Madgwick, R.J. (1984). The use of computer applications at BCL Limited in planning pillar extraction and design of mining layouts. In Brown-ET-Hudson-JA (Ed.), Proceedings of the International Society for Rock Mechanics (ISRM) Symposium: Design and Performance of Underground Excavations, pp. 53 – 63. London: British Geotechnical Society.

Walls, EJ., Mpunzi, P and Joughin, WC. (2015). Room and pillar stability analysis using linear elastic modelling and probability of failure- a case study. Australian Centre for Geomechanics, Perth, ISBN 978-0-9924810-3-2

Watts, Griffis and McOuat Limited Chapman, C. (2007). Feasibility Study on the Al Masane Project for Arabian Shield Development Company.

Watts, Griffis and McOuat Limited Chapman, C. (1994). Feasibility Study on the Al Masane Project for Arabian Shield Development Company.

William, J. (2022). Timbering of small mines. https://www.911metallurgist.com/underground-mines-timbering-support/

Wang, L.; Zhang, X.; Yin, S.; Zhang, X.; Jia, Y.; Kong, H. (2022). Evaluation of Stope Stability and Displacement in a Subsidence Area Using 3Dmine–Rhino3D–FLAC3D Coupling. Minerals 2022, 12, 1202. https://doi.org/10.3390/ min1210120

Wandke, A.D. (1977). Al Masane Massive Sulfide Zone, Saudi Arabia, for Arabian Shield Development Co. Private Report, 7 p.

Wagner, H. (1980). Pillar design in coal mines. Journal of the South African Mining and Metallurgy, vol. 80, pp. 37 – 45.

Wagner, H and Salamon, M.D.G. (1979). Practical Experience in the Design of Coal Pillars. Safety in Mines Research Proceedings of the 21st International Conference. Sydney, October: Safety In Mines Research Advisory Committee.

Wang, X.; Zhu, W.; Xie, J.; Han, H.; Xu, J. (2022).Borehole-Based Monitoring of Mining-Induced Movement in Ultrathick-and-Hard Sandstone Strata of the Luohe formation.

Won, R.G. (1979). The Jabal Ishmas-Wadi Tathlith Gold Belt, Kingdom of Saudi Arabia. Saudi Arabian Mission, Project Report 264, 108 p.

Xingdong, Z., Huaibin, Li., Shujing. Z and Xiaoming Y. (2022). Stability Analyses and Cable Bolt Support Design for A Deep Large-Span Stope at the Hongtoushan Mine, China. 11(21), 6134; https://doi.org/10.3390/su11216134

Zamten, V. (1986). Geotextiles and Membraines in civil engineering. AA Balkema/ Boston ISBN 9061916240 Page 158

Zaki, M. (2022). Long Hole Mining Method Modeling. Retrieved from https://promine.com/blog-en/long-hole-mining-method-modeling/

Zhou J, Li X, and Mitri, HS. (2015). Comparative performance of six supervised learning methods for the 594 development of models of hard rock pillar stability prediction. Nat Hazards. 79:291–316.

Zhang S, Wang XF, Fan GW, Zhang DS, Cui JB. (2018). Pillar size optimization design of isolated island panel gob-side entry driving in deep inclined coal seam-case study of Pingmei No. 6 coal seam. J Geophys Eng. 2018;15:816-828.

Zhang, P, Dougherty. H, Su. D, Trackemas, T, and Tulu, B. (2020). Influence of longwall mining on the stability of gas wells in chain pillars. International Journal of Mining Science and Technology, vol. 30, no. 1, pp. 3–9, 2020

Zvarivadza, T. (2012). Evaluation of Pillar Design Systems for Low Reef Platinum Mining. MSc Thesis. University of Witwatersrand, Johannesburg, South Africa

APPENDICES

Appendix 1: Geotechnical Mapping Sheet for data collection

section ID	From	To	Discontinuity Type	INTACT ROCK STRENGTH (IRS)		ROCK QUALITY DESIGNATION (RQD)		SPACING OF DISCONTINUITIES (JS)		A1	CONDITION OF DISCONTINUITY (JC)										A2	GROUNDWATER CONDITION (GWC)		ADJUSTMENT FOR DISCONTINUITY ORIENTATIONS		A3	RMR TOTAL RMR (A1+A2+A3)	ROCK MASS CLASS	GSI	Q-VALUE
											Persistence		Aperture (mm)		Roughness		Infilling (mm)		Weathering											
			Jn	value(Mpa)	Rating	value (%	Rating	value(cm)	Rating		value	Rating	value	Rating	Description	Rating	Description	Rating	Description	Rating		Description	Rating	Description	Rating					

Appendix 2: Displacement measurements data form

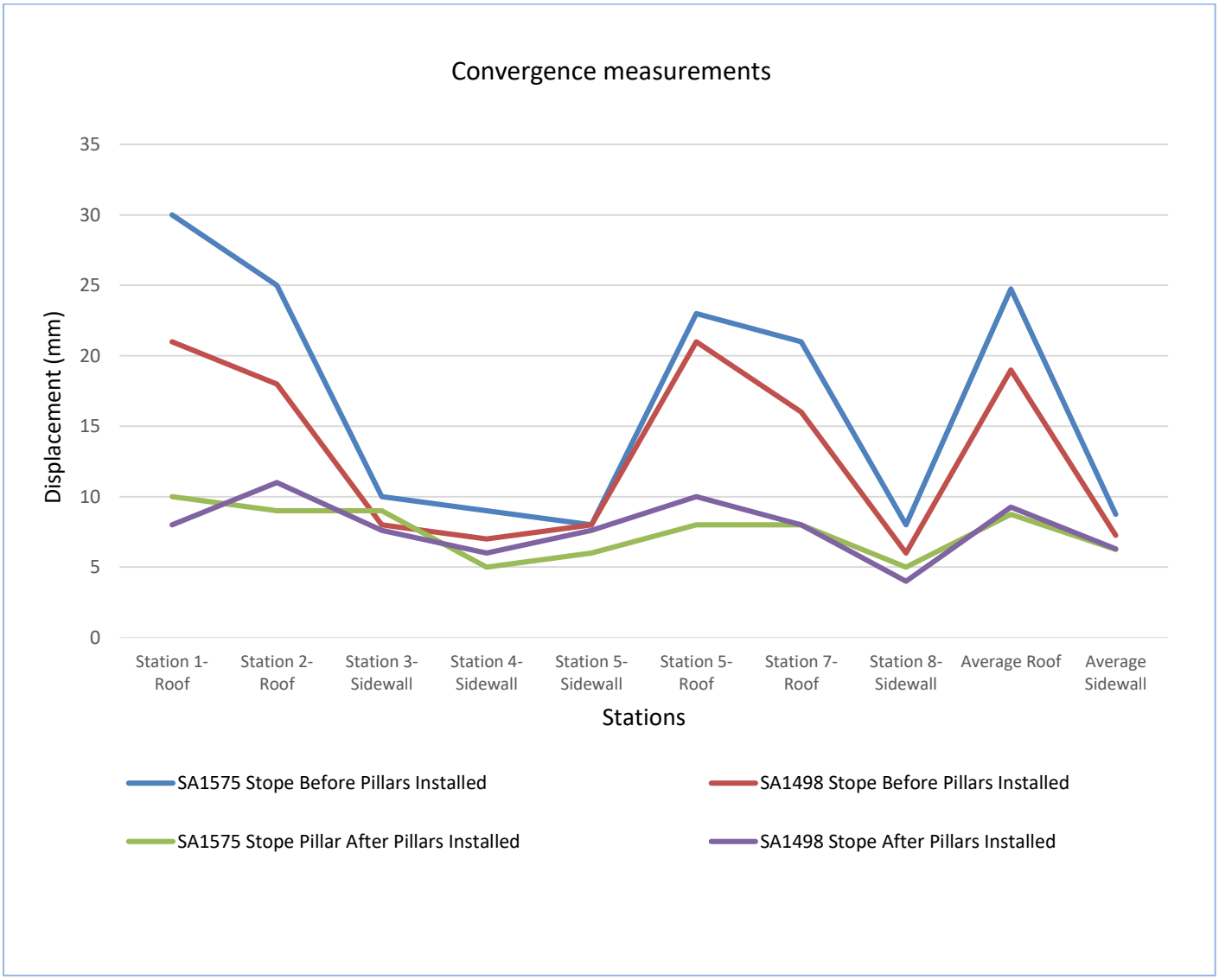

Appendix 3: FLAC3D Script

```
FLAC3D>model deterministic on
FLAC3D>model precision 6
FLAC3D>model random 10000

FLAC3D>project new
FLAC3D>model deterministic on
FLAC3D>model precision 6
FLAC3D>model random 10000
FLAC3D>program call "first.dat"
FLAC3D>model restore "pillars1"
******************************************
Type: ITASCA SAVE FILE
Created By: FLAC3D 7.00.141
Date: Tue Aug 1 16:49:51 2023
Total Cycles: 0 SuperCycles 0
Title:
Customer:
:
******************************************
FLAC3D>zone face skin
--- 542 surface faces found.
--- 6 surface face collections found.
--- 542 surface faces assigned names in slot Skin.
FLAC3D>zone face apply velocity-x 0 range group "east" or "west"
--- Apply conditions added to 110 gridpoints.
FLAC3D>zone face apply velocity-y 0 range group "south" or "north"
--- Apply conditions added to 256 gridpoints.
FLAC3D>zone face apply velocity 0 0 0 range group "bottom"
--- 48 gridpoints with conflicting conditions had those conditions removed.
--- Apply conditions added to 143 gridpoints.
FLAC3D>
FLAC3D>; properties in kPa
FLAC3D>zone property density 2.8 young 40e3 poisson 0.24 range group "hangingwall"
--- Property young set in 340 zones using the mohr-coulomb model.
--- Property poisson set in 340 zones using the mohr-coulomb model.
FLAC3D>zone propert density 2.7 young 50e3 poisson 0.25 cohesion 4 friction 30 range group "orebody"
--- Property young set in 480 zones using the mohr-coulomb model.
--- Property poisson set in 480 zones using the mohr-coulomb model.
--- Property cohesion set in 480 zones using the mohr-coulomb model.
--- Property friction set in 480 zones using the mohr-coulomb model.
FLAC3D>zone property density 2.8 young 45e3 poisson 0.26 cohesion 7 friction 40 range group "footwall"
--- Property young set in 290 zones using the mohr-coulomb model.
--- Property poisson set in 290 zones using the mohr-coulomb model.
--- Property cohesion set in 290 zones using the mohr-coulomb model.
--- Property friction set in 290 zones using the mohr-coulomb model.
FLAC3D>model gravity 9.81
--- Gravity has been set to: ( 0.000000e+00 0.000000e+00 -9.810000e+00).
FLAC3D>zone ini-stress ratio 1.5
--- Stresses initialized in 1110 zones.
FLAC3D>model large-strain off
FLAC3D>model solve elastic
Cycle Total Timestep Mech Ratio Clock
--------- ---------- ----------- ---------- -----------
293 293 1.00000e+00 9.9708e-06 00:00:00:01
```

```
1.0000e-05
--- Limit ratio of 1.0000e-05 met in process(es): mech Zone Main (9.9708e-06),mech Ball (0.0000e+00),mech
Clump (0.0000e+00),mech RBlock (0.0000e+00),mech Struct Main (9.9708e-06),mech BlockMechanical
(0.0000e+00).
--- Cycling ended at: 2023-08-16 07:23:09
Cycle Total Timestep Mech Ratio Clock
--------- ---------- ----------- ---------- -----------
14151 14444 1.00000e+00 4.6841e-04 00:00:03:05
1.0000e-05
--- Cycling ended at: 2023-08-16 07:26:14
*** Processing interrupted by user.
While processing line 14 of source C:/Users/POWER/Documents/Itasca/FLAC3D700/My Projects/first.dat.
FLAC3D>model restore "SA1575CrownPillar.sav"
**********************************************
Type: ITASCA SAVE FILE
Created By: FLAC3D 7.00.141
Date: Tue Aug 1 15:28:53 2023
Total Cycles: 0 SuperCycles 0
Title:
Customer:
:
**********************************************
FLAC3D>project new
FLAC3D>model deterministic on
FLAC3D>model precision 6
FLAC3D>model random 10000
FLAC3D>model restore "SA1575CrownPillar.sav"
**********************************************
Type: ITASCA SAVE FILE
Created By: FLAC3D 7.00.141
Date: Tue Aug 1 15:28:53 2023
Total Cycles: 0 SuperCycles 0
Title:
Customer:
:
**********************************************
```

Appendix 4: Estimate of the Geological Strength Index (GSI)